Investigating Potential Nano- and Micro-Drug Delivery Systems toward the Non-invasive Treatment of Glioblastoma Brain Tumours

KINANA HABRA

A thesis submitted in partial fulfilment of the requirements of Nottingham Trent University for the degree of Doctor of Philosophy

June 2023

Copyright statement

This work is the intellectual copyright of the author. You may copy up to five per cent of this work for private study, or personal, non-commercial research. Any reuse of the information contained within this document should be fully referenced, quoting the author, title, university, degree level and pagination. Queries or requests for any other use, or if a more substantial copy is required, should be directed in the first instance to the owner of the Intellectual Property Rights.

Abstract

Glioblastoma is one of the most aggressive and fatal brain tumours and is uncurable in most cases. The complete removal of glioblastoma brain tumours (GBM) is impossible by surgery alone. Despite aggressive chemotherapy and radiotherapy treatments following surgery, tumour cells continue to grow, leading to the death of patients within 15 months after diagnosis. The carnosine dipeptide is an attractive option for treating GBM, with growing numbers of studies now demonstrating its tumour accessibility, resulting in improved survival in pre-clinical GBM models. Several attempts at carnosine treatments have been developed and tested in GBM patients, however, these trials have not progressed due to the short lifetime of carnosine as a result of its enzymatic degradation in the presence of the naturally occurring carnosinase enzyme in the brain. This project aims to investigate the potential of using nano- and micro-drug delivery systems for non-invasive treatment of GBM for applying carnosine as a complementary therapy.

Carnosine was successfully embedded within a carrier that can be externally triggered to release its full oncological treatment potential of the dipeptide in situ. The drug delivery device was comprised of novel nano-rod-shaped superparamagnetic iron oxide nanoparticles (*ca*. 86 × 19 × 11 nm) capped with a branched polyethyleneimine, capable of loading carnosine. The therapeutic agent was released by the drug delivery carrier in the presence of heat or a rotating magnetic field, as an external trigger. The new drug delivery system was characterised using electron microscopy, dynamic light scattering, elemental analysis, and magnetic resonance imaging (MRI) techniques. In addition, the cytotoxicity studies were also investigated which enabled the determination of the safety margin of applying the coated iron oxide nanorods on U87 MG cells.

To determine the effectiveness of the carnosine delivery systems as a treatment for glioblastoma, the coated iron oxide nanorods were screened *in vitro* using the U87 MG human glioblastoma astrocytoma cell line. Labile carnosine (100 mM) was determined to suppress the proliferation and mobility of U87 MG cells within 48 hours, significantly reducing migration and potential metastasis. The cytotoxicity studies enabled calculating the half maximal inhibitory concentration (IC50) and the half maximal effective concentration (EC50) of the carnosine. The active carnosine was found to be fully released from the carrier, with only mild hyperthermia conditions at 40 ˚C being necessary. This is achievable in clinical applications, for both sustained and triggered release treatment of glioblastoma brain tumours, utilising the paramagnetic properties of iron oxide nanorods. This demonstrates the potential to inhibit post-surgery metastasis with the benefit of non-invasive monitoring *via* MRI scanning.

The controlled release of carnosine treatment was also inspected by applying external trigger. Therefore, the nano-rod-shaped superparamagnetic iron oxide and the carnosine were encapsulated inside poly(lactic-co-glycolic acid) beads (10 μm) using a hydrodynamic microfluidic flow focusing system, and the formulation was characterised by scanning and transmission electron microscopy (SEM, TEM)

and Fourier-transform infrared spectroscopy (FT-IR). A non-heating rotating magnetic field (Halbach magnet array, 1 Tesla, 20 Hz, 30 min) was utilised to stimulate the release of carnosine from the polymeric beads by rotating the nano rods from distance. Additional potential treatment in intranasal application was also investigated *via* a spray device. The microfluidic flow focusing system was utilised to encapsulate the carnosine therapeutic inside a liposome (*ca.* 300 nm diameter) matrix with a stability profile of 30 days. The sub-microscale size of the liposomes and the mucoadhesive properties were expected to enhance the nasal bioavailability of carnosine over a prolonged time. The liposomal formulation was optimised to load the carnosine (75% w/w). The characterisation of the liposomes was confirmed *via* microscopic imaging, dynamic light scattering (DLS), Liquid chromatography–mass spectrometry (LC-MS), and Fourier-transform infrared spectroscopy (FT-IR). The stability and sustained release profiles were investigated using physicochemical studies of membrane dialysis over time. The carnosine-loaded liposomes were stable (30 days at 8 ˚C) as a ready-to-use suspension for intranasal spray application. Overall, these results provide a promising optimised formula for complementary carnosine treatment, which is recommended to be studied *in vivo* in rat models in the near future.

Spheroids, a complex 3-dimensional (3D) structure, resemble *in vivo* tumour growth more closely. As part of this project, a protocol has been developed towards a rapid and high throughput method for the generation of single spheroids using various cancer cell lines, including different cancer cells (U87 MG, SEBTA-027, SF188), prostate cancer cells (DU-145, TRAMP-C1) and breast cancer cells (BT-549, Py230) in 96-round bottom well plates. The proposed method was associated with significantly low costs per plate without the need for refining or transferring. The homogeneous compact spheroid morphology was evidenced within one day after following this new protocol. Proliferating cells, on the surface of the spheroid, were traced using confocal microscopy and the Incucyte® live cell analysis system. In contrast, dead cells were found to be located inside the core region of the spheroid. Hematoxylin and eosin (H&E) staining of spheroid sections was utilised to investigate the tightness of the cell packaging. This method enabled the determination of the EC50 of the anti-cancer dipeptide carnosine on a U87 MG 3D culture. This new protocol allows for the robust generation of various uniform spheroids that show 3D morphological characteristics. As such, further studies will be developed towards an *in vivo* animal model to demonstrate the potential clinical viability of this work on various cancer types, such as brain and prostate tumours.

Acknowledgements

Firstly, I acknowledge all my supervisory team, specially, Dr. Stéphanie E. B. McArdle, and Prof. Robert H. Morris who have been an enduring supply of invaluable knowledge and inspiration throughout my studies. Also, I appreciate the efforts of my independent supervisors Prof. Pierscionek, Dr. Tinsley, and Dr. Cross who used to provide constructive and encouraging comments.

I would like to express my appreciation and gratitude to Nottingham Trent University and the Council for At-Risk Academics (CARA) fellowship program for the generous award and significant support along the tough and good times of the last five years. This opportunity made a huge turn in my personal and professional life.

I acknowledge the following contributions:

• Dr. David Boocock and Dr. Clare Coveney for supporting the analytical work of LC-MS assays which were presented in two published papers.
• Dr. Graham Hickman and Dr. David J. Belton for the constant support and knowledge in optimal imaging. There technical support with the electron, scanning, and confocal microscopy studies helped to publish significant figures in many papers and posters.
• Dr. Alan Hargreaves and Dr. Biola Egbowon for their support with the cell differentiation techniques.
• Dr. Gemma Foulds for the support during the development of flow cytometry method.

I would like to dedicate my warmth thanks to the best examples of kindness and professional attitude in mentoring the research environment where we can thrive and develop creative ideas; Prof. Wallis, Dr. Garner, Dr. Moss, Dr. Hanley, Prof. Rutella, Prof. Perry and Emma Rixon.

I acknowledge the precious support from the technical staff in different labs, especially, Barabara and Diago, the post doc research fellows, and the PhD students.

My sincere thanks go to the Global lounge team for the unforgettable memories I had as an assistant on both campuses for over five years. Stephen, Cheryl, Dona, Kat, Maggie, Sam, Ajay, and Kitty all mean a lot to me. Also, many thanks to the library, employability, wellbeing, and security teams for being the backbone of Nottingham Trent University under any circumstances.

Last but not the least, I dedicate my special thanks to my son ‘Kinan’ who was my whole family in the UK. His mature attitude made it all possible by following his natural kind intuitions. He was never tired of telling me ‘I love you’ in uncountable ways to make me smile. He tried to keep me sane during tough times and provided me with determination no matter how bad luck was lingering.

Contents

Copyright statement 2
Abstract 3
Acknowledgements 5
Contents 6
List of figures 11
List of tables 23
List of abbreviations 24
Chapter 1: Literature review 27
1.1 Cancer definition 27
1.2 Glioblastoma 27
1.3 Current techniques 28
1.4 Carnosine 29
1.5 Drug transport strategies to the brain 30
1.1.1 Intranasal drug delivery 31
1.1.2 Convection enhanced delivery 31
1.1.3 Vectors for enhanced brain drug delivery and medical imaging 32
1.6 Microfluidics based synthesis of nanoparticles, liposomes, and microbeads 35
1.7 Magnetic field trigger for controlled drug release and medical imaging 36
1.8 Non- heating rotating magnetic field 38
1.9 Project aim and objectives 39
Chapter 2: Super paramagnetic nanorods 42
1.2 Overview 42
1.2.1 The shapes of SPIO nanoparticles 42
1.2.2 The coating of the SPIO nanoparticles 43
1.2.3 The advantages of elongated SPIO nanoparticles 43
1.2.4 The advantages of using SPIO nanoparticles over other metals 44
1.3 Method development 45
1.3.1 Co-precipitation 45
1.3.2 Conventional hydrothermal method 46
1.4 Results and discussion 48
1.4.1 Characterisation 48
1.4.2 IONRs colloidal stability 52

1.4.3 Trace and localisation of IONRs 56
1.5 Conclusions 60
1.5.1 Synthesising SPIO nanoparticles 60
1.5.2 Estimating the fate of the SPIONs 61
Chapter 3: In-vitro studies 62
1.1 Overview 62
1.1.1 The mechanisms of carnosine in GBM brain tumour treatment 62
1.1.2 The advantages of PLGA beads and liposomes vesicles for cancer drug delivery and modified release 63
1.1.3 The safety studies on healthy cells (carnosine, PEI, PLGA, and liposomes) 64
1.1.4 How the project is going to expand other groups recommendations 65
1.2 U87 MG cell line optimisations for 2D and 3D models 65
1.2.1 Cell Proliferation 65
1.2.2 Scratch wound assay (migration / invasion) 65
1.2.3 Single spheroids development 68
1.3 Results and discussion 73
1.3.1 Applying the carnosine treatment on U87 MG and the mechanisms of effect 73
1.3.2 Safety studies for applying BPEI-coated IONRs on U87 MG 82
1.3.3 The effect of (IONRs/carnosine) combination and mild hyperthermia application on the controlled release of carnosine 88
1.3.4 Sustained released carnosine application in single spheroids 91
1.4 Conclusions 95
1.4.1 The controlled sustained release of carnosine using mild hyperthermia 95
1.4.2 The mechanisms of carnosine effect on Glioblastoma U87 MG cancer cells 95
1.4.3 In vitro investigations for sustained released carnosine using 3D model 95
Chapter 4: Micro vectors for drug delivery 96
1.1 Overview 96
1.2 Liposome vesicles for drug delivery and sustained release treatment 96
1.2.1 Applications of direct nose-to-brain therapy 97
1.2.2 Advantages of current intranasal application methods 98
1.2.3 Improvements in liposomes of previous biomedical applications 99
1.2.4 Current techniques for liposome preparation 99
1.3 Optimising the microfluidic preparation of liposomes 100
1.1 Liposomes characterisation and physicochemical studies 103
1.1.1 Optical, SEM, and TEM images 103
1.1.2 DLS: Diameter (DI), Polydispersity (PD), and Zeta potential 103

1.1.3 FT-IR 105
1.1.4 Stability profile 105
1.1.5 Sustained release study 105
1.2 Safety study for nasal application 108
1.2.1 Haemolysis test 108
1.2.2 MAD Nasal™ device optimisation and characterisation 109
1.2.3 Nasal cavity deposition testing on rodents (mice and rats) 110
1.3 Controlled release of carnosine from poly(lactic-co-glycolic acid) (PLGA) beads using nanomechanical magnetic trigger towards the treatment of Glioblastoma 113
1.3.1 The advantages of magnetic fields applications in drug delivery 113
1.3.2 How the project is going to expand other groups recommendations 115
1.3.3 PLGA beads preparation 115
1.3.4 PLGA beads characterisation and physio-chemical studies 116
1.4 Conclusions 125
1.4.1 The potential use and limitations of liposome production by microfluidics 125
1.4.2 The controlled release of carnosine loaded PLGA beads 126
Chapter 5: Experimental 127
1.5 Synthesis of iron oxide nanorods 127
1.6 Surface coating towards water dispersible colloid 127
1.7 Characterisation 127
1.7.1 General information 127
1.7.2 SEM-EDS 128
1.7.3 TEM 128
1.7.4 FT-IR 128
1.7.5 XRD 128
1.7.6 TGA-GC-MS 128
1.7.7 DLS 129
1.8 Inductively coupled plasma mass spectrometry (ICP-MS) 129
1.9 Magnetic resonance imaging (MRI) 129
1.10 Rotating magnet device 129
1.11 Preparation of poly lactic co glycolic acid (PLGA) microbeads 130
1.12 Dialysis membrane tubing 130
1.13 Liquid chromatography- mass spectrum (LC-MS) 131
1.14 Quantitative estimation of carnosine by bicinchoninic acid (BCA) 131
1.15 Cell studies 131
1.15.1 Cell culture 131

1.15.2 Cell viability assay by tetrazolium dye (MTT) 132
1.15.3 Cell cytotoxicity assay by lactate dehydrogenase (LDH) 132
1.15.4 Live cell imaging (Incucyte® system) 132
1.15.5 Uptake and localisation (SEM, TEM) 133
1.15.6 U87 MG cell differentiation 134
1.15.7 Flow cytometry analysis for cell life cycle by DNA staining (Hycult biotech) 134
1.15.8 The controlled release of (NRs/carnosine) synergism (MTT) 134
1.16 Spheroid modelling 135
1.16.1 The protocol of spheroids generation 135
1.16.2 Localisation of cell death and proliferation within spheroids 136
1.16.3 Imaging studies 136
1.16.4 Hematoxylin and eosin (H&E) stain of spheroid cross-sections 136
1.17 Carnosine effect on red blood cells 137
1.18 MAD Nasal™ device characterisation 137
1.19 Ex vivo experiments 138
1.19.1 The BPEI-coated IONRs loaded PLGA microbeads as contract agents 138
1.19.2 Nasal cavity deposition 138
1.20 In vivo suggested application 138
1.20.1 Tumour implantation surgery 138
1.20.2 Animal groups 139
1.20.3 Treatment application 140
1.20.4 Monitoring 140
1.20.5 Post treatment potential tests 140
1.21 Statistical Analysis 140
Chapter 6: Conclusions and Future work 141
Conclusions 141
1.1 The functionalised superparamagnetic iron oxide nanorods as carriers for controlled drug delivery 141
1.2 The potential of using carnosine-loaded liposomes for glioblastoma nasal sustained release therapy 141
1.3 The sustained release of carnosine treatments from PLGA beads by using the functionalised superparamagnetic iron oxide nanorods as triggers 142
1.4 The validity of using a robust, cost-effective single spheroid model to bridge the gap between the in vitro and in vivo trials 142
Future work 143
1.1 The development of the nanobiotechnology-based delivery strategies in GBM targeted therapies 143

1.2 Combining the traditional therapies with immunotherapy 144
1.3 Investigating the potential use of carnosine as a localised treatment for different tumours such as prostate cancer 145
1.3.1 MTT assay (IC50/EC50) 146
1.3.2 Proliferation and cytotoxicity (IC50/EC50) 147
1.3.3 Utilising carnosine within a sustained release designed experiment 151
1.3.4 Real-time ATP rate assay 151
1.4 Summary 154
References 155
Appendices 191
1.1 Appendix A: Published papers 191
1.2 Appendix B: Copy of ethics approval 191

List of figures

Figure 1. Diagram presents the drug transport routes to the brain. *The investigated strategies in this project. 31

Figure 2. Colloidal carriers (liposomes, dendrimers, nanoparticles, micelles, and nanogels) which have been used as vectors for enhanced brain drug delivery and medical imaging. 32

Figure 3. Schematic shows a hydrodynamic flow focusing microfluidic system which mediates the synthesis strategy of nanoparticles, liposomes, and microbeads. 36

Figure 4. Magnetic field map with allowable intensity limits for frequency range. The technique which is indicated by asterisks refer to an intensity of ~1 T at f < 1 kHz in physiotherapy of nanomechanical magnetic activation (Golovin et al., 2021). 37

Figure 5. (A, B) SEM images show the aggregates of naked iron oxide nanorods before coating. The scale bars are 1µm, 100nm. (C) TEM image shows similar aggregates for uncoated IONRs. 48

Figure 6. Transmission electron microscopic (TEM) images of (A) uncoated IONR exhibiting significant agglomeration, (B) mono disperse BPEI-coated IONRs, (C) single IONR with tetragonal prism-dipyramid morphology, (D) Fast Fourier transformation (FFT) crystal structure diffraction pattern of BPEI-IONRs, (E) the images show the uniformity size and shape of the BPEI-coated IONRs in various magnifications and spots. 49

Figure 7. (A) Image J analysis for the dimension distribution for the tetragonal prism-dipyramid morphology of the iron oxide nanorods (length, width, depth, and hypotenuse). (B) TGA shows the repeatability in coating method for three batches. (C) XRD displays the labelled characteristic planes (111, 220, 311, 222, 400, 511, 440) for the iron oxide crystal pattern (naked, tuned with polymer and coated with extra layer of polymer). 50

Figure 8. TGA shows the carnosine compounds. Carnosine shows a distinct two stage weight loss with an onset at 196°C. A first weight loss of 46.04% and a second weight loss of 45.79% equate to a total mass loss of 91.83%. The major loss of β-Alanine happens between 200 and 300°C. L-Histidine is the responsible for the loss pattern between 600 and 900°C. 50

Figure 9. TGA results between 50 and 700 °C of uncoated IONRs (green), IONR capped with BPEI (blue) and capped IONR loaded with carnosine (red). 51

Figure 10. GC-MS spectrums analyse the organic coat on the IONRs which evaporate at (A) 13 minutes, (B) 22 minutes and (C) 25 minutes which cover the range between 150 and 600˚C. (D, E) Specific peak for carnosine/PEI coated NRs between 600 and 800°C matches imidazole in MS library from L-histidine. 51

Figure 11. FT-IR spectra show changes in the spectrum of uncoated IONRs (red), IONR capped with BPEI (green) and capped IONR loaded with carnosine (blue). Arrows indicate the representative frequencies from the imidazole ring of L-histidine and peptide bond. 52
Figure 12. Colloidal stability studies via DLS compering intensity distribution measurements at room temperature: (A) hydrodynamic diameter of uncoated IONR at pH 7 (pink), IONR capped with BPEI at pH 7 (blue) and IONR capped with BPEI at pH3 (brown) over one hour; (B) hydrodynamic diameter polydispersity of uncoated IONR at pH 7 (pink), IONR capped with BPEI at pH7 (blue) and IONR capped with BPEI at pH 3 (brown) over one hour; (C) hydrodynamic diameter of IONR capped with BPEI at pH 7 (blue) and IONR capped with BPEI at pH 3 (brown) over one month; (D) hydrodynamic diameter polydispersity of IONR capped with BPEI at pH 7 (blue) and IONR capped with BPEI at pH 3 (brown) over 30 days. 54
Figure 13. DLS compering the intensity distribution of the iron oxide nanorods hydrodynamic diameter before and after coating. The polymer coating prevents the aggregation. After coating, the rods had a relative stable hydrodynamic stable diameter over an hour. Each measurement is the mean of 60 measurements repeated 3 times over 3 minutes to reduce the error to the minimum. 54
Figure 14. (A) MR images show the BPEI-coated IONRs as blue contrast agents at the concentration range of coating in this project and (B) the colloidal sedimentation of BPEI-coated IONRs under different conditions: water pH 3/pH 7, PBS, FCS, MEM. MEM/FCS, Opti-MEM, Opti-MEM/FCS and HEPES at room temperature after 1, 24 and 48 hours. The difference found between 1 and 24 hours is more than that which is found between 24 and 48 hours. The colour codes are related to sedimentation in arbitrary units. The yellow shadow refers to sedimentation and the blue shows the stability of the suspension. 56
Figure 15. SEM images show the uptake and localisation of BPEI-coated IONRs in U87 MG cells at different concentrations after 24 hours of incubation: (A, B) a 5 µg/mL concentration shows the uptake of BPEI-coated IONRs without affecting the live cells; (C, D) a concentration of 10 µg/mL BPEI-coated IONRs shows the overloaded uptake of BPEI-coated IONRs, which affects the nucleus. (E) The localisation around the nuclei was detected by the EDS map scan spectrum. Areas with iron localisation are distinguished by pseudo-colour that was applied simultaneously to the images to highlight IONRs as yellow. Scale bars are 25 µm for (A and C) and 50 µm for (B and D). 58
Figure 16. SEM images showing uptake and localisation of BPEI-coated IONRs most likely inside the destroyed nucleus of a U87 MG cell at a concentration of 10 µg/mL of BPEI-coated IONRs. 58
Figure 17. TEM images of U87 MG cells' sections. The pictures represent: (A–F) Cells treated 1 hour after the addition of BPEI-coated IONRs at a concentration of 5 µg/mL and show the rods on the border of the cell membrane. (G–I) Cells after 4 h of being incubated with BPEI-coated IONRs at a

concentration of 5 µg/mL for 4 hours. The IONRs that are under 100 nm start to enter the cells and localise in the cytoplasm. (J, K) Cell division 4 h after the addition of carnosine (25 mM). The mitochondria are loaded with carnosine. (L) This organelle is likely to play a pivotal role in relation to MTT assay and the size and distribution most probably refer to the mitochondria. (M) The general observed trend of cell reacting was changing its morphology into spherical shape. 59

Figure 18. TEM images of U87 MG cells section without any treatment. The image shows the component of the control cell. The arrows refer to the expected organelles such as, Mitochondrion, Golgi apparatus, Ribosomes, Nucleus, Rough endoplasmic reticulum. 60

Figure 19. Proliferation of different cell densities per well were monitored on 3 technical triplicates from untreated cells passage number (12). The plots show the confluence ratio of U87 MG cells over 48 hours (4000 cell/well is the best density). Error bars represent the standard error of the mean (SEM) 66

Figure 20. (A) The number of the adherent U87 MG cells after 18 hours has no significant difference in comparable study on 6 technical replicates of cells with and without adding mitomycin C. (B) The percentage of the viable U87 MG cells after 18 hours has no significant difference in comparable study between 6 technical replicates of cells with and without adding mitomycin C. Error bars represent the standard error of the mean (SEM). 66

Figure 21. Incucyte® live cell system images analysis for U87 MG cells confluence phase reflect (A) The effect of carnosine on the cells was not affected by using mitomycin C (B) the difference between the normal increase of proliferation for the cells and the effect of adding mitomycin C to stop the proliferation. Phase confluence proves the continuous dividing for control cells. However, the cells with mitomycin C stop splitting and start dying naturally after 24 hours. (C) Images of the cells in control sample and with mitomycin C at (1, 24, 48 hours). Error bars represent the standard error of the mean (SEM). (Scale bars = 400 µm) 67

Figure 22. Incucyte® live cell system (×4) live spheroids images analysis shows the proliferation curves of the confluence ratio of the U87 single spheroid upon using the protocol steps. The blue graph of the control showed the inability of the cells to convert the aggregates of cells into a spheroid without using the washing solution. Whereas consistent single spheroid formation reproducibility was achieved for the three different wells when the protocol was followed. The experiment was repeated on triplicate and the images show the difference between the shape of the aggregates and the successful shape of the spheroid, (scale bar = 500 µm). The series of images below the graph show the growth of the spheroids from days 1 to 7, (scale bar = 400 µm) 69

Figure 23. Incucyte® Live-Cell System show (a) A. The proliferation curves of individual U87 single spheroids from individual locations in the 96-well plate (C2, C3, D2, D3). The spheroid area decreased

during the first day. Then, each spheroid grew over seven days. B. The instant adherence of the cells when the step of washing was missed. C. Represent the cells in different wells as referred in well A. The cells were gathered after washing with the anti-adherence solution with a 96-well round-bottom standard growth surface for adherent cells (red code). (b) The U87 cells in the 96-well plate image turned into spheroids in various horizontal and vertical in the center of each seeded well after one day, with a size distribution of 216 ± 9 nm for individual spheroids. The figure shows that spheroids were not randomly growing in different locations which reflects the reproducibility in all wells..... 70

Figure 24. Fluorescence cell Imaging (a) Incucyte® live-cell system (4×). Live spheroid images after 10 days. A. The confluence of the live U87 MG cells around the spheroid is shown by the phase image to be distributed uniformly. B. The localisation of the dead cells in the center of the spheroid is shown by the Cytotox red stain. C. The 3D localization of the live cells around the spheroid is shown by the phase with a green channel filter image. D. The 3D shape of the dead/live cells in the same spheroid is shown by the overlap of the red and green channels. E. The mask of the invasion area. (b) The live green cells stained by CFSE, and the blue nucleus stained by DAPI are both shown located on the rim of the spheroid in the confocal images. A & C. The dark shade of the dead cells is shown by the 5- and 10-day spheroid images across the center. B & D. The 5- and 10-day spheroid images of the proliferating cells across the rim area. 71

Figure 25. Cell tightness and interaction analysis of U87 MG spheroids H&E stain of spheroid cross-sections from (A) the core area, and (B) top rim area of 7 days spheroid generated from 400 cells. Scale bar is 250 µm for both images. 72

Figure 26. Incucyte® live cell system (×10) Live cell images analysis shows (A) proliferation curves of the confluence ratio of U87 MG cells upon carnosine exposure over 48 hours. Cells were treated with different concentrations between 0 and 125 mM. (B) To prove the same effect of carnosine on cell proliferation, a supportive study was applied with delayed carnosine addition until 24 hours for 0, 100 and 125 mM. In both cases (A, B), the treatment effect started after 8 hours. An MTT cell viability assay was conducted on the U87 MG cell line with different carnosine concentrations. (C) The UV absorbance at different concentrations refers to (IC50 = 28.62 mM) and (IC90 = 79.43 mM). Error bars represent SEM. The test was applied on the same six samples at the end point of the proliferation study. (D) The images of the critical carnosine concentrations are shown. Each image was displayed as the phase of U87 MG cells upon carnosine exposure over 1 and 2 days. Error bars represent the standard error of the mean (SEM). (Scale bars are 400µm) 74

Figure 27. Incucyte® live cell system (×10) images show proliferation of U87 MG cells upon carnosine exposure after 24 hours. Cells were compared with and without treatment of 100 mM carnosine concentration in the presence of CytoLight Rapid Dye for live-cell green labelling dye (200 nM) which

crosses live cells membrane and emit green fluorescence. Each photo was displayed as phase and green channel without mask. A decrease in cells population appeared after 24 hours. However, the cells with no morphology change are the daughters who stay alive. (Scale bars are 400 µm)..... 75

Figure 28. Incucyte® live cell system (×10) images show cytotoxicity on U87 MG cells upon carnosine exposure after 24 and 48 hours. Cells were treated with different carnosine concentrations in the presence of Cytotox Red dye (250 nM), which enters dead cells after losing the membrane and binds to the DNA to emit red fluorescence. Each photo was displayed as a phase and as a red channel with a blue mask. (Scale bars are 400µm) 76

Figure 29. Incucyte® live cell system (×10) live cell images analysis shows IC50/EC50 curves of the inhibition of cells' proliferation and the efficiency of carnosine in killing the tumour cells. Upon carnosine exposure at different concentrations (0, 50, 100, 125 mM) over 48 hours, IC50 is indicated by the confluence phase ratio, while EC50 is the ratio of the Cytotox Red dye that enters dead cells. The carnosine effect has three phases: No effect plateau, Cytostatic around EC50, and Cytotoxic. .. 77

Figure 30. (A) The matrix of relative wound density for 6 samples of each concentration (0, 50, 100, 150 µM respectively) over 2 days. (B) The effect of different carnosine concentrations added on U87 MG cells after 18 hours of adherence when the scratch was applied. The scratch wound starts healing by proliferation and migration. Cells were imaged in 96 well plate while growing in media with different carnosine treatments using Incucyte® live cell imaging system to take two snaps per well each hour over 2 days. The phase confluence was analysed by the standard Incucyte® software, and the relative wound density was analysed by the integrated Incucyte® wound scratch software and plotted against elapsed time in hours. 0 hour indicates the cell density half hour after placing the plate in the Incucyte®. All cells' variations in growth arised after approximately 8 hours. The supportive movies of cell migration are available in the supplementary movies. (C) The statistical analysis of the normalised wound density shows that the significant effect starts between 50 and 100 mM of carnosine on cell density 10^3 per well. The statistical analysis shows a significant effect caused by carnosine (50 mM) at a cell density of 10^3 per well. The statistical significance level and indicated with (*) for $p < 0.05$, and (****) for $p < 0.0001$..... 78

Figure 31. Phase images with mask shows the effect of different carnosine concentrations on U87 MG cells wound healing by proliferation and migration. Cells were imaged in 96 well plate while growing in media with different carnosine treatments using Incucyte® live cell imaging system each 12 hours for 2 days..... 79

Figure 32. Effect of carnosine concentration on U87 MG cells' wound healing by migration after ceasing their proliferation with mitomycin C. The software able to quantify the space that was generated by the wound. Cells were imaged in a 96 well plate while growing in media with different

carnosine treatments using the Incucyte® live cell imaging system to take two snaps per well each hour, (A) during the first day, when the relative wound density was analysed by the integrated Incucyte® wound scratch software and plotted against the elapsed time in hours. After 18 hours of adherence, the scratch was applied, then mitomycin C (10 µg/ mL). was added after an hour. The carnosine treatment was applied at different concentrations and the plate was placed inside the Incucyte® device to start the 0-hour image after about half an hour. All variations in cell growth were initiated after about 4 hours. (B) The statistical analysis of the normalised wound density shows a slight increase in cell mobility caused by carnosine at a cell density of 10^3 per well. Error bars represent the standard error of the mean (SEM). 80

Figure 33. Effect of carnosine concentration on U87 MG cells' wound healing by invasion over 48 hours. (A) The same criteria as migration were applied to quantitatively address the effect of carnosine. (B) The statistical analysis of the normalised wound density shows a significant effect caused by carnosine (50 mM) at a cell density of 10^3 per well. The statistical significance level and indicated with (*) for $p < 0.05$, and (****) for $p < 0.0001$. 81

Figure 34. Incucyte® live cell system (×10) live cell images analysis shows IC50/EC50 curves of the inhibition of cells' proliferation and the efficiency of carnosine in killing the tumour cells. Upon carnosine exposure at different concentrations (0, 50, 100, 125 mM) over 48 hours, the IC50 is indicated by the relative wound density, while the EC50 is the wound width. The images and videos of scratch wound healing by cell migration are available in the Supplementary Materials. 82

Figure 35. Microscopic images show the difference of the cell morphology after the differentiation treatment. A. after 48 hours and B. after 7 days. The differentiated cells are more elongated than the mitotic cells. The scale bar is 50 µM. 83

Figure 36. Microscopic images (EVOS) show the live U87 MG tumour cells coloured in fluorescent green after the treatment to differentiate them for 48 hours and a week. (Scale bars are 150 µM) . 83

Figure 37. Microscopic images (Leica) with magnification x20 show the U87 MG tumour cells nucleus coloured in blue DAPI after the treatment to differentiate them for 48 hours and a week. The red antibody maker for the differentiated cells appeared in the sample of the 7 days. (Scale bars are 150 µM) 84

Figure 38. Flow cytometer peaks of life cycle for the mitotic (control) and differentiated U87 MG cell line. The peaks showed the difference between both types in all stages G1, S, and G2. Significant differences were evidenced in G1 and S stages. The test was performed on biological triplicate and Error bars represent the standard error of mean (SEM). 85

Figure 39. (A) ICP-MS test was applied after finishing the MTT test (48 hours). Measuring the iron concentration showed similar percentage of BPEI coated IONRs left in the wells of both mitotic and differentiated U87 MG. 86
Figure 40. LDH test on U87 MG cell line with various concentrations of BPEI coated IONRs after 48 hours. No significant difference was observed after applying IONRs (5, 7.5 and 10 µg/mL) in individual triplicate. Error bars represent the standard error of mean (SEM). 86
Figure 41. MTT cell viability assay on U87 MG cell line (A. mitotic vs. B. differentiated) with various concentrations of BPEI coated IONRs after 48 hours. No significant difference was observed in individual triplicate. Error bars represent the standard error of mean (SEM). 87
Figure 42. MTT cell viability assay on U87 MG cell line (passages 14, 15, and 16) with varying concentrations of BPEI-coated IONRs after 48 hours. No significant difference in the normalised UV absorbance was observed in individual triplicate. Error bars represent the standard error of the mean (SEM). The statistical significance level and indicated with (*) for $p < 0.05$. 88
Figure 43. LC-MS assay for the released carnosine from dialysis membranes containing carnosine free or loaded BPEI-coated IONRs, under different conditions, at temperatures of 37˚C and 40˚C. Free carnosine had a linear trend of the release percentage while the release ratio of carnosine from the BPEI-coated IONRs embedded carnosine was enhanced exponentially in all conditions. Mild hyperthermia allowed the carnosine to be fully released after 3 to 5 hours. 89
Figure 44. MTT assay on U87 MG cell line with same carnosine concentration 25 mM for all plates and different concentrations of BPEI-coated IONRs (A) carnosine loaded BPEI-coated IONRs and mixed for 5 min with the media (B) BPEI-coated IONRs added to the soluble carnosine in the media. In both cases, mild hyperthermia was applied by changing the temperature of separate the incubator. Comparing the controls shows the inefficiency of mild hyperthermia in killing cells because of the insignificant difference between the controls in all plates. The heat released the carnosine from the BPEI-coated IONRs after 3 to 5 h when it was bonded, while the effect was equal, without any significant difference, when the nanorods existed in the same vicinity. Each treatment was repeated on 6 samples, then the T test was applied to address the significant changes. (C) Comparison of the repeatability of all controls from (A, B). (Abs = absorbance at 570 nm). The statistical significance level and indicated with (*) for $p < 0.05$, (**) for $p < 0.01$. 90
Figure 45. Incucyte® live cell system (×4) live spheroids images show the comparison between the morphology and size of single spheroids on day one and day seven after applying different doses of carnosine treatment. The mimicked sustained release of carnosine concentration ≥ 100 mM affected spheroid growth and tightness, and a significant difference was reported in phase exposure. The

statistical significance level of phase exposure time of the spheroids on day seven was indicated with (*) for $p < 0.05$, (**) for $p < 0.01$. (n=3) Error bars represent the standard error of the mean (SEM). 91
Figure 46. Incucyte® live cell system (×4) live spheroids images converted to graphs which show the potential of using the protocol to obtain EC50 of carnosine on multiple points for drug delivery study and in vitro sustained release profile. The EC50 of carnosine on monolayer cells was calculated for seven days. 92
Figure 47. Incucyte® live cell system (×4) live spheroids images show the potential of using the protocol in chapter 5 paragraph 1.16 to obtain single spheroids from various cell lines. 94
Figure 48. Dolomite micromixer hydrophilic or hydrophobic chip. The alcoholic mixture is the central stream, while the water flows from inputs 1 and 3. 100
Figure 49. Microscopic images showing the mixing patterns during the optimisation of the pump pressure. The pressure of the continuous central flow increased from left to right while the size of generated vehicles decreased. 100
Figure 50. Microscopic images for liposomes before and after loading carnosine. (A & B) Optical, SEM, and TEM images were compared between the characterisation of empty blank liposomes (blue) and carnosine-loaded liposomes (green). (C) The histograms show the distribution of the liposome diameters. The diameters of liposomes $n \geq 50$ were measured using ImageJ. The mean diameter size for the blank liposomes was 82.9 ± 19.4 nm and 284.1 ± 91.1 nm for the carnosine-loaded liposomes. The scale bar of TEM images = 100 nm. 102
Figure 51. The DLS normalised and cumulative intensity distribution of the blank and carnosine-loaded liposomes. The repeatability of the distribution for three individual batches of liposomes is shown in both. The red curve is the average cumulative intensity for three liposomal batches. 104
Figure 52. FT-IR spectra for liposomes with carnosine, lipids as empty liposomes, and carnosine crystals. The carnosine-loaded liposomes displayed characteristic bending bands around 1600 cm^{-1} attributed to the carnosine peptide bond. 104
Figure 53. Stability studies via DLS measurements at room temperature: hydrodynamic diameter and polydispersity of carnosine-loaded liposomes over 30 days. Every measurement for three individual batches of liposomes was averaged after 60 readings from the DLS ± SD, which were repeated over 3 minutes. 105
Figure 54. Membrane dialysis experiment over a week. The LC-MS results were averaged to show the released carnosine from three membrane bags, including carnosine-loaded liposomes. Many points were measured during the first 6 hours of day 1. Then, a sample was measured daily until the end of the week. The graduate release from the liposomes exposed to the mechanical rotation of a magnetic

bar with 100 rpm stirring speeds is shown by the LC-MS cumulative analysis for the released carnosine. 107

Figure 55. The DLS results of the normalised intensity distribution of the liposomes were at the beginning of the study (blue peak) higher than after a week of releasing the carnosine from the liposomes through the membrane dialysis bag (black peak). At the same time, a magnetic bar was stirred at a speed of 100 rpm. 108

Figure 56. Carnosine effect on red blood cells. The 2% sheep blood erythrocyte suspension was washed with PBC and centrifuged. Then, the blood erythrocyte suspension was added to cuvettes containing carnosine concentrations free or loaded in liposomes (100, 200, and 400 mM) and cuvettes containing positive control of distilled water (red) and negative control of saline buffer (transparent). The resulting colour in each incubated and centrifuged mixture showed no cell membrane damage, except in the DI water samples. 109

Figure 57. Comparison between applying water or liposomal solution using the original and modified MAD Nasal™ device. No significant difference was observed. The pressure of the device was about 20 psi. 110

Figure 58. The lateral view of the mouse nasal cavity shows that (A) spraying 10 µl of dye by the modified MAD Nasal™ device resulted in deposition on the olfactory epithelium area of the nasal cavity (the left naris). The administering of 10 µl of the dye using the pipette resulted in localising the dye in the respiratory epithelium and partially in the olfactory epithelium (the right naris). (B) After 5 minutes, the dye coloured the posterior two-thirds of the olfactory turbinates on the left side. 111

Figure 59. MRI images of a series of water and various gadolinium solutions show the best concentration of the gadolinium loaded inside liposomes and demonstrate a similar T1 contrast. 112

Figure 60. (A) Ex vivo MRI images of the rat brain after intranasal application for gadolinium 10^{-5} mol/L loaded liposomes using a pipette or the spray device. The location of injected gadolinium is shown by white shades. The signal showed a decrease in intensity over time. (B) The MRI image shows the rat head anatomy and the gadolinium-loaded liposomes localised in the Nasoturbinates close to the olfactory region. 113

Figure 61. Microscopic images for PLGA beads after encapsulation and during evaporation. 116

Figure 62. FT-IR spectra for PVA, PLGA, empty beads, L-carnosine (with/without PLGA), and IONRs (with/without PLGA). 116

Figure 63. Empty Beads, SEM images compare the characterisation of empty (0.1%, 1% PLGA beads) and the uniform distribution of the water phase inside the beads. IONRs Beads, SEM images for IONRs loaded 0.1% PLGA beads, EDS mapping the blue colour of iron traces inside the red carbon colour of the PLGA, and the iron peaks confirm the images. The histogram refers to a mean diameter size of 7.4

± 2.3 µm. Carnosine Beads, SEM images for carnosine loaded 1% PLGA beads showed the carnosine distribution and the MS spectrum identifies the peaks of carnosine pattern. The histogram refers to a mean diameter size of 11.6 ± 7.0 µm. Carnosine/IONRs Beads, SEM images for (carnosine & IONRs) loaded 1% PLGA beads. The size of the beads/shells shifts to 10 times larger than the previous beads. 117

Figure 64. The effect of a rotating Halbach array on a suspension of nanorods embedded in agarose (2% w/v) over time. Masking the dark areas showed the difference before and after 3 hours of external magnetic rotation. 118

Figure 65. (A) Ex vivo MRI images of the mice brains injected with IONRs. The location of injected beads of IONRs or controls is shown by red circles. The colour codes the signal intensity which is proportional to the value of $T2^{eff}$ in ms. The signal is shown to decrease in intensity for the 50 ppm and 25 ppm areas confirming the presence of a negative contrast agent which is expected from the magnetic nanoparticles. (B) Comparative curves of the control (left) and IONRs beads (right) showed the drop in signal intensity as a function of echo time, with a steeper change in the case of free IONRs indicating a shorter $T2^{eff}$. 119

Figure 66. Membrane dialysis experiment. (A) SEM images show the PLGA beads in the beginning which had holes in the structure after a week and became completely empty after a month. (B) The LC-MS cumulative analysis for the released carnosine shows faster release from the beads which were exposed to the higher mechanical rotation..... 120

Figure 67. The DLS results of the normalised intensity distribution of the beads over a week with different stirring speeds..... 121

Figure 68. The temperature fluctuations for applying the rotating MF on __ water vs. _ _ PLGA beads. 121

Figure 69. (A) Schematic illustration for the rotating magnet system designed for this application. The arrows indicate the direction of the magnetic field which produces an intense uniform magnetic field within their central air gap, and zero field outside. (B) LC-MS assay for the normalised concentrations of carnosine shows the advantage of using the hydrophobic chip (dark curves with high load of carnosine) and the hydrophilic chip (light curves with low load of carnosine) for the initial emulsification. (C) LC-MS assay for the normalised concentrations of carnosine shows the comparison between adding the encapsulated IONRs to the carnosine before or after the initial emulsification. Curves with light colours are for beads before the application of the magnetic field and the curves with dark colours are for after the application of the magnetic field. Red spheres are carnosine and black rods are IONRs. The dotted lines are trend lines fitted to the experimental data..... 123

Figure 70. ICP assay for IONRs normalised concentrations shows the comparison between adding the encapsulated IONRs to the carnosine as seeds vs. beads. The decrease in the concentration is because of the attachment with the released carnosine over time. The dotted lines refer to the trend lines. 124

Figure 71. Zeta potential measurements for 15 days to compare the freeze frying effect on the stability profile. (A) Freeze drying the sample induced the initial release of carnosine, while (B) shows multiple waves for the released carnosine because of using vacuum oven. The dotted lines refer to the trend lines. 125

Figure 72. Carnosine affects mitochondrial functionality and slows down the proliferation of cells after 48 hours. (A) PC346Flu1 and (B) TRAMP-C1. MTT dose-response curve indicates that carnosine induces cell death and slows down proliferation dose-dependently with an EC50 of ~100 mM after 48 hours in both cell lines. (n=3)..... 146

Figure 73. Incucyte® live cell system (×10), live cell image analysis shows that carnosine affects the mitochondrial functionality within hours for both PC346Flu1 cells (A) and TRAMP-C1 cells (B). Carnosine significantly inhibited the growth of each cell line in a dose and time dependent manner. The maximum effect on proliferation was shown at carnosine concentration 300 mM.The Incucyte® live cell imaging system was used to study the dose-dependent effect of carnosine on proliferation. PC346-Flu1 and TRAMP-C1 prostate cancer cells were cultured in the absence or presence of various carnosine concentrations using a density of 3×10^5 cells/well for PC346Flu1 and 10^3 cells/well for TRAMP-C1. Proliferation was observed on an hourly basis (Figure 73). 147

Figure 74. Incucyte® live cell system (×10), dead cell image analysis shows that carnosine increases death of A) PC346Flu1 cells, B) TRAMP-C1 cells. Carnosine significantly inhibited cell growth in a dose and time dependent manner due to the relatively different growth rates of the cells studied. The higher the dose of carnosine the shorter the time required for cell death over 6 days for the human cells and over 48 hours for the murine cells. The maximum effect was shown starting from carnosine concentration 300 mM for PC346Flu1 cells and 200 mM on TRAMP-C1. 148

Figure 75. Incucyte® live cell system (×10) images show cytotoxicity upon carnosine exposure after 48 hours (A) PC346Flu1 cells. (B) TRAMP-C1 cells. Cells were treated with different carnosine concentrations in the presence of Cytotox Red dye (250 nM), which enters dead cells after membrane integrity is lost and binds to DNA to emit red fluorescence. Each photo was displayed as a phase and with a red mask for dead cells. Significant carnosine induced cell death was shown from a concentration of 100 mM upwards; Scale bars are 900 µm..... 149

Figure 76. Incucyte® live cell system (×10), dead/live cell images analysis shows IC50/EC50 curves of the inhibition of cell proliferation and the efficiency of carnosine in killing the tumour cells. Upon

carnosine exposure at different concentrations, ranging between 0 and 400 mM over 48 hours, the IC50 is indicated by the confluence phase ratio. At the same time, EC50 is the ratio of the Cytotox Red dye that enters dead cells. The carnosine effect has three phases: no effect, cytostatic, and cytotoxic. 150

Figure 77. Carnosine Incucyte® images show the effect of sustained treatment using carnosine on single spheroids in (A) PC346Flu1 and (B) TRAMP-C1 cells. Carnosine was added every other day at different concentrations ranging from 0 to 150 mM. The images were collected after seven days. The spheroid tightness was affected by carnosine concentration > 100 mM and a significant difference was reported in the largest brightfield object area (µM2). The statistical significance level on day seven indicated with (*) for $p < 0.05$, (**) for $p < 0.01$. Scale bars 500 µM. (n=3) 151

Figure 78. Seahorse flux analysis of cells treated with carnosine. (A) mitochondrial ATP production rate data (basal and induced rates), (B) glycolysis ATP production rate data (basal and induced rates), (C) total ATP production rate data (basal and induced rates), (D) induced rates average of ATP production. 152

List of tables

Table 1. R^2 for the Hydrodynamic diameter and polydispersity of the IONRs in different conditions over 1 hour. 55

Table 2. The diameter and polydispersity of empty and carnosine loaded liposomes by DLS..... 103

List of abbreviations

3D
3 Dimensional 96
A549
lung tumour cells 32
ADT
Androgen deprivation therapy 141
AIDS
Acquired immune deficiency syndrome 95
ANOVA
The one-way analysis of variance 136
BBB
blood brain barrier 28
BPEI
polyethyleneimine 37
CAIX
carbonic anhydrase IX 28
CFSE
Carboxyfluorescein succinimidyl ester fluorescent dye 69
CNS
Central nervous system 94
CpG ODNs
cytosine guanine dinucleotide oligodeoxynucleotides 32
CS
chitosan 31
DI
Deionised water 105
Diameter 99
DMEM
Dulbecco Modified Eagle Medium 131
DNA
Deoxyribonucleic acid 26
DOX
Doxorubicin 140
DRE
Digital rectal exam 141
DU145
Human Prostate cancer 131
ECAR
Extracellular acidification rate 150
EDS
The energy-dispersive X-ray spectroscopy 54
EDTA
Ethylenediaminetetraacetic acid 34
EE
Encapsulation efficiency 102
EGFR
epidermal growth factor receptor 26
EMEM
Eagle's minimal essential medium 53
FCS
fetal calf serum 53

FDA
Federal Drug Administration 27
Fe_3O_4
magnetite 40
FFT
Fast Fourier transformation 46
GBM
Glioblastoma multiforme 25
GFAP
Glial fibrillary acidic protein 79
H&E
Hematoxylin and eosin 69
IC50/ EC50
half maximal inhibitory/ effective concentration 38
ICP-MS
Inductively Coupled Plasma Mass Spectrometry 117
IDH1
Isocitrate dehydrogenase 1 26
IONR
iron oxide nano rods 45
IV
Intravenous 140
LC-MS
Liquid chromatography–mass spectrometry 102
LE
Loading efficiency 102
MAD110
MAD 108
mCRPC
Metastatic castration resistant prostate cancer 141
MDSCs
myeloid derived suppressor cells 26
MF
magnetic field 35
MHFF
Microfluidic hydrodynamic flow focusing 96
MPI
magnetic particle imaging 38
MPLA
monophosphoryl lipid A 32
MRI
Magnetic resonance imaging 34
MTT
3-(4,5-dimethylthiazol-2-yl)-2,5-diphenyltetrazolium bromide 38
NMMA
Nanomechanical magnetic activation 36
OCR
Oxygen consumption rate 150
OLIG2
oligodendrocyte transcription factor 2 26
OXPHOS
Mitochondrial oxidative phosphorylation 147
PBS
phosphate buffer solution 53

PD
Polydispersity 99
PDGFRA
Platelet derived growth factor receptor A 26
PDK4
Pyruvate dehydrogenase 4 60
PEPT2, PHT1, and PHT2
Three proton-coupled oligopeptide transporters 60
PGA
poly (glycolic acid) 31
PI
Propidium iodide 80
PLA
poly (lactic acid) 31
PLGA
poly (D.L-lactide-co-glycolide) 31
POD
Precision Olfactory Delivery 94
PSA
Prostate-specific antigen 141
RNA
Ribonucleic acid 26
ROS
reactive oxygen species 54
RP
Radical prostatectomy 141
SDS
sodium dodecyl sulfate 44
SPIO
Super paramagnetic iron oxide 34
SPIONs
Superparamagnetic iron oxide nanoparticles 30
TEM
transmission electron microscopy 44
TGA
thermal gravimetric analysis 47
TLR9
Toll-like receptor 9 32
TMZ
Temozolomide 27
TP53
tumour protein 53 26
TRAMP-C1
Murine prostate cancer 131
U251
Glioblastoma cells 94
U87 MG
human brain tumour cell line 38
WHO
World Health Organisation 25
XRD
X-ray diffraction 44
γ-Fe_2O_3
meghamite 40

Chapter 1: Literature review

1.1 Cancer definition

Cancer is a primary global health problem as considered by the World Health Organisation (WHO) in 2005 (World Health Organisation, 2005). Cancer is responsible for a significant number of annual deaths globally which needs an action plan towards controlling it (World Health Organisation, 2008-2013). The difficulty in the treatment of this highly complex disease resulted from the characterisation of its multi-forms (Hanahan and Weinberg, 2000). The last published update classification for cancer mechanisms incorporated the deregulated androgen metabolism by enzymes (Mitsiades et al., 2012) the ability to overcome the immunosurveillance defence of the body (Carlo et al., 2009) , and the instability of cancer cells with recognised increase in the number of chromosomal artifacts (Dahiya et al., 1997). This disease is generally associated with tissue chronic inflammation (Sfanos and Marzo, 2012). Despite the remarkable efforts in categorising cancer, the treatment versus prognosis is still associated with various possibilities (Mason, 2009). A genomic study for 2000 breast cancer patients identified 10 multiple forms of the disease (Curtis et al., 2012). Immunostaining of tumours proves the characteristics of the main and sub-groups of cell protein expression (Broers et al., 1987). Cancer heterogeneity extends even to within the individual tumour by showing various sub-cell populations, that support the theory of both clonal evolution and cancer stem cells (Campbell and Polyak, 2007). According to the follow up of the global action plan for the prevention and control of non-communicable diseases 2013-2020, a wide range of managements are currently considered to prevent cancer nowadays (World Health Organisation, 2013). WHO updates guidelines and fact sheets about cancer, regularly. In 2018, this disease was estimated to be the second most fatal global disease, leading to one in six deaths (9.6 million). The most common types among both genders are lung and colorectal cancer (World Health Organisation, 2021).

1.2 Glioblastoma

Glioblastoma multiforme (GBM) is the most malignant central nervous system tumour with prognosis of 15 months after diagnosis. Its incidence increases with age and more common in men than women (Kromer et al., 2017). Glioblastoma multiforme are mainly primary, however, secondary glioblastoma multiforme may occur from lower grade gliomas (Bleeker, Molenaar, and Leenstra, 2012). Glioblastoma histology shows that GBM consists of highly differentiated and pleomorphic astrocytic cells with high mitotic activity. Vascular proliferation and necrosis exist in some sections of the tumour (Young et al., 2015). Glioblastoma multiforme was further categorised in four subtypes by their gene expression profiles: classical, mesenchymal, proneural and neural subtypes. These subtypes occur at different rates; 22% classical, 32% mesenchymal, 32% proneuronal, and 14% neural. The classical

subtype is identified by the loss of chromosome 7 and the amplification of Epidermal growth factor receptor (EGFR). The mesenchymal subtype expresses the mesenchymal markers Chitinase-3-like protein 1(YKL40) and hepatocyte growth factor receptor (MET). In addition, this subtype expresses several genes in the tumour necrosis factor super family and nuclear factor kappa-light-chain-enhancer of activated B cell (NF-κB) pathways. The proneural subtype is typically identified by the amplification of platelet derived growth factor receptor A (PDGFRA), point mutations in isocitrate dehydrogenase 1(IDH1), mutations in tumour protein 53 (TP53), loss of heterozygosity, high expression of homeobox protein Nkx-2.2 (NKX2-2), and oligodendrocyte transcription factor 2 (OLIG2). The neural subtype is defined according to the expression of neuron markers and potassium-chloride transporter member 5 (SLC12A5) (Verhaak et al., 2010). GBM has a wide range of mutations in gene expression which lose the function by evading growth suppression. Metastasis is rarely seen in GBM; however, invasion is a hallmark of the disease (Hanahan and Weinberg, 2011). GBM cells downregulate connexin 43 (cnx43/GJA1) protein which reduces their adherence and as a result increases their invasion capacity (Verhaak et al., 2010). GBM tumours develop many mechanisms to avoid immune destruction such as the recruitment of immunosuppressive myeloid derived suppressor cells (MDSCs) and the expression of immune inhibitory checkpoint proteins (Gabrilovich, 2017; Mosella et al., 2017).

1.3 Current techniques

Many approaches are now available to tackle glioblastoma brain tumours with a variety of complexity. Until 2015, the WHO had considered 30% of cancers as curable types (McGuire, 2016). Some notable successes include the tumour-initiating vaccination (Tay, 2012), in addition to the completely treatable retinoblastomas through current therapies (Dimaras and Corson, 2019). Beyond surgical intervention, the traditional treatments include chemotherapy and radiotherapy (Cairncross et al., 2006). Both techniques introduce the patient to scheduled doses of cytotoxic drugs which commonly inhibit the Deoxyribonucleic acid (DNA) and Ribonucleic acid (RNA) synthesis, and transcription. However, the death of the patient was faster than the reoccurrence of the tumour after numerous side effects in all cases. The current cancer therapies are often combinational techniques that limit the chance of the tumour resistance (Zhang et al., 2012). Over the last few decades, novel and promising cancer treatments have been developed to improve both the detection and prognosis of the disease. These new strategies include gene-, targeted- and immune- therapy. The gene therapy example is the virus-directed enzyme with an oncolytic virus. It results in the tumour cells expressing the nitro-reductase enzyme which produces a cytotoxic drug. The advantage is that only the infected cancerous cells are affected by the cytotoxic drug (Hedley, Ogilvie, and Springer, 2007). Examples of the targeted therapy to a specific molecule through drugs or antibodies would be the tyrosine kinase inhibitor which affects the epidermal growth factor receptor, implicated in damages in the cell cycle of lung cancer (Sawyers, 2004), and the hormone therapy treated the denial of androgens (Olov Hedlund et al., 2008). Using the immunotherapy form of treatment activates the immune system *via* vaccination (MacDonald et al.,

2020). Few vaccines are licensed for use such as Sipuleucel-T a vaccine against hormone-refractory prostate cancer which showed prolonged survival in phase III clinical trials (Kantoff et al., 2010). Up until now, vaccines only provide an extension of life, however, the potential is thereby investigating better targets and strategies (Zhou and Levitsky, 2012; Antonarakis and Drake, 2012).

Currently, the course of cancer treatment consists of surgical removal of the tumour followed by traditional radiotherapy and chemotherapy. In spite of that aggressive multimodal course of regime, the prognosis of the patients is nearly 15 months (Stupp et al., 2005). In addition, corticosteroid dexamethasone is used preoperatively to reduce the peritumoral swelling of the craniotomy which is the preferred "asleep-awake" surgical method (Conte et al., 2010; Conte et al., 2013). Another method for resecting GBM tumours is stereotactic ablation by laser-induced thermal therapy (von Tempelhoff, Ulrich and Schwarzmaier, 2014; Bredlau et al., 2016; Linz et al., 2016). Glioblastoma multiforme is highly resistant due to the infiltrative and diffuse nature of the cells which are observed after the surgery (Holland, 2000). Post-surgery, Temozolomide (TMZ) can be administered orally (Zhang, Stevens and Bradshaw, 2012). The body absorbs TMZ and metabolise it to produce the active component methyl-diazonium. This cation methylates DNA at the O6 position of guanine towards a cytotoxic effect on the brain cancer cells. Unfortunately, the lethal O6 guanine adducts may be repaired by methylguanine-DNA methyltransferase enzyme (Zhang, Stevens and Bradshaw, 2012). In addition, several micro RNAs are implicated in the resistance to TMZ chemotherapy (Ujifuku et al., 2010). The other Federal Drug Administration (FDA) approved treatment for GBM patients is Bevacizumab (Cohen et al., 2009). Bevacizumab had little benefit when used in newly diagnosed patients (Fine, 2014; Wen and Junck, 2014). However, it provides an alternative to corticosteroids for cerebral oedema. In 2011, the FDA approved the Optune device which involves wearing scalp electrodes that apply alternating electric fields. It affects the mitosis of tumour cells and showed to improve the progression in the number of survived patients. However, this technique still requires improvements towards the curative target (Hottinger, Pacheco, and Stupp, 2016; Mittal et al., 2017).

1.4 Carnosine

Modern research and development to treat Glioblastoma will likely be in the multitude of treatment modalities. Single therapy has been ineffective so far (Stupp et al., 2005), however, a combination of therapeutic approaches could be a key factor in increasing the potential survival, however, some will be associated with deleterious side effects. For instance, combining anti-PD-1 and anti-CTLA-4 immune checkpoint blockade increased the adverse immune events in the melanoma (Hassel et al., 2017). Early studies found that even the diet could be an essential part of the treatment of GBM by altering metabolism (Zuccoli et al., 2010; Champ et al., 2014).

Some types of supplementary materials are relatively enigmatic compounds which was shown to have many functions in numerous settings. For example, carnosine dipeptide is a compound of two amino

acids (β-alanine and L-histidine) which is abundant within the brain and skeletal muscle. It has been proven that carnosine possesses many roles such as free radical scavenger, metal ion chelator, neurotransmitter, immunomodulatory, antioxidant and pH buffer with pKa value of 6.83 (Hipkiss et al., 1998). Carnosine has been shown to have anti-tumour effect *via* different mechanisms. Carnosine inhibits human GBM cell growth (Oppermann et al., 2018) and reduces the acidification which contributes towards a reduction in the amount of carbonic anhydrase IX (CAIX) enzyme activity within these tumour cells. The carnosine treated tumours were also shown to express high levels of HIF-1α (Ditte et al., 2014). This extracellular acidification has been investigated as a potential treatment strategy for cancer due to the buffering ability of carnosine. Carnosine was shown to have an anti-proliferative effect on the gastric cancer cell line SGC-7901 effect without inducing the apoptosis or necrosis. Further analyses revealed that carnosine treatment reduces the basal oxygen consumption rate of SGC-7901 cells which indicates that carnosine has the potential to inhibit glycolysis (Shen et al., 2014). In addition to using carnosine alone, combining it with chemotherapeutic agent 5-fluorouracil has also shown therapeutic potential against HT29 colon cancer cells (Iovine et al., 2016). The downside of carnosine is cytotoxicity for the human renal cell line Caki-2 by inducing the apoptotic protein caspase-3 (Pandurangan et al., 2016). However, carnosine is rapidly broken down by the enzyme carnosinase which is downregulated in GBM patient plasma compared to healthy control plasma (Gautam et al., 2012). Hence, the anti-cancer effect of carnosine is enhanced to affect the cell death or to supress the proliferation of cancer cells. Using carnosine holds promises as a therapeutic agent against GBM since it has previously demonstrated a relatively safe potential therapy. Therefore, the model of carnosine delivery and release require further investigations (Habra et al., 2021).

1.5 Drug transport strategies to the brain

In spite of the tremendous improvement in drug delivery for treatment to the brain there is still a need for novel brain targeted strategies. The blood brain barrier (BBB) is the main hurdle due to its tight endothelial network which protects the brain from any harmful materials passing *via* the circulatory system. The substances usually allowed to penetrate the BBB under specific hydrophilicity, molecular weight and surface charge.zeta Only lipophilic and positively charged drugs can easily cross it such as antidepressant and many hormones. This sophisticated system results in a limitation of the treatment options for targeting the brain cancer (Pardridge, 2005). Therefore, drug transport routes to the brain are regularly presented. The non-invasive transport of drug delivery is highly desirable such as the olfactory pathway which showed a desirable therapeutic effect at lower doses with less side effects. This direct drug transportation to brain throughout the transmucosal olfactory delivery or trigeminal pathway to bypass the BBB is a recommended route to connect the brain with the nose (Mistry, Stolnik, and Illum, 2009). The nasal route permeability has gained attention for the delivery of many formulations in animal and human studies. The deposited drug at the olfactory epithelium increased the

drug delivery from nose to brain (Illum, 2000; van Woensel et al., 2013). Also, the convection enhanced delivery showed a consistent drug concentration in the targeted area (Saloni et al., 2021) (Figure 1).

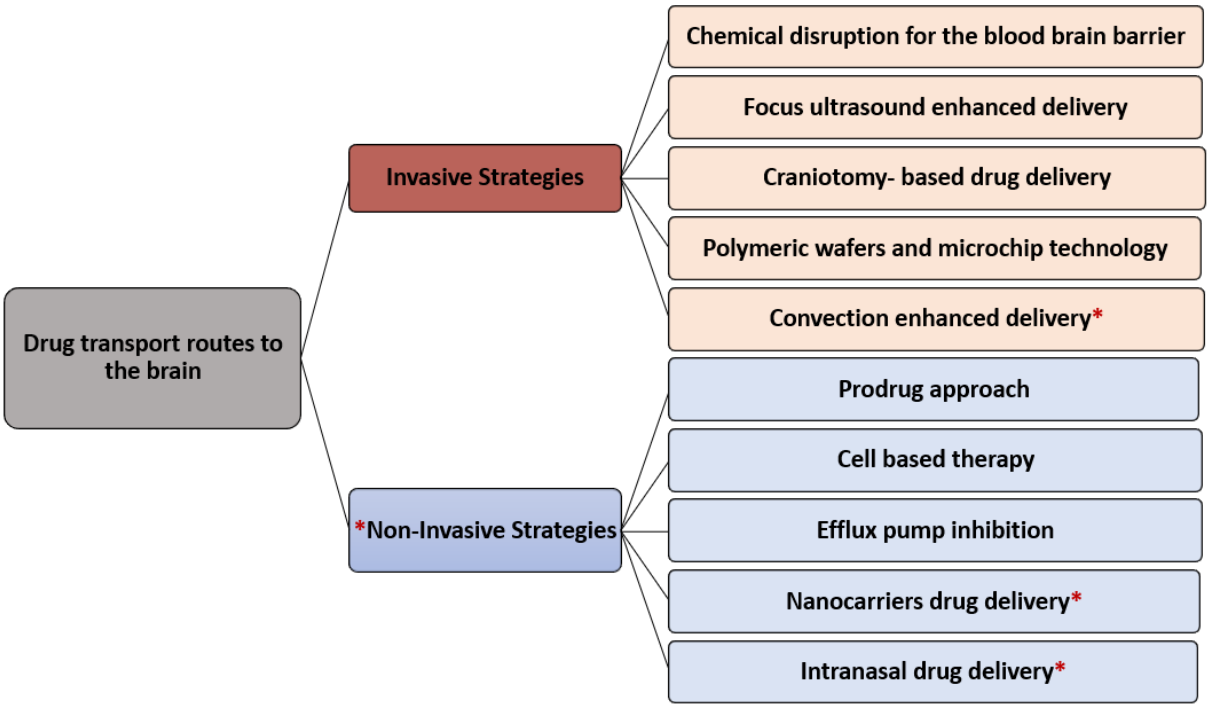

Figure 1. Diagram presents the drug transport routes to the brain. *The investigated strategies in this project.

1.1.1 Intranasal drug delivery

Drug absorption through nasal route sends the drug into the systemic circulation through the nasal respiratory epithelium, followed by a transcytosis mechanism (Saloni et al., 2021). However, the administrated substances pose the challenge of BBB restriction. Therefore, applying the vectors deep into the nasal cavity gets it closer to the nasal mucosa which leads to the direct transmission of the drug into the brain *via* the olfactory pathway. The olfactory neurons carry the drugs non-invasively and slow the degradation with a fast transportation by the paracellular mechanism (Popat Jadhav et al., 2020).

1.1.2 Convection enhanced delivery

Convection delivery is a technique for local drug administration into the targeted brain tissue. However, this is invasive because of the insertion of more than one catheter through cranial burr holes into the brain to deliver the therapeutic agents by micro infusion pump (Harbaugh, Saunders, and Reeder, 1988; Chen et al., 1999). This method showed effective drug concentration in the targeted region where the catheter is placed, without producing cerebral oedema or measurable increase in intracranial pressure. The high drug concentrations can be delivered to the brain with drug distribution and the least systemic side effect towards the targeted tissues (Cunningham et al., 2008; Lu et al., 2014).

1.1.3 Vectors for enhanced brain drug delivery and medical imaging

Various types of colloidal carriers included liposomes, dendrimers, nanoparticles, micelles, and nanogels were recommended as potential vectors towards the achievement of successful direct brain drug delivery (Figure 2). However, the limitations in finding the right combination of the applied vectors and the route of delivery are still expected to be investigated. For example, using the polyethylene glycol PEGylated nanoparticles to cross the blood brain barrier and coupling the doxorubicin to enhance the brain uptake (Khan et al., 2017). The focus of the future works should investigate the optimum distribution of the anti-cancer agents by using the suitable vector.

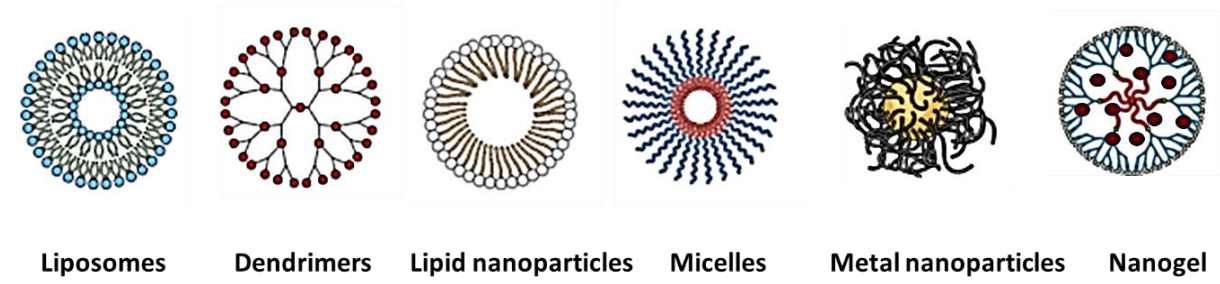

Figure 2. Colloidal carriers (liposomes, dendrimers, nanoparticles, micelles, and nanogels) which have been used as vectors for enhanced brain drug delivery and medical imaging.

In this project the focus will be on formulations consisting of coated iron oxide nano particles, polymeric beads, and liposomes to discuss the advantages of triggering these vectors as adjuvants for controlled release drug delivery and medical imaging. These approaches are promising for nano- and micro-noninvasively drug delivery applications.

1.1.3.1 Magnetic nanoparticles

Magnetic nanoparticles have demonstrated therapeutic and diagnostic potential as brain tumour delivery devices. Superparamagnetic iron oxide nanoparticles (SPIONs) can be directed with remote magnetic fields to target a specified region as well as distinguishing the tumour cells among the healthy tissues (Khan et al., 2017). SPIONs have the advantage of being a supplementary treatment which could be used in combination with radiotherapy for tracking the therapy and act as imaging contrast agents (Khan et al., 2017). For instance, combining SPIONS with the endothelial vascular cell adhesion molecule-1 as a sensitive indicator of brain metastasis helped in early detection of brain tumour (Serres et al., 2012). In addition, SPIONs were encapsulated inside liposomes and conjugated with transferrin protein to facilitate brain uptake through transferrin receptor mediated delivery. The magneto liposomes of paclitaxel increased the brain uptake four times and provided sustained released paclitaxel *in vivo* (Dilnawaz et al., 2012).

1.1.3.2 Polymers

The submicron-sized polymeric based nanoparticles usually contain a therapeutic or diagnostic agent either conjugated or functionalised into a polymeric matrix (Panyam and Labhasetwar, 2003). Some of the most popular polymeric nanoparticles for brain targeted delivery are poly (D.L-lactide-co-glycolide) (PLGA), poly (lactic acid) (PLA), and poly (glycolic acid) (PGA) (Beduneau, Saulnier, and Benoit, 2007). Coating the polymeric surface with PEG, chitosan, and dendrimers, elevate the site-specific targeting ability of the polymers (Yoon et al., 2014). In addition, conjugating them with cell penetrating peptides provoke the brain uptake significantly which results in a longer median survival time due to the improved anti-tumour effect (Khan et al., 2018). The common advantages of using the previous polymers are the biocompatible, biodegradable, and improving the drug stability and release (Tafaghodi et al., 2004; Makadia and Siegel, 2011).

The potential use of PLGA in brain drug delivery was investigated *in vitro* and *in vivo* ten years ago. Loading olanzapine in PLGA nanoparticles increased the uptake into the brain by ~ 6-fold after intravenous administration, and *ca.* 10-fold *via* intranasal administration (Seju, Kumar and Sawant, 2011). Also, donezepil-loaded PLGA nanoparticles were superior in delivering donezepil to the brain (Md et al., 2014). PEG with PLA polymer was used to improve the diffusion across the mucus barrier by minimising muco-adhesion with no signs of toxicity (Zhang et al., 2006; Wang et al., 2008; Jain et al., 2010). Whereas chitosan (CS) contains primary amines which are positively charged in most physiological fluids and present mucoadhesive and is permeation-enhancing (Kang, Cho and Yoo, 2009). This excipient showed a decrease in the muco-ciliary clearance for intranasal powder formulations (Soane et al., 2001). Moreover, CS can open the tight junction of the mucosal epithelium which enhances the permeability of large molecules such as peptides and proteins (Amidi et al., 2010). Many CS nanoparticle formulation were introduced as Alzheimer's disease treatments which showed stability due to the positive zeta potential and high transport percentage as compared to the drug in solution (Alam et al., 2012; Fazil et al., 2012). For example, the symptoms of Parkinson's disease were reversed in mice model by applying bromocriptine-loaded chitosan nanoparticles *via* intranasal route whereas the brain/blood ratio of the formulation was negligible in the brain following the intravenous administration (Lim et al., 2009; Shadab et al., 2013). Versatile molecules can attach onto the surface of a dendrimer which consists of repetitive branches grown from a core (Figure 2). This resulted in nanoparticles electrostatically attaching to the active material. Upon the intranasal administration, the dendrimer shows a wide distribution into the brain and clear therapeutical effect (Kim et al., 2012).

1.1.3.3 Liposomes

Liposomes are phospholipid vesicles (Figure 2) which have been utilised for the delivery of antigens or adjuvants (Bolhassani, Safaiyan, and Rafati, 2011; Temizoz, Kuroda, and Ishii, 2016). During the 1970's, Gregoriadis explored the liposomes which were described as lamellae of swollen phospholipids. He investigated the entrapment of enzyme and protein inside liposomes and optimised their localisation

in vivo to improve the targeting of drugs. Since then, all their derivatives nanovesicles have attracted the attention as delivery systems. The 1980's research improved the stability of liposomes, and during the 1990's clinical trials were initiated toward the approval of injectable products such as AmBisome® and Doxil® (Gregoriadis, 2016).

Some key advantages of using liposomes are their versatility, plasticity, biocompatibility, and biodegradability. Various choices of lipids can form the desired cancer immunotherapeutic with a specific charge, size, distribution, traveling, and location of antigens or adjuvants (e.g., immunostimulatory adjuvants such as agonistic and non-agonistic ligands for TLRs, C-type lectin receptors, retinoic acid-inducible gene I-like receptors and stimulator of interferon gene) (Cuzzubbo et al., 2021). Many animal models showed that liposomal formulations have superior efficacy over non-liposomal. For example, liposomal delivery of cytosine guanine dinucleotide oligodeoxynucleotides (CpG ODNs) provided potent anti-tumour effects in a mouse model of neuroblastoma, whereas the CpG oligonucleotides -alone group failed because RNA interference reduced Toll-like receptor 9 (TLR9) expression (Brignole et al., 2010). Also, in mice challenged with Lewis cells, the liposomal adjuvant monophosphoryl lipid A (MPLA) induced a tumour-specific antibody and Th 1-type immune responses in lung carcinoma (Zhong et al., 2010). In addition, the first clinical trials in follicular lymphoma patients using liposomes as a vaccine carrier system for a tumour- idiotype antigen showed safety and capability of inducing prolonged antigen-specific CD4+ and CD8+ T-cell responses (Neelapu et al., 2004). The previous series of studies led to some options for current commercial cancer therapeutics (e.g., Annamycin®, Vincxome®, and Daunoxome®) (Sharma and Agrawal, 2021).

In the past, some reviewers emphasised that using liposomes for human applications is restricted due to the lack of manufacturing stability and their excessive cost (Schwendener, 2014; Temizoz, Kuroda, and Ishii, 2016). To resolve the instability, a study introduced a manufacturable synergistic anionic liposome with TLR4/TLR7 adjuvant which was made of pharmaceutical excipients and agonists to be ready for human clinical trials (Fox et al., 2014). The next generation of designed liposomal adjuvants were cost-effective, also, offering a strong platform for the delivery of subunit and nucleic acid (Perrie et al., 2016). Liposomes were conjugated with peptides (Lipopepsomes) that promote their efficacy by enhancing the internalisation in αvβ3-overexpressing A549 lung tumour cells (Qiu et al., 2018). The GP2 peptide conjugation in lipopepsomes was applied prophylactically and therapeutically as a composition of DMPC- DMPG- Chol-DPOE and MPL adjuvant which increased splenocytes INF-γ production and reduced the tumour growth in HER2/neu-overexpressing TUBO breast cancer model (Razazan et al., 2017). For superior antitumor activities, astragalus saponins were utilised as a valuable additive in highly effective vaccines and tumour therapy by constructing adjuvant formulation of lipo-saponins/bFGF complex (Zhang et al., 2018). In addition, liposome-DNA complexes (Lipoplexes) were developed taking into consideration the scaling up because they can be lyophilised and stored at room temperature without aggregation or loss of efficiency. The lipoplexes demonstrated the GMP

requirements in gene therapies and vaccines within advanced cures for the diseases at the genetic level (Gregoriadis, 2016). Moreover, an encapsulated complex of DOTAP/Chol/DSPE-PEG cationic liposomes as a cationic liposome/protamine complex evoked the conventional RNA *in vitro* vaccines by stronger uptake and stimulation for anti-tumour immune response in aggressive Lewis's lung cancer model (Mai et al., 2020). Another lipopolyplexe were formulated lately for mRNA nasal vaccines. A tripartite formulation with RNA, cationic polymer, and anionic liposomes was encapsulated with RNA into neutral formulation (Van Der Jeught et al., 2018). A novel lipopolyplex vector for the *in vivo* delivery of mRNA was also proposed to target the dendritic cells without cell-specific functionalisation or ligands. Multi-LP incorporated the immune adjuvant α-galactosylceramide (α-GalCer) and a multivalent cationic lipid (Guevara et al., 2019).

In summary, liposomes became versatile delivery systems which can load antigens, proteins, peptides, nucleic acids, and carbohydrates to construct new types of vaccines targeting the macrophage immune cells, the lymphatic system, and dendritic cells (Lai et al., 2018; Stolk et al., 2020). The liposomes can target different organs including the skin (Shah et al., 2012; Stolk et al., 2020), brain (Hong et al., 2019), mucosal routes (Ramvikas et al., 2017) to decrease the adverse effects throughout the body (Yu et al., 2019). Many liposomal carriers for chemotherapeutical drugs have been approved under the following commercial names: Dau-noXome®, DepoCyt®, Ambisome®, Visudyne®, and Doxil/Caelyx®. The treatments targeted several types of cancer such as brain, breast, and skin (Lippens, 1999; Torchilin, 2006).

1.6 Microfluidics based synthesis of nanoparticles, liposomes, and microbeads

Traditional methods for synthesising micro and nanoparticles are spray drying, polymerisation, sol–gel reaction, co-precipitation, hydrolysis, coagulation, emulsification, and microfluidic systems. The advanced microfluidic flow focus system produces monodisperse emulsions with droplets in uniform shape and size. Therefore, the mechanical properties and functionality have showen an improved impact on biomedical applications. The microfluidic control methods consist of single phase laminar which is segmented as either single-emulsion phase or a multi-emulsion phase (Kung et al., 2020). Both PLGA beads and liposomes can be synthesised by the microfluidic solvent diffusion method. They are generated inside a micromixer chip which consists of microchannels. By rapid mixing, PLGA-dichloromethane or lipid-alcohol solution are nucleated by the aqueous continuous phase using the hydrodynamic flow focusing mechanism.

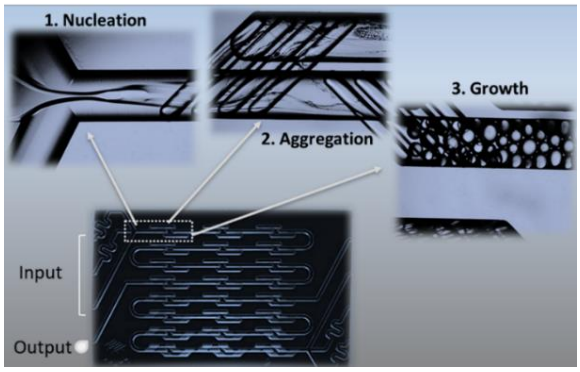

Figure 3. Schematic shows a hydrodynamic flow focusing microfluidic system which mediates the synthesis strategy of nanoparticles, liposomes, and microbeads.

A stable laminar focussed stream flows along the central channel to meet two adjacent water streams flowing at higher flow rates. The flow focusing squeezes between two anti-solvent water streams, resulting in rapid solvent exchange by diffusion. The particles formation takes place spontaneously at the nucleation spots that are distributed through the mixture then aggregates or grow by self-assembly. The hardening occurs throughout and post the growth stage by the solvent diffusion from the matrix into the surrounding mixture (Figure 3). Many types of cancer treatments have been prepared using this single emulsification method including polymer single core-shell or multiple cored droplets carriers to be pH responsive and protect the drug in the pH of the gastrointestinal track, then release the treatment for the colorectal cancer (Hasani-Sadrabadi et al., 2016; Lian et al., 2020), and metal particles such as embedded silver nanoparticles for breast cancer treatment (Aftab et al., 2020). Many challenges were shown by the coupling and proximity effects between the different components (Yu et al., 2019). However, these problems can be solved by generating core–shell structure nanomaterials for multiple emulsions water-in-oil-in-water (W/O/W) droplets. For example, this technique facilitated a formulation for enhanced *in vivo* imaging-guided cancer photothermal therapy (Rao et al., 2017). The Dolomite microfluidic method produces batches with nearly 100% encapsulation efficiency and monodispersity < 5% which can be scaled up with no waste; uniform ingredients distribution can be formed without filtering (Damiati et al., 2020).

1.7 Magnetic field trigger for controlled drug release and medical imaging

The main contributing factor to the low survival rates of GBM is attributed to the persistence of residual malignant cells which have been found to be resistant to chemotherapy and radiotherapy therapies, resulting in rapid recurrence (Jain, 2018). It is therefore imperative to look towards new theragnostic approaches to treat this downside in the treatment strategy of such a terminal disease (Wang et al., 2018; Pearson et al., 2019). In order to mitigate the risk of residual malignant cells post-surgery, real time medical imaging (e.g., MRI) during surgery is emerging as a new tool for surgeons to help reduce

recurrence, however, to optimise this process a targeted contrast agent is required (Chen et al., 2016; Hebelmann et al., 2017; Wach et al., 2019).

Nowadays, chelated gadolinium is used in over than 30% of all magnetic resonance imaging (MRI) scans as a contrast agent, however, its widespread clinical use is limited (Aime and Caravan, 2009). Despite being fully chelated (typically with Ethylenediaminetetraacetic acid (EDTA) analogues) (Rees et al., 2018), gadolinium ions are reported to leach into the blood stream, resulting in nephrogenic systemic fibrosis and signs of neurological disorders (Unterweger et al., 2018). Super paramagnetic iron oxide, (SPIO), nanoparticles are therefore emerging as clinically approved alternatives (Gale and Caravan, 2018). This can be attributed to their lower toxicity, colloidal stability at physiological conditions which should be always optimised to prevent cases of severe reactions and blood clots (Veiseh et al., 2010; Fulop et al., 2018), controllable surface charge and their low nonspecific protein adsorption (Nie, 2010; Chapman et al., 2013). The combined medical imaging and potential therapeutic properties of SPIO nanoparticles have been recently demonstrated for biocompatibility in both preclinical and clinical trials (Cai et al., 2013; Hola et al., 2015; Kandasamy and Maity, 2015). Uniquely, SPIO nanoparticles have also been investigated as a medical device for localised hyperthermia therapies to induce cell death in cancer tissues (Gupta et al., 2007; Rivera Gil et al., 2010). The application of magnetic field (MF) triggers a following biological response such as the hyperthermia which depends on the characteristics of the MF and the magnetic nanoparticles' nature.

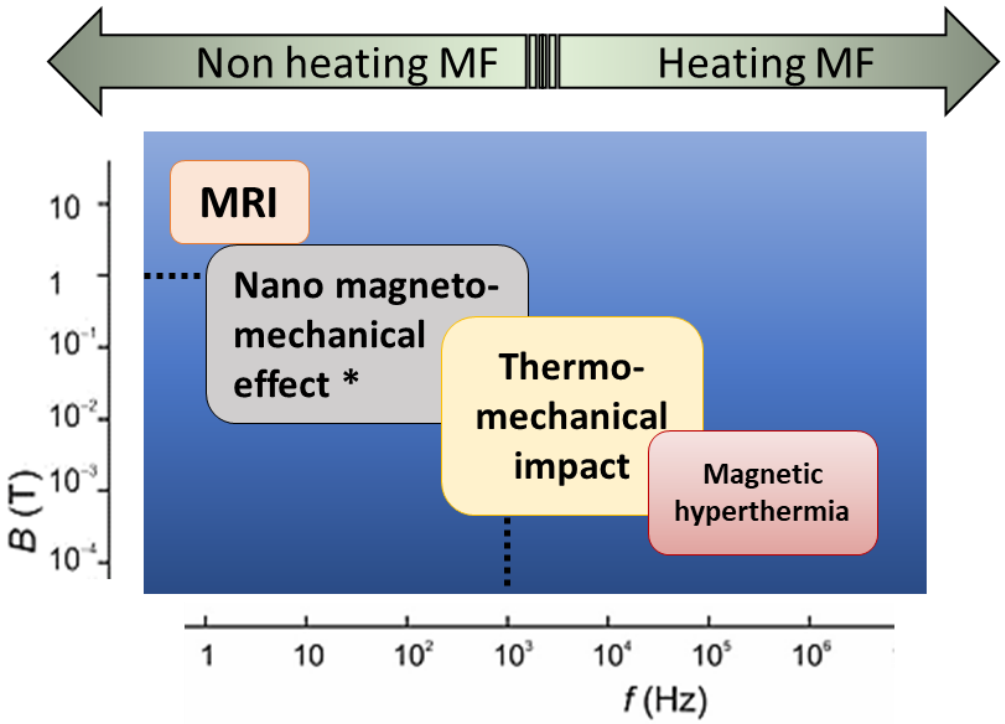

Figure 4. Magnetic field map with allowable intensity limits for frequency range. The technique which is indicated by asterisks refer to an intensity of ~1 T at f < 1 kHz in physiotherapy of nanomechanical magnetic activation (Golovin et al., 2021).

In physiotherapy, the heating of soft tissues is caused by MF (5–30 MHz), and the neuron stimulation is caused by an electric field generated with an intensity of ~1 T and a duration of ~1 ms. The lower the MF frequency, the higher the maximal allowed field intensity during maintaining an electromagnetic equipment (Figure 4). The two approaches to convert the MF energy into biochemical effects are the form of thermal energy which takes place in magnetic hyperthermia at frequency 100–800 kHz and the local forces that induce deformation in biomolecules which are adjacent to rotating magnetic nanoparticles in non-heating low-frequency < 1 kHz (Figure 4). Many studies showed that heating cannot be localised in a region smaller than a few millimetres, and each magnetic nanoparticle cannot be over heated more than 10^{-6} ˚C. Thus, the forces of the nanomechanical approach attracted the attention.

By applying an alternating magnetic field, SPIO nanoparticles rotate, and their kinetic energy is translated into a localised increase in tissue temperature (up to *ca.* 46˚C), resulting in targeted cellular apoptosis with minimal side effects (Rachakatla et al., 2010; Deatsch and Evans, 2014). SPIO nanoparticles in the range of (20-150 nm) are reported to have good renal clearance and avoid opsonisation with serum proteins, before being removed from the bloodstream by macrophages; this can be significantly quickened by controlling the surface charge on the SPIO *via* the addition of a surface coating (Cai et al., 2013; Kandasamy and Maity, 2015). Functionalising SPIO can also prevent their degradation and convert them into efficient carriers for pH-triggered drug release (Fan et al., 2013a), as well as suppress their aggregation (Wu et al., 2015; Kandasamy and Maity, 2015). These surface coatings can also be utilised to attach prodrugs; thus, the whole functional nano-complex has both diagnostic and therapeutic potential properties (Gupta and Gupta, 2005). However, translating metal oxide nanoparticle formulations from the aqueous solutions into physiological conditions is problematic, due to their inherent immediate or gradual sedimentation in media conditions that are rich with ions such as physiological buffers and bodily fluids (Fan et al., 2013), resulting in flocculation of the SPIO nanoparticles and protein binding.

1.8 Non- heating rotating magnetic field

Nanomechanical magnetic activation (NMMA) represents the techniques that employ the nanoscale deformation of molecular structures by means of nanomagnetic particles which are activated by non-heating low-frequency [< 1 kHz rotating magnetic field (MF)], (Golovin et al., 2021). Over the last two decades, NMMA techniques have been developed to utilise the sensitivity of the body components to the induced deformations (Suresh, 2007; Belaadi, Aureille and Guilluy, 2016; Master et al., 2016; Naud et al., 2020). The biochemical responses to the mechano-transduction with the cell apoptosis received a particular attention since it has opened up a wide perspective in the development of new approaches and techniques in the treatment of oncological (Rakesh K Jain, Martin and Stylianopoulos, 2014; Chen et al., 2020). The nanoparticles act as mediators that localise and apply forces to target biomolecular

structures including enzymes, transport vesicles and cell organelles, without significant heating. Therefore, NMMA demonstrates a biophysical platform for various therapies including the sustained and controlled release of therapeutics, without increasing toxicity (Golovin et al., 2021). Paramagnetic nanoparticles have been used as non-thermal contrast reagents in magnetic resonance imaging and as carriers in drug delivery by nanoscale modules (Cheng et al., 2016; Armenia et al., 2019). However, clusters of superparamagnetic nanoparticles have also been demonstrated to induce magnetic hyperthermia therapies when enshrouded with a polymer coating, impregnated with a drug (Zhang et al., 2020; Caizer, 2020). Therefore, introducing paramagnetic nanoparticles to a living organism can result in both thermal and non-thermal therapies; simply by changing the frequency of the alternating magnetic field (Golovin et al., 2021). These combined properties have successfully been utilised to induce controlled anticancer doxorubicin from a nanoscale vector which was called smart responsive nanoparticles (Hayashi et al., 2014; Hervault and Thanh, 2014).

In oncology, NMMA techniques have been employed in the deformation of molecular structures, where in, the paramagnetic nanoparticles are utilised to manipulate the sensitivity of tissue, cells, and vesicles (Golovin et al., 2021) The biochemical response to this mechano-transduction is cell death or apoptosis (Jain, Martin, and Stylianopoulos, 2014; Chen et al., 2019). It has, unfortunately, also been seen to stimulate tumour growth. This is attributed to the transmission of force from the rigid malignant cells to the soft surrounding healthy ones, leading to metastasis (Broders-Bondon et al., 2018). Functionalising the paramagnetic nanoparticles and utilising magnetic actuation to trigger mechanical forces offers an exciting strategy to remotely control the drug release from coupled magnetic materials (Diab et al., 2018). The contactless mechanical disruption of the polymer coating triggers the release of the therapeutic material which triggers apoptosis cascade within the targeted cells (Broders-Bondon et al., 2018). In anticancer drug delivery system based on calcium carbonate particles loaded with a photosensitizer, the physical stimulation has been shown to be advantageous, compared to photon or thermal triggering. Thanks to the possibility of achieving deep activation in a controllable and non-invasive manner which targets intracellular delivery with a high selectivity to cancer cells due to the pH-controlled release (Svenskaya et al., 2013a).

1.9 Project aim and objectives

This work aims to create a principle ready formulation of modified superparamagnetic iron oxide nanorods for biomedical applications, and to utilise them in PLGA and liposome encapsulated formulations for the controlled release of carnosine. Using different triggers including mild hyperthermia and rotating magnetic field, will introduce many non-invasive approaches toward a triggered or sustained release treatment. The investigation outcomes will reflect the long-term curing effect of carnosine treatment at the same time as monitoring the brain tumour cells.

The research objectives and techniques to be used in this project are:

1. Synthesising biocompatible coated oxide nanorods for biomedical applications:

In terms of high surface area, magnetisation, blood circulation availability and long retention in cancer cells, it has been proved that one dimensional (1D) iron oxide nanostructures possess considerable advantages over the spherical and cubic shapes (Das et al., 2016). Tuning the iron oxide magnetics properties by decreasing the surface and the amount of coating is tedious because engineering the size and shape affects the spin, also, limits the magnetic properties. Moreover, different coating material might entirely change the crystallinity (Kandasamy and Maity, 2015). Thus, using the branched polyethyleneimine (BPEI) with reactive primary amines is a great advantage to form a hydrophilic, stable, biocompatible, and positively charged surface which displays a relatively high R^2 relaxivity (Wang et al., 2009; Cai et al., 2013). To achieve the best potential formulation, the research will be following the recommendations from the previously published methods and avoiding the drawbacks (Wan et al., 2005; Wang et al., 2009; Ebrahiminezhad et al., 2012; Ding, Liu and Jiang, 2013; Cai et al., 2013; Mohapatra et al., 2015).

2. Assessing the magnetic properties of the synthesised nanorods to check the physical efficacy:

The thermal effect for the iron oxide nanorods is essential in hyperthermia treatment to initiate the cancer cells apoptosis, (Kandasamy and Maity, 2015). To produce pulses of heat the synthesised iron oxide nanorods should keep the magnetic properties to stimulate the release of carnosine from the surface coat of the iron oxide nanorods. Also, it is necessary to evaluate the T2 relaxivity of the iron oxide nanorods because it affects the ability of censoring the cancer tissues to monitor the size of the solid cancer *via* MRI or magnetic particle imaging (MPI) (Mohapatra et al., 2015; Wu et al., 2015; Xie et al., 2018). To study the diagnostic potential of the synthesised iron oxide nanorods, phantoms and/ or *ex vivo* mice models will be utilised.

3. Investigating the cytotoxicity of the optimised iron oxide nanorods using human brain tumour cell line (U87 MG) to estimate their safety margin for the brain tumour applications:

Although the iron oxide toxicity was estimated to be low, it cannot be ensured yet since results from *in vitro* studies are sometimes contradictory in the literature. Iron oxide inhibits the tumour growth by pro-inflammatory macrophage polarisation (Zanganeh et al., 2016). Therefore, the cell viability of the core iron oxide particles should be appreciated by applying the necessary tests such as the 3-(4,5-dimethylthiazol-2-yl)-2,5-diphenyltetrazolium bromide (MTT) assay (Mahmoudi et al., 2009). *In vivo* studies are also rare and human epidemiological studies are nearly inexistent. Due to the useful presence of iron oxide, the tolerability of human healthy brain cells toward formulations include iron oxide must be established to determine the safe dose (Valdiglesias et al., 2016). Also, the dose response of carnosine

will be addressed by calculating the half maximal inhibitory/ effective concentration (IC50/ EC50) to estimate the amount to be embedded onto the prepared core of PEI coated iron oxide nanorods.

4. **Studying the uptake and localisation of the formula and the migration ability of the tumour cells after treatment:**

Surgery followed by radiotherapy cannot assure the removal of all Glioblastoma cells that often migrate away amongst healthy cells (Liu et al., 2012; Wang et al., 2018). Therefore, it is important to check if the formula inhibit the tendency of malignant cells towards developing metastasis. The wound healing assay is reliable to be used for the migration and invasion studies of the U87 MG cells after applying carnosine as a treatment. Moreover, different microscopic imaging techniques are quite useful for tracing the nanoparticles. The scanning and transmission electronic imaging will reveal the morphology of the material and the cells for the characterisation of the resulted applications. Also, the fluorescent dye will be used for cell studies and detected either by the confocal microscopy or the Incucyte® live cell system.

5. **Comparing the critical parameters of time, temperature, and carnosine concentration to induce the tumour cell death under a controlled conditions for the drug release.**

   It is essential to assess the *in vitro* effect of the formulations of loaded carnosine on PEI coated iron oxide nanorods while applying hyperthermia to stimulate the controlled drug release. The tolerability of a control U87 MG cells towards the suggested formulations must be monitored to determine the safety margin and the effective dose of carnosine during releasing time (Valdiglesias et al., 2016). Also, hyperthermia effect should be addressed alongside the applied treatment. MTT assay is a reliable indicator for the comparative studies of cell viability.

6. **Optimising encapsulated iron oxide nanorods with/ without carnosine to formulate PLGA beads or liposomes for drug delivery and sustained release:**

Using drug release systems is an advantage to preserve biodegradable drugs such as the dipeptide carnosine which attracts the attention as a natural regulator of oxidative metabolism in brain tissues (Boldyrev, 2012). In this work, PLGA or liposomes encapsulation will be developed with stability profile to increase the bioavailability of the formula for longer time (Budama-kilinc, Cakir-koc and Kecel-gunduz, 2018). Tailoring a controlled dimension for the particles is crucial for the best potential uniformity, so, the nanorods will be precisely adjusted around 70 nm (Jahn et al., 2007; Danhier et al., 2012). Moreover, both shell and core of will be tuned to get the optimal theranostic balance of the nanorods. The dolomite microfluidic flow focus system provides producible conditions to optimise the aimed encapsulation by using various microchips according to the recommended protocols as a reliable starting point. Thereafter, a Halbach array rotating magnet system will be designed for studying the controlled release application.

Chapter 2: Super paramagnetic nanorods

1.2 Overview

Superparamagnetic nanoparticles have shown advantages in cancer therapeutic and diagnostic applications. Primarily, superparamagnetic iron oxide (SPIO) nano-theranostic particles attracted the attention for the *in vitro* and *in vivo* bio-applications. Practically, SPIO particles at size below 30 nm exhibit the superparamagnetic behaviour at room temperature because SPIO nanoparticles with only a single magnetic domain exhibit high magnetic susceptibility and provide a fast strong magnetic response (Nee Koo et al., 2019). Among many examples, the recent developments were administrated on magnetite (Fe_3O_4) and maghemite (γ-Fe_2O_3) for drug delivery, hyperthermia treatments, and magnetic resonance imaging (MRI). Even with many beneficial properties, the toxicity of SPIO nanoparticles on healthy cells must be considered (Kandasamy and Maity, 2015).

1.2.1 The shapes of SPIO nanoparticles

Modifying the shape of the superparamagnetic iron oxide nanoparticles is a key strategy. Practically, changing the geometry while avoiding chemical composition amendments will directly affect the magnetic anisotropy of the SPIO nanoparticles (Gavilán, Posth, et al., 2017). Moreover, the morphology changes of SPIO nanoparticles showed an impact on the magnetic heating effect (Walter et al., 2014; Das et al., 2016a; Simeonidis et al., 2016; Nemati et al., 2018). For example, the nano cube shape of iron oxide crystals demonstrated one of the best magnetic heat promoters. SPIO nano-cubes display the highest hysteresis losses which have been reported in the literature so far, provided that the field amplitude is enough to ensure the remagnetisation. The hyperthermia efficiency is desirable with size ranging between 15 and 50 nm for the internalisation into mammalian cells (Guardia et al., 2012). Both shape and magnetic field intensity are crucial in these studies. Another interesting system for investigation is the elongated SPIO nanoparticles which were well defined by the property of single magnetisation axis. elongated SPIO nanoparticles are several. They have strong shape anisotropy which align when an external magnetic field is applied and flow with low resistance within the bloodstream. Also, they show a favourable uptake by cells due to their large surface area which allows multivalent interactions with the receptors of the cell membrane (Gavilán, Posth, et al., 2017; Avolio et al., 2019). In general, the target of challenging strategies is the synthesis of the elongated SPIO nanoparticles with size of less than 100 nm. The templates of iron oxide in aqueous phase are the initial start in SPIO nanoparticles growth preparation (Ocaña, Morales, and Serna, 1995).

For decades, the most accessible SPIO nanoparticles shape was the spherical which can be prepared *via* various methods. Amongst these techniques, co-precipitation is the most popular which consists of mixing ferrous and ferric precursors in alkaline aqueous media (Roca et al., 2009; Ammar and Fievet,

2020). Using co-precipitation, a certain SPIO nanoparticles assembly was predictable with the size distribution by controlling the key parameters of the synthesis. This followed by the changes in the characteristics of the crystal which affect the anisotropy energy and magnetic effect (Gavilán, Sanchez, et al., 2017). The importance of the selectivity of the synthetic route rises from the high impact of the stability of the produced colloid. Thus, the chemical properties on the surface of SPIO nanoparticles depict the degree of their aggregation.

1.2.2 The coating of the SPIO nanoparticles

The coating of the SPIO nanoparticles by biocompatible surfactants prevents the direct contact between the SPIO nanoparticles because of the dipolar magnetic interactions which exploit hindrance (Cabrera et al., 2018). In fact, improving the stability of SPIO nanoparticles by increasing the anisotropy barriers enhances their thermal fluctuations and superparamagnetic relaxation (Binns et al., 2002; Burrows et al., 2010). Several stability strategies have shown positive impact on the magnetic heating energy (Mehdaoui et al., 2013; de La Presa et al., 2015; Arteaga-Cardona et al., 2016; Engelmann et al., 2018). However, unwanted effects on heating efficiency can also be caused by strong dipolar bio-interaction which reduces the stability and induce the agglomeration, aggregation, and sedimentation phenomena (Ovejero et al., 2016). This is due to such changes as the size, demagnetisation effect will slow the relaxation and degradation (Zrínyi, Barsi, and Buki, 1997; Xu et al., 2012).

1.2.3 The advantages of elongated SPIO nanoparticles

The most commonly used shape for nanocarriers is the spherical which includes micelles, liposomes, and polymers. Those nanostructures reduce the rapid biological clearance barrier because the phagocytic cells opsonise the spherical nanoparticles by the mechanism of adsorption at their surface (Lundqvist et al., 2008). The size distribution of the nanoparticles also plays a significant influence on the filtration process and the elongation of circulation time. For instance, the spherical nanoparticles with diameter of 20 nm or below showed an extended lifetime after surface modification with coating material such as the PEGelation with stealth polymers (Klibanov et al., 1990; Gref et al., 1994).
Switching the shape of nanocarriers changes the initial point of contact with the cell membrane. The geometrical structure with long axis spreads in parallel to the cell membrane which leads to a reduction in phagocytosis occurrence (Champion and Mitragotri, 2006; Champion and Mitragotri, 2009; Sharma et al., 2010). Trials on the clearance delay were initiated *in vivo* by forming filo-micelles. The di-blocks of PEG flexible micelles survived in the animal bloodstream for a week despite the biodegradation (Geng et al., 2007). Persistent delivery by the filo-micelle formulation was notable with previous intravenous delivery of drugs and dyes by using the highly elongated filo-micelles (Mahmud et al., 2017). The advantage of the filo-micelles was using them to load double dose of lung cancer treatment which demonstrated sustained shrinkage for the tumour in the mouse model (Cai et al., 2007; Christian

et al., 2009). Therefore, combining the size, shape, and surface functionalisation effects to generate collections of optimised parameters for diverse designs of new drug carriers is paramount.

Many reports investigate cell targeting, blood distribution, and transportation pathway for controlled complexes of nanoparticles *in vivo* (Simone, Dziubla, and Muzykantov, 2008; Decuzzi et al., 2009; Pillai et al., 2011; Venkataraman et al., 2011; Truong et al., 2014; Zhao et al., 2019). For example, the renal clearance of 20 to 150 nm SPIO nanorods was reported as not the opsonisation/ macrophage's removal from the bloodstream (Cai et al., 2013; Hola et al., 2015). pH-triggered modification for the surface of SPIO nanorods control the release, as well as reduced their aggregation (Fan et al., 2013; Wu et al., 2015; Kandasamy and Maity, 2015). These surface coatings can also be utilised to attach prodrugs. Thus, the whole functional nano-complex has both diagnostic and therapeutic potential properties (Gupta and Gupta, 2005). Recent investigations have reported the forces of unidirectional nanoparticles growth which allow the generation of pure nanodrugs instead of unnecessary loading of extra cytotoxic materials. Therefore, elongated self-assembled nanocarrier formation was preferred for advanced therapeutic applications (Avolio et al., 2019; Mougin, Bourgaux and Couvreur, 2021).

Heat generation by magnetic forces was compared between cubic and spheroid SPIO nanoparticles for hyperthermia application. The reports found that the magnetic heating efficiency was higher from the SPIO nano cubes with 20 nm size (Martinez-Boubeta et al., 2013). Afterwards, another comparison between the nano-cube and nano-rod SPIO particles showed that similar volume of SPIO nanorods exhibit more enhanced hyperthermia (Das et al., 2016). In spite of the previous advantages of the nano-rod carriers, translating metal oxide nanoparticle formulations from the aqueous solutions into physiological conditions is problematic, due to their immediate or gradual sedimentation in ion-rich media conditions, such as physiological buffers and bodily fluids, which inherently results in protein binding and the flocculation of SPIO nanoparticles (Fan et al., 2013). Hence, stability profiles should be studied thoroughly after each SPIO nanoparticles development.

1.2.4 The advantages of using SPIO nanoparticles over other metals

Chelated gadolinium is used in over than 30% of all MRI scans as a contrast agent; however, its widespread clinical usage is limited (Aime and Caravan, 2009). Despite being fully chelated (typically with EDTA analogues) (Rees et al., 2018), gadolinium ions are reported to leach into the blood stream, resulting in nephrogenic systemic fibrosis and signs of neurological disorders (Unterweger et al., 2018). SPIO nanoparticles are, therefore, emerging as clinically approved alternatives (Gale and Caravan, 2018). This can be attributed to their lower toxicity and colloidal stability at physiological conditions, which should be optimised to prevent cases of severe reactions and blood clots (Veiseh et al., 2010; Fülöp et al., 2018), controllable surface charge and their low nonspecific protein adsorption (Nie, 2010; Chapman et al., 2013). The combined medical imaging and potential therapeutic properties of SPIO nanoparticles have recently been demonstrated for biocompatibility in both preclinical and clinical trials (Gupta et al., 2007; Rivera Gil et al., 2010; Cai et al., 2013; Hola et al., 2015; Kandasamy and Maity,

2015; Jain, 2018). Uniquely, SPIO nanoparticles have also been investigated as a medical device for localised hyperthermia therapies to induce cell death in cancer tissues (Gupta et al., 2007; Rivera Gil et al., 2010).

Further potential applications for SPIO nanoparticles currently attracted attention as the wireless on-demand response. For instance, applying an alternating magnetic field triggers the SPIO nanoparticles to rotate, and their kinetic energy is translated into a localised increase in tissue temperature (up to *ca.* 46 °C), resulting in targeted cellular apoptosis with minimal side effects (Zhao et al., 2012; Stocke et al., 2017). Personalised SPIO nanoparticles can control drug delivery efficiency. They can be controlled spatially by a static magnetic field to the targeted site to release the loaded drug according to the frequency of the applied magnetics forces (Wang and Kohane, 2017). Hyperthermia can be added to certain cases too (Golovin et al., 2015). In spite of the previous advantages, these novel approaches still have limitations at the moment. These systems should be provided with sensors for the exact temperature inside the body to measure the intensity and frequency of the magnetic field precisely to avoid off-target side effects. Designing a control system is essential to induce the temperature before developing random necrosis or hyperthermic shocks to the cells. The stability of the nano-packages could be affected by the leak or leaching of the active material from the nano-carriers (Mirvakili and Langer, 2021).

In summary, SPIO nanoparticles have been extensively used in cancer theranostics for imaging and various magnetic targeting, resonance, heating, and mechanical forces. Some of the SPIO nanoparticles usages are associated as the following: contrast agents, fluorescence stains, near infra-red and ultrasound imaging. They were synchronised with the other types of cancer treatments such as, the chemo, gene, immune, antibodies, photo, and thermal therapies. Nano-packages of conjugated vectors showed both effectiveness and downsides in recent cancer treatment (Kandasamy and Maity, 2015).

1.3 Method development

The synthesis of iron oxide nanostructured crystals in aqueous media dominates the methods of developing SPIO particles due to the fact of the abundance of the iron precursors naturally. Furthermore, the easy accessibility and cost-effective starting materials derived a considerable desire for the formation of excellent magnetic SPIO nanoparticles (Li and Zhu, 2020). Some synthetic methods for SPIO nanoparticles are coprecipitation, combustion, gyrothermal, thermolysis, sol–gel, and hydrothermal processes (Bae et al., 1998; Rigneau et al., 1999; Deb and Basumallick, 2001; Dong and Zhu, 2002; Khollam et al., 2002; Woo et al., 2004; Deshpande, Mukasyan, and Varma, 2004; Zou et al., 2005; Zhang et al., 2008).

1.3.1 Co-precipitation

The co-precipitation synthesis is likely the most popular, applicable, and efficient method to generate SPIO nanoparticles (Wu et al., 2011). The straightforward steps include dissolving ferrous and ferric

salts ratio of (2:1) in aqueous solution, then adding an alkaline reagent to trigger the homogeneous precipitation of iron oxide while stirring vigorously at specific temperature (Wong-Molina et al., 2008; Pereira et al., 2012). Due to the instability of the iron oxide in the presence of oxygen, the reaction usually conducted under nitrogen in closed flask. The final physical structure to the crystals is strongly related to the parameters and conditions such as the temperature, pressure, time, alkaline reagent, and speed of mixing (Salavati-Niasari, Mahmoudi, and Amiri, 2012).

The mechanisms of iron salt transformation to iron oxide crystals were observed using advanced technology such as including transmission electron microscopy (TEM), X-ray diffraction (XRD) for the characterisation and the particle growth or changing from rice like shape into spheres (Liu et al., 2011; Suh et al., 2012). Urea and ammonia are the common precipitation agents. However, using different alkaline reagents enabled variation of saturation magnetisation. Moreover, using a surfactant in the reaction affects the size, shape, and magnetisation of the nanoparticles too (Li et al., 2008). For example, adding different amount of surfactant sodium dodecyl sulfate (SDS) during a coprecipitation reaction produced nano-spheres, nano-needles, and nano-cubes Fe_3O_4 particles (Woo et al., 2004).

Coating the SPIO nanoparticles with sodium oleate or PEG polymers decreases the size of the generated nanoparticles (Bronstein et al., 2007; Wang et al., 2012). Also, doping with Cu or Sn forms small sizes due to the reduction in the band gap to the smallest (Liang et al., 2006). The choice of reactor of the coprecipitation reaction can have a significant influence, for instance, using a micro-channel reactor obtained uniform size distribution for high crystalline nanoparticles with small size and large surface area (Hu et al., 2012). In general, the conventional coprecipitation reaction with straightforward process, ingredient, and conditions made this method promising for the scale-up production of SPIO nanoparticles. Even with the ease of the coprecipitation method, the control of the properties of SPIO nanoparticles is still difficult as long as the rate and kinetic factors are uncontrollable (Wu et al., 2011).

1.3.2 Conventional hydrothermal method

The hydrothermal templated synthesis was first applied to produce crystalline structures five decades ago (Guo et al., 2015). In general, water is used to dissolve the reactants. A sealed autoclave which should be heated to maintain a specific temperature and high pressure for a fixed time is the most common instrument for this process. The certain parameters during the hydrothermal synthesis are the key to generate the growth of the crystals out of the precursors in accelerated process. Any modification to the conditions will strongly implicate a change in the size, morphology, and other physical/ chemical properties. Hydrothermal synthesis is reported to yield different structure shapes such as, mushroom, cube, sphere, and hierarchical iron oxide nanostructures with various morphologies and sizes. Simultaneously, changes in crystals could depend on adding a surfactant beside adjusting the experimental conditions (Trpkov et al., 2018).

An interesting example when producing an Fe_2O_3 hollow sea urchin-like nanostructured from aqueous solution of $FeCl_3$ and Na_2SO_4 as building blocks (Zhang et al., 2009). Afterwards, the research reported the templated mechanism to produce the growth of Fe_2O_3 nanorods (Ni et al., 2009; Almeida et al., 2010). Moreover, assembling Fe_3O_4 microspheres was investigated by using ascorbic acid as the reductant, urea as the precipitator, and poly(ethyleneglycol)-6000 as a template (Lv et al., 2009). In another work, controlling the hydrothermal reaction by adding polyacrylamide averaged the size to 230 nm (Leshuk, Krishnakumar and Gu, 2015). whereas, using sodium oleate instead of poly(acrylic acid sodium salt) demonstrated an influence on the hydrophilicity/hydrophobicity and the dispersion properties of the Fe_3O_4 nanoparticles (Kolen'Ko et al., 2014). Currently, many more options have become available in iron oxide based nano composites including amorphous nanorods, three-dimensional hierarchical porous graphene structure, and flower-like nanosheet composite (Suma and Deng, 2015; Zhang et al., 2016; Zhang et al., 2017).

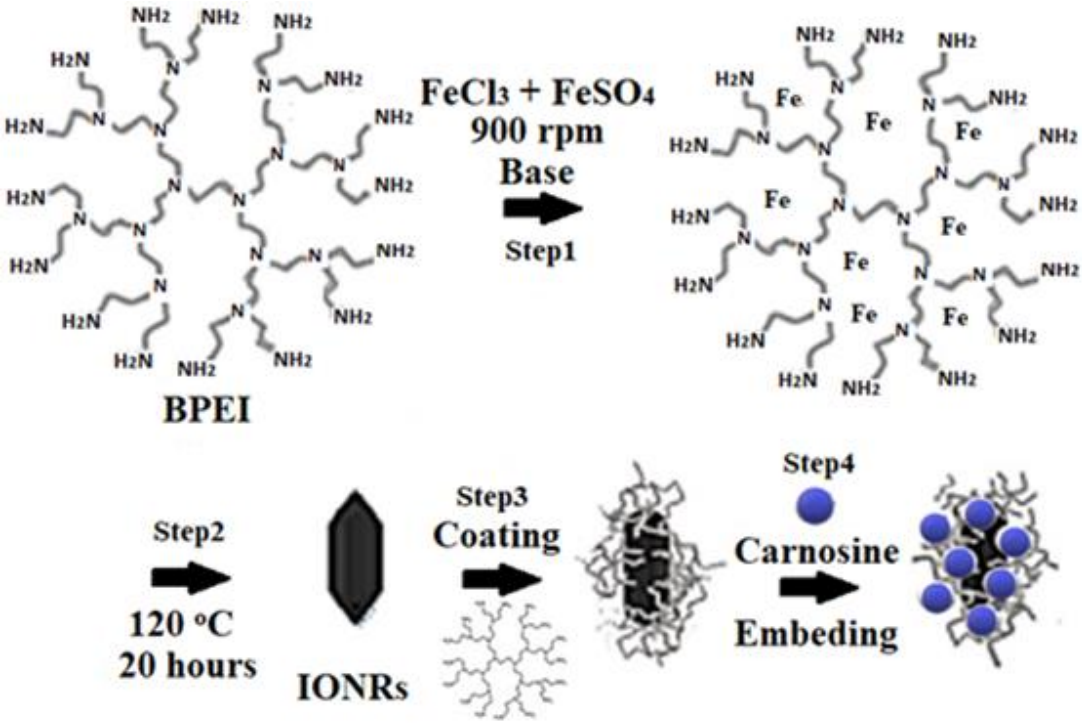

Scheme 1. Synthesis of nanotherapeutic carrier, loaded with carnosine. Step1 is the coprecipitation, Step2 is the thermal degradation, Step3 is coating with BPEI, and step4 is embedding the carnosine into the BPEI branches.

In this project, the synthetic route of carnosine embedded within an iron oxide nano rod (IONR)-functionalised carrier is illustrated in (Scheme 1). Branched polyethyleneimine polymer (BPEI), with its high density of cationic amino functional groups, dendritic structure, and inherent interstitial voids, was selected as a template for the IONRs (Nie, 2010). In step one of the syntheses, the ferrous and ferric iron precursors were loaded into the polymer template before the addition of ethylenediamine. The latest resulted in the co-precipitation of Fe_3O_4. The template was then removed, in step 2, *via* thermal

degradation in a sealed reaction vessel (120 °C, 20 h), and the IONRs were washed with dry dimethyl formamide to avoid aggregation (Habra et al., 2021).

1.4 Results and discussion

1.4.1 Characterisation

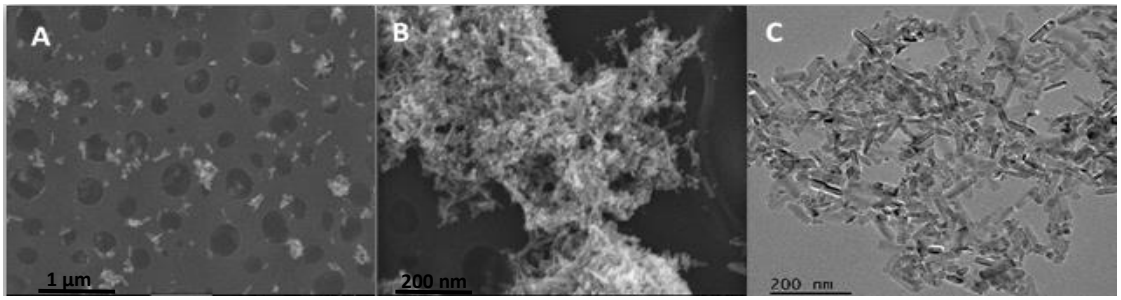

Figure 5. (A, B) SEM images show the aggregates of naked iron oxide nanorods before coating. The scale bars are 1µm, 100nm. (C) TEM image shows similar aggregates for uncoated IONRs.

Figures 5, 6 and 7 for SEM, TEM, XRD and thermal gravimetric analysis (TGA) studies confirmed that the IONRs were repeatable (85.9 ± 17.1 × 19.1 ± 1.8 × 11.3 ± 2.1 nm) Fe_3O_4 nanoscale crystals (Figure 7A). The powder XRD spectrum of the capped IONRs corresponded (Cai et al., 2013c), as expected, to the two individual components, with the inorganic lattice displaying the (111, 220, 311, 222, 400, 511, 440) planes of Fe_3O_4 (Figure 6C). The IONRs were then capped in fresh BPEI (13.4 ± 2.3% w/w coating ratio), an efficient transfection agent (Whittaker and Davis, 2009), before being washed with water, centrifuged, and dried under vacuum, resulting in a black powder (84.4 ± 5.5% yield), before being stored under a nitrogen atmosphere until further use (Wan et al., 2005; Ebrahiminezhad et al., 2012; Ding, Liu and Jiang, 2013; Mohapatra et al., 2015; Medeiros et al., 2015). TEM microscopy (Figure 7B) of the BPEI-coated IONRs was found to be a crystalline, with a tetragonal prism-dipyramid morphology and mean length of 85.9 ± 17.1 nm. The electron microscopy images show prolific agglomeration and a lack of uniformity prior to coating with the BPEI, whereupon they transition to monodispersed tetragonal bipyramidal nanorods (Figure 7C) (Sun et al., 2012; Mohapatra et al., 2015). The BPEI polymer adsorbs onto the surface of the BPEI-coated IONRs, thus making a steric stabilisation, which enhances the dispersion state. Optimising the polymer density on the surface of the BPEI-coated IONRs is essential to avoid the cross-bridging effects reported at higher concentrations (Ogura et al., 1996).

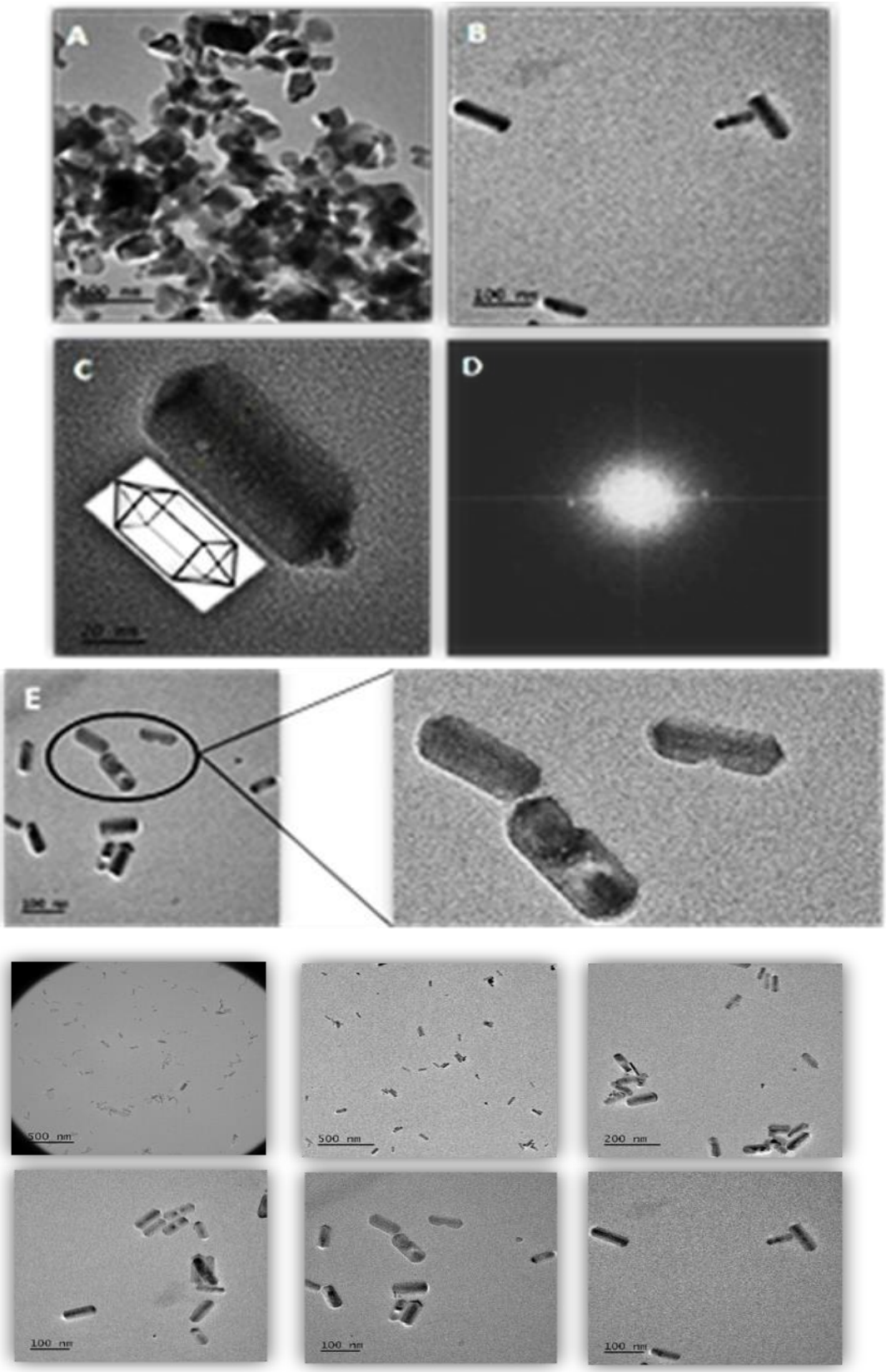

Figure 6. Transmission electron microscopic (TEM) images of (A) uncoated IONR exhibiting significant agglomeration, (B) mono disperse BPEI-coated IONRs, (C) single IONR with tetragonal prism-dipyramid morphology, (D) Fast Fourier transformation (FFT) crystal structure diffraction pattern of BPEI-IONRs, (E) the images show the uniformity size and shape of the BPEI-coated IONRs in various magnifications and spots.

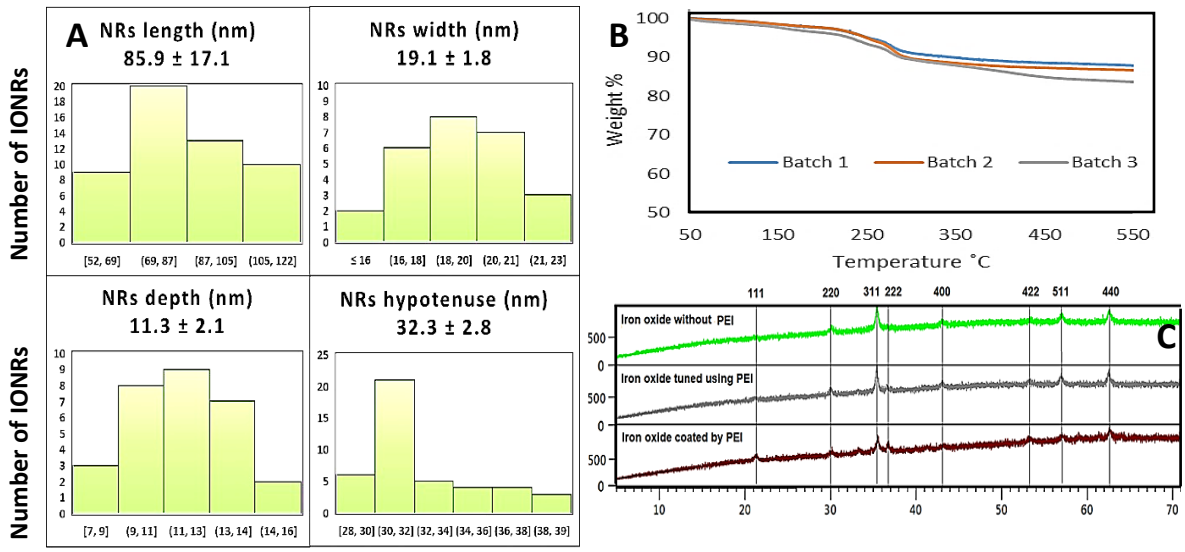

Figure 7. (A) Image J analysis for the dimension distribution for the tetragonal prism-dipyramid morphology of the iron oxide nanorods (length, width, depth, and hypotenuse). (B) TGA shows the repeatability in coating method for three batches. (C) XRD displays the labelled characteristic planes (111, 220, 311, 222, 400, 511, 440) for the iron oxide crystal pattern (naked, tuned with polymer and coated with extra layer of polymer).

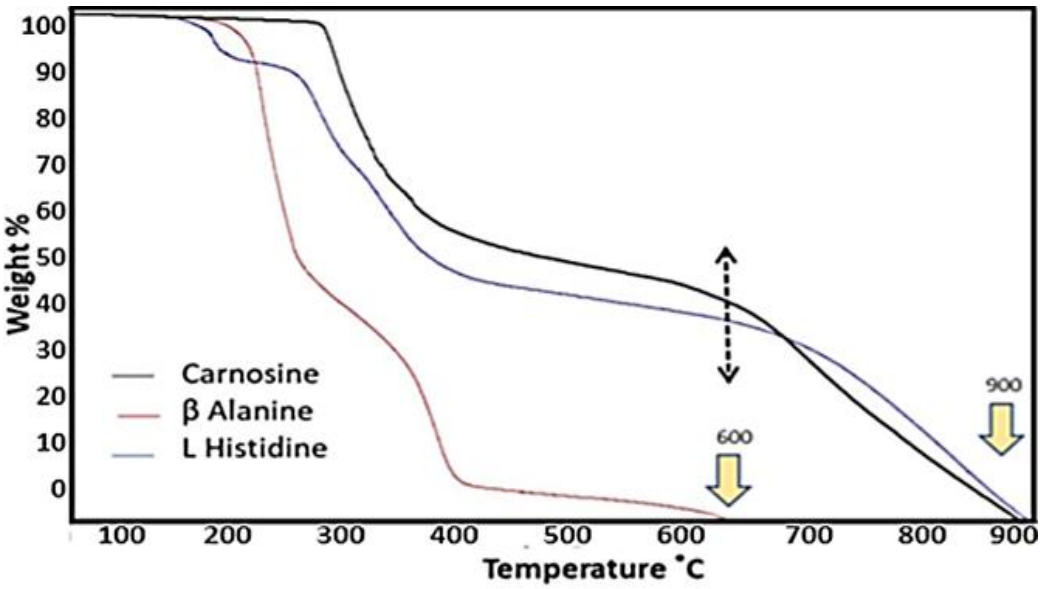

Figure 8. TGA shows the carnosine compounds. Carnosine shows a distinct two stage weight loss with an onset at 196°C. A first weight loss of 46.04% and a second weight loss of 45.79% equate to a total mass loss of 91.83%. The major loss of β-Alanine happens between 200 and 300°C. L-Histidine is the responsible for the loss pattern between 600 and 900°C.

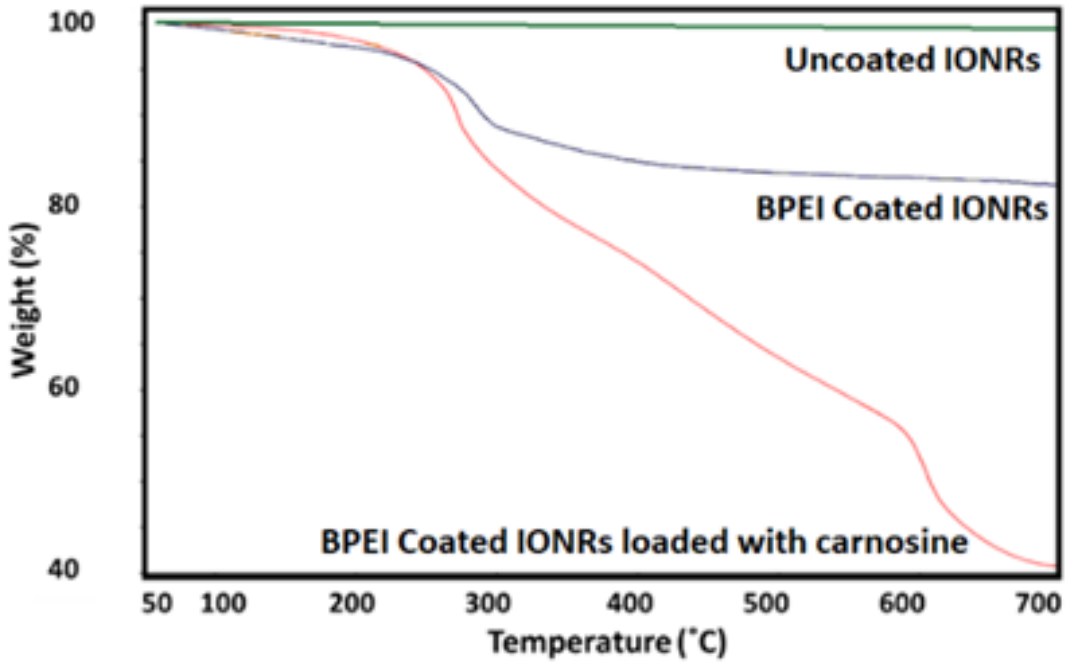

Figure 9. TGA results between 50 and 700 °C of uncoated IONRs (green), IONR capped with BPEI (blue) and capped IONR loaded with carnosine (red).

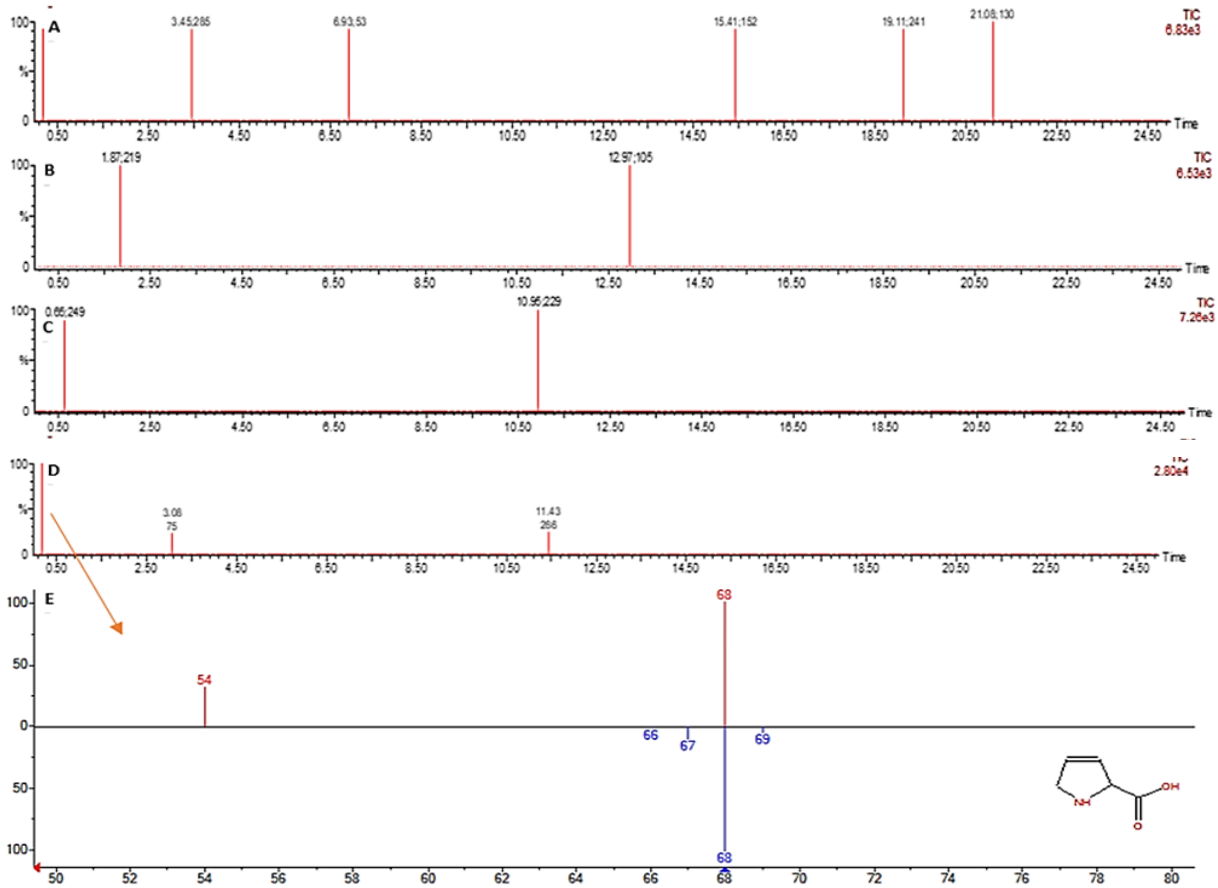

Figure 10. GC-MS spectrums analyse the organic coat on the IONRs which evaporate at (A) 13 minutes, (B) 22 minutes and (C) 25 minutes which cover the range between 150 and 600˚C. (D, E) Specific peak for carnosine/PEI coated NRs between 600 and 800°C matches imidazole in MS library from L-histidine.

TGA with hyphenated FTIR-GC-MS (shown in Figures 8 and 9), confirmed that the IONRs were coated with BPEI (87% w/w) (Mohapatra et al., 2015; Wang et al., 2018). Figure 8 and 9 shows a carnosine loading of *ca.* 60% mg carnosine/µg IONR/mL water, as analysed by evolved gas analysis using TGA-FTIR-GC-MS (Figure 10). The polymer is observed, in Figure 8, to be completely dissociated between 150 and 300 °C, while the β-alanine and L-histidine from the carnosine degraded between 300 and 700 °C. This is similar to the results observed for the pure carnosine and the two amino acids (β-alanine between 200 and 300 °C and L-histidine between 600 and 900 °C (Figure S3), evidencing that carnosine is embedded within the structure of the carrier (Balog et al., 2015).

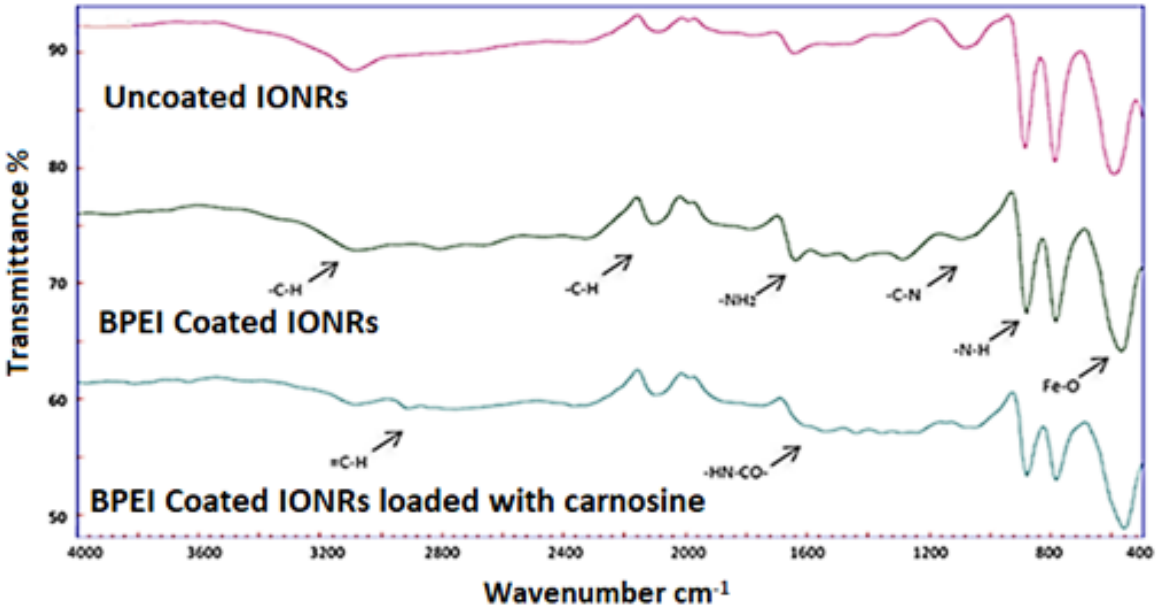

Figure 11. FT-IR spectra show changes in the spectrum of uncoated IONRs (red), IONR capped with BPEI (green) and capped IONR loaded with carnosine (blue). Arrows indicate the representative frequencies from the imidazole ring of L-histidine and peptide bond.

The infra-red attenuated total reflectance (FT-IR) ATR spectrum of the carnosine loaded carrier displays characteristic bending bands between 1474 and 1630 cm^{-1} that are attributed to the peptide bond of carnosine, and a band at 2900 cm^{-1} from the imidazole ring of L-histidine. In addition, the strong stretch at 3000 cm^{-1} is due to the absorbance alkane C-H (Mohapatra et al., 2015) (Figure 3), and the peptide bond overlaps the strong bending band at 1474 and 1630 cm^{-1} of the NH_2 group. Despite the annealing of the BPEI as a template during the synthesis of the IONRs, it is clear that there remains trace residual polymer on the nanorods.

1.4.2 IONRs colloidal stability

Aggregation of nanoparticles can lead to anomalies in results and limit reproducibility. As a time-dependent process, this can result in changes when measuring their cellular responses and the toxicity profiles (Ogura et al., 1996; Butkus and Grasso, 1998; Ebrahiminezhad et al., 2012). Metal oxide

nanoparticles, including those investigated as MRI contrast agents, are often susceptible to agglomeration or sedimentation over prolonged periods of time, especially under physiological conditions (Mohapatra et al., 2015; Unterweger et al., 2018). Therefore, the colloidal stability of SPIONs is commonly demonstrated in deionised water in order to eliminate the detrimental interactions of electrolytes and variations in pH. This is, however, not representative of real-world behaviour and, thus, their colloidal stability in physiological solutions and media is of paramount importance when considering their potential biomedical applications (Sader, Carnie, and Chan, 1995; Butkus and Grasso, 1998). The zeta potential is often used as an indication of the net charge of a cloud of counter ions around the particle, which differ because of their environment due to the ionisation dissociation of surface groups (McCartney and Levine, 1969; Ogura et al., 1996; Bhattacharjee, 2016). It is reported that the addition of a BPEI coating, onto metal oxide nanoparticles, improves charge and overall electro-steric stabilisation *via* the induced steric hindrance provided by the formation of a hydrophilic macro-shield (Ebrahiminezhad et al., 2012).

In order to evaluate the stability of the BPEI-coated IONRs, dynamic light scattering (DLS) measurements are usually conducted (Edwards and Williams, 2004). However, due to the limitation in DLS sensitivity when using bio-logical buffers, serum, and complex media, they often lead to inaccurate refractive index results (Saini et al., 1987). Therefore, the samples described herein were studied using biological media and MRI techniques. Thanks to the paramagnetic properties of the IONRs, MRI can be utilised to provide spatial resolution and contrast of the samples. The stability of the IONR in water was evaluated for hydrodynamic diameter and polydispersity changes, measured using DLS over the course of one hour and 30 days (Figure 12).

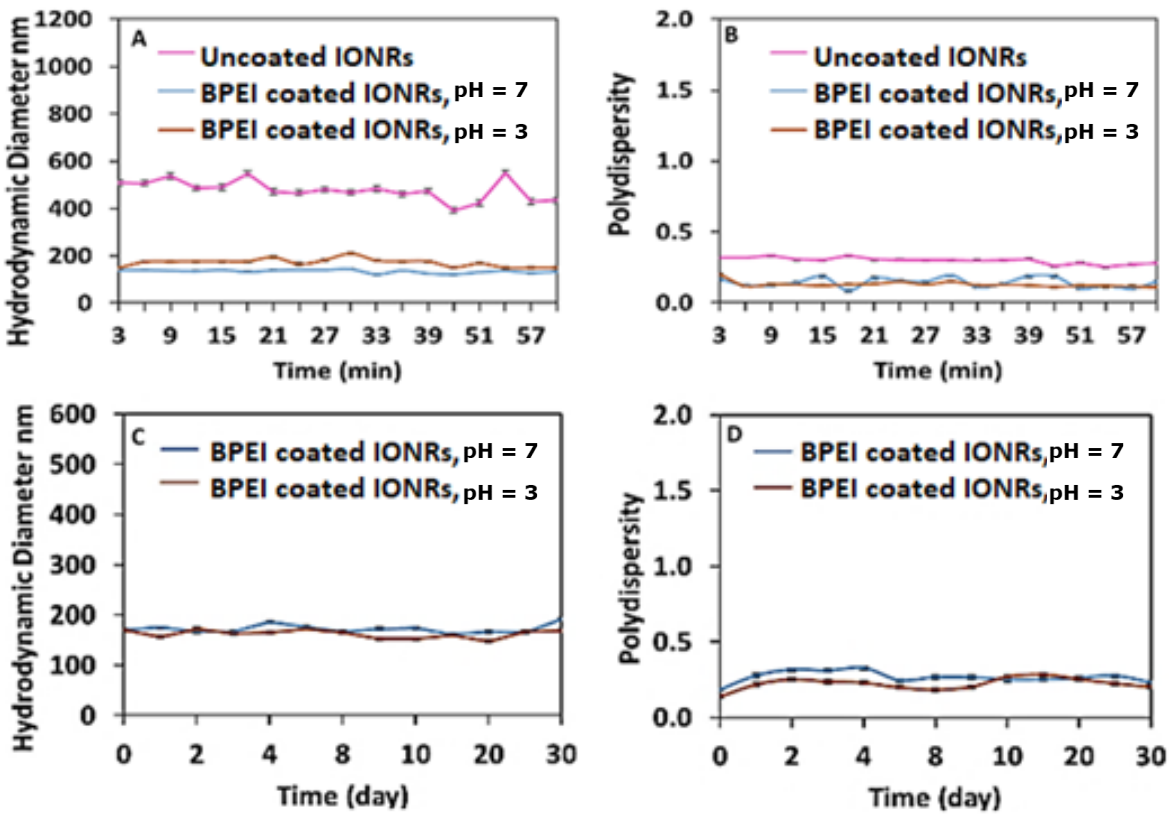

Figure 12. Colloidal stability studies *via* DLS compering intensity distribution measurements at room temperature: (A) hydrodynamic diameter of uncoated IONR at pH 7 (pink), IONR capped with BPEI at pH 7 (blue) and IONR capped with BPEI at pH3 (brown) over one hour; (B) hydrodynamic diameter polydispersity of uncoated IONR at pH 7 (pink), IONR capped with BPEI at pH7 (blue) and IONR capped with BPEI at pH 3 (brown) over one hour; (C) hydrodynamic diameter of IONR capped with BPEI at pH 7 (blue) and IONR capped with BPEI at pH 3 (brown) over one month; (D) hydrodynamic diameter polydispersity of IONR capped with BPEI at pH 7 (blue) and IONR capped with BPEI at pH 3 (brown) over 30 days.

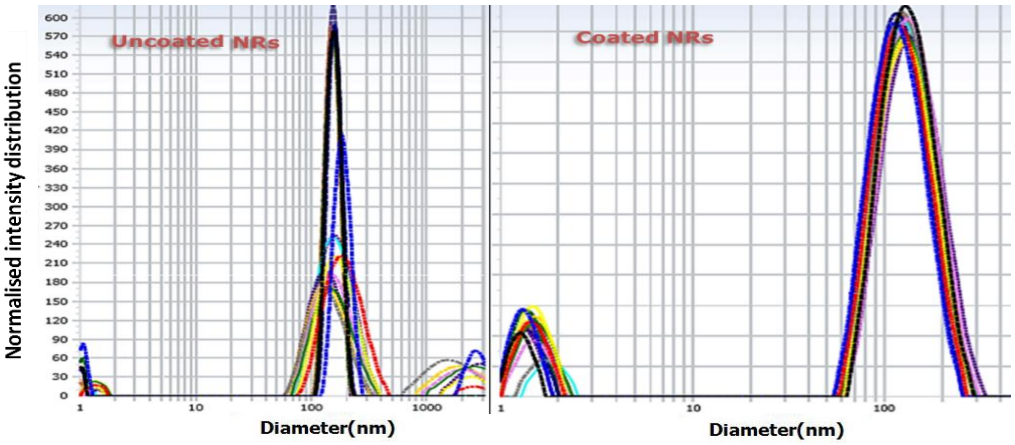

Figure 13. DLS compering the intensity distribution of the iron oxide nanorods hydrodynamic diameter before and after coating. The polymer coating prevents the aggregation. After coating, the rods had a relative stable hydrodynamic stable diameter over an hour. Each measurement is the mean of 60 measurements repeated 3 times over 3 minutes to reduce the error to the minimum.

Table 1. R^2 for the Hydrodynamic diameter and polydispersity of the IONRs in different conditions over 1 hour.

1 hour	Uncoated IONRs	BPEI coated IONRs pH = 7	BPEI coated IONRs pH = 3
Hydrodynamic diameter (µm)	0.311	0.254	0.123
Diameter polydispersity	0.653	0.277	0.012

The IONR size and polydispersity did not show any significant changes over time in water at pH 7, indicating that the formula is colloidally stable for over one hour at room temperature (Figure 13). By comparison, the uncoated IONRs show significant aggregation even after sonication, with a mean hydrodynamic diameter of *ca.* 500 nm (Figure 12A). Reducing the pH down to three did not have a significant effect on the hydrodynamic diameter of the IONR; however, the polydispersity was observed to be more uniform (Figure 12B). The R^2 of the coated IONRs, at both pH 3 and 7, was below 0.5 and, therefore, has an insignificant effect on the hydrodynamic diameter and polydispersity. However, the polydispersity for the uncoated IONRs was 0.65, which refers to a moderate effect in the uniformity from the first hour (Table 1). The initial hydrodynamic diameter and polydispersity were *ca.* (165, 0.2), and ended *ca.* (500, 0.35) after an hour.

The results of the 30-day DLS stability trial show that at pH 7, the IONR has stability in the hydrodynamic diameter (172 ± 8.8 nm), and also demonstrates polydispersity (0.267 ± 0.038). Similar results were also observed at pH 3, with a mean hydrodynamic diameter of 163 ± 8 nm and a polydispersity of 0.228 ± 0.031. There was an absence of aggregation indications, and no precipitation would have been developed over a month, which is essential for biomedical applications (Wang et al., 2009) (Figure 12). This study showed a wide range of safe pH storage conditions as a ready suspension that will be buffered before the application instead of a longer process of hydrolysing the dry powder by sonication. In-deed, the suspension had been reserved over a year and did not show sedimentation or change in specifications.

In line with the DLS results, the two dispersions of IONR in water, at pH 3 and 7, show uniform dispersion throughout the 48 hours, with little to no evidence of any sedimentation or flocculation of the carrier. The carriers quickly agglomerated with the addition of phosphate buffer solution (PBS) resulting in a black precipitate that completely fell out of solution within 48 hours, yielding similar results for the 1 hour and 48 hours images. PBS (1×) showed rapid sedimentation, while sedimentation of the carrier was slower over the course of the experiment when dispersed into HEPES buffer. The main ingredient of the Eagle's minimal essential medium (EMEM) is PBS and, therefore, it was substituted with OptiMEM media, which contains HEPES. The carrier was observed to remain colloidal in the third component of the cell media, fetal calf serum (FCS); however, when combined with MEM,

the IONR was sedimented out of the solution. Conversely, when OptiMEM-reduced serum media was substituted for MEM, the IONR remained sus-pended as a colloidal dispersion (Figure 14).

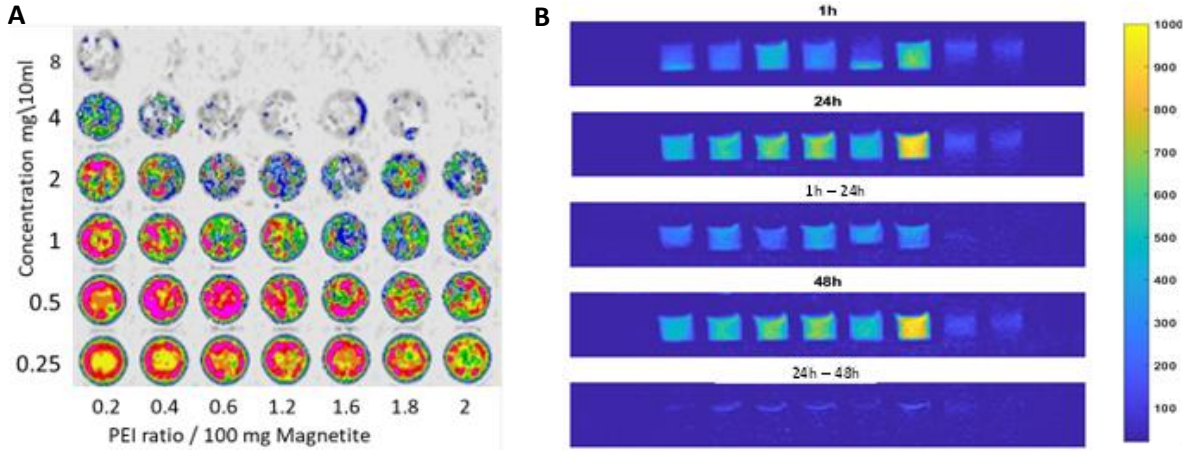

Figure 14. (A) MR images show the BPEI-coated IONRs as blue contrast agents at the concentration range of coating in this project and (B) the colloidal sedimentation of BPEI-coated IONRs under different conditions: water pH 3/pH 7, PBS, FCS, MEM. MEM/FCS, Opti-MEM, Opti-MEM/FCS and HEPES at room temperature after 1, 24 and 48 hours. The difference found between 1 and 24 hours is more than that which is found between 24 and 48 hours. The colour codes are related to sedimentation in arbitrary units. The yellow shadow refers to sedimentation and the blue shows the stability of the suspension.

The MRI results included herein confirm that the use of PBS, alone or within a media, results in rapid sedimentation. This is due to the relatively high sodium ion concentrations and the subsequent compression of the electrical double layer that surrounds the BPEI-coated IONRs (Saini et al., 1987), and ultimately the collapse of the colloidal system. It is also re-ported that sedimentation can be reduced by substituting PBS for the zwitterionic HEPES buffer since it is proposed that the FCS proteins attach to the surface of the BPEI-coated IONRs and sterically hinder any potential to agglomerate (Ogura et al., 1996). This further MRI experiment was undertaken simultaneously to evaluate this process by determining the effective spin lattice relaxation time constant (T_2^{eff}) since the paramagnetic properties of the nanorods are known to shorten this value (Liang, Park and Guan, 2007). These results show that the ionic charge, between the BPEI-coated IONRs and media, can be balanced by using Opti-MEM as the media in combination with FSC. Furthermore, the BPEI-coated IONRs within the carrier preserve their super paramagnetic properties, enabling them to be utilised as MRI contrast agents. The overall nano-carrier foundation is also proven to be stable as both a dry powder - that can be readily re-suspended - and directly as suspension in sterilised water, for at least one month.

1.4.3 Trace and localisation of IONRs

The uptake and localisation of the IONRs was studied in U87 MG cells. The intercellular transportation and intracellular localisation of BPEI-coated IONRs are vital in their overall interactions due to their theragnostic applications (Wani, 2017). Many factors impact the uptake of IONR, such as particle size,

polydispersity, and the surface charge of the functionalised coating. The SEM images show the uptake and localisation of BPEI-coated IONRs in U87 MG cells after incubation for 24 hours.
Figure 15 showed the nanorods in the cytoplasm and probably localised inside the nucleus. The iron ions overloaded heavily in the images of cells treated with BPEI-coated IONRs at a concentration of (10 μg/mL); however, a concentration of 5 μg/mL kept the cells alive. The energy-dispersive X-ray spectroscopy (EDS) detected the elements and proved the iron peaks in the map scan of the cells. This toxicity was dictated in previous works when the BPEI-coated IONRs became overloaded (*ca.* 10 μg/mL) (Wani, 2017), while the BPEI-coated IONRs at a concentration of around 5 μg/mL can be considered safe for use in the treatment of glioblastoma brain tumours (Wang et al., 2018).

Nanomaterial with positively charged surface functionalisation allows cellular adhesion and transportation through the ionic interaction with negatively charged cell surfaces. The delivery will be increased which enhances their cytotoxicity margin (Foged et al., 2005; Vasir and Labhasetwar, 2008; Patil et al., 2018). The BPEI-coated IONRs may cause DNA damage by breaking the hydrogen bonding, which generates the reactive oxygen species (ROS) and, at high doses, a damage inside the nucleus injures the actin cytoskeleton structure due to the extra charge (Hass and Barnstable, 2016) (Figure 16).

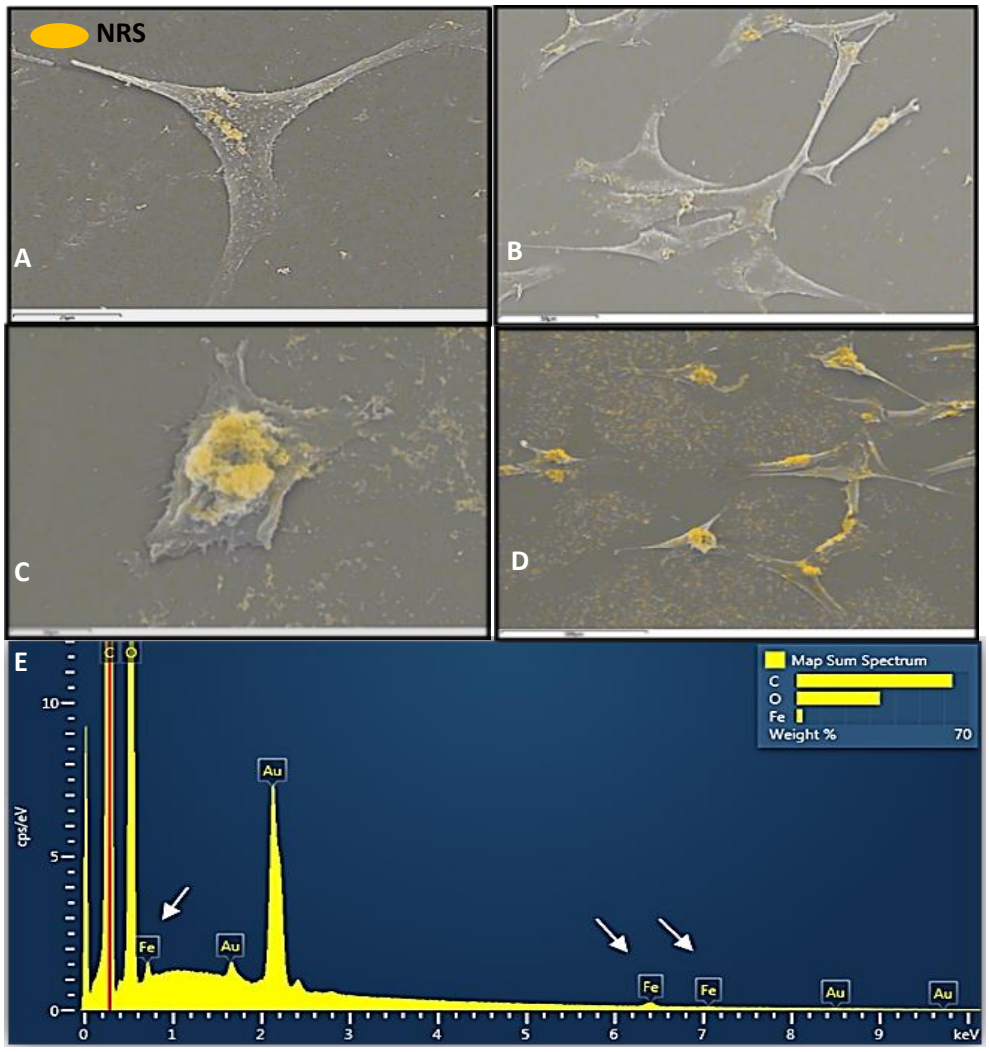

Figure 15. SEM images show the uptake and localisation of BPEI-coated IONRs in U87 MG cells at different concentrations after 24 hours of incubation: (A, B) a 5 µg/mL concentration shows the uptake of BPEI-coated IONRs without affecting the live cells; (C, D) a concentration of 10 µg/mL BPEI-coated IONRs shows the overloaded uptake of BPEI-coated IONRs, which affects the nucleus. (E) The localisation around the nuclei was detected by the EDS map scan spectrum. Areas with iron localisation are distinguished by pseudo-colour that was applied simultaneously to the images to highlight IONRs as yellow. Scale bars are 25 µm for (A and C) and 50 µm for (B and D).

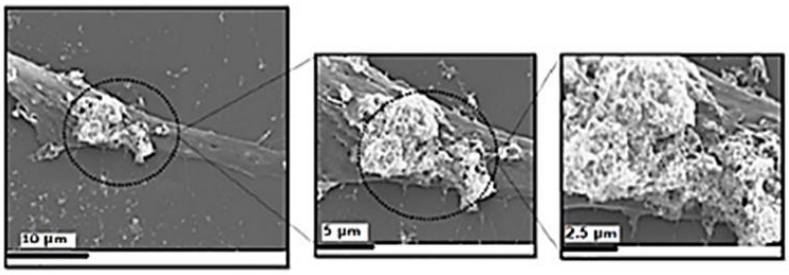

Figure 16. SEM images showing uptake and localisation of BPEI-coated IONRs most likely inside the destroyed nucleus of a U87 MG cell at a concentration of 10 µg/mL of BPEI-coated IONRs.

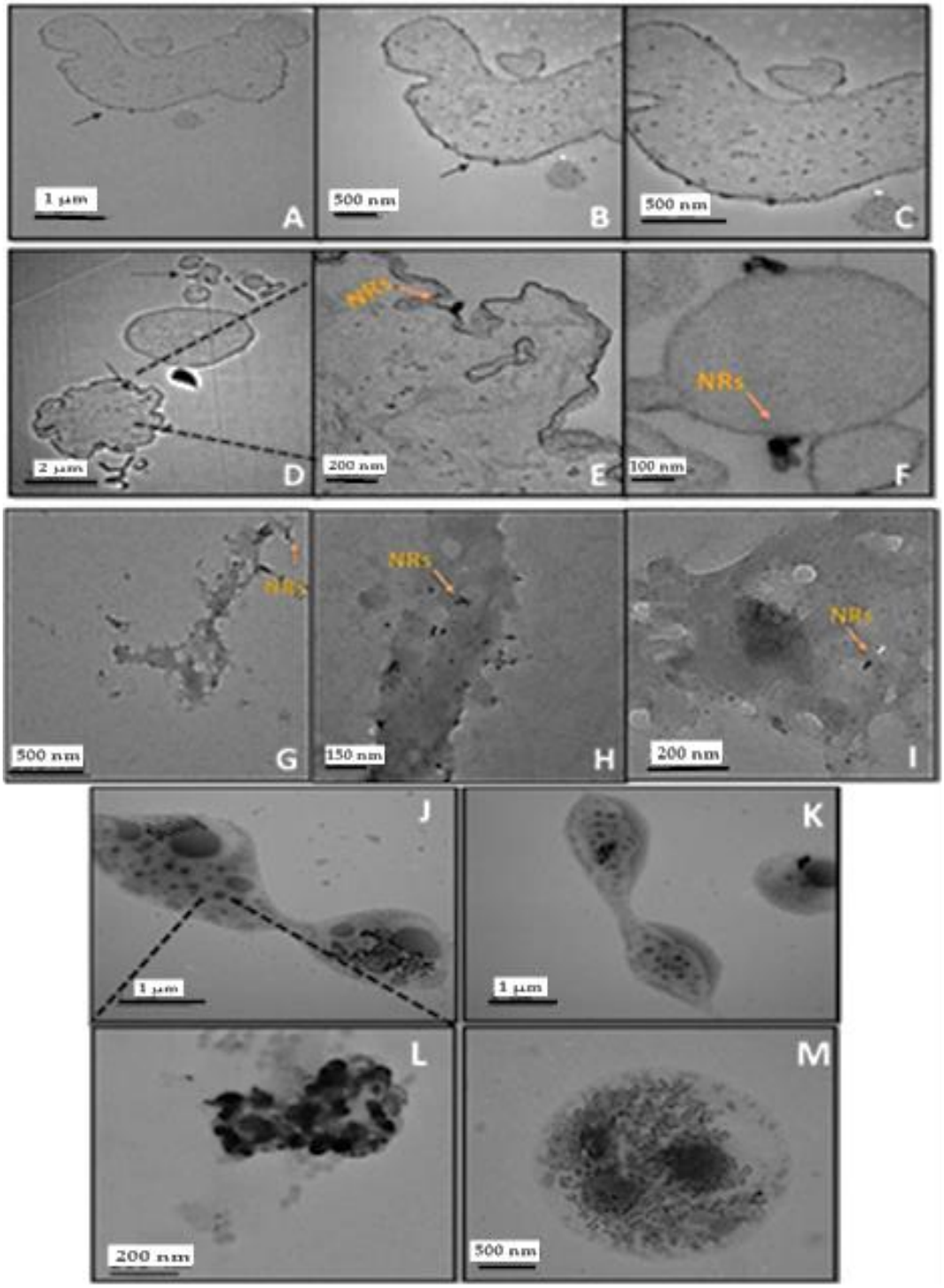

Figure 17. TEM images of U87 MG cells' sections. The pictures represent: (A–F) Cells treated 1 hour after the addition of BPEI-coated IONRs at a concentration of 5 µg/mL and show the rods on the border of the cell membrane. (G–I) Cells after 4 h of being incubated with BPEI-coated IONRs at a concentration of 5 µg/mL for 4 hours. The IONRs that are under 100 nm start to enter the cells and localise in the cytoplasm. (J, K) Cell division 4 h after the addition of carnosine (25 mM). The mitochondria are loaded with carnosine. (L) This organelle is likely to play a pivotal role in relation to MTT assay and the size and distribution most probably refer to the mitochondria. (M) The general observed trend of cell reacting was changing its morphology into spherical shape.

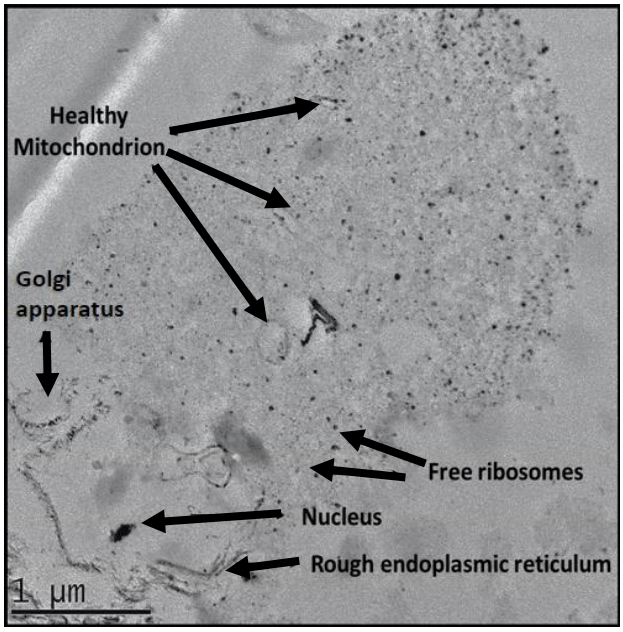

Figure 18. TEM images of U87 MG cells section without any treatment. The image shows the component of the control cell. The arrows refer to the expected organelles such as, Mitochondrion, Golgi apparatus, Ribosomes, Nucleus, Rough endoplasmic reticulum.

TEM images were taken of the resin embedded U87 MG cell sections to support the entrance of the rods inside the cells, as opposed to merely settling on the surface. The sections of the cells, after an hour of incubation with BPEI-coated IONRs at a concentration of 5 µg/mL, exhibited BPEI-coated IONRs that were spread around the cell membrane. TEM images of the tumour cells, after 4 h of exposure to the BPEI-coated IONRs, demonstrated the capability of rods < 100 nm to penetrate the cell border and reach the cytoplasm that was moving towards the nucleus regions (Figures 17). The blank cell shows the basic component of the cell (Figures 18).

1.5 Conclusions

1.5.1 Synthesising SPIO nanoparticles

SPIO nanoparticles could be defined as the nanostructured molecules which develop paramagnetic nature due to the effect of external magnetic field and tend to lose the magnetic oscillation or rotation property once the applied magnetic field is turned off. The relation between the size and the modified surface area of SPIO nanoparticles is proportionally inverted. Thus, the smaller the size of the nanoparticles, the more reactive functions can be added such as coating with surfactants, polymers, lipids. Those additions electrical and spatial hindrances on the surface of SPIO nanoparticles maintain the stability of the colloids by preventing the agglomeration and sedimentation development over time. However, the surface functionalisation can affect the size, shape, and the super-magnetism of the initial

SPIO nanoparticles depending on many parameters including the amount, nature, and thickness of the coating.

1.5.2 Estimating the fate of the SPIONs

The TEM images enabled the tracking of entry into U87 MG cells over (1 and 4 hours), and the SEM images with the EDS traced the distribution of BPEI-coated IONRs in the target organelle nucleus after 24 hours (Hass and Barnstable, 2016; Arachchige et al., 2017). The TEM images represented the morphology change in the U87 MG cells' cytoplasm after 4 hours of carnosine treatment, which was similar to that of rapamycin (Lenzi et al., 2016). The carnosine crystals exacerbated the damage caused to the structure of the mitochondria, which was explained in detail by the Incucyte® live cell studies and MTT assay in chapter 3.

Chapter 3: *In-vitro* studies

1.1 Overview

As mentioned in chapter 1, carnosine has potential therapeutic effects in health and disease. Carnosine is a naturally occurring histidine-containing dipeptide which is produced in some regions of the brain to neutralise the reactive species and regulate detoxification (Artioli, Sale, and Jones, 2018).

1.1.1 The mechanisms of carnosine in GBM brain tumour treatment

The first potential antineoplastic effect for carnosine was proposed nearly four decades ago. The sarcoma tumour cells were implanted subcutaneously *in vivo*, and carnosine was administrated every other day in close proximity to the implantation site. As a result, both tumour growth and mortality were reduced (Nagai and Suda, 1986). Since then, over the years other supportive projects have been interested in proving the selective effect of carnosine in supressing transformed and neoplastic human glioblastoma cells (Holliday and McFarland, 1996; Renner et al., 2008; Renner et al., 2010). After daily application of *in vivo* intraperitoneal treatment with 1 M carnosine the delay in the aggressive growth of tumour model was evidenced despite the uncompleted reverse for the tumour (Renner et al., 2010). The main advantage of carnosine is the contradicted effect it has on healthy cells versus cancer cells where it seems to increase the healthy cells' viability while impeding the proliferation of the cancer cells (Gaunitz and Hipkiss, 2012). Normal cells usually depend on the oxidative phosphorylation to produce energy in normoxic conditions. However, mitotic cells rely on the glycolysis Warburg effect which generates lactate (Oppermann et al., 2016). The primary mechanism for carnosine effect is the ability to inhibit the glycolysis pathway in the tumour cells, particularly (Renner et al., 2013). The reports explanation included activities of the glycolytic enzymes, metabolic regulatory, protein glycation, cell apoptosis, gene expression, redox biology, and metastasis (Hipkiss and Gaunitz, 2014). In 2018, a co-culture model has been developed from patient-derived glioblastoma cells and fibroblasts cells. The presence of carnosine reduced the ATP compared to the untreated cells. The mitotic cells did not make colonies after 4 weeks of carnosine exposure. However, the layers of fibroblasts were healthy. The study showed the elimination of the tumour cells in the model which shadowed the effect on cell mobility (Oppermann et al., 2018).

In this project, the anti-migration and anti-invasion effect of the carnosine on glioblastoma U87 MG cell line was proven with the anti-proliferative effect of mitomycin C (Habra et al., 2021). Another group confirmed the carnosine effect which suppresses human glioma cells under normoxic and hypoxic conditions by the inhibition of glutamine metabolic pathway (Fang et al., 2020). Carnosine targets the tumour metabolism by promoting protein degradation in the proteasome pathway and influences transcription *via* epigenetic regulation to inhibit the proliferation and metastasis of tumour

cells (Oppermann et al., 2019; Fang et al., 2020). The efficient uptake for carnosine to enter the tumour cells has been proved to be accomplished by three proton-coupled oligopeptide transporters (PEPT2, PHT1, and PHT2). Any absence or reduction in one of them should be considered during the cancer treatment because it will reduce the carnosine uptake (Oppermann et al., 2019). The half-life of carnitine has not been established, it is presumed to be short, and the excretion takes 90 minutes. Thus, carnosine with high quantity to affect tumour cells need to be protected in a biodegradable storage which provide the sustained release. The antineoplastic effect of carnosine is independent of its cleavage, but the experiments identified a strong induction of expression of the gene encoding pyruvate dehydrogenase 4 (PDK4) under the influence of L-histidine too. This conclusion means that single amino acids can regulate key metabolic pathways in the body. (Oppermann et al., 2019).

1.1.2 The advantages of PLGA beads and liposomes vesicles for cancer drug delivery and modified release

Traditional chemotherapeutic treatments are known for their toxicity to healthy cells because they showed non-selectivity in the biological effects. Many cancer drugs are considered hydrophobic active materials that create a challenge in drug application and delivery. However, many investigations introduced methods for entrapping the therapeutic compounds in nano-/ micro- colloidal formulations to enhance the efficacy and minimise the side effects (Brigger, Dubernet, and Couvreur, 2012). The FDA-approved polymer of PLGA has attracted great attention due to its safety as well as many potential applications such as the possibilities of sustained release, surface modification, and specific targeting to provide a better interaction with biological materials (Danhier et al., 2012). PLGA encapsulation was the solution for the water insolubility for cancer drugs, for example, the paclitaxel loaded PLGA microspheres (Zhang et al., 2018). Furthermore, the surface modification of PLGA developed to be pH sensitive or to enable the release of drugs to be controlled such as the encapsulation of antitumor drug doxorubicin hydrochloride (DOX) and Gadolinium (NaGdF4) for cancer cell imaging and drug delivery. (Taghavi et al., 2017; Zhao et al., 2017). Similar to the effect of PLGA in drug delivery, encapsulation using liposomes has showed benefits in vaccine preparations. In a comparative study between PLGA encapsulation and liposomes for subcutaneous vaccine formulation, loaded cationic liposomes showed a superior functional cytotoxic CD8+ T cell immune response *in vivo*. The liposomes demonstrated a stable safety storage to accommodate the antigens (Varypataki et al., 2016).

The rapid release of the drug could be triggered by ultrasound. To combine the stability, the liposomal vesicles were formulated with lipid, cholesterol, and PLGA-NPs. Afterward, Mitoxantrone was encapsulated into the liposomes. With optimised stable liposomes, adding PLGA-NPs showed the rapid ultrasonic responsive ability. PLGA-NPs vibration affects the lipid membrane and trigger the *in vitro*/ *in vivo* release (Xin et al., 2017). Another interesting hybrid system was the liposomal doxorubicin-loaded thermogel which was generated the sustained delivery of doxorubicin as a local treatment of

breast cancer. The liposomal doxorubicin-loaded PLGA-PEG-PLGA thermogel was a solution at room temperature and transformed into a solid gel *in vivo*. This formula exhibited a steady prolonged release of DOX without a distinct initial burst. The gel gradually degraded and the entrapped drug pass through the liposomal bilayer. This thermogel has significantly inhibited tumour growth in the mouse model (Cao et al., 2019).

1.1.3 The safety studies on healthy cells (carnosine, PEI, PLGA, and liposomes)

The main materials in this project were carnosine as an active pharmaceutical ingredient (API), PEI, IONRs, PLGA for beads, and liposomes. Each component should be extensively investigated to guarantee safety application on normal cells and tissues. The therapeutic benefits of carnosine have been investigated preclinically and clinically for many neurological diseases associated with complexity and it was gradually biodegraded. Current reports supported the significant boost in health when using carnosine without showing side effects in humans (Xing et al., 2019). Carnosine was reported with undesirable side effects just in one study where a benign sensation of tingling and numbness which was observed with a concentration over 100 µM (Derave et al., 2010; Boldyrev, Aldini, and Derave, 2013). The healthy benefits assessment of carnosine was proved clinically in a dose ranging between 0.8 to 2.8 g/day if the degradative enzyme carnosinase was in the normal abundant levels (Houjeghani et al., 2018). However, the cases with carnosinaemia disease associate with the lack of carnosinase (Kyriazis, 2010). Overall, carnosine is a safe bioactive component as a dietary supplement. The healthy properties overweigh the only downside of paraesthesia.

Extensive evaluations have been reported on the ability of PLGA to deliver many therapeutic agents with sustained and/ or targeted release (Liu et al., 2015; Park et al., 2017). PLGA toxicity of the biological distribution have been studied *in vivo* (Semete et al., 2010; Pan and Ding, 2012). Also, PEI has been reported as a useful pulmonary gene carrier with a low effect on the production of cytokine in the lungs (di Gioia and Conese, 2008). Most of the safety studies focused on the adulthood duration, but the effect of the exposure to PLGA and PEI was detected in preimplantation embryos during early pregnancy. A labelled nano-tracer was used in gametes and preimplantation embryos in mouse models. The results showed that PLGA and PEI are safe and biocompatible because they do not affect the developmental programming of the early embryos in the next generation of mice. Thus, the embryo was developed to the blastocyst safely in the presence of PEI and PLGA (Kim et al., 2018).

Currently, various liposomal formulations are on the market or in the pipeline for cancer treatment. Since 2014, the improvements in liposomes were patented as formulations and analysed by many experts such as the liposomes that contain Ciprofloxacin Nanocrystals. Those improvements included the ingredients, stability, and release profile. The new liposomal systems showed longer circulation with novel structures and functionalisation for theranostic applications. Moreover, they became well adapted for passive and active drug delivery (El-Hammadi and Arias, 2019). Increasing the complexity

of the lipid vesicles requires accuracy in the analysis performed from *in vitro* experiments before they can be translated into clinical studies. After the identification of the liposomal formulation, both toxicity and compatibility studies are always mandatory to proceed for efficiency and delivery (Bozzuto and Molinari, 2015).

1.1.4 How the project is going to expand other groups recommendations

Effective delivery strategies should be applied to protect the carnosine from carnosinase, as well as, to increase its level in the tumour site. In this project, many optimisations and preliminary studies have been reported including using the IONRs as carnosine carriers which release the treatment *in vitro* upon applying a thermal trigger of mild hyperthermia. The same approach could be used for various therapeutic bio-applications and for imaging (Habra et al., 2021). For controlled and/ or sustained release trigger by an external magnetic field, loaded PLGA beads were formulated for hydrophilic IONRs and/ or carnosine *via* double emulsification using the flow focus microfluidic systems (Damiati et al., 2020). Finally, carnosine-loaded liposomes for prolonged release in brain tissues were generated and applied intranasally on animal model.

In the future, any analogue treatment or active material which synergises with the therapeutic effect of carnosine should be considered by the researchers. For example, it was reported that long-term physical exercises increase the carnosine naturally (Artiol, Sale, and Jones, 2018). Thus, another novel exploration about natural carnosine may support cancer treatment.

1.2 U87 MG cell line optimisations for 2D and 3D models

1.2.1 Cell Proliferation

Prior to the proliferation and cytotoxic studies of the U87 MG cell line, cell density studies were conducted to define the cell number required to attain a significant adherence to the bottom of the 96 well plate within 18 hours and without reaching the full confluence after 48 hours. As such, the optimum cell density was found to be 4000 cells per well because wells seeded with higher cell density were found to have cells growing on top of each other by 48 hours affecting the exponential growth. This was reflected by the increase in the deviation of the error bars over the last 6 hours (Figure 19).

1.2.2 Scratch wound assay (migration / invasion)

Scratch wound assay is a convenient and inexpensive method for the analysis of cell migration *in vitro* (Liang, Park, and Guan, 2007). To study the effect of carnosine on the metastasis of U87 MG, the migration and invasion of the cells were assessed over 48 hours course in the same plate in the presence of a concentration of mitomycin C known to prevent cell proliferation (10 µg/ mL) without killing the cells. To confirm the independency and the non-toxicity of mitomycin C on carnosine, a series of tests were carried out to validate the cell adhesion, viability, and proliferation (McCarroll et al., 2004;

Afshordel et al., 2015). The adherence and viability of the cells were similar with and without using mitomycin C and no significant difference was recorded (Figures 20). In addition, no synergism appeared between carnosine and mitomycin C against the growth of the cells. That was proved by imaging the live cells during their migration which was conducted to monitor the intracellular interactions between the mitotic cells and the healthy adjacent cells (Figures 21).

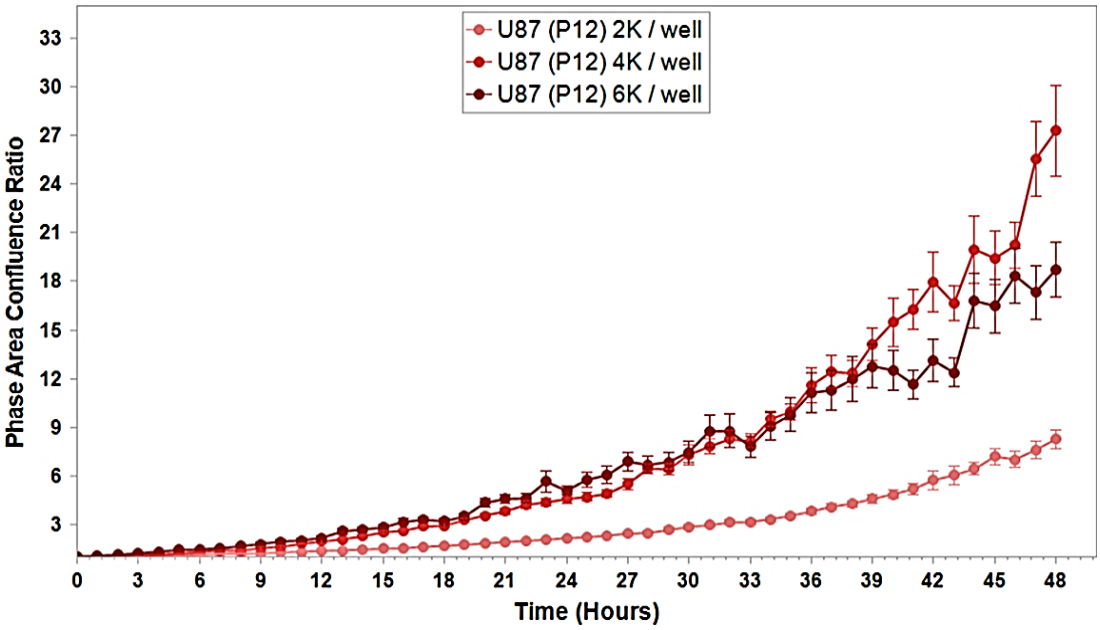

Figure 19. Proliferation of different cell densities per well were monitored on 3 technical triplicates from untreated cells passage number (12). The plots show the confluence ratio of U87 MG cells over 48 hours (4000 cell/well is the best density). Error bars represent the standard error of the mean (SEM)

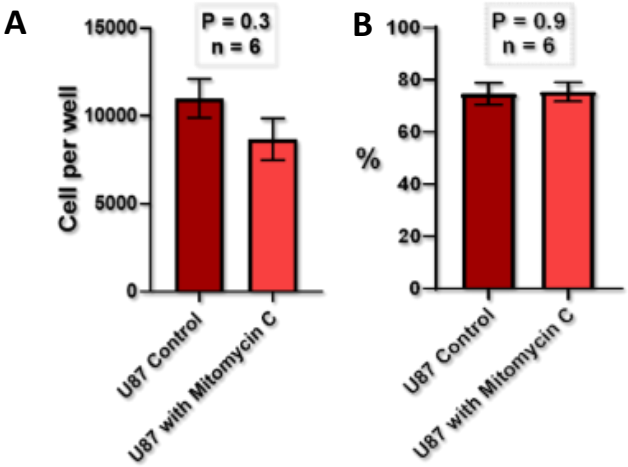

Figure 20. (A) The number of the adherent U87 MG cells after 18 hours has no significant difference in comparable study on 6 technical replicates of cells with and without adding mitomycin C. (B) The percentage of the viable U87 MG cells after 18 hours has no significant difference in comparable study between 6 technical replicates of cells with and without adding mitomycin C. Error bars represent the standard error of the mean (SEM).

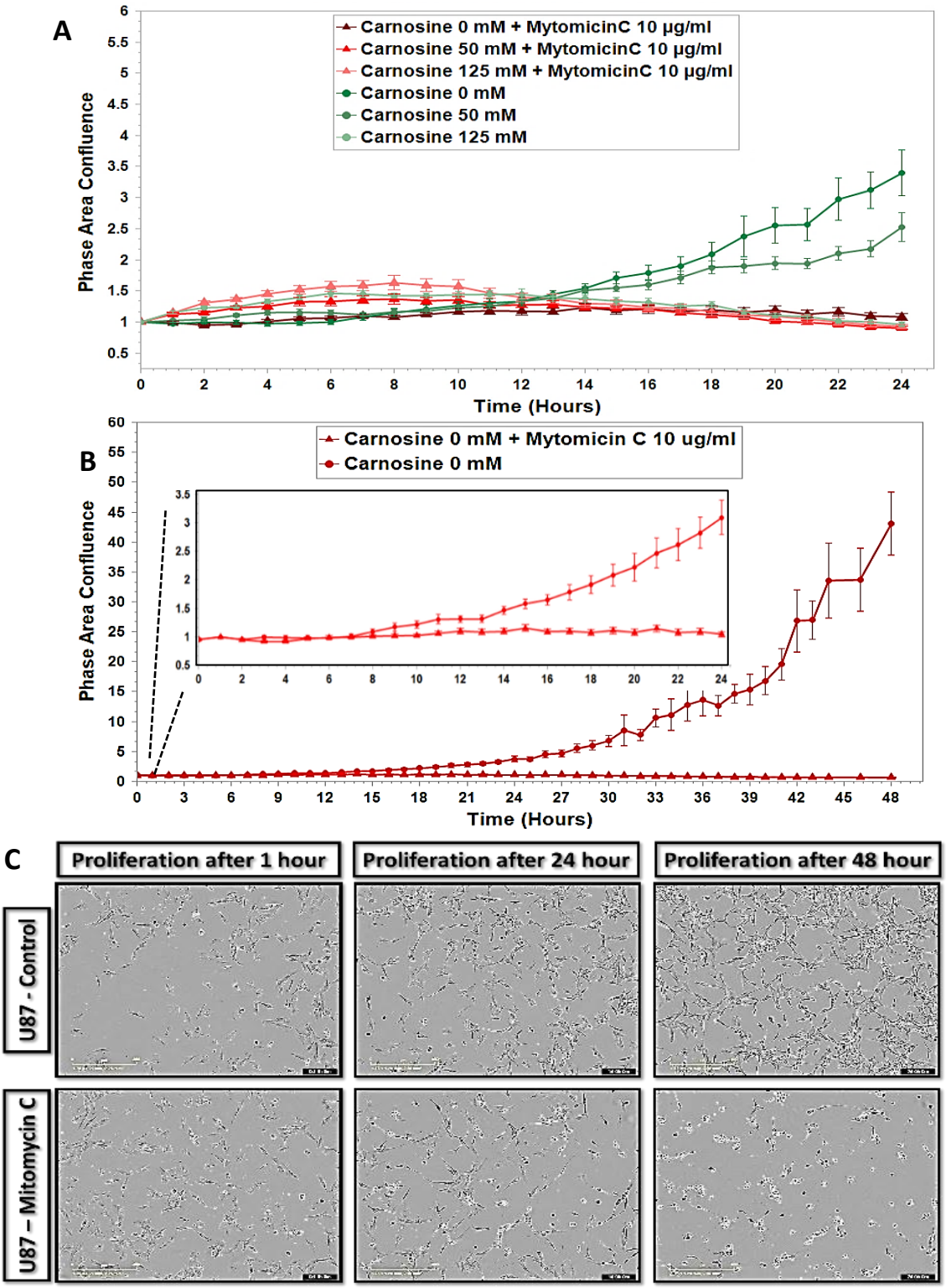

Figure 21. Incucyte® live cell system images analysis for U87 MG cells confluence phase reflect (A) The effect of carnosine on the cells was not affected by using mitomycin C (B) the difference between the normal increase of proliferation for the cells and the effect of adding mitomycin C to stop the proliferation. Phase confluence proves the continuous dividing for control cells. However, the cells with mitomycin C stop splitting and start dying naturally after 24 hours. (C) Images of the cells in control sample and with mitomycin C at (1, 24, 48 hours). Error bars represent the standard error of the mean (SEM). (Scale bars = 400 µm)

1.2.3 Single spheroids development

Three-dimensional models have been shown to have many advantages over monolayer cell systems. Spheroids have attracted attention due to their complex microenvironment and behaviour which mimic many of the natural *in vivo* conditions (Ravi et al., 2015). While single spheroids cannot replace *in vivo* models' scientific investigation, they represent a valuable bridge between monolayer cell studies and the more complicated structure of *in vivo* tumours (Kunz-Schughart, 1999). Spheroid formation has shown potential for high-throughput investigations of anti-cancer treatments (LaBarbera, Reid, and Yoo, 2012). The current standard methods for spheroid generation include the liquid-overlay (Carlsson and Yuhas, 1984), hanging-drop (Timmins, Dietmair, and Nielsen, 2004), and shaking methods (Ivascu and Kubbies, 2006; Shi et al., 2018). The limitations of these methods were found in the amount of spheroid formation and the relative excessive costs. Some available examples for commercial ultra-low attachment 96 or 24 well plates are Corning®, Costar®, Brand® and Kuraray® multiple pore type which all have the same basic principle. Other methods such as magnetic levitation (Haisler et al., 2013), NASA Bioreactor (Hammond and Hammond, 2001), and micro-cages require expensive tools while the uniformity of the generated spheroids remains low (He et al., 2020). Therefore, a method that would combine the reproducibility of forming copious quantities of uniform spheroids while keeping the costs low is required. Herein, the methodology describes a detailed cost-effective protocol for establishing an *in vitro* 3D single spheroid model which can be used to identify potential new therapeutic approaches. The results have shown that the method can be applied to many human and murine cancer cell lines of different origins (prostate cancer, TNBC, and GBM). More specifically it was shown that the formation of spheroids, i.e., when the cells stop reducing in size and started to grow is cell-type dependent and will need to be optimised for each cell line, these can then be utilised for the investigation of targeted drugs, antibodies, and immunoconjugates (Winter et al., 2003). In summary, using a conventional glioblastoma cell line such as U87 MG cells must be studied due to its tumour stem cell-like features (Pontén and Macintyre, 1968; Qiang et al., 2009; Allen et al., 2016). Herein, a method to generate single spheroid was established and used to assess the effect of carnosine, successfully. The anti-tumour carnosine di-peptide which was added each other days showed the potential sustained-release therapy better than the single dose application on single spheroids of glioblastoma cell line (Winter et al., 2003; Tredan et al., 2007; Shi et al., 2018; Habra et al., 2021).

1.2.3.1 Concise method to generate reproducible single spheroids

The experimental protocol in chapter 5 was applied to evaluate the homogeneity of growing single-well spheroids, and the size distribution was quantified by the Incucyte® spheroids software (Habra et al., 2021). The cells were seeded in 3 wells (Triplicate 1-3) of a 96-well plate, and an additional well was used as control (i.e., no washing referred to as triplicate 4) these were left to grow for seven days to form spheroids while being monitored hourly. The mean confluence of the phase area for individual

spheroids was calculated using the Incucyte® spheroid software. This setting was then repeated 2 more times keeping the same position for all triplicates.

The results demonstrated that following the protocol single spheroid could be obtained with consistent reproducibility for triplicates 1, 2, and 3, while triplicate 4 failed to convert the cells into spheroids. Instead, aggregates were formed highlighting the importance of the washing step. The cells in triplicates 1 to 3 gathered over the first day as detected by a reduction in the number of largest brightfield area (Figure 22). Thereafter, unlike the aggregates seen in triplicate 4, the spheroids displayed a regular morphology with a uniform spherical geometry and a narrow size deviation. Seeding U87 MG 400 cells per well on day 0 was sufficient to convert them into homogeneous spheroids that ranged in diameter from 216 ± 9 µm after 1 day to 475 ± 8 µm after 5 days and then 847 ± 11 µm after 7 days. The homogeneity of the spheroids was reflected by the small standard deviation ranging from the mean.

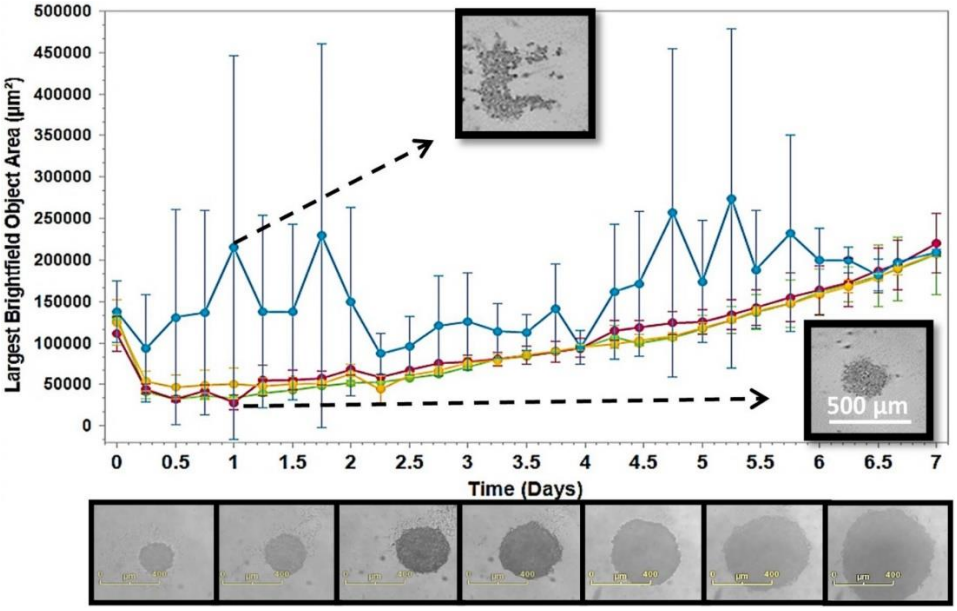

Figure 22. Incucyte® live cell system (×4) live spheroids images analysis shows the proliferation curves of the confluence ratio of the U87 single spheroid upon using the protocol steps. The blue graph of the control showed the inability of the cells to convert the aggregates of cells into a spheroid without using the washing solution. Whereas consistent single spheroid formation reproducibility was achieved for the three different wells when the protocol was followed. The experiment was repeated on triplicate and the images show the difference between the shape of the aggregates and the successful shape of the spheroid, (scale bar = 500 µm). The series of images below the graph show the growth of the spheroids from days 1 to 7, (scale bar = 400 µm).

In addition to washing the wells with anti-adherence solution, another critical factor to consider was the type of plate. The use of a 96-well round bottom plate with a hydrophobic surface designed for suspension cells (Green code: 83.3925.500, Sarstedt, Nümbrecht, Germany) proved to be a key step, which promoted the formation of homogenous spheroids. Single spheroids could not be generated using a 96-well round bottom with a standard growth surface for adherent cells (Red code: 83.3925, Sarstedt,

Nümbrecht, Germany) despite washing the surface of the wells with the anti-adherence solution. The cells adhered to the bottom of the wells forming an incomplete circle after centrifugation (Figure 23, a). By centrifugation, the cells are pelleted at the bottom of each well. This ensures equal number of cells for the initiation of the formation of a single spheroid (Ivascu and Kubbies, 2006). The most critical steps in the protocol were the use of both green code plate and anti-adherence washing solution which consists of an amphipathic component to prevent cell adhesion as explained in the experimental chapter (Schlenoff, 2014). This method showed cells forming spheroids in every seeded well at various locations horizontally and vertically. This monitoring confirmed the consistency and reproducibility of producing spheroids in the 96 wells (Figure 23, b).

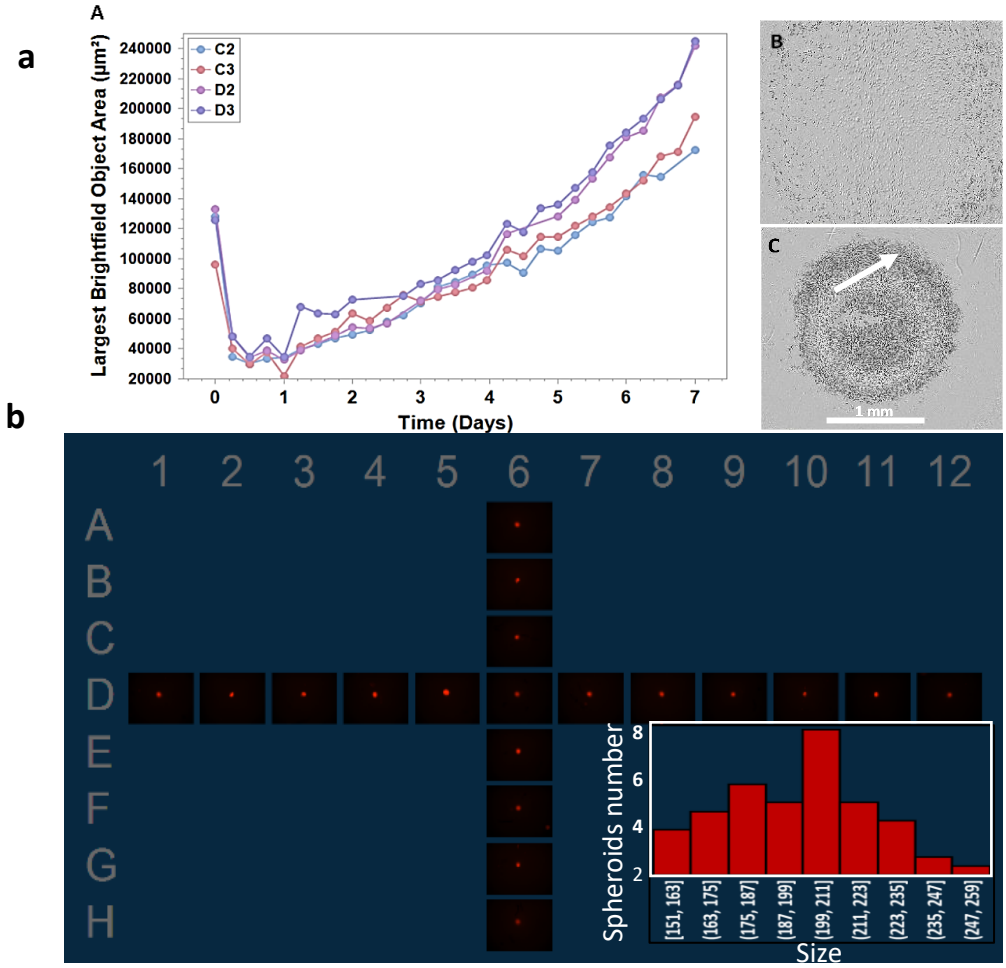

Figure 23. Incucyte® Live-Cell System show (a) A. The proliferation curves of individual U87 single spheroids from individual locations in the 96-well plate (C2, C3, D2, D3). The spheroid area decreased during the first day. Then, each spheroid grew over seven days. B. The instant adherence of the cells when the step of washing was missed. C. Represent the cells in different wells as referred in well A. The cells were gathered after washing with the anti-adherence solution with a 96-well round-bottom standard growth surface for adherent cells (red code). (b) The U87 cells in the 96-well plate image turned into spheroids in various horizontal and vertical in the center of each seeded well after one day, with a size distribution of 216 ± 9 nm for individual spheroids. The figure shows that spheroids were not randomly growing in different locations which reflects the reproducibility in all wells.

The spheroids obtained were further characterised using the Incucyte® live cell imaging system. The 3D structure of the spheroids was shown to be achieved uniformly in all seeded wells. The spheroids grew consistently for up to 10 days.

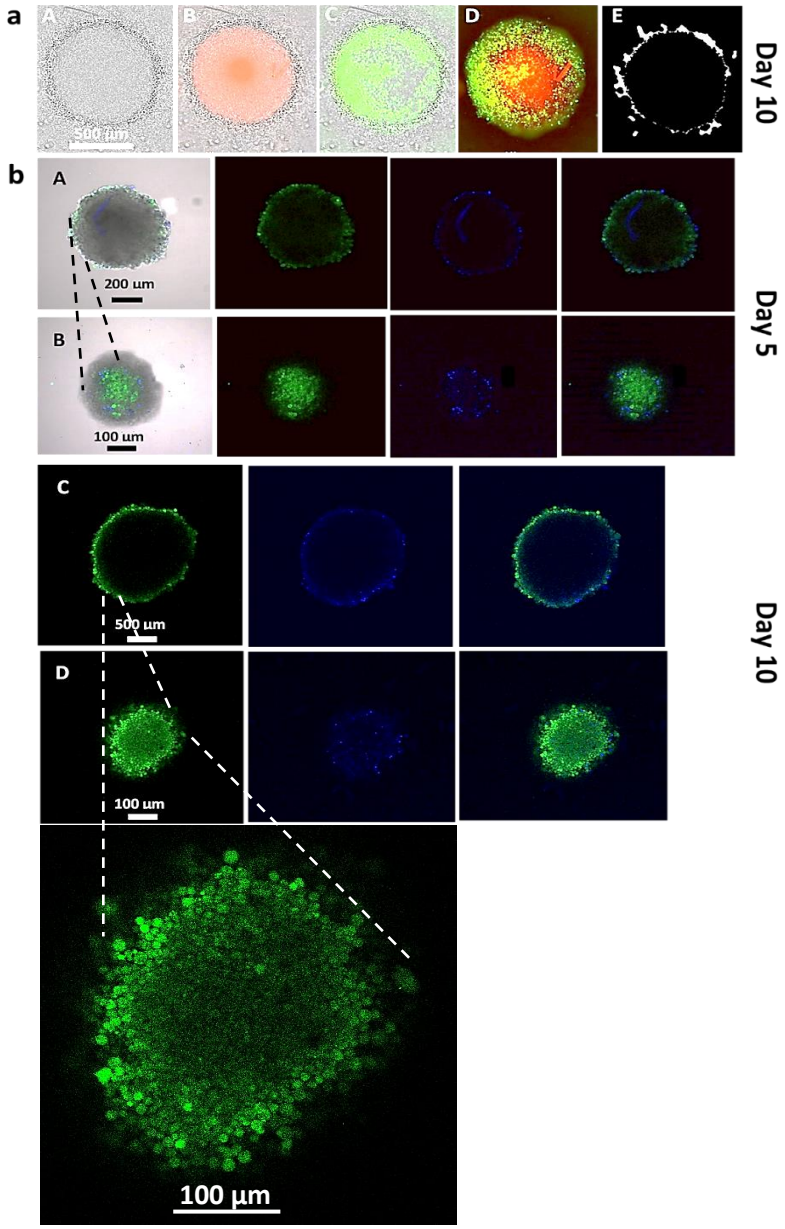

Figure 24. Fluorescence cell Imaging (a) Incucyte® live-cell system (4×). Live spheroid images after 10 days. A. The confluence of the live U87 MG cells around the spheroid is shown by the phase image to be distributed uniformly. B. The localisation of the dead cells in the center of the spheroid is shown by the Cytotox red stain. C. The 3D localization of the live cells around the spheroid is shown by the phase with a green channel filter image. D. The 3D shape of the dead/live cells in the same spheroid is shown by the overlap of the red and green channels. E. The mask of the invasion area. (b) The live green cells stained by CFSE, and the blue nucleus stained by DAPI are both shown located on the rim of the spheroid in the confocal images. A & C. The dark shade of the dead cells is shown by the 5- and 10-day spheroid images across the center. B & D. The 5- and 10-day spheroid images of the proliferating cells across the rim area.

The observed morphology confirmed the overall transformation from forming aggregates to generating tight single spheroids where the dead cells (stained in red) localised in the centre and the live cells proliferated at the rim of the spheroid. The Incucyte® images with a green channel filter showed the live cells stained with carboxyfluorescein succinimidyl ester fluorescent dye (CFSE) surrounding the Cytotox red colour which was taken up by dead cells at the core of the spheroid (Figure 24, a/ A-D). This has the advantage of assessing the mobility of the tumour cells and it enables the monitoring of the invasion of the U87 MG cells from the surface of the spheroid. The invasion area was estimated after applying an invasion mask and subtracting the area of the dead cells from the whole spheroid (Figure 24, a/ E). The confocal microscopic images for the spheroid morphology showed a significant increase in growth from day 5 which was confirmed by the viability of the cells at the rim of the spheroid (CFSE green live cells and DAPI blue nucleus) (Figure 24/ A-B), and 10- days spheroid images across the centre showed the dark shade where the dead cells are located (Figure 24/ C-D).

1.2.3.2 Cell tightness and interaction analysis of U87 MG spheroids

To investigate the tightness of the cell packaging in the single spheroid, histological sections were examined for spheroids which were grown for 7 days in culture. H&E stain was applied to these spheroids after fixation and embedding. The hematoxylin stains cell nuclei a purplish-blue colour, while eosin stains the extracellular matrix and cytoplasm pink. Figure 25 shows the H&E stain from the centre and the rim cross-section of a spheroid. This visual analysis for the section showed that the cell density was high in the core region, whereas the daughter cells gathered around the rim to tighten and increase the spheroid size.

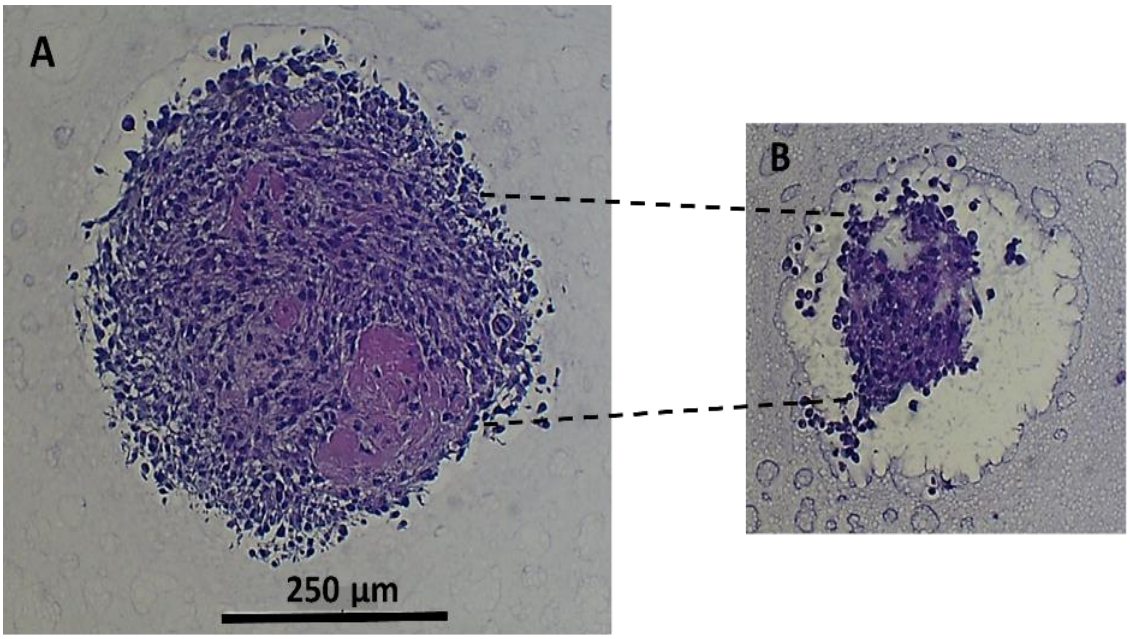

Figure 25. Cell tightness and interaction analysis of U87 MG spheroids H&E stain of spheroid cross-sections from (A) the core area, and (B) top rim area of 7 days spheroid generated from 400 cells. Scale bar is 250 µm for both images.

An easy method for mass production of homogeneous and uniform 3D cultures would lead to a highly efficient process that minimises both setup time and wasted 3D cultures (Leu et al., 2020). Utilising the Incucyte® system and confocal imaging for 3D image analysis enabled the characterisation of the 3D cellular matrix of different spheroids. The spheroids were characterised by studying the 3D structures, cell viability, and necrosis.

1.3 Results and discussion

1.3.1 Applying the carnosine treatment on U87 MG and the mechanisms of effect

1.3.1.1 Proliferation and cytotoxicity (IC50/ EC50)

The inhibition in U87 MG cell proliferation was observed upon increasing the added carnosine concentration from 0 to 125 mM after 18 hours to these seeded cell cultures. The cells were imaged hourly during the 48 hours exposure in complete Opti-MEM culture media. The growth of U87 MG cells was relatively inhibited after 8 hours and completely affected after 48 hours when the applied carnosine reached *ca.* 125 mM (Figure 26, A). To confirm that the change of the behaviour was not due to cell death by other conditions in these wells, U87 MG cells were first seeded, and their proliferation was monitored for 24 hours, before carnosine was added. Figure 26B clearly shows the suppression of U87 MG growth within 8 hours after the addition of carnosine, which led to a complete growth inhibition and cell death after 2 days. The IC50 was determined after the MTT assay was performed as a colorimetric assay for assessing cell metabolic activity. Results were analysed by GraphPad Prism software (San Diego, CA, USA). A range of (23.6 to 34.7 mM) carnosine with a confidence level of 95% and a regression value of $R^2 = 0.8195$ was found (Figure 26, C). The effect of carnosine on U87 MG proliferation was clearly observed using phase contrast images of the cells with and without carnosine over 2 days (Figure 26, D).

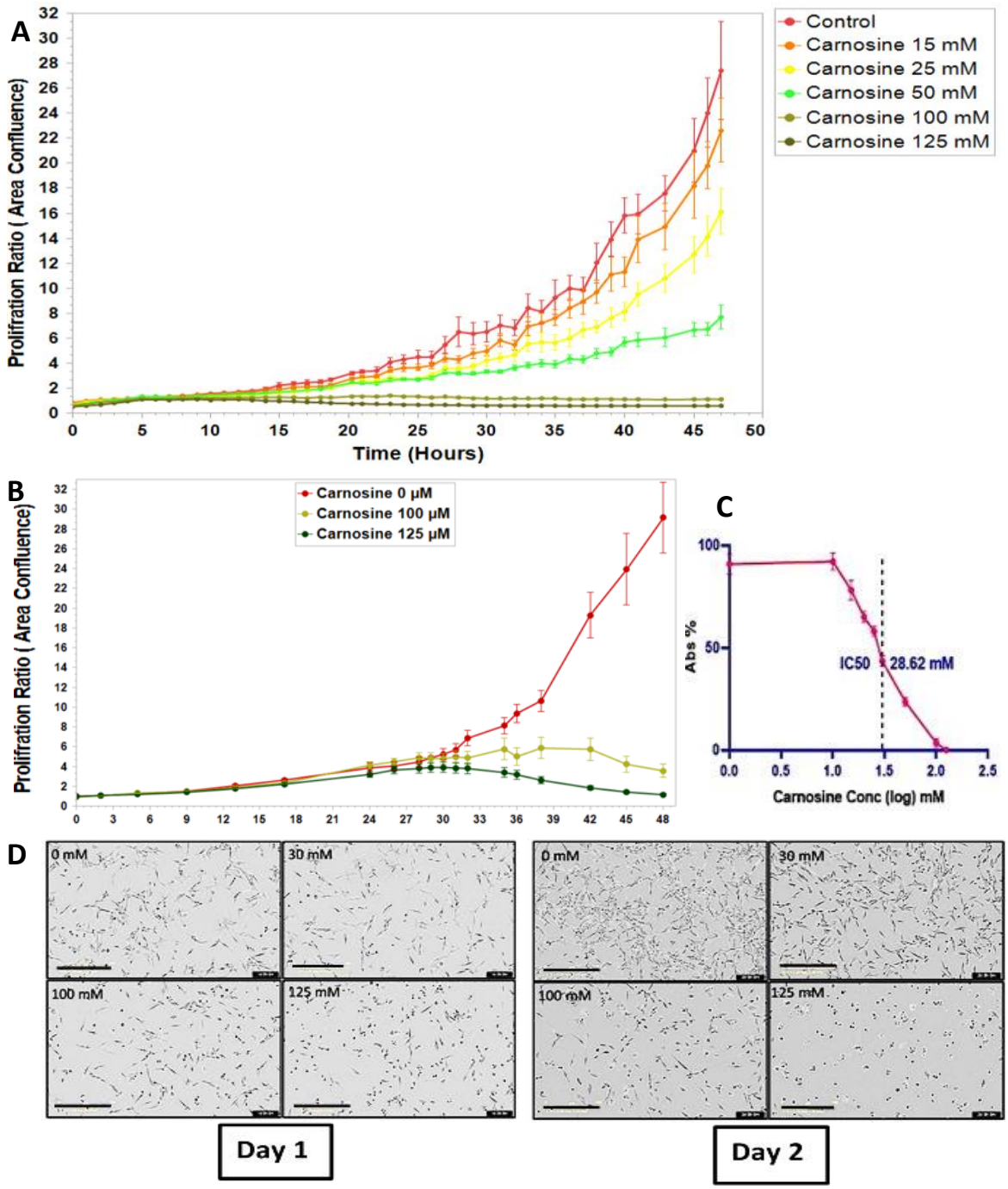

Figure 26. Incucyte® live cell system (×10) Live cell images analysis shows (A) proliferation curves of the confluence ratio of U87 MG cells upon carnosine exposure over 48 hours. Cells were treated with different concentrations between 0 and 125 mM. (B) To prove the same effect of carnosine on cell proliferation, a supportive study was applied with delayed carnosine addition until 24 hours for 0, 100 and 125 mM. In both cases (A, B), the treatment effect started after 8 hours. An MTT cell viability assay was conducted on the U87 MG cell line with different carnosine concentrations. (C) The UV absorbance at different concentrations refers to (IC50 = 28.62 mM) and (IC90 = 79.43 mM). Error bars represent SEM. The test was applied on the same six samples at the end point of the proliferation study. (D) The images of the critical carnosine concentrations are shown. Each image was displayed as the phase of U87 MG cells upon carnosine exposure over 1 and 2 days. Error bars represent the standard error of the mean (SEM). (Scale bars are 400µm)

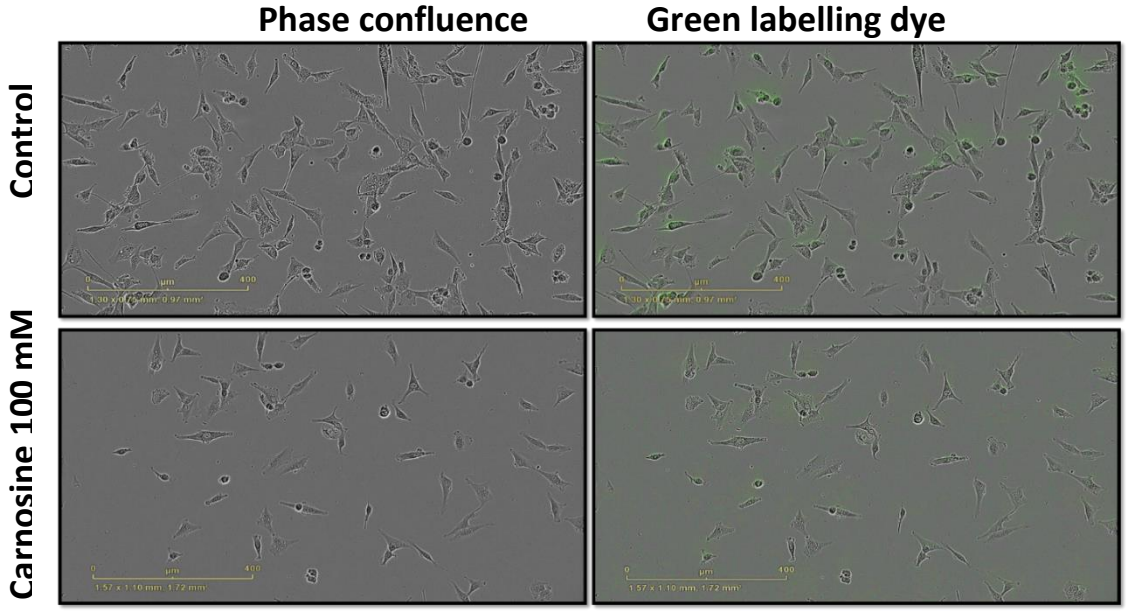

Figure 27. Incucyte® live cell system (×10) images show proliferation of U87 MG cells upon carnosine exposure after 24 hours. Cells were compared with and without treatment of 100 mM carnosine concentration in the presence of CytoLight Rapid Dye for live-cell green labelling dye (200 nM) which crosses live cells membrane and emit green fluorescence. Each photo was displayed as phase and green channel without mask. A decrease in cells population appeared after 24 hours. However, the cells with no morphology change are the daughters who stay alive. (Scale bars are 400 µm)

To study the dead and live cells performance due to the carnosine treatment, the live cells were monitored by using the Incucyte® after applying the CytoLight Rapid green dye (Figure 27), while Incucyte® Cytotox red reagent was used for real-time quantification of cell death. The number of live cells was shown to decrease while the number of dying cells increased in a dose-dependent manner. The analysis of the phase images enabled the real-time evaluation of cell membrane integrity and cell death in response to carnosine exposure after 24 and 48 hours (Figure 28).

The half maximal effective concentration curve was defined (EC50 = 28.2 mM). The red fluorescent areas with blue masks were quantified for different carnosine treatments using IncuCyte® standard analysis software. This was integrated with the previous proliferation test at (IC50 = 34 mM) (Figure 29). The plots representing live and dead cells initially showed no effect, followed by a cytostatic phase starting from 30 mM carnosine. However, the cell cytotoxicity could be seen to start immediately after the integration point. The mechanism of cell death is the effect of carnosine on the functionality of mitochondria, which lose the metabolic capability to develop the purple colour in the MTT assay and allow the red dye to penetrate.

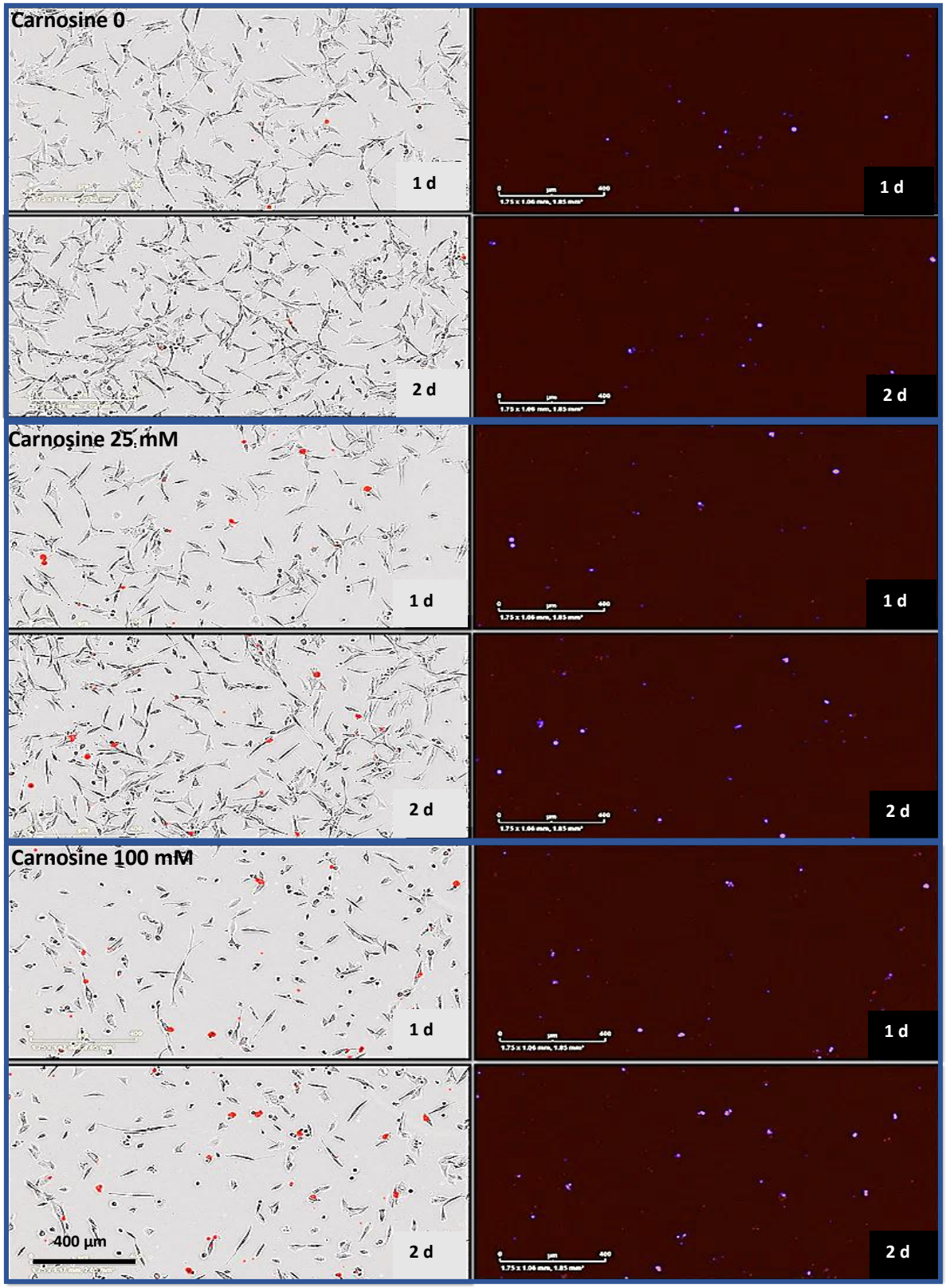

Figure 28. Incucyte® live cell system (×10) images show cytotoxicity on U87 MG cells upon carnosine exposure after 24 and 48 hours. Cells were treated with different carnosine concentrations in the presence of Cytotox Red dye (250 nM), which enters dead cells after losing the membrane and binds to the DNA to emit red fluorescence. Each photo was displayed as a phase and as a red channel with a blue mask. (Scale bars are 400µm)

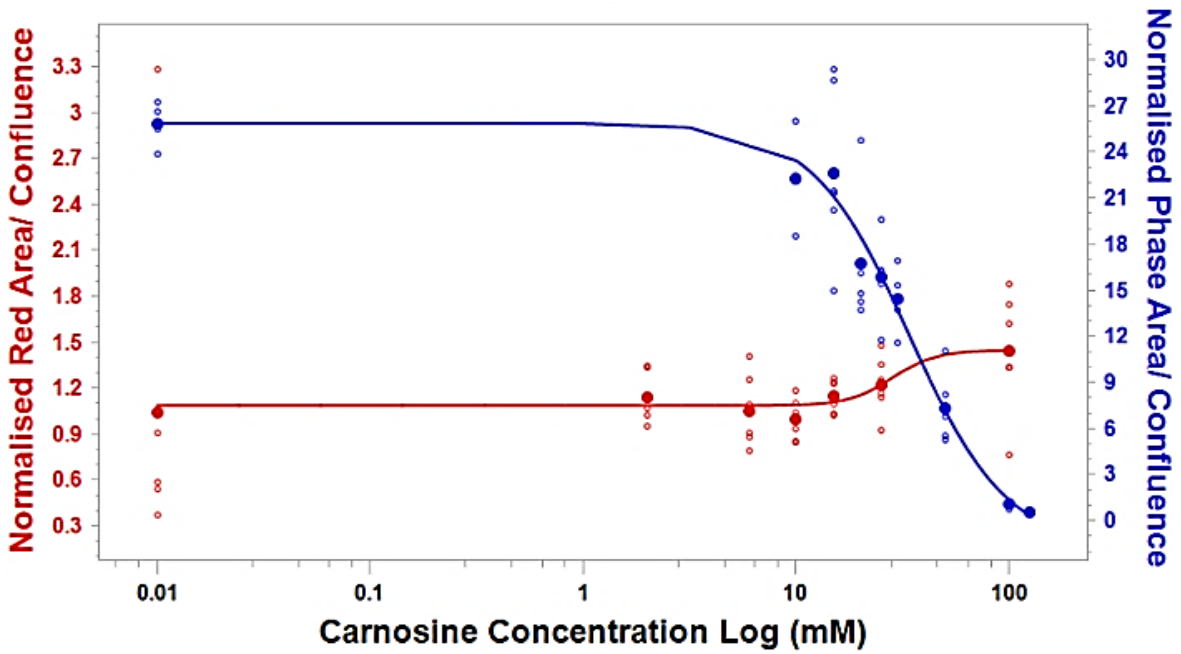

Figure 29. Incucyte® live cell system (×10) live cell images analysis shows IC50/EC50 curves of the inhibition of cells' proliferation and the efficiency of carnosine in killing the tumour cells. Upon carnosine exposure at different concentrations (0, 50, 100, 125 mM) over 48 hours, IC50 is indicated by the confluence phase ratio, while EC50 is the ratio of the Cytotox Red dye that enters dead cells. The carnosine effect has three phases: No effect plateau, Cytostatic around EC50, and Cytotoxic.

1.3.1.2 Cell migration and invasion

In vitro migration was studied by creating a wound in a U87 MG cell monolayer, then capturing the images at regular intervals during the closure of the wound due to the migration of the cells. By comparing the images of the same cells in media alone, it was possible to quantify the migration rate of the cells, which reflected the effect of the treatment on cell mobility (Liang, Park, and Guan, 2007). Also, the invasion assay was studied by embedding a monolayer of U87 MG tumour cells inside a biomatrix to monitor the speed at which the cells invade through the matrix to the neighbour cells (Figure 30) (Brekhman and Neufeld, 2009). The quantification of phase images assessed cell morphology at every time point. After proliferation was suppressed by mitomycin C, migration was reduced after 24 hours but not abolished by carnosine ($p < 0.2$ from 100 mM, 6 experimental replicates). Such as proliferation, the migration of the cells decreased following the addition of carnosine. In a time-dependent manner, both effects were seen to increase after 24 hours, with a potential effective decrease in the concentration of intracellular ATP as detected by (Renner et al., 2008) starting from adding a moderate concentrated of carnosine. Over the second day, the wound density showed a plateau because mitomycin C formed covalent cross-links between complementary strands of DNA, thereby no new cells were available for replication or migration (Figures 31, 32 and 33) (Ueda and Komano, 1984; Tomasz, 1995).

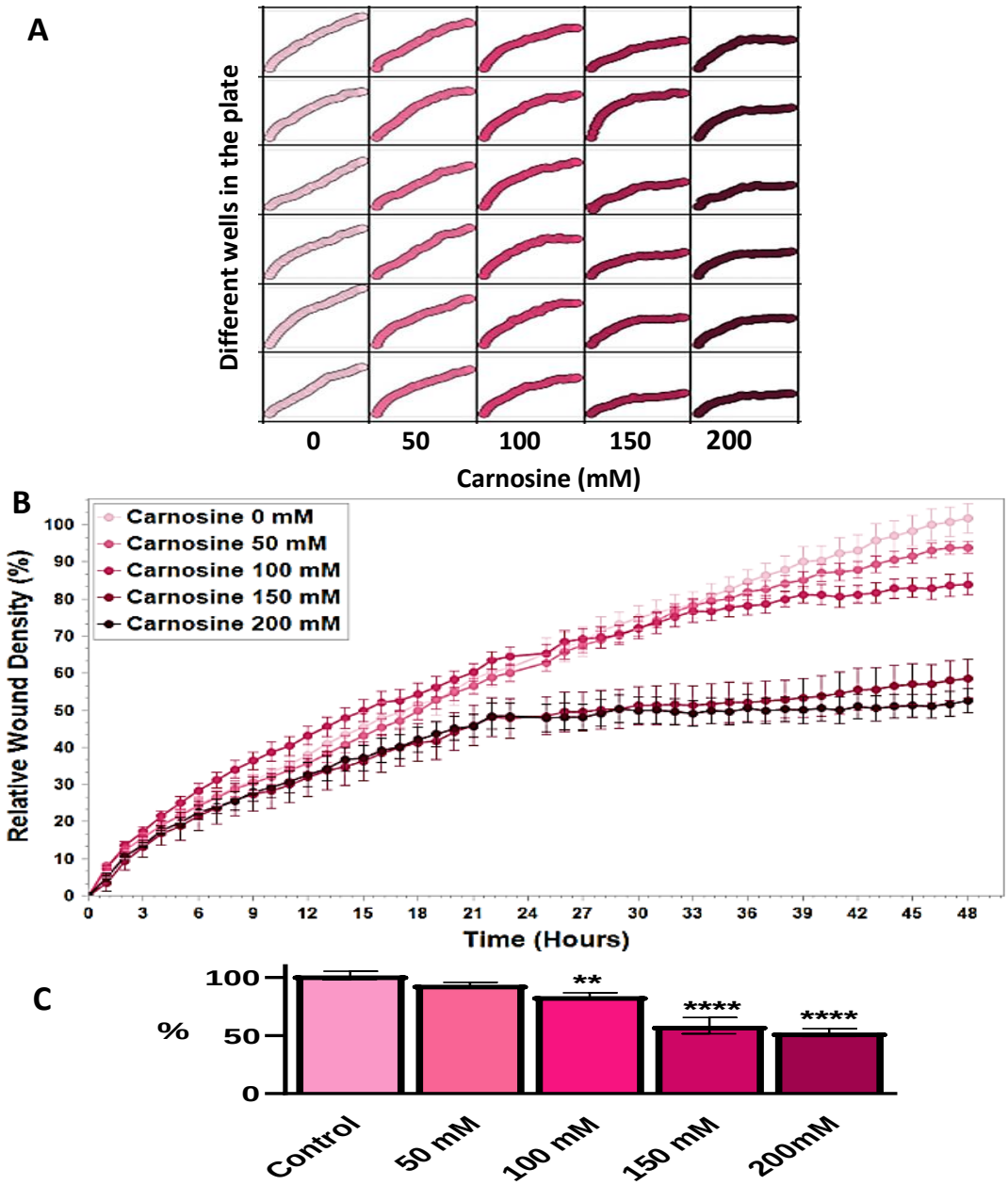

Figure 30. (A) The matrix of relative wound density for 6 samples of each concentration (0, 50, 100, 150 µM respectively) over 2 days. (B) The effect of different carnosine concentrations added on U87 MG cells after 18 hours of adherence when the scratch was applied. The scratch wound starts healing by proliferation and migration. Cells were imaged in 96 well plate while growing in media with different carnosine treatments using Incucyte® live cell imaging system to take two snaps per well each hour over 2 days. The phase confluence was analysed by the standard Incucyte® software, and the relative wound density was analysed by the integrated Incucyte® wound scratch software and plotted against elapsed time in hours. 0 hour indicates the cell density half hour after placing the plate in the Incucyte®. All cells' variations in growth arised after approximately 8 hours. The supportive movies of cell migration are available in the supplementary movies. (C) The statistical analysis of the normalised wound density shows that the significant effect starts between 50 and 100 mM of carnosine on cell density 10^3 per well. The statistical analysis shows a significant effect caused by carnosine (50 mM) at a cell density of 10^3 per well. The statistical significance level and indicated with (*) for $p < 0.05$, and (****) for $p < 0.0001$.

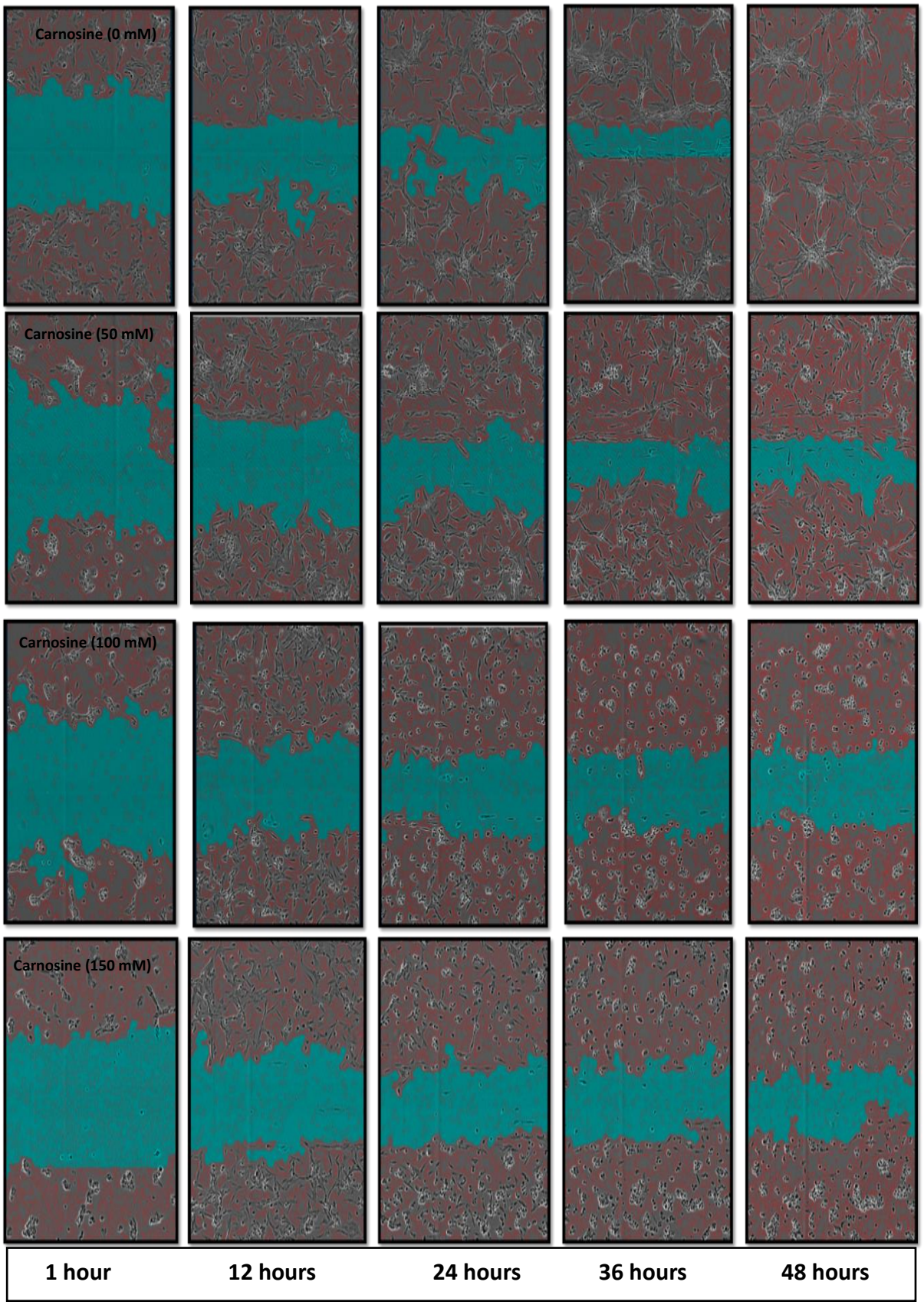

Figure 31. Phase images with mask shows the effect of different carnosine concentrations on U87 MG cells wound healing by proliferation and migration. Cells were imaged in 96 well plate while growing in media with different carnosine treatments using Incucyte® live cell imaging system each 12 hours for 2 days.

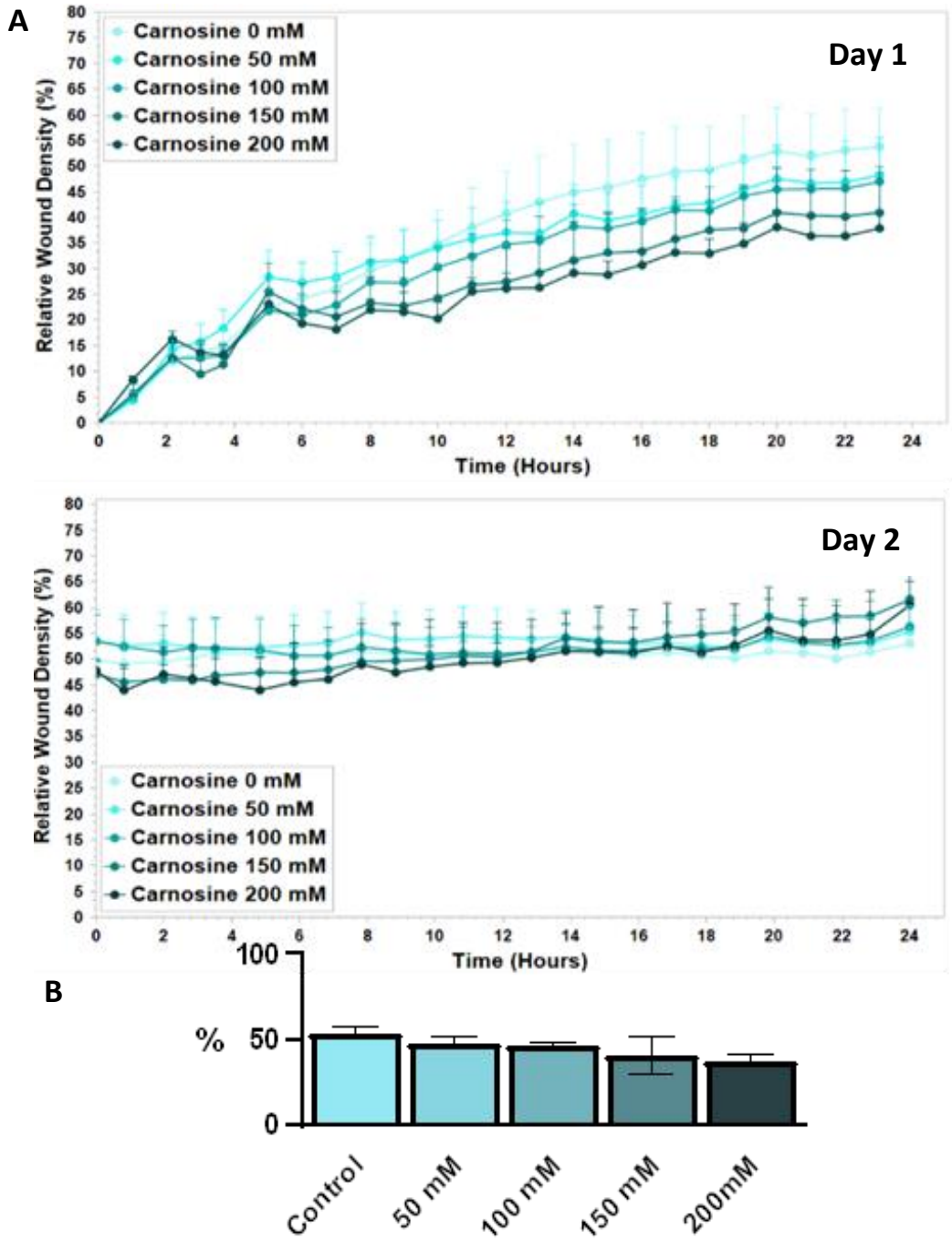

Figure 32. Effect of carnosine concentration on U87 MG cells' wound healing by migration after ceasing their proliferation with mitomycin C. The software able to quantify the space that was generated by the wound. Cells were imaged in a 96 well plate while growing in media with different carnosine treatments using the Incucyte® live cell imaging system to take two snaps per well each hour, (A) during the first day, when the relative wound density was analysed by the integrated Incucyte® wound scratch software and plotted against the elapsed time in hours. After 18 hours of adherence, the scratch was applied, then mitomycin C (10 µg/ mL). was added after an hour. The carnosine treatment was applied at different concentrations and the plate was placed inside the Incucyte® device to start the 0-hour image after about half an hour. All variations in cell growth were initiated after about 4 hours. (B) The statistical analysis of the normalised wound density shows a slight increase in cell mobility caused by carnosine at a cell density of 10^3 per well. Error bars represent the standard error of the mean (SEM).

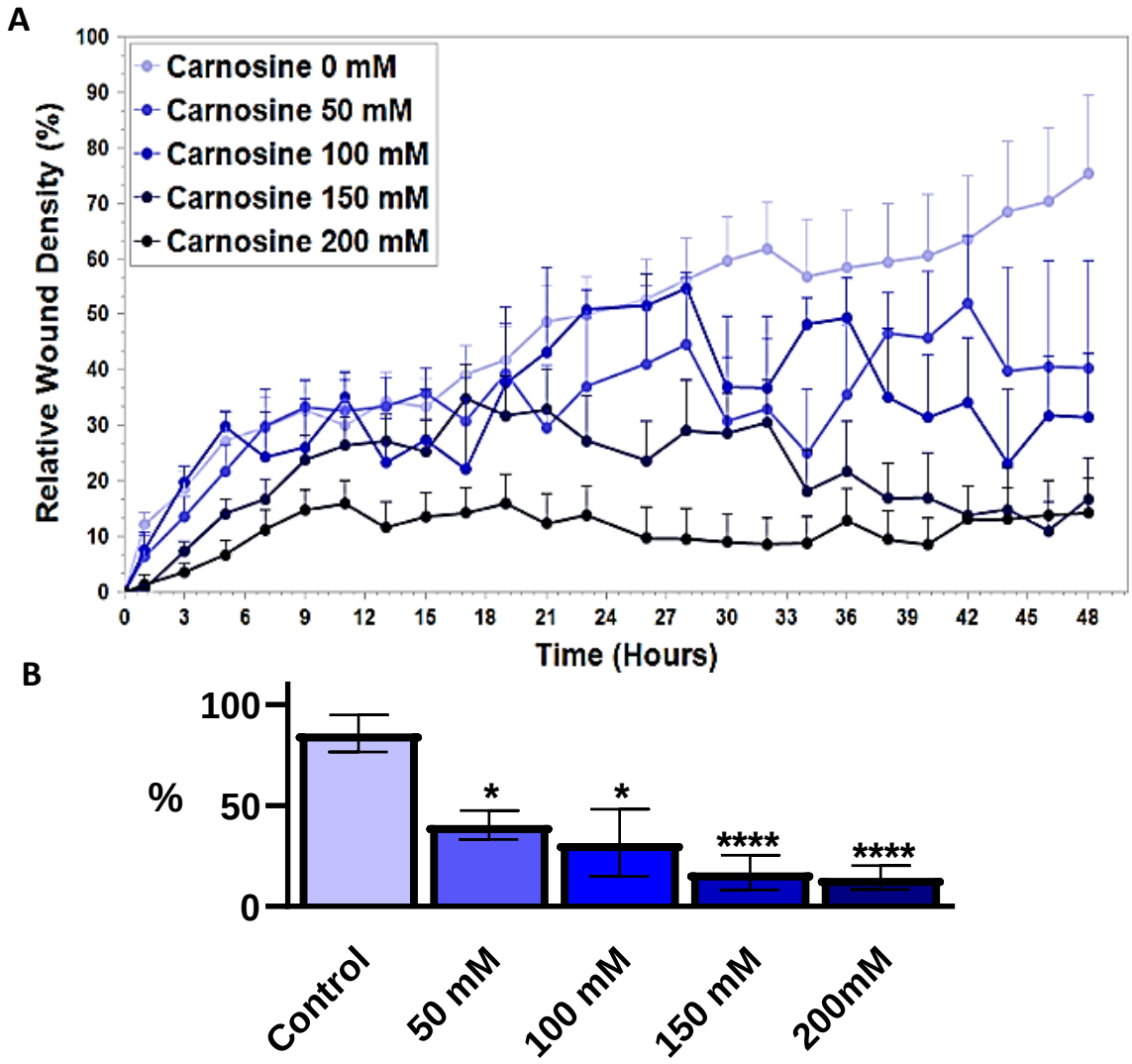

Figure 33. Effect of carnosine concentration on U87 MG cells' wound healing by invasion over 48 hours. (A) The same criteria as migration were applied to quantitatively address the effect of carnosine. (B) The statistical analysis of the normalised wound density shows a significant effect caused by carnosine (50 mM) at a cell density of 10^3 per well. The statistical significance level and indicated with (*) for $p < 0.05$, and (****) for $p < 0.0001$.

Carnosine affects the migration and metastasis by suppressing the cells' mobility regardless of the effect of proliferation (McCarroll et al., 2004). The effects of the cell matrix and interactions in cell invasion mimic the cells during wound healing *in vivo*. Carnosine affects the invasions and metastases significantly when the concentration exceeds 50 mM (Figure 33).

The data of migration and invasion were used as indicators to recalculate the IC50/ EC50 of carnosine. The IC50 was determined by the relative wound density ratio, and the EC50 was determined using the width of the wound. The IC50/ EC50 are *ca.* 100 mM at a density of 10^3cell/well (Figure 43). These values corroborated the results which were found from previous live/dead cell curves (Figure 30).

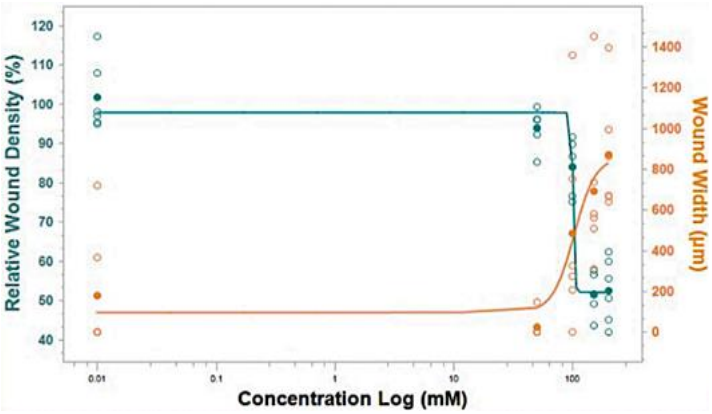

Figure 34. Incucyte® live cell system (×10) live cell images analysis shows IC50/EC50 curves of the inhibition of cells' proliferation and the efficiency of carnosine in killing the tumour cells. Upon carnosine exposure at different concentrations (0, 50, 100, 125 mM) over 48 hours, the IC50 is indicated by the relative wound density, while the EC50 is the wound width. The images and videos of scratch wound healing by cell migration are available in the Supplementary Materials.

1.3.2 Safety studies for applying BPEI-coated IONRs on U87 MG

1.3.2.1 The differentiation of malignant U87 MG cell line

The comparison between the morphology of differentiated and undifferentiated control U87 MG cells is essential to investigate the effect of the application of BPEI-coated IONRs on both healthy and mitotic cells. The cells were grown in a serum-free medium supplemented with dibutyryl cyclic adenosine monophosphate (dbcAMP; 0.3 mM) and B27 Supplement (1% v/v). Following the differentiation, a fluorescent green dye CFSE was added to show the cell proliferation after 48 hours and 7 days (Figures 35 and 36). Also, DAPI was used for the blue nucleic colouring, and red mouse antibody marker glial fibrillary acidic protein (GFAP) dye was applied to stain the differentiated cells (Figure 37) (Gomes, Paulin and Moura Neto, 1999; Chemmarappally et al., 2020). If more investigation is needed, using a cholinergic antibody marker will give a clearer specific colouring for the differentiated cells (Liu et al., 2019).

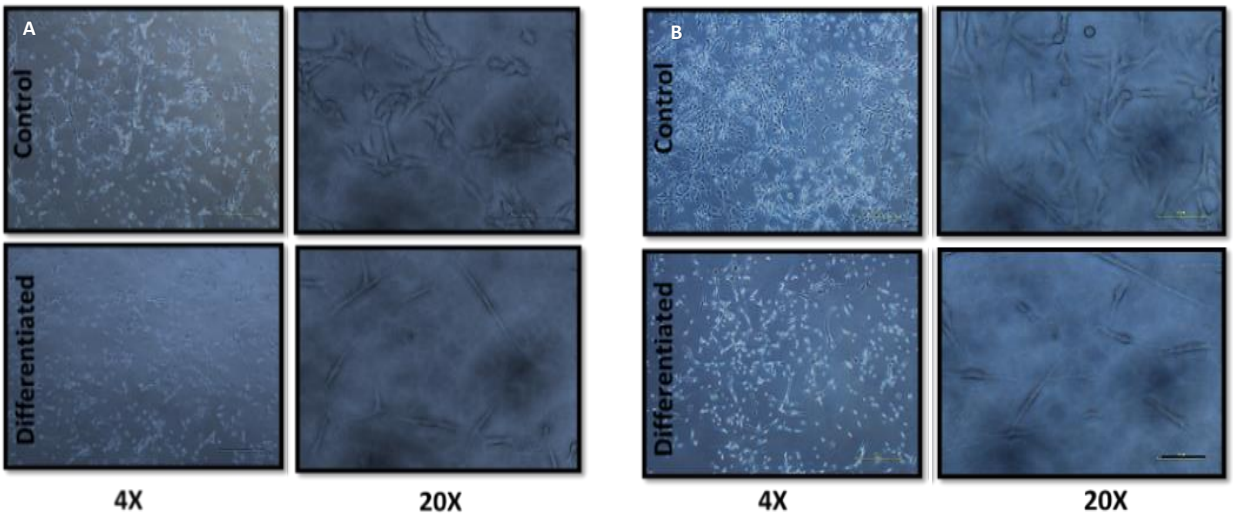

Figure 35. Microscopic images show the difference of the cell morphology after the differentiation treatment. A. after 48 hours and B. after 7 days. The differentiated cells are more elongated than the mitotic cells. The scale bar is 50 µM.

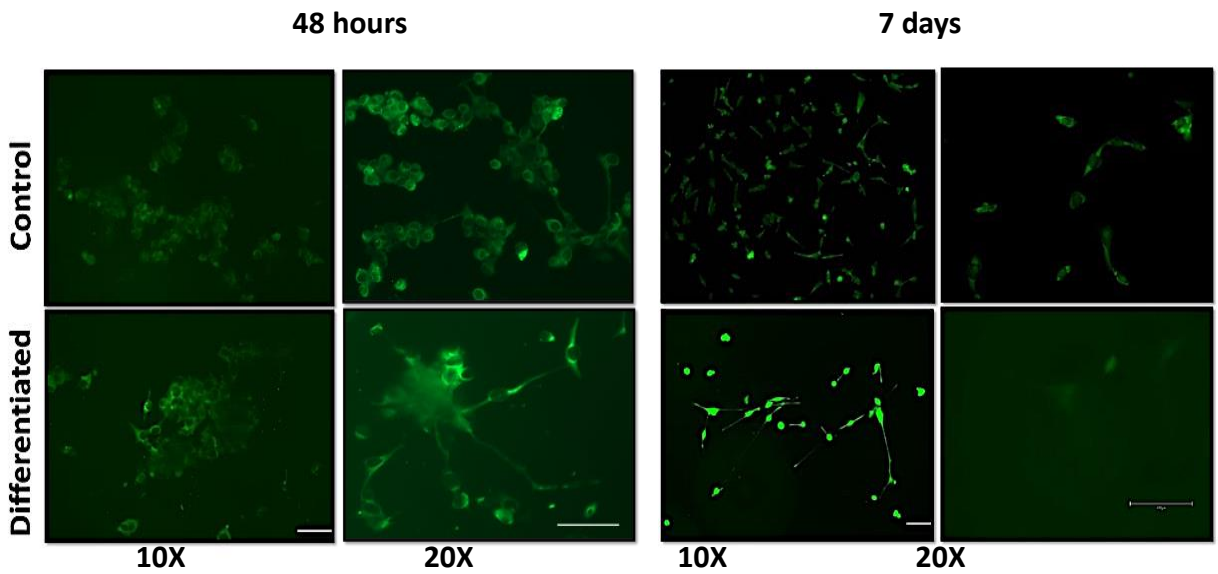

Figure 36. Microscopic images (EVOS) show the live U87 MG tumour cells coloured in fluorescent green after the treatment to differentiate them for 48 hours and a week. (Scale bars are 150 µM)

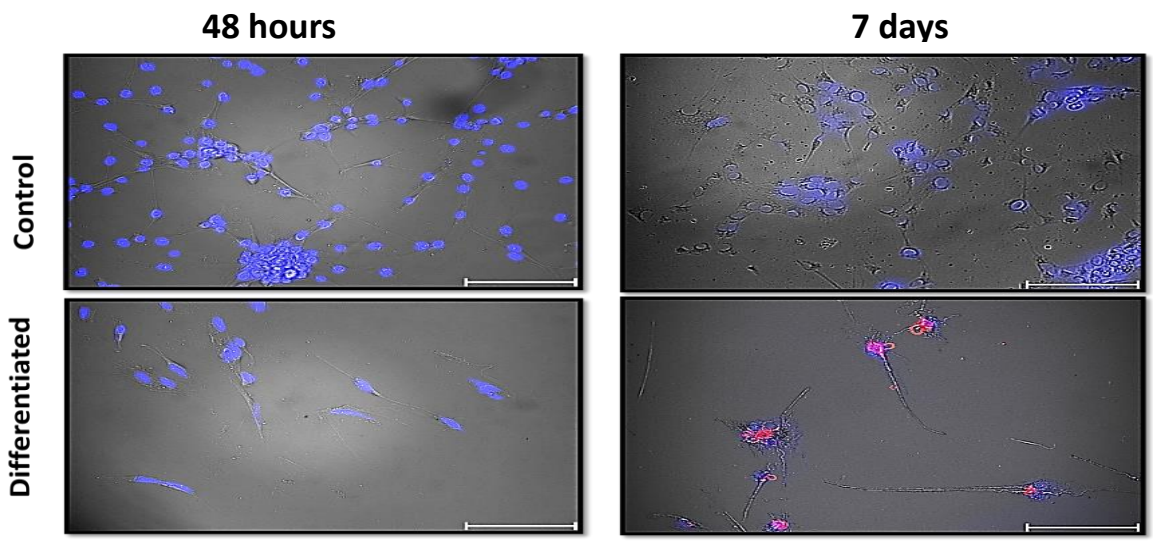

Figure 37. Microscopic images (Leica) with magnification x20 show the U87 MG tumour cells nucleus coloured in blue DAPI after the treatment to differentiate them for 48 hours and a week. The red antibody maker for the differentiated cells appeared in the sample of the 7 days. (Scale bars are 150 µM)

1.3.2.2 The cell cycle of the differentiated and malignant U87 MG cell line

To confirm the successful differentiation, the life cycle of the cells before and after differentiation was compared. After the differentiation of the U87 MG cells, samples with high density were prepared and the flow cytometer cell cycle test was applied on three independent passages (Pozarowski and Darzynkiewicz, 2004). The test was performed 48 hours after adding the differentiation treatment to the malignant U87 MG cell. After staining the cells with propidium iodide (PI), the fluorescence was measured. The estimated percentage for the cells in the G1, S, and G2 phases of the cell cycle. The mitotic cells were faster in moving from G1 to the next phases which makes the intensity of the S and G2 stages significantly higher than the differentiated cells (Figure 38).

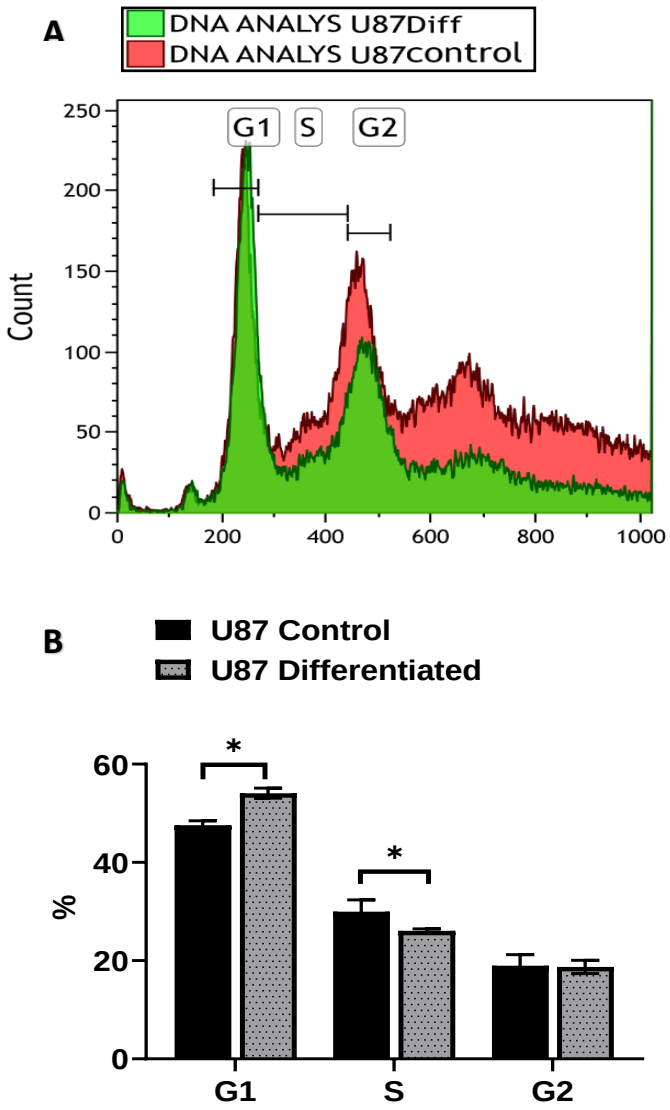

Figure 38. Flow cytometer peaks of life cycle for the mitotic (control) and differentiated U87 MG cell line. The peaks showed the difference between both types in all stages G1, S, and G2. Significant differences were evidenced in G1 and S stages. The test was performed on biological triplicate and Error bars represent the standard error of mean (SEM).

1.3.2.3 The effect of BPEI-coated IONRs on mitotic vs. differentiated U87 MG cells

1.3.2.3.1 BPEI-coated IONRs accumulation (ICP), cell cytotoxicity assays of lactate dehydrogenase (LDH) and MTT

U87 MG cells were grown in a serum-free medium supplemented with dibutyryl cyclic adenosine monophosphate (dbcAMP; 0.3 mM) and B27 Supplement (1% v/v). After the successful optimisation of the U87 MG differentiation, comparison studies for the cytotoxicity/ proliferation between the mitotic and differentiated cells were essential by applying the ICP-MS analysis, LDH test, and MTT assay in the same conditions (Au et al., 2007; Valdiglesias et al., 2016). The ICP test showed similar leftovers from the applied IONRs on the cells with and without differentiation after the same time

exposure and conditions. No significant difference was detected between both types of cells (Figure 39). The LDH test and the MTT assay on 3 passages showed a similar effect for each concentration of IONRs (5, 7.5, and 10 µg/mL) (Figures 40 and 41). The effect of BPEI-coated IONRs is nonselective, and the IONRs showed less effect on the metabolism of the differentiated U87 MG cells (Chemmarappally et al., 2020). However, it was not a significant difference because the astrocytes harbour protective mechanisms including neurotrophic factors and anti-oxidative stress molecules (Pla, Pascual, and Guerri, 2016; Hass and Barnstable, 2016).

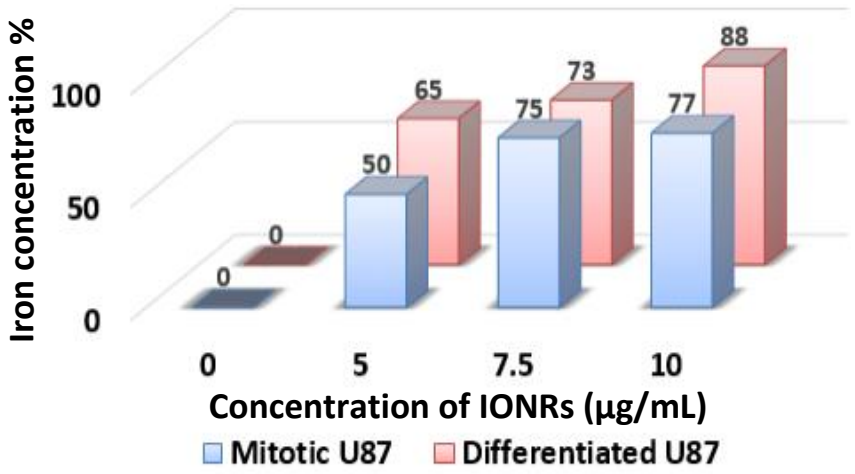

Figure 39. (A) ICP-MS test was applied after finishing the MTT test (48 hours). Measuring the iron concentration showed similar percentage of BPEI coated IONRs left in the wells of both mitotic and differentiated U87 MG.

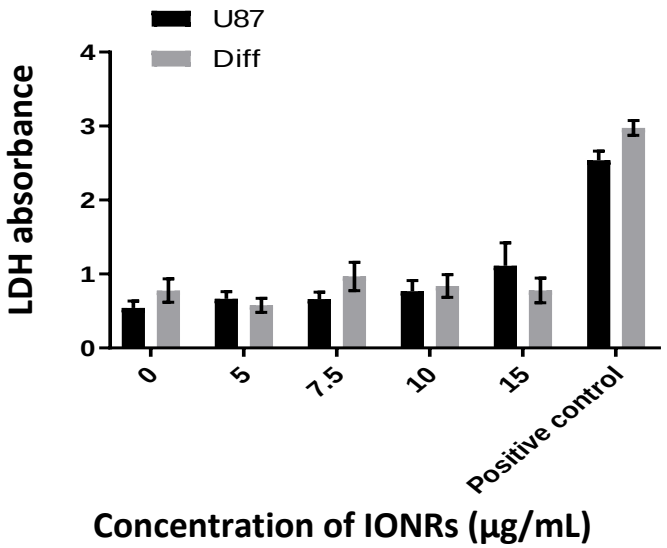

Figure 40. LDH test on U87 MG cell line with various concentrations of BPEI coated IONRs after 48 hours. No significant difference was observed after applying IONRs (5, 7.5 and 10 µg/mL) in individual triplicate. Error bars represent the standard error of mean (SEM).

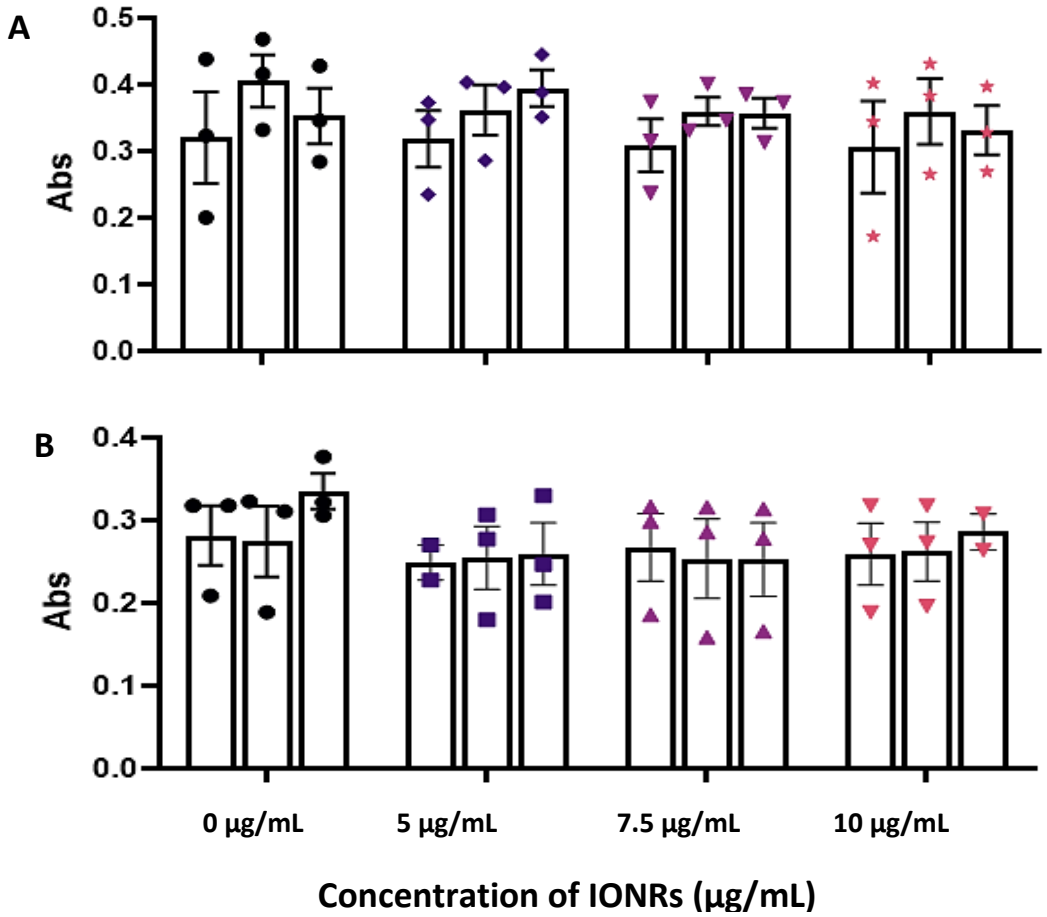

Figure 41. MTT cell viability assay on U87 MG cell line (A. mitotic vs. B. differentiated) with various concentrations of BPEI coated IONRs after 48 hours. No significant difference was observed in individual triplicate. Error bars represent the standard error of mean (SEM).

1.3.2.4 Safety margin of BPEI-coated IONRs in malignant U87 MG cells (MTT)

The quantitative MTT assay data shows that the viability of cells treated with BPEI-coated IONRs at concentrations of (0 to 10 µg/mL) did not display a significant statistical difference in one passage. However, two other passages showed cytotoxicity caused by IONRs at a concentration of 10 µg/mL. Hence, the surface modifications, which occur via positive charge (+19.14 mV) at pH 7, are safe to be applied on U87 MG cells using BPEI-coated IONRs concentrations of less than 10 µg/mL for an exposure period of 48 hours (Figure 42).

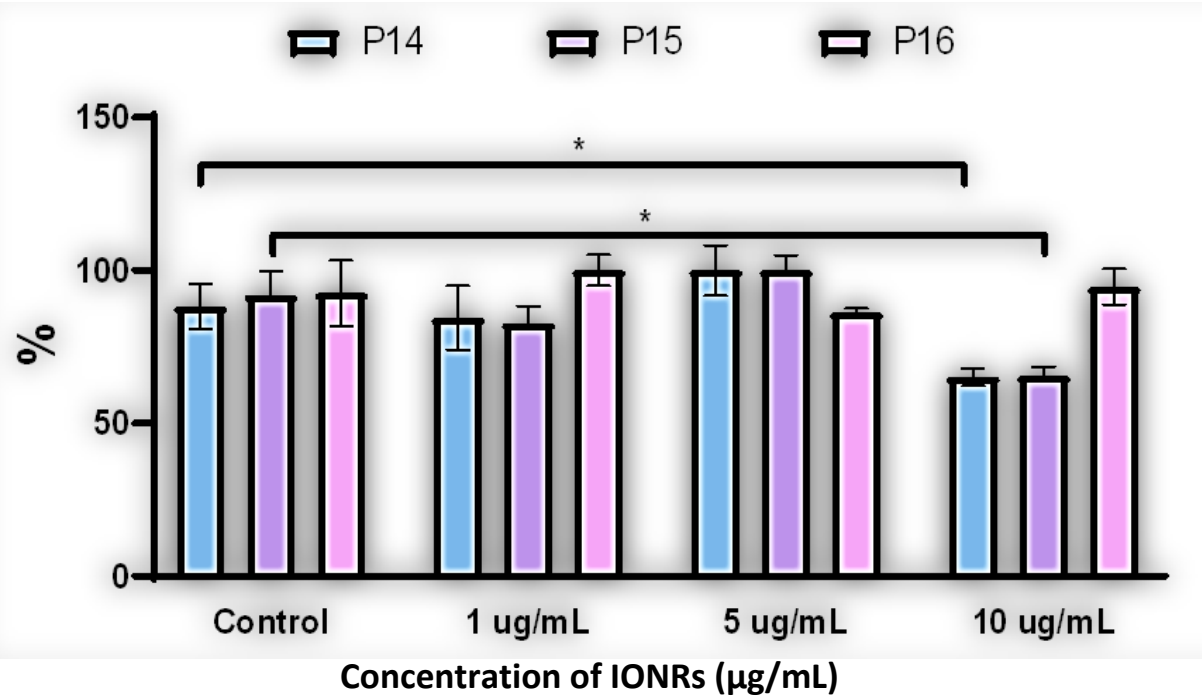

Figure 42. MTT cell viability assay on U87 MG cell line (passages 14, 15, and 16) with varying concentrations of BPEI-coated IONRs after 48 hours. No significant difference in the normalised UV absorbance was observed in individual triplicate. Error bars represent the standard error of the mean (SEM). The statistical significance level and indicated with (*) for $p < 0.05$.

1.3.3 The effect of (IONRs/carnosine) combination and mild hyperthermia application on the controlled release of carnosine

Using dialysis tubing to model the release of free carnosine, figure 43 predicts that water entered *via* osmosis, and the carnosine left the tubing *via* diffusion. The IONRs' BPEI coated size prevented them from having permeability through the membrane. Increasing the temperature to 40 ˚C accelerated the complete release of carnosine after 2 hours. The BPEI-coated IONRs partially retained the carnosine at 37 ˚C. Free carnosine had a linear trend of release, which might have extended until 8 hours, thus delaying the effect of the treatment, as mentioned in the proliferation study. Using the carnosine-loaded BPEI-coated IONRs may offer the advantage of a more quickly controlled treatment relative to the traditional application of carnosine. By comparing the results from the LC-MS, it was seen that the carnosine structure was not affected by mild hyperthermia. All samples and standards showed identical peaks, which appeared due to the release of carnosine without any impurities or structural modification (Figure 43).

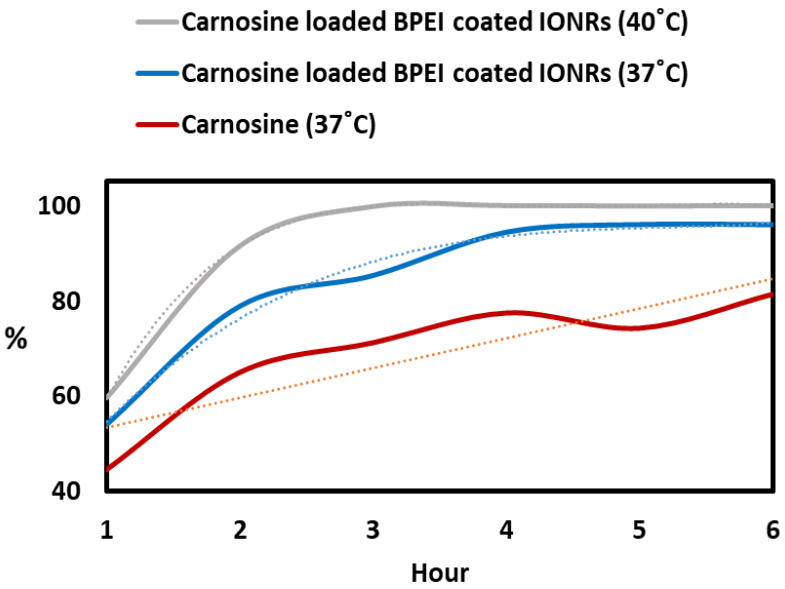

Figure 43. LC-MS assay for the released carnosine from dialysis membranes containing carnosine free or loaded BPEI-coated IONRs, under different conditions, at temperatures of 37˚C and 40˚C. Free carnosine had a linear trend of the release percentage while the release ratio of carnosine from the BPEI-coated IONRs embedded carnosine was enhanced exponentially in all conditions. Mild hyperthermia allowed the carnosine to be fully released after 3 to 5 hours.

In all plates, the controls of seeded cells, alone or with carnosine, showed no significant changes in terms of live cells, which proves the lack of an effect caused by mild hyperthermia conditions (40˚C, 5% CO_2) on cell growth. In the samples of bonded IONR nano-carrier with 25 mM carnosine, the normal incubation in (37˚C, 5% CO_2) showed that the effect of carnosine was hindered because the polymer is attached to the BPEI-coated IONRs. However, applying heat of 40˚C for 3 hours initiated the release of carnosine. A maximum of 5 hours of mild hyperthermia could de-attach the carnosine inside the cells, which was reflected in the treatment result after the completion of 48 hours in normal incubation (Figure 44A). When the samples contained carnosine that was already mixed with the media, the added BPEI-coated IONRs had no influence on the regular effect of carnosine, in all conditions. The BPEI-coated IONRs' existence in the same vicinity of carnosine *in vitro* did not mask the treatment because the carnosine stayed free (Figure 44B).

The presented results show that cationic BPEI-coated IONRs are promising in terms of their intracellular delivery into brain tumour cells, which is like that of colon cancer cells (Pla, Pascual, and Guerri, 2016). The fast uptake and localisation of BPEI-coated IONRs in the nucleus were used in drug delivery for GBM gene therapy or in the *ca.* 20-fold enhancement of the cell entry of hydrophobic drugs (Arachchige et al., 2017; Wang et al., 2018). Adding the mild hyperthermia treatment gives the advantage of controlled released carnosine from the IONRs to the mitochondria. Thus, the presence of a safe amount of heated iron oxide in the same vicinity as the encapsulated drug could lead to long-term

GBM therapy and improve the safety profile of the astrocytes' viability without alterations in blood-brain barrier permeability (Au et al., 2007).

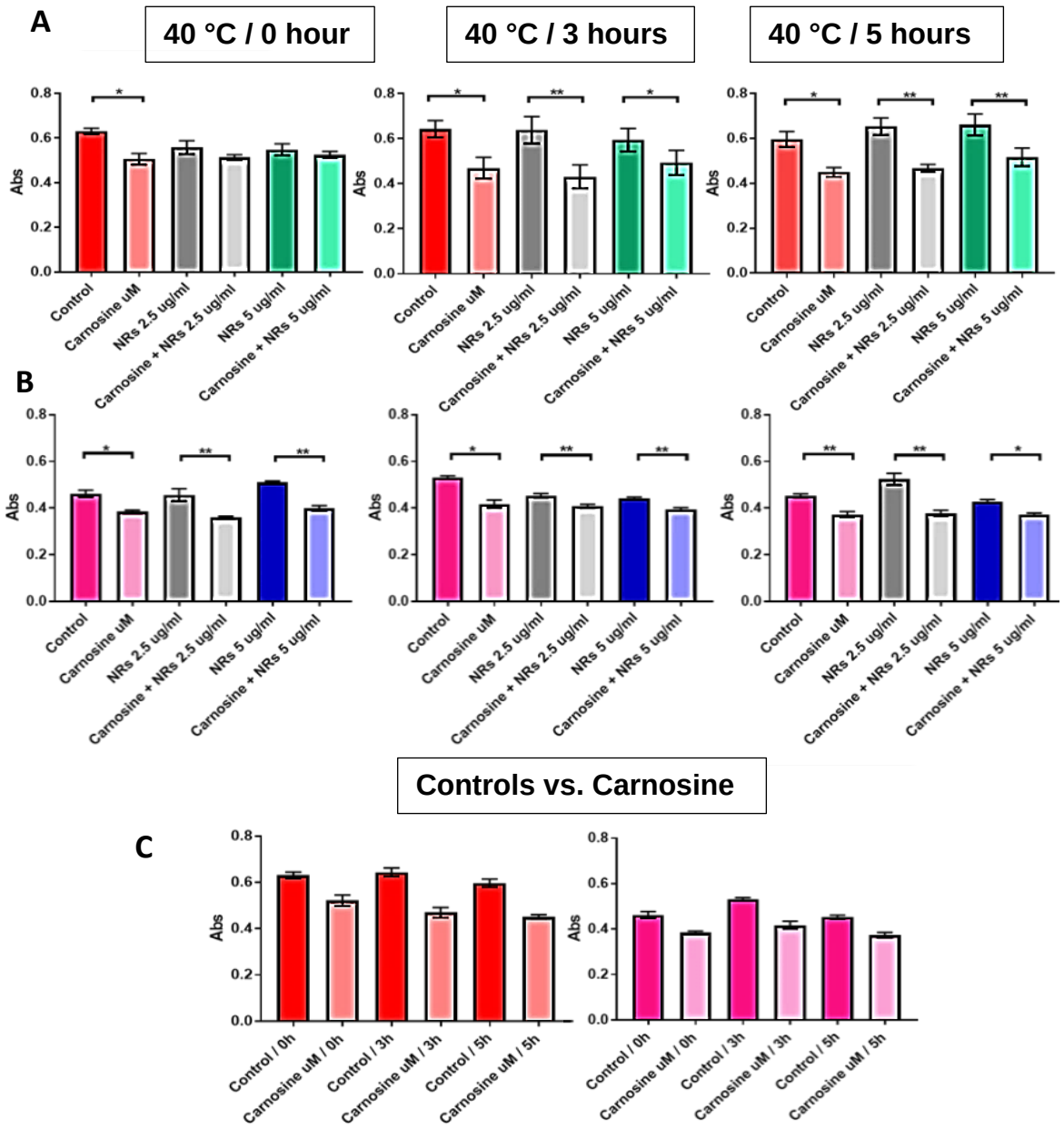

Figure 44. MTT assay on U87 MG cell line with same carnosine concentration 25 mM for all plates and different concentrations of BPEI-coated IONRs (A) carnosine loaded BPEI-coated IONRs and mixed for 5 min with the media (B) BPEI-coated IONRs added to the soluble carnosine in the media. In both cases, mild hyperthermia was applied by changing the temperature of separate the incubator. Comparing the controls shows the inefficiency of mild hyperthermia in killing cells because of the insignificant difference between the controls in all plates. The heat released the carnosine from the BPEI-coated IONRs after 3 to 5 h when it was bonded, while the effect was equal, without any significant difference, when the nanorods existed in the same vicinity. Each treatment was repeated on 6 samples, then the T test was applied to address the significant changes. (C) Comparison of the repeatability of all controls from (A, B). (Abs = absorbance at 570 nm). The statistical significance level and indicated with (*) for $p < 0.05$, (**) for $p < 0.01$.

1.3.4 Sustained released carnosine application in single spheroids

1.3.4.1 The effect of the sustained treatment of carnosine on U87 MG single spheroids

The efficacy of carnosine was applied at different concentrations (0, 50, 100, 150 mM) to U87 MG cells grown as single spheroids, on days 1, 3, and 5 to mimic sustained-release therapy. The change in morphology of the single spheroids after day 3 proved the effect of carnosine in suppressing the proliferation of these spheroids. From the series of carnosine concentrations, the critical amount to hinder the spheroid growth was found to be over 100 mM (Figure 45).

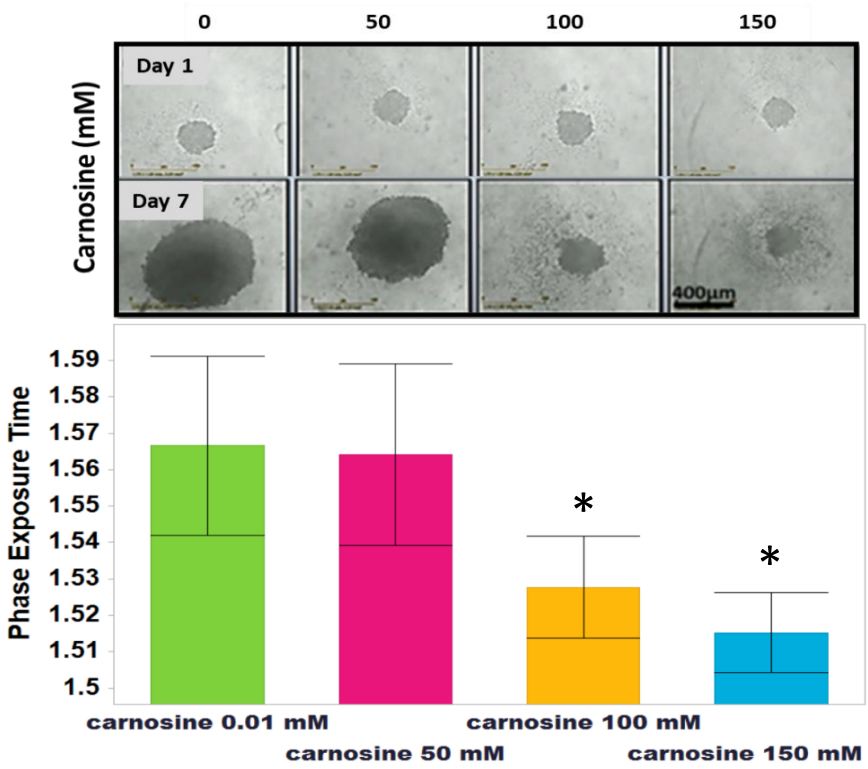

Figure 45. Incucyte® live cell system (×4) live spheroids images show the comparison between the morphology and size of single spheroids on day one and day seven after applying different doses of carnosine treatment. The mimicked sustained release of carnosine concentration ≥ 100 mM affected spheroid growth and tightness, and a significant difference was reported in phase exposure. The statistical significance level of phase exposure time of the spheroids on day seven was indicated with (*) for $p < 0.05$, (**) for $p < 0.01$. (n=3) Error bars represent the standard error of the mean (SEM).

The concentration of carnosine required to affect the viability of U87 MG was found to be around 30 mM in a previous investigation that utilised a monolayer 2D model (Habra et al., 2022). The same results were obtained in Figure 46 at 22 hours when EC50 was calculated before the complete of forming spheroid. Comparing drug sensitivity in 2D and 3D cultures was feasible daily by measuring EC50 using the change of spheroids phase exposure. The increment of EC50 on day 2 to 155 mM was an important indicator to add the second carnosine dose on day 3. The EC50 was stable at around 100 mM between days 3 and 7 which confirmed the suitability of the dose frequency (Figure 46).

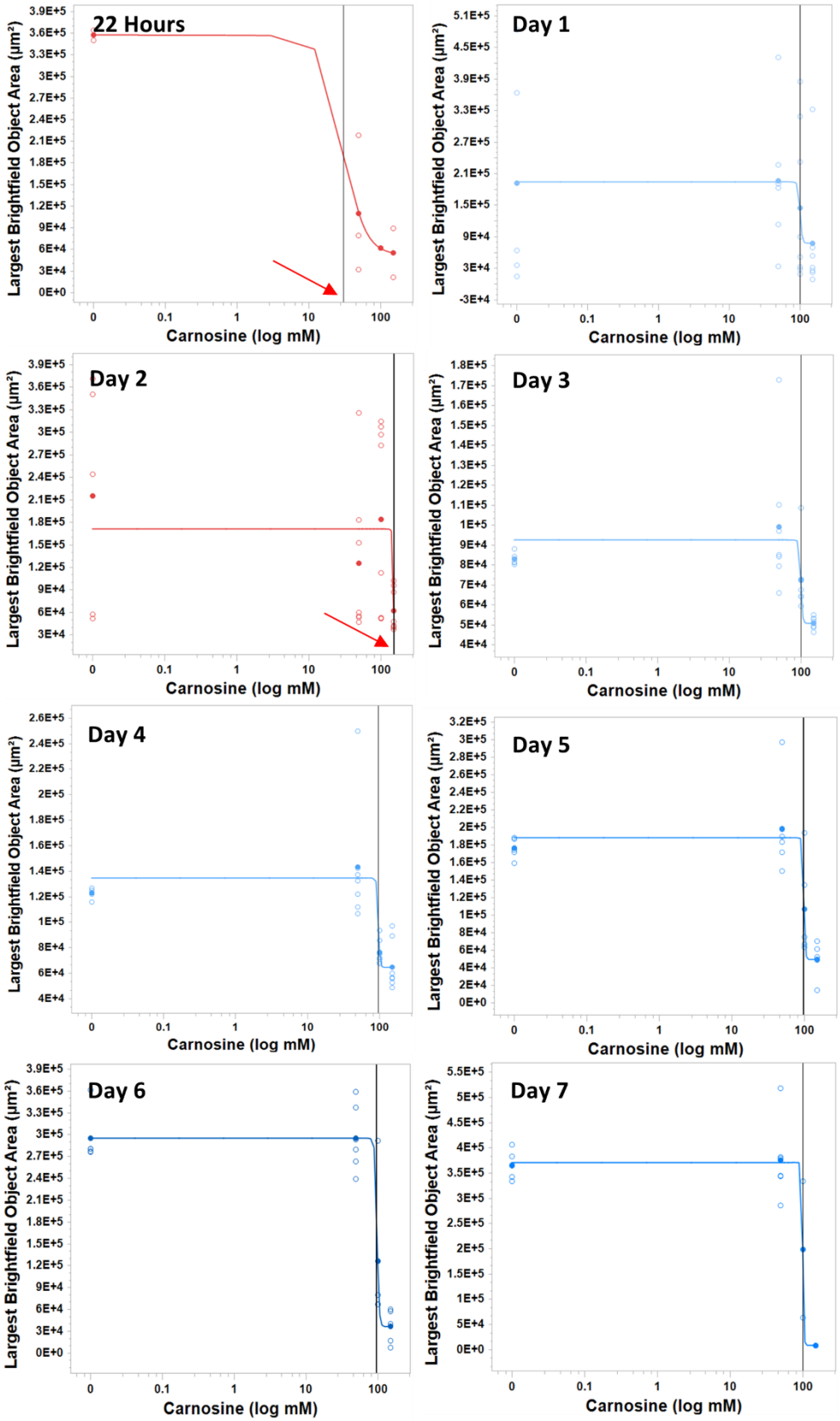

Figure 46. Incucyte® live cell system (×4) live spheroids images converted to graphs which show the potential of using the protocol to obtain EC50 of carnosine on multiple points for drug delivery study and *in vitro* sustained release profile. The EC50 of carnosine on monolayer cells was calculated for seven days.

The penetration and binding of compounds into spheroids have been shown to be a promising predictor of compound uptake in thick tissues (Hjelstuen et al., 2009). The formed tumour spheroids of U87 MG reflected the effect concentration EC50 by using carnosine as a treatment (Habra et al., 2022). By utilising different concentrations (0, 50, 100, 150 mM) of carnosine in a sustained release designed experiment, the inhibition of the single spheroids' growth was significant compared to untreated spheroids (Habra et al., 2021).

1.3.4.2 Obtaining single spheroids from various cell lines

The applicability and reproducibility of the method in chapter 5 paragraph 1.16 were demonstrated using different cell lines from various cancer types (originating from either humans or mice) (Figure 47). Generating single spheroids from seven different murine and human tumour cell lines showed the potential of this method for generating spheroids from various cancer types (brain, prostate, and breast) starting with the same cell density per well. The size of the spheroids can be adjusted by seeding different cell numbers and manipulating the time of incubation according to the personalised experiment design. One should however keep in mind that the core region consisting of a necrotic area will also increase with the spheroid size and therefore experiments aiming to assess treatment efficacy will have to be carefully planned (Carlsson et al., 1983). For U87 MG cell line, the presence of dead cells in the spheroid centre was due to hypoxia (Kolenda et al., 2011). Tumour hypoxia has been attributed to tumorigenesis and therapeutic resistance by maintaining the undifferentiated state of tumour stem cells. Thereby, therapeutic strategies should take oxygen tension into account (Kolenda et al., 2011). The loss of green CFSE fluorescent signal throughout the z depth of spheroids exhibited a reproducible exponential decay function (Leary et al., 2018). Monitoring the changes in the content of live, dead, and apoptotic cells enables observation of the consequences of compound exposure on the spheroid (Sirenko et al., 2016). The H&E staining of the middle cross-section of the spheroid encompassed the complete tight structures from core to rim. The rim of the spheroid consisted of even layers of packed cells toward the centre despite the death of the cells which formed a necrotic core region (Bull et al., 2020). During spheroid formation, a small proportion of cells did not integrate into the sphere and lost cell-cell adhesion properties. The reason for this separation is gravity-sedimentation (Stadler et al., 2018). After the optimisation towards mimicking various stages of avascular tumour regions, the resulting single spheroids can easily be transferred to any plate or cell culture vessel due to the ease of mechanical access for further investigation or analysis. Cell viability assays such as the MTT, trypan blue exclusion, and LDH release assays can be used for *in vitro* therapeutic screening in spheroids (Daunys et al., 2021). Consistent culture conditions need to be kept during the spheroid growth as this otherwise might affect proliferation significantly by altering the expression of tight junction molecules, which establish a delay in the initial shrinking of the spheroid size (Ivascu and Kubbies, 2006). On average the spheroids reach a stable symmetrical size after 24 to 48 hours post-seeding. However, some cell lines require a longer time such as the DU145 cells which needed around 5 days to produce firm

spheroids. The observed diameter was *ca*. 200 nm at which the spheroids started to show a necrotic core and a proliferative outer layer. In the future, adding cells of the tumour microenvironment to develop multicellular 3D cultures will make the models more representative of the *in vivo* tumour situation (Zraikat and Alshelleh, 2020). This protocol could also be tested on essential tumour stem cells such as SJ-1 (Kolenda et al., 2011).

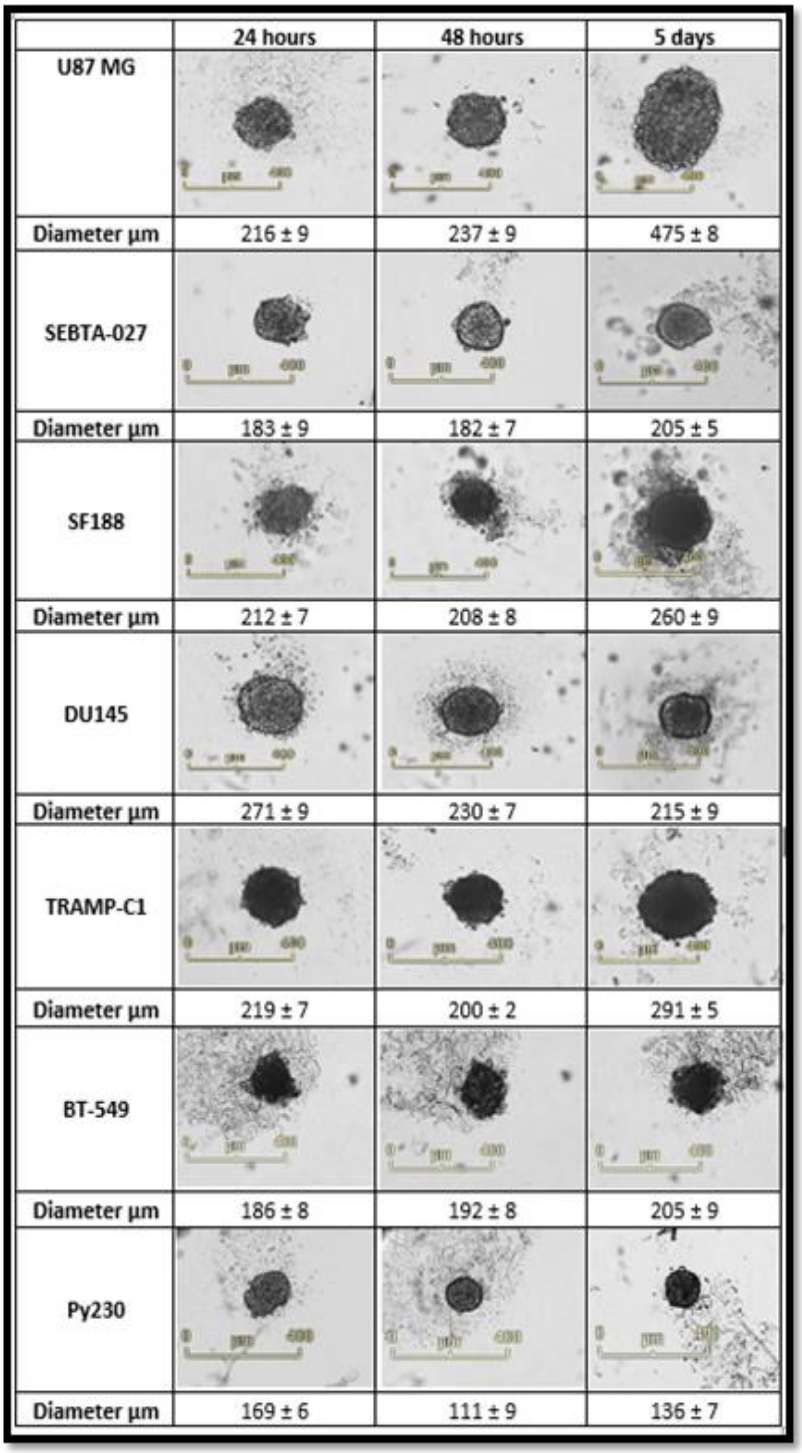

Figure 47. Incucyte® live cell system (×4) live spheroids images show the potential of using the protocol in chapter 5 paragraph 1.16 to obtain single spheroids from various cell lines.

1.4 Conclusions

1.4.1 The controlled sustained release of carnosine using mild hyperthermia

To realise the full oncological potential of carnosine, the dipeptide was embedded within a novel nano rod-shape superparamagnetic iron oxide of about 80 nm capped with a branched polyethyleneimine. After the safety studies, the IONRs were used as carriers loaded with carnosine. The application of the combination with carnosine was found to stimulate the full release of carnosine from the vector following the use of only mild hyperthermia conditions of 40˚C. The outcome results from the effect of (IONRs/carnosine) combination and mild hyperthermia application facilitated an achievable application of slow controlled sustained release treatment of glioblastoma brain tumours that demonstrates potential to inhibit the post-surgery metastasis with MRI monitoring.

1.4.2 The mechanisms of carnosine effect on Glioblastoma U87 MG cancer cells

Glioblastoma is the most aggressive form of all brain cancers, with a prognosis of only 15 months after diagnosis (Kromer et al., 2017). Unfortunately, despite the surgeon's bests efforts, the complete removal of the tumours cannot be achieved by surgery alone due to the complex finger-like structure of the tumour. Also, these tumours are highly resistant to current radiation and chemotherapy treatments (Stupp et al., 2005). The results have demonstrated that carnosine lowers the growth and mobility rate in the Glioblastoma U87 MG cancer cells. However, there is a necessity for a suitable sustained drug delivery system to be implanted into the post-surgical cavity and be used as a complementary treatment with imaging advantage to improve the prognosis of this devastating disease.

1.4.3 *In vitro* investigations for sustained released carnosine using 3D model

Monolayer cultured tumour cells exhibit less resistance to therapeutic interventions than *in vivo* cells (Ravi et al., 2015). Developing a 3D model that more resembles solid tumours is important, especially when trying to bridge the gap between *in vitro* and *in vivo* tumour models. The use of 3D models is nowadays largely used, and the commonly used protocols were followed by significant updates. The protocol described here demonstrated reproducible findings in generating single spheroids using a simple cost-effective method that other researchers and different laboratories can benefit from. Uniform single spheroids without any additives were consistently obtained. The spheroids exhibited the typical characteristic morphology consisting of a proliferating rim and a necrotic core. The 3D model was used to assess drugs EC50 as was highlighted using sustained released carnosine treatment. Preliminary optimisation for different cell lines of single spheroids is proposed to provide the research workers with an easily accessible and average 20-fold cheaper method than the ultra-low adherent plates calculated based on the current prices of the purchased items from the market. In the future, the reported data needs to be further studied to find the validity of patient-derived tumour cells.

Chapter 4: Micro vectors for drug delivery

1.1 Overview

Despite the advantages of the synthesised BPEI-coated IONRs shown in chapter 2, the formulation has a limitation. The high buffering capacity of carnosine helps keep the pH around its physiological value. However, the pH in the alkaline spectrum enhances the sedimentation of the BPEI-coated IONRs due to the neutralisation of the surface charge. When the zeta potential is reduced to zero, the repulsion forces among the particles disappear dramatically (Edwards and Williams, 2004). Thus, the amount of functionalised material should be carefully studied, and the optimum amount should not affect the stability of BPEI-coated IONRs.

Drug delivery research has led to many types of suitable carriers for molecules, which can also have the advantage of tuning the release (Nance et al., 2021). For example, liposomes are safe candidates for use as biocompatible vehicles for carnosine. This is because their core is a hydrophilic solution within a lipid shell that can be modified to target hard-to-treat glioblastoma tumours *via* the nasal route (Hong et al., 2019). Loading carnosine inside polymer beads, such as spherical cages, can also be designed to control the release of carnosine. By incorporating the synthesised BPEI-coated IONRs into neighbouring beads, they leach out of the beads and break the polymer shell by rotating. Mechanical spinning movement can be induced from a distance by applying a rotating magnetic field. Thereafter, pulses of carnosine are released to provide a healing effect (Habra et al., 2022). Both previous vectors were investigated in formulations with cytotoxicity, stability, and release investigations.

1.2 Liposome vesicles for drug delivery and sustained release treatment

Most therapeutic compounds have limited entry into the brain due to the restrictions of the BBB for the accessibility of small molecules from the systemic circulation (Pardridge, 2007). Nanoparticle formulations are delivery carriers of the central nervous system (CNS). Liposomes have attracted clinical development, particularly for intranasal applications (Nance et al., 2021). Over the last few years, the effectiveness of hydrophilic liposomes has been reported to enhance nose-to-brain drug delivery (Hong et al., 2019). Optimising studies for the formulation of liposomes is therefore essential to deliver the active material and surface modifiers into the phospholipid shell of the liposome which also plays a vital role. Further stability studies, drug release, and bioavailability were considered due to the immediate impact of the integrated functionalised materials, such as surfactants (Illum et al., 2002), or many more, including the formulations that develop cationic aggregates in intranasal physiological conditions (Nakamura et al., 2017). Validated tests should be applied *in vitro* and *ex vivo* to facilitate safe formulations for brain treatment. Solid evidence of the predominant contribution of drug-loaded liposomes should be shown in chemical and mechanistic studies. Strategies for distinguishing

opportunities in the nose-to-brain direct transport of drugs may be the futuristic solution to treating brain-related diseases (Bozzuto and Molinari, 2015; Hong et al., 2019). The liposomes in this project belong to micro-sized drug delivery vectors with diameter of 300 nm.

1.2.1 Applications of direct nose-to-brain therapy

The olfactory system has attracted the attention of applying therapies to spread the treatment directly in the brain. It consists of the olfactory epithelium, where the drug is transported through the cribriform plate to reach the olfactory bulb (OB) (diagram 1).

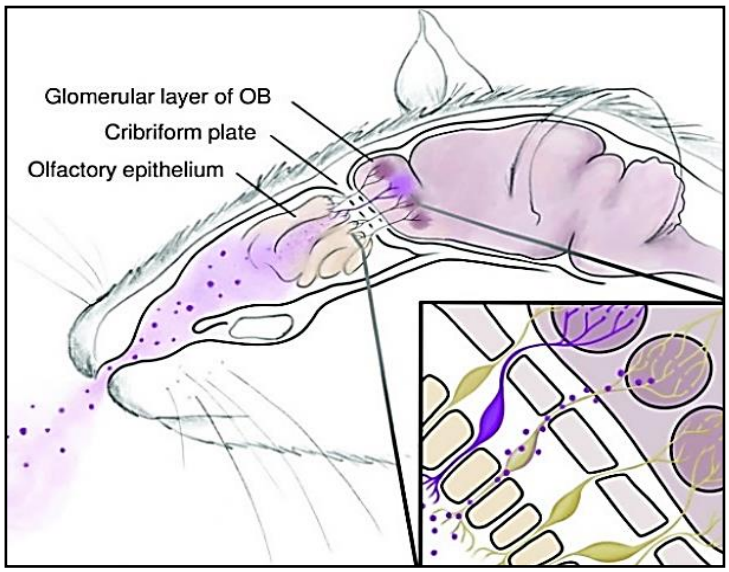

Diagram 1: The structure of the rat nasal passages and the proposed treatment pathway. The formulation contacts the olfactory epithelium, which contains dendritic processes from olfactory receptor neurons. The axonal projections extend through channels in the cribriform plate and into the glomerular layer of the olfactory bulb. Zoom box: liposomes (purple dots) crossing the cribriform plate to gain access to neuron bundles in the olfactory bulb (Boyles et al., 2021).

Many diseases have been managed in clinic using intranasal applications for insulin-like growth factor 1, such as brain stroke, neurodegeneration and Alzheimer's cases (Gomez et al., 2012; Salameh et al., 2015; Kalviainen, 2015; Jiang, Li and Liu, 2015). Moreover, gene therapeutics are delivered without having the side effect of spreading the molecules through physiological fluids (Born et al., 2002; Li et al., 2015; Aly and Waszczak, 2015). Despite the advantages of nose-to-brain transport, the intracranial application has received more attention in modality (Serwer and James, 2012; Peterson et al., 2014). The significant direct effect of antineoplastic agents through olfactory bulbs has been proven in a few *in vivo* applications for chemotherapy (Wang, Gao, and Yun, 2005; Sakane et al., 2009; Shingaki et al., 2009; Shingaki et al., 2010). For example, a comparison study administered methotrexate intraperitoneally and intranasally to rats with 9L glioma cell brain tumours. After 10 days of treatment, tumour weight from treated rats was 20% lighter than untreated rats. However, the intranasal route

resulted in an 80% reduction in tumour burden, which proved the effective cross of methotrexate through the BBB (Blakeley et al., 2008; Shingaki et al., 2010). In the context of extending survival, blocking the telomerase function by daily intranasal application for a phosphonamidite-based oligonucleotide was reported in a successful study. Rats with U251 glioblastoma cells implanted in their brains had two times longer survival rates than the control (Hashizume et al., 2008). The treatment of the brain implanted with C6 glioma cells by using camptothecin as a chemotherapeutic inhibitor was attempted in another study. Camptothecin was loaded inside nano-sized micelles and integrated with a cell-penetrating peptide (Tat analogue) on the surface. The importance of modification strategies was demonstrated in the results because they increased the efficiency of drug uptake at a high concentration of 2 mM/mL without cytotoxic side effects (Taki et al., 2012; Djupesland, 2013). The work in this project aims to load carnosine at a high concentration (300–400 mM) inside stable liposomes with a negative surface charge. The liposomes should reserve the carnosine to release it over time as an extended treatment to eliminate any left malignant cells after surgery without affecting the brain.

1.2.2 Advantages of current intranasal application methods

Bypassing the BBB is a route from the blood vessels of the olfactory and trigeminal nerves to the parenchyma *via* perivascular convection. It has been shown to be effective for targeting the central nervous system (CNS) non-invasively using various active materials, including insulin with rapid efficiency after intranasal administration (Lochhead and Thorne, 2012; Thorne et al., 2004; Miller et al., 2008; Frey, 2013; Appu et al., 2016). Aerosol propellants have been employed in some studies to the olfactory epithelium or the pipette to the sinus cavity concerning positioning the animals upright or supine for high drug uptake (Apostolatos et al., 2012; Xiao et al., 2013). The advantage of the self-administrative technique is that no skill is needed for the application except for small volumes, when accuracy and consistency become challenging. A drastic drop in therapeutic drug delivery with a small volume was reported in these cases. This happened because of the drainage of the applied treatment to the oesophagus (Landis, Boyden, and Pegg, 2012).

The transition of fluids to the brain was not facilitated by traditional applications using a pipette. The therapy should be delivered to reach the upper and posterior areas of nasal cavities where cranial nerves are found (Guastella et al., 2013). Thus, despite the downsides of the intranasal route because of the difficulties during *in vivo* application, it is still the most promising route for bypassing the BBB (Lochhead and Thorne, 2012). One of the recommended devices for intranasal treatment is precision olfactory delivery (POD, Impel NeuroPharma), which was used to deliver tritium-labelled pralidoxime. The device demonstrated the feasibility of intranasally applying the oximes for neuroprotection against organophosphate threat agents, regardless of the weight or age of the animal (Krishnan et al., 2016; Krishnan et al., 2017).

1.2.3 Improvements in liposomes of previous biomedical applications

As shown in Figure 2, liposomes are lipid vesicles prepared to be employed as vectors for biomedical purposes which used to be characterised as closed shells consisting of mono- or multi-phospholipid bilayer lamellae surrounding a small volume of aqueous liquid. Carugo et al. reviewed many protocols and produced diverse options for nano- to micro- liposomes for different final uses. Their medical preparations were unilamellar liposomes with an average diameter of around 100 nm. The assembly was driven by the spatial organisation of the amphiphilic molecules towards the core to minimise interactions entropically with the surrounding aqueous phase. Hundreds of biologically hydrophobic active compounds were integrated within these carriers. Water-soluble materials are intercalated in the lipid bilayer to be entrapped inside the aqueous interior compartment (Carugo et al., 2016).

The inherited preparation process usually includes lipid film hydration, forming large unilamellar vesicles by freezing and thawing and then applying extrusion through polycarbonate filters to obtain single bilayer vesicles with size-exclusion purification and drug active loading encapsulation (Allen and Cullis, 2013). Over the decades, a batch of liposomes has been generated by developed techniques relying on either mechanical manipulation of the dispersed bilayers or the aggregation of the lipids (Akbarzadeh et al., 2013). Lately, modern microfluidic approaches control the physical properties of liposome efficiently within the microenvironment. Therefore, the microfluidic technique will be explained in this chapter, along with its advantages and downsides. The current focus is on addressing experimental evidence for reliability before scaling up liposome production to an industrial batch size. Herein, forming the liposomes included adding the cholesterol with the lipid as a stabiliser to control the time of blood circulation and accumulation. Critical physicochemical studies were applied to characterise the liposome size distribution, zeta potential for surface charge, encapsulation efficiency, stability and biosafety. Afterwards, the designed formulation should be tested by comparing the effect of free and loaded drugs in the preclinical stage on the animal model (Chang and Yeh, 2012). The reported results in the field included comprehension identification studies. Additionally, a comparison between the control of blank liposomes and the carnosine-loaded liposomes over a sustained release time was provided. However, a scaled-up study of the liposomal formulation is still needed.

1.2.4 Current techniques for liposome preparation

Many microfluidic approaches have been investigated, such as pulsed jetting (Stachowiak et al., 2008), double emulsification (Chu et al., 2007), transient ejection (Pautot, Frisken, and Weitz, 2003), droplet emulsification (Ota, Yoshizawa, and Takeuchi, 2009), hydrodynamic flow focusing (Mazzitelli et al., 2013) and hydrodynamic pinch-off mechanism to improve liposome preparation (Deshpande et al., 2016). The previous methods produce microscale liposomes, however, they are not strictly microfluidics except for microfluidic hydrodynamic flow focusing (MHFF). Advanced encapsulation and loading efficiency were accomplished by producing unilamellar liposomes with diameters ranging

between 5 and 20 μm (Carugo et al., 2016). The particular physical characteristic of MHFF liposomes is the nano-unilamellar morphology, which has the potential to be scaled up and applied in clinical trials. Microchips are usually designed with a circular cross-section in 3D annular coaxial geometry (Hood et al., 2014) or a rectangular cross-section to force crossflow (Kastner et al., 2015). Both types promote the focus forces hydrodynamically, which intersect and sheath the two phases. The lateral or coaxial channel of the lipid consists of an aqueous phase stream (distilled water or buffer). The central or inner channel streams of the lipid phase are dissolved in an alcoholic solvent (Figure 48).

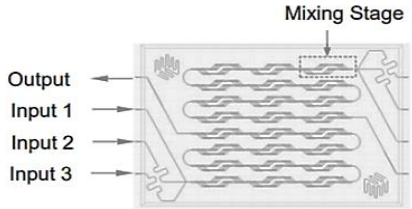

Figure 48. Dolomite micromixer hydrophilic or hydrophobic chip. The alcoholic mixture is the central stream, while the water flows from inputs 1 and 3.

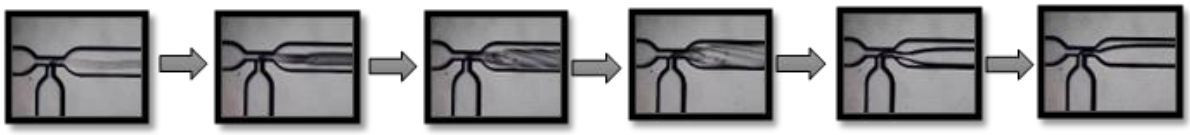

Figure 49. Microscopic images showing the mixing patterns during the optimisation of the pump pressure. The pressure of the continuous central flow increased from left to right while the size of generated vehicles decreased.

The volumetric and total flow rates for each phase should be controlled to noticeably adjust the size of the liposomes (Capretto et al., 2013). Diffusion dominates mass transfer at the liquid interface. The alcohol solubilises into the water phase until a critical concentration level is reached. Then, the self-assembly of phospholipids triggers the liposome generation (Jahn et al., 2007) (Figure 49). The lipid molecules precipitate and the simultaneous structure forms the vesicles to minimise the repulsion forces between the lipids and the water (Jahn et al., 2010). The final morphology was controllable by the physical pressure and temperature parameters and by modifying the chemical conditions. The repeatability and reproducibility of the microfluidic techniques surpassed the bulk-phase preparations. This happened because they followed an analogous protocol that overcame the high polydispersity and heterogeneity of traditional liposomal suspensions (Kastner et al., 2014). Besides the previous advantages, MHFF offers the possibility of in-process control and monitoring during the continuous formation and scaling up of liposomes by multiple synchronised reactors (Capretto et al., 2013).

1.3 Optimising the microfluidic preparation of liposomes

The main improvements in the parameters of microfluidic technology have been investigated during the last two decades. It was reported that the average size of the liposomes was related directly to the

lipid concentration (Hood et al., 2013; Mijajlovic et al., 2013) and inversely to the flow rate. A higher rate of central alcoholic fluid forming smaller liposomes was observed (Jahn et al., 2007; Jahn et al., 2010). The total flow rate and the geometry of the current microchip designs produced similar liposome suspensions, even with the recent micromixer of the Y cross-section shape, which is supposed to be the fastest turbulent micromixer to induce chaotic advection (Kastner et al., 2014; Walter et al., 2015; Hood et al., 2015). More studies are still needed to overcome the limitations of the available microchips for MHFF. Also, more studies should consider using cationic lipid mixtures and functionalisation, which may produce liposomes for biomedical applications, such as drug delivery for anticancer treatments in commercial medicines (Yang et al., 2013; Ran et al., 2019; Hamano et al., 2019). Moreover, the toxicity study of the isopropanol residual needs to be extended because it used to be the principal solvent in MHFF protocols, whereas ethanol was used by just a few studies as a safe alternative. During the development of ready-to-use liposomal products, specific dilution should be optimised before MHFF to guarantee the availability of the end product with the required fluid viscosity (Webb et al., 2020). Many limitations are still gapping and yet to be resolved to obtain stable and scalable liposomal therapeutic formulations.

In this project, the lipid mixture was composed of lecithin 90% soybean (LC), cholesterol 95% stabilised (CH) and tetrabutylammonium bromide (TBAB). TBAB is a double-chained quaternary ammonium surfactant that helps form unilamellar vesicles in water. A mixture from the previous compounds at a ratio of 0.1:0.1:0.1 g was suspended in 10 mL of alcohol at room temperature and stirred for 8 hours at 25 ˚C. The saturated solution was then collected and filtered using a Millipore 0.22 μm filter. Deionised water was used as an antisolvent. The microfluidic hydrodynamic focus relied on using a hydrophilic micromixer chip with crossflow geometry. At a ratio of water-to-alcohol 1:1 flow focus rate, the lipid in the centred alcohol stream exceeded the solubility level. Spontaneous self-assembly was generated in a supersaturated environment to form spherical structures that enclosed the liposomal vesicles.

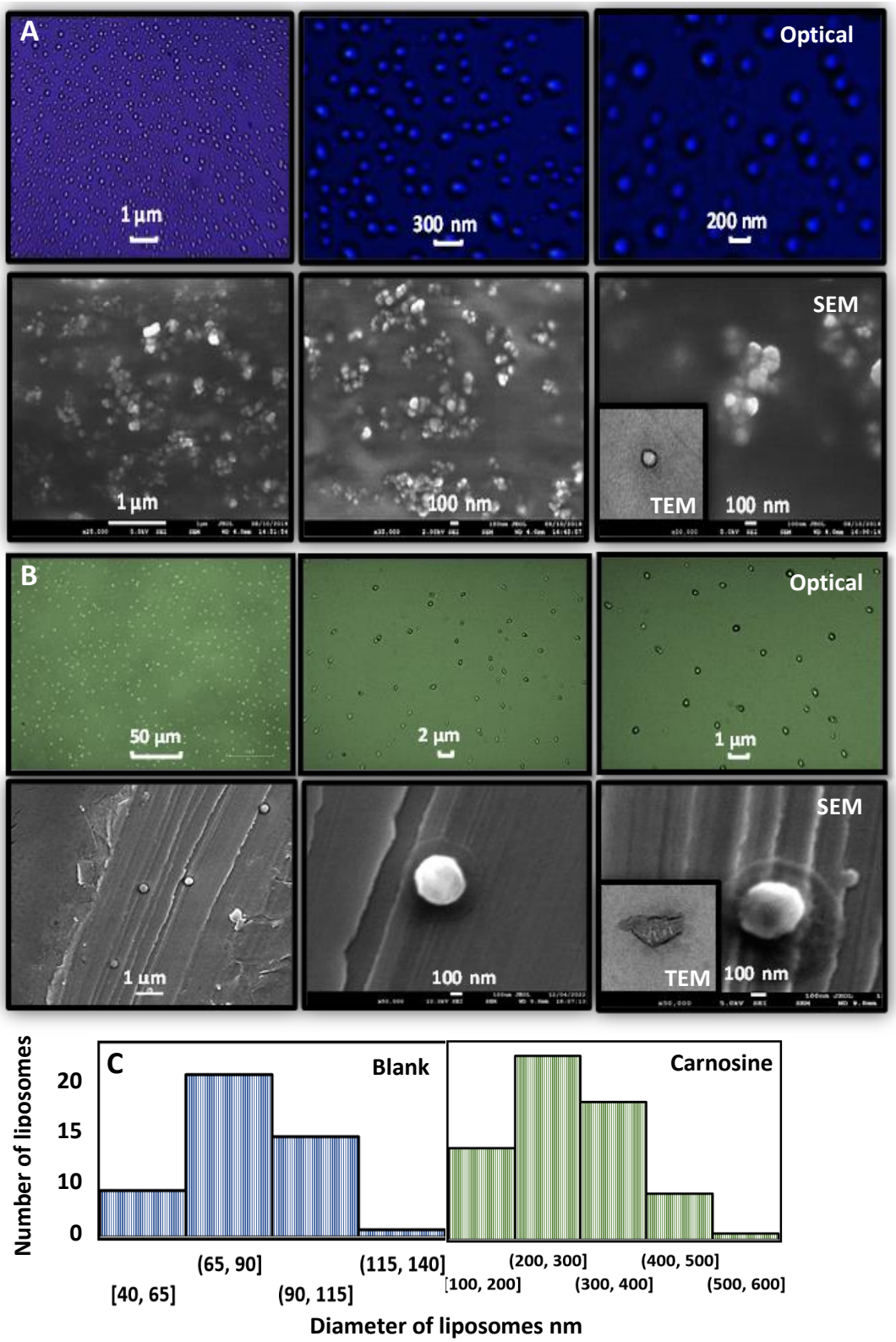

Figure 50. Microscopic images for liposomes before and after loading carnosine. (A & B) Optical, SEM, and TEM images were compared between the characterisation of empty blank liposomes (blue) and carnosine-loaded liposomes (green). (C) The histograms show the distribution of the liposome diameters. The diameters of liposomes n ≥ 50 were measured using ImageJ. The mean diameter size for the blank liposomes was 82.9 ± 19.4 nm and 284.1 ± 91.1 nm for the carnosine-loaded liposomes. The scale bar of TEM images = 100 nm.

1.1 Liposomes characterisation and physicochemical studies

1.1.1 Optical, SEM, and TEM images

During the preparation process, many images were captured with a camera attached to an optical microscope to show the size of the liposomes. The best technique to check the morphology of the liposomes is usually cryo-TEM operating at -194 °C. Herein, many samples were prepared for the available SEM and TEM imaging. An aliquot of the sample suspension was mounted on formvar films over copper grids and coated with 5 mm of gold. The air-dried liposomes were examined in the environmental chamber of fully automated vitrification SEM and TEM devices, with a relative air humidity of 100% and a temperature of 22 °C (Figure 50, A & B). The phospholipid bilayer lamellae dark shell surrounding a small chamber volume, which included the carnosine crystals in the loaded liposomes, was shown in the TEM images of the bright field (Figure 49B). The diameters of the blank and loaded liposomes were measured from the SEM and TEM images using ImageJ software. The mean diameter size for blank liposomes $n \geq 50$ was 82.9 ± 19.4 nm and 284.1 ± 91.1 nm for the carnosine-loaded liposomes. Carnosine-loaded liposomes are a few times larger than unloaded probably because of the interaction of carnosine with the lipid on the liposomal surface (Tahara, et al., 2013).

1.1.2 DLS: Diameter (DI), Polydispersity (PD), and Zeta potential

A particle size analysis of the liposome dispersions was performed using the DLS. The differential intensity percentage and the cumulative distribution were measured by DLS to show the hydrodynamic diameter and the dispersity of the liposomal formulation. The mean particle size was obtained from the results of three experiments for liposome preparation on different days. The hydrodynamic diameter and polydispersity measurements of the generated liposomes were carried out at 22 °C, diluted in the InVivoPure pH 6.0T dilution buffer (Table 2). It was indicated in the reported results that the similarity between the liposomes because of PD was 0.3, which refers to the uniformity in the size distribution of the liposomes before and after loading carnosine (Figure 51). Zeta potential was also measured by DLS for the liposomes in distilled water and was -77 ± 1 mV, which is expected from the negative charge of lipids. At the same time, using InVivoPure pH 6.0T dilution buffer to dilute the liposomes reduced the negative charge to -26 ± 1 mV, still high enough to maintain the dominance of the electrostatic forces. The use of InVivoPure pH 6.0T dilution buffer demonstrated suitability as a storage liquid that physiologically matches the pH of the nasal tissues (Edwards and Williams, 2004).

Table 2. The diameter and polydispersity of empty and carnosine-loaded liposomes by DLS.

	Blank liposomes	**Carnosine liposomes**
DI size (nm)	120.9	480.2
PD	0.3	0.3

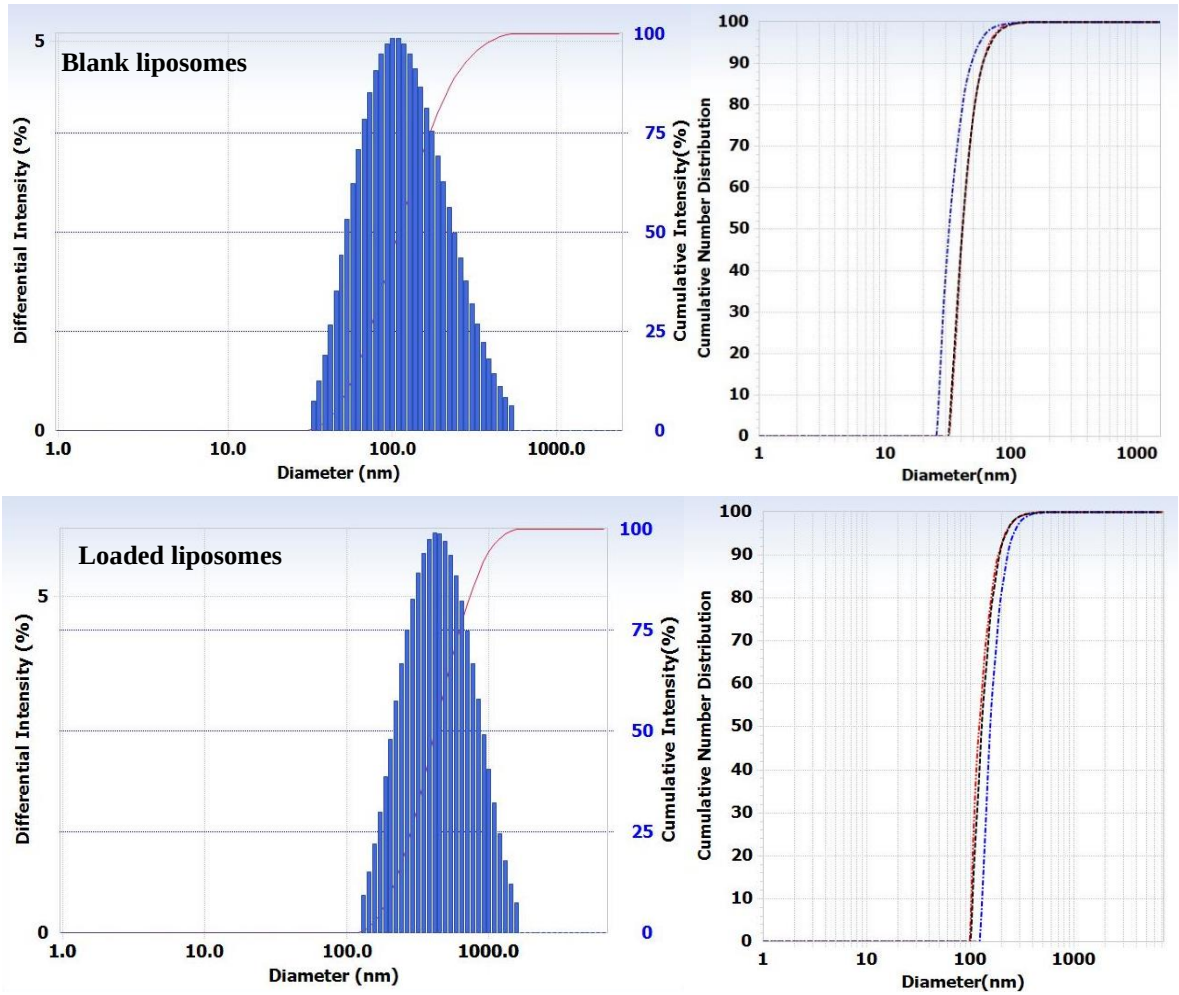

Figure 51. The DLS normalised and cumulative intensity distribution of the blank and carnosine-loaded liposomes. The repeatability of the distribution for three individual batches of liposomes is shown in both. The red curve is the average cumulative intensity for three liposomal batches.

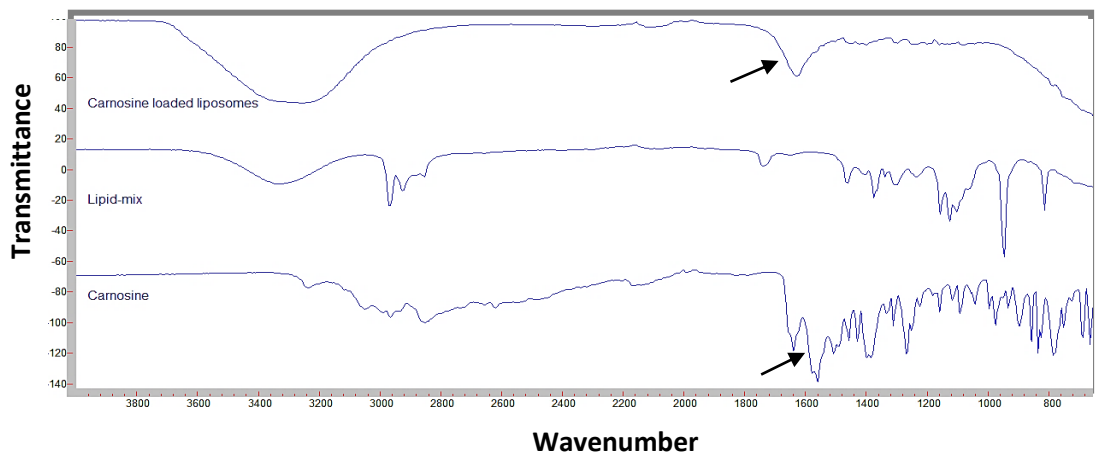

Figure 52. FT-IR spectra for liposomes with carnosine, lipids as empty liposomes, and carnosine crystals. The carnosine-loaded liposomes displayed characteristic bending bands around 1600 cm^{-1} attributed to the carnosine peptide bond.

1.1.3 FT-IR

FT-IR spectra were acquired by spectrometer on the fine dry powder of carnosine and blank and carnosine-loaded liposomes after checking a blank background. Characteristic bending bands around 1600 cm^{-1} attributed to the peptide bond of carnosine were displayed by the total reflectance spectrum of the carnosine-loaded liposomes (Figure 52), which were attenuated by FT-IR. The carnosine bands proved the loading of carnosine by the liposomes.

1.1.4 Stability profile

The stability of carnosine liposomes in InVivoPure pH 6.0T dilution buffer was evaluated for hydrodynamic diameter and polydispersity change for three distinct samples. DLS measurements of hydrodynamic diameter and polydispersity were taken over 30 days (Figure 53). The reported results were diameter is 480.2 ± 80.0 nm, polydispersity is 0.299 ± 0.023, and no dramatic change was observed for the samples stored in the fridge between (2 and 8 ˚C).

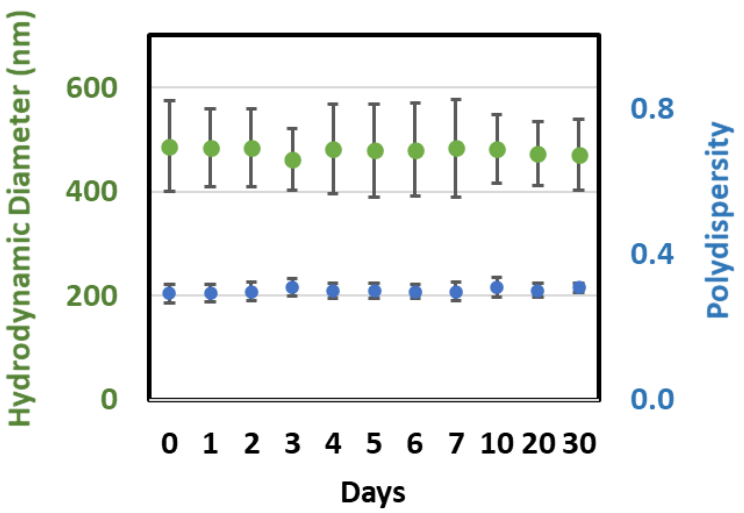

Figure 53. Stability studies *via* DLS measurements at room temperature: hydrodynamic diameter and polydispersity of carnosine-loaded liposomes over 30 days. Every measurement for three individual batches of liposomes was averaged after 60 readings from the DLS ± SD, which were repeated over 3 minutes.

1.1.5 Sustained release study

1.1.5.1 Membrane dialysis assay

The sustained release simulation from carnosine-loaded liposomes was studied for carnosine investigations by performing a dialysis membrane experiment. The mechanical rotation was created by a magnetic stirrer bar rotating inside a semi-permeable membrane bag of (1–10 nm) pores containing 300 mM carnosine-loaded liposomes. The comparison was between *in situ* 0 rpm and 100 rpm, miming human fluid dynamics (Schneider, Rasband and Eliceiri, 2012). The samples were retained for a week at 37 ˚C. The distiled water in the beaker was changed at specific time points to investigate the sustained

release of carnosine out of the bag after (a) 5, 15, and 30 minutes, (b) 1, 2, 3, 4, 5, and 6 hours, (c) 1, 2, 3, 4, 5, 6, and 7 days. The final component of the liposomes was free of carnosine, as proven by the liquid chromatography-mass spectrometry (LC-MS) assay (Figure 54). The DLS measurements for the hydrodynamic diameter did not drastically change in size and the carnosine probably released through a damaged wall, as shown in the TEM image (Figure 50). The liposomes did not disappear totally over time (Figure 55).

1.1.5.2 Encapsulation efficiency (EE) and loading efficiency (LE)

The determination of drug entrapment efficiency in liposomes began with a carnosine concentration of 1 M. It was performed after purification by dialysis membrane of 1–10 nm pores for 24 hours or loading 1 mL of a liposome dispersion into a gel filtration Sephadex column (1.0 cm in diameter and 10 cm long) eluted with distiled water and without applying pressure. The void volume peak fractions of water were thrown away. The volume peak fractions containing drug-loaded liposomes were collected. The carnosine concentration was quantified to measure the drug content by LC-MS.

Carnosine EE and EL were calculated as follows:

EE = (carnosine inside the liposomes / total carnosine) × 100 = 60.43 ± 13%

EL = (carnosine weight / carnosine & lipid weight) × 100 = 76.1 ± 11.8%

Starting from a total concentration of 1 M of carnosine solution loaded in liposomes, the resulting purified liposomes had a concentration of around 300 mM. Using gel filtration column (Sephadex® G-75, Sigma-Aldrich, UK), in the purification, either the total amount of carnosine or half of the carnosine concentration was extracted. This occurred because of the overlapping between the carnosine and the liposome vesicle filtration. The G-50 gel filtration column (Sephadex® G-50, Sigma-Aldrich, UK) with a larger particle size is recommended to separate the carnosine from the liposomes without overlapping. The free carnosine with small particles found its way out of the gel separately from the liposomes which could be distinguished visually from the milky colour. Despite the success of the separation by 50G, the downside of using gel filtration was the diluted liposome-associated product, which was at least five times that of making the suspension not concentrated enough for the aimed sustained release treatment application for cancer. Using bag membrane filtration was a suitable method for the purification of the liposomal formulation in this project.

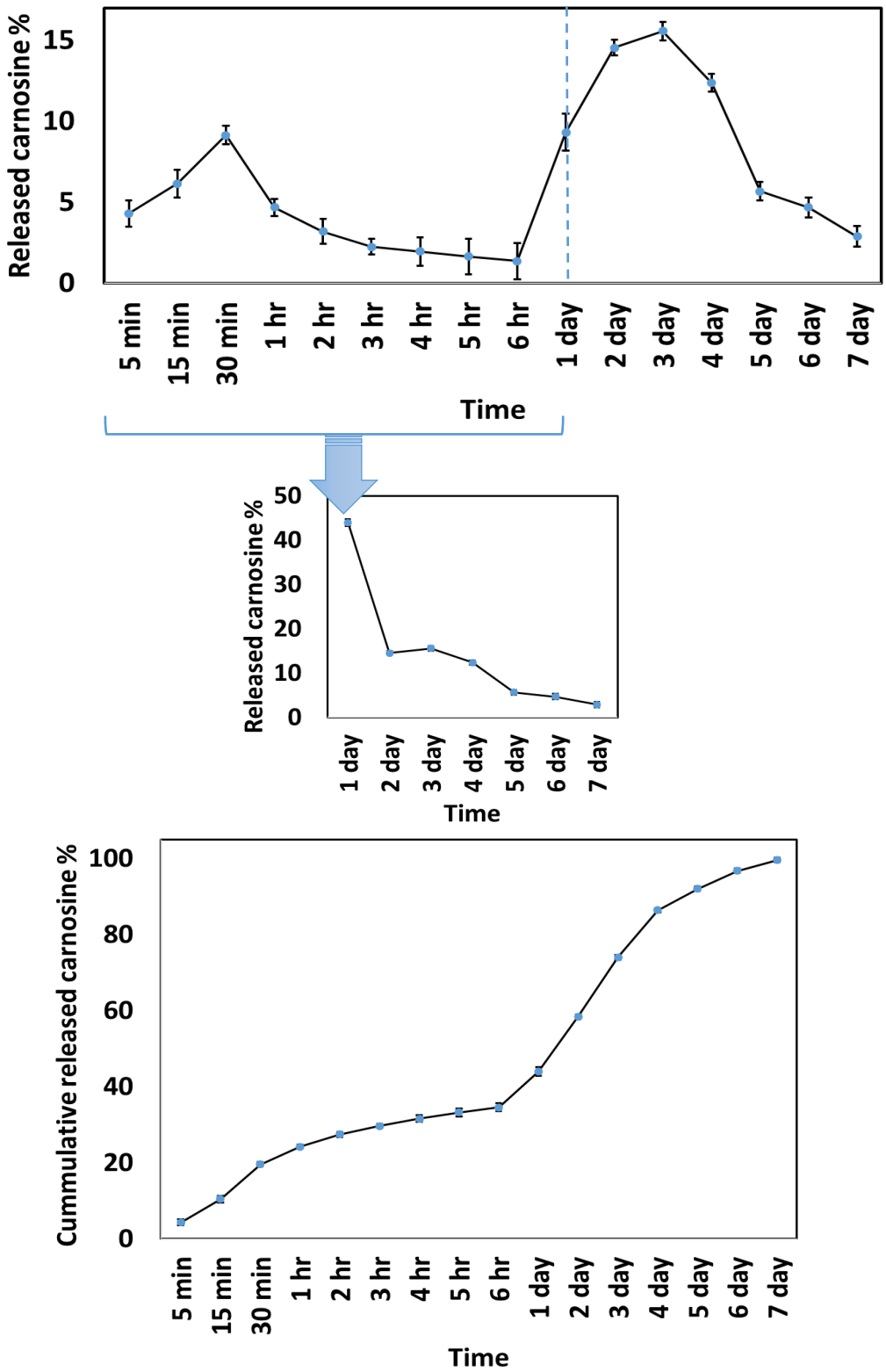

Figure 54. Membrane dialysis experiment over a week. The LC-MS results were averaged to show the released carnosine from three membrane bags, including carnosine-loaded liposomes. Many points were measured during the first 6 hours of day 1. Then, a sample was measured daily until the end of the week. The graduate release from the liposomes exposed to the mechanical rotation of a magnetic bar with 100 rpm stirring speeds is shown by the LC-MS cumulative analysis for the released carnosine.

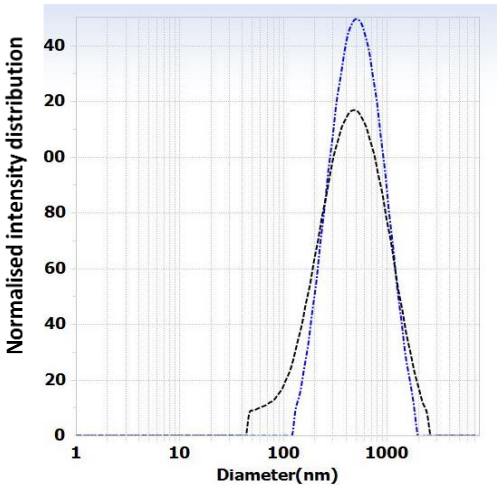

Figure 55. The DLS results of the normalised intensity distribution of the liposomes were at the beginning of the study (blue peak) higher than after a week of releasing the carnosine from the liposomes through the membrane dialysis bag (black peak). At the same time, a magnetic bar was stirred at a speed of 100 rpm.

1.2 Safety study for nasal application

1.2.1 Haemolysis test

Haemolysis reflects the lysis of erythrocytes and the release of their cytoplasm contents into the surrounding fluid. A haemolytic experiment was used to assess the toxicity effects of the liposome formulation on the cell membranes. Whole sheep blood (Sheep Blood Defibrinated, TCS Biosciences, Buckingham, UK) was warmed to room temperature. The prepared positive and negative control groups were 2 mL distilled water and an InVivoPure pH 6.0T dilution buffer. Each tube was mixed with 2 mL of 2% erythrocyte suspension. Then, all tubes were incubated for 1 hour at 37 °C. All tubes were cooled to room temperature. Then, they were centrifuged for 5 minutes at 2500 rpm. The absorbance of the supernatant was measured at 540 nm (HP 8453 UV-visible Spectrophotometer G1103A, Agilent, California, USA). All experiments were conducted in triplicate. The haemolysis rate was calculated using the following formula:

Haemolysis rate (%) = $(Abs_t - Abs_{nc}) / (Abs_{pc} - Abs_{nc}) \times 100\%$

Abs_t the absorbance of the test solutions.

Abs_{nc} the absorbance of the negative control.

Abs_{pc} the absorbance of the positive control.

When the concentration induces smaller haemolysis, the membrane damage is more significant. A ratio of more than 5% was regarded as haemolysis, reflecting the haemolysis effect more intuitively (Yang et al., 2013). The erythrocyte suspension with the buffer was measured as a negative control, showing 0% haemolysis. In comparison, deionised (DI) water was added to the erythrocyte suspension as the

positive control, showing 100% haemolysis. The haemolysis ratio of all carnosine formulations prepared with InVivoPure pH 6.0T dilution buffer showed no erythrocyte lysis by destroying the cell membranes. Overall, the visual observation showed that the haemolytic effect of carnosine solution, blank liposomes and carnosine-loaded liposomes on the cell membrane was not significantly different from that of the InVivoPure pH 6.0T dilution buffer. This result indicated that there would not be any prominent nasal toxicity of carnosine-buffered formulations (Figure 56).

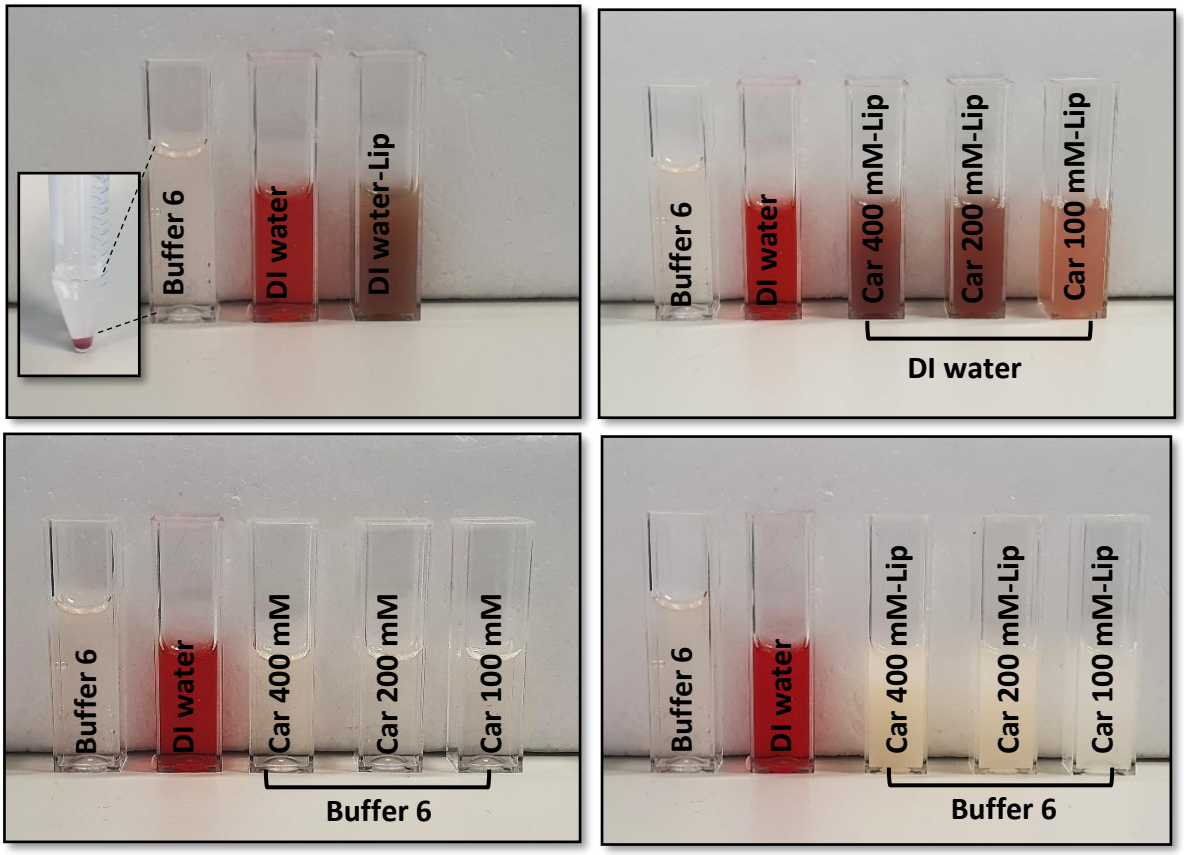

Figure 56. Carnosine effect on red blood cells. The 2% sheep blood erythrocyte suspension was washed with PBC and centrifuged. Then, the blood erythrocyte suspension was added to cuvettes containing carnosine concentrations free or loaded in liposomes (100, 200, and 400 mM) and cuvettes containing positive control of distilled water (red) and negative control of saline buffer (transparent). The resulting colour in each incubated and centrifuged mixture showed no cell membrane damage, except in the DI water samples.

1.2.2 MAD Nasal™ device optimisation and characterisation

The MAD Nasal™ Intranasal Mucosal Atomization Device from Teleflex is a safe and painless way to deliver medications. It is approved for human use in a simple, non-sterile, reliable and cost-effective delivery technique for rapid absorption across mucosal membranes into the bloodstream, avoiding first-pass metabolism (Corrigan, Wilson and Hampton, 2015; Rajagopalan et al., 2017). The device atomises the sprayed solution into a fine mist of liposomal micro-droplets 30–100 µl. Before the pilot animal experiment, the product was applied to rodent cadavers using a modified MAD Nasal™ device. The tip

of the device was modified by narrowing the spray to fit the diameter of the rodent nostril (Schulz et al., 2021). The driving pressures of the device were tested before and after modification. It was measured using Honeywell MPRLS. The sensor was connected between the device and a syringe using a coupling tee to measure the peak pressure required to drive the water or the liposome suspension through the spray device. The test was applied to water as a blank and liposomes loaded with carnosine 300 mM to represent the main experiment. The main experiment will be conducted using carnosine 300 mM loaded in liposomes made of the same formulation, which is the maximum carnosine that can be loaded. The resulting pressure was measured in triplicate. The average was close to 20 psi, which could be used for rat nasal delivery (Hoekman and Ho, 2011). No significant differences were observed between the original and modified devices (Figure 57). Also, preparing the product and preserving it as a suspension in the fridge suits the suggested treatment application by using the modified MAD Nasal Device (MAD110) containing a syringe with spray in the tip. The intranasal mucosal atomisation device from Teleflex is a safe and painless way to deliver medications that spray atomises drugs into a fine mist of particles 30–100 µL. This will target the olfactory area deep in the nose towards direct drug delivery to the brain tumour (MAD Nasal, 2014). The device was approved in the market for the self-application of complementary and alternative medicine by patients.

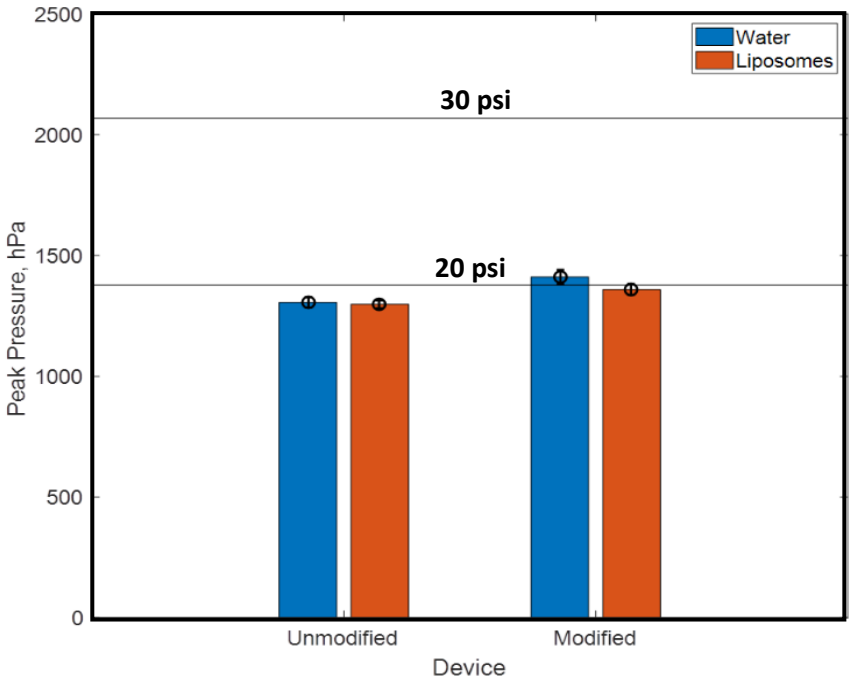

Figure 57. Comparison between applying water or liposomal solution using the original and modified MAD Nasal™ device. No significant difference was observed. The pressure of the device was about 20 psi.

1.2.3 Nasal cavity deposition testing on rodents (mice and rats)

Coomassie Brilliant blue (Sigma-Aldrich, St. Louis, MO), a triphenylmethane dye, was traced after intranasal administration to mice cadavers to test nasal cavity deposition (Hoekman and Ho, 2011). Each mouse received a dye solution (1 mg/mL) as a nasal instillation of 10 µl *via* a pipette into one

nostril. The modified MAD Nasal™ device was applied inside the other device in the supine position. Shortly after administration was complete (< 5 min), the skin was removed, and the tissues were examined to trace the dye localisation. Figure 56 shows a lateral view of the mouse nasal cavity. Spraying 10 µl of dye with the modified MAD Nasal™ device resulted in deposition on the olfactory epithelium area of the nasal cavity (the left naris). The dye was found primarily on the posterior two-thirds of the olfactory turbinates close to the cribriform plate region of the nasal cavity, which is linked to the brain cavity. There was a minor deposition on the respiratory epithelium near the centre of the nasal cavity. Administering 10 µl of dye per naris as nose drops resulted in the dye being entirely localised to the respiratory epithelium and on the olfactory epithelium, possibly partially (in the right naris) (Hoekman and Ho, 2011).

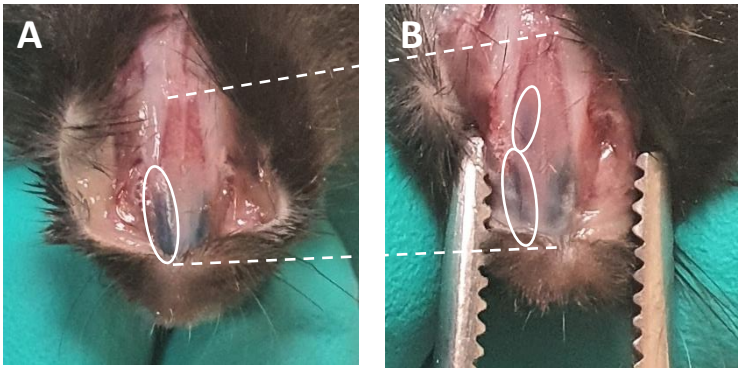

Figure 58. The lateral view of the mouse nasal cavity shows that (A) spraying 10 µl of dye by the modified MAD Nasal™ device resulted in deposition on the olfactory epithelium area of the nasal cavity (the left naris). The administering of 10 µl of the dye using the pipette resulted in localising the dye in the respiratory epithelium and partially in the olfactory epithelium (the right naris). (B) After 5 minutes, the dye coloured the posterior two-thirds of the olfactory turbinates on the left side.

MRI was used to determine whether the total desired volume was dispensed from the device to the olfactory area with each actuation. A study was performed on water, and various concentrations of gadolinium sulphate $Gd_2(SO_4)_3$ ranged between (10^{-2} and 10^{-9}) mol/L. Different concentrations were loaded inside capillary tubes, and MRI was used to compare the contrast at room temperature. The gadolinium sulphate 10^{-5} mol/L showed the brightest contrast (Figure 59). Since the gadolinium liposomal contrast agent has demonstrated higher particle-based T1 relaxivity *in vitro* (Ghaghanda et al., 2009), the latest solution has been loaded into the previously optimised formulation of liposomes. The images confirmed that gadolinium 10^{-5} mol/L loaded liposomes showed an optimum contrast, which can mimic the localisation of carnosine-loaded liposomes *ex vivo* (Figure 59). The conditions for preparing and preserving the product are suitable for the suggested treatment application by using the modified MAD Nasal Device (MAD110), which is approved in the market. The intranasal mucosal atomisation device from Teleflex is a safe and painless way to deliver medications that spray atomises

drugs into a fine mist of particles of 30–100 µL. This will target the olfactory area deep in the mouse nose toward direct drug delivery to the brain tumour (MAD Nasal, 2014).

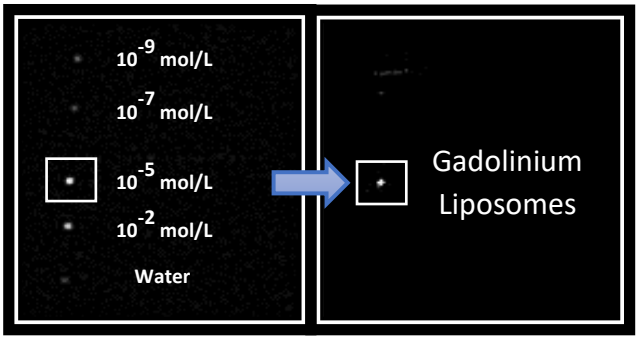

Figure 59. MRI images of a series of water and various gadolinium solutions show the best concentration of the gadolinium loaded inside liposomes and demonstrate a similar T1 contrast.

Rat heads were used as an *ex vivo* model to trace the localisation of the sprayed formulations. The heads were taped on a board, and an MR image was taken as a background to exclude the specific shade of gadolinium liposomes. The heads were categorised into two groups, and each group was treated using either a pipette or a modified MAD Nasal™ device. The horizontal section plane of the rat nasal cavity showed that the liposomes were located above the nostrils (dotted line) in the transitional respiratory nasal region in both application methods. However, the sprayed liposomes moved farther toward the olfactory bulb. The MRI scan was applied to obtain an image per 10 min for the cadaver at the same position. After 60 minutes, the gadolinium liposome contrast was observed to fade over time because the surrounding tissues were absorbing it, and the distribution of drops from pipettes did not reach near the olfactory area as much as the sprayed liposomes reached (Figure 60A). The dorsal view of the rat head and nasal cavity showed that the spray device spread the applied liposomal gadolinium. It appeared in a white shade to fill the nasal turbinates instead of staying in the respiratory septum area, where the cilia usually filtered the solution down to the digestive or respiratory systems (Figure 60B). The expected route that the liposomal treatment will take when the spray device is used, instead of the traditional drops of the pipette, was shown in this experiment.

It was shown in previous work that using upright vs. supine posture did not significantly affect 3H-2-PAM concentrations in different brain regions (Krishnan et al., 2017). Older animals with high weights required increased doses to achieve the same drug concentration throughout the brain compared to younger animals with lower weights. The bioavailability of the therapy in the olfactory bulbs was increased by the intranasal aerosol-propelled delivery device. Still, it did not reliably push the drug to other brain regions. More drug was delivered with the simple pipette administration in some brain regions (Krishnan et al., 2017).

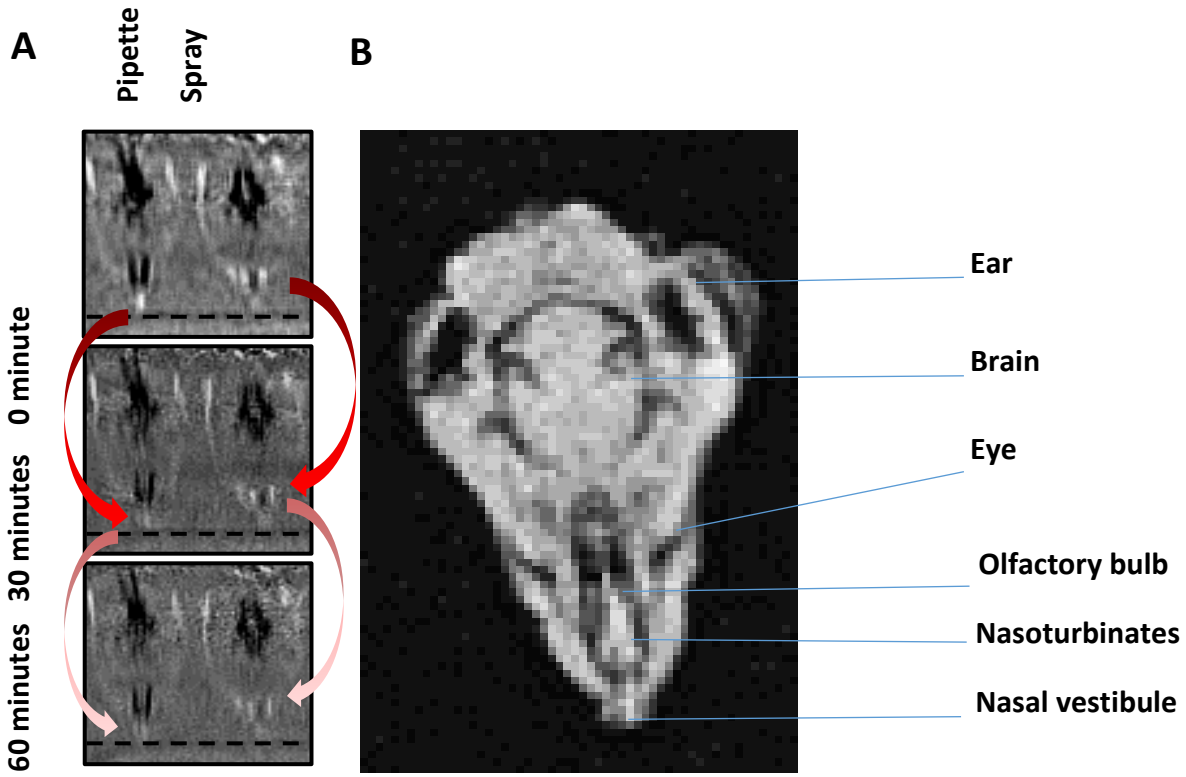

Figure 60. (A) *Ex vivo* MRI images of the rat brain after intranasal application for gadolinium 10^{-5} mol/L loaded liposomes using a pipette or the spray device. The location of injected gadolinium is shown by white shades. The signal showed a decrease in intensity over time. (B) The MRI image shows the rat head anatomy and the gadolinium-loaded liposomes localised in the Nasoturbinates close to the olfactory region.

1.3 Controlled release of carnosine from poly(lactic-co-glycolic acid) (PLGA) beads using nanomechanical magnetic trigger towards the treatment of Glioblastoma

1.3.1 The advantages of magnetic fields applications in drug delivery

Magnetic fields have found application in many clinical applications since they are not inherently damaging to the body, though therapies often lack selectivity and locality (Moore and Barnett, 2015). Current research strategies therefore often couple the application of magnetic fields with biochemical and physical properties of some additional agent to aid in overcoming these limitations (Duncan and Gaspar, 2011; Bamrungsap et al., 2012; Zhang et al., 2012; Quarta et al., 2019; Racca and Cauda, 2021). Specifically, the adoption of nanometre scale paramagnetic materials into such therapies enhanced the localisation effect, while also reduced the biotoxicity (Majewski and Thierry, 2008; Mahmoudi, Simchi, and Imani, 2010). The biomedical application of functionalised paramagnetic nanoparticles has stimulated much interest, specifically in NMMA by non-heating low-frequency alternating magnetic fields (f< 1 kHz). The nanoparticles act as mediators that localise and apply forces to target biomolecular

structures including enzymes, transport vesicles and cell organelles, without significant heating. Therefore, Nanomechanical magnetic activation (NMMA) demonstrates a biophysical platform for various therapies including the sustained and controlled release of therapeutics, without increasing toxicity (Golovin et al., 2021). Paramagnetic nanoparticles have been used as non-thermal contrast reagents in magnetic resonance imaging and as carriers in drug delivery by nanoscale modules (Cheng et al., 2016; Armenia et al., 2019). However, clusters of superparamagnetic nanoparticles have also been demonstrated to induce magnetic hyperthermia therapies when enshrouded with a polymer coating, impregnated with a drug (Liu et al., 2020; Caizer, 2020). Therefore, introducing paramagnetic nanoparticles to a living organism can result in both thermal and non-thermal therapies; simply by changing the frequency of the alternating magnetic field (Golovin et al., 2021). These combined properties have successfully been utilised to induce controlled drug release from a nanoscale vector (Hayashi et al., 2014; Hervault and Thanh, 2014).

In oncology, NMMA techniques have been employed for the deformation of molecular structures, where in, the paramagnetic nanoparticles are utilised to manipulate the sensitivity of tissue, cells, and vesicles (Hsieh and Nguyen, 2005; Golovin et al., 2021). The biochemical response to this mechano-transduction is cell death, or apoptosis (Rakesh K. Jain, Martin, and Stylianopoulos, 2014; Chen et al., 2019; Liu et al., 2020). It has, unfortunately, also been seen to stimulate tumour growth. This is attributed to the transmission of the forced movement from the rigid malignant cells to the soft surrounding healthy ones, leading to metastasis (Broders-Bondon et al., 2018). Functionalising the paramagnetic nanoparticles and utilising magnetic actuation to trigger mechanical forces offers an exciting strategy to remotely control the drug release from coupled magnetic materials (Diab et al., 2018). The contactless mechanical disruption of the polymer coating triggers the release of the therapeutic material which triggers an apoptosis cascade within the targeted cells (Broders-Bondon et al., 2018). This physical stimulation has been showing to be advantageous, compared to photon or thermal triggering, thanks to the possibility of achieving deep activation in a controllable and non-invasive manner for *in vivo* applications (Svenskaya et al., 2013).

The method of formulating carnosine with superparamagnetic nanorods of magnetite (Fe_3O_4) was reported towards the controlled release treatment at the targeted GBM cells by applying mild hyperthermia (Habra, et al., 2021). To improve the preliminary model, the conjugated nanorods and carnosine from our previous work were embedded in microbeads of poly(lactic-co-glycolic acid) (PLGA) as a potential magnetically triggered drug delivery device. PLGA is commonly used in the preparation of clinical drug delivery systems, specifically for drug molecules with short half-life protein structures, as the PLGA constructs have been showed to increase the bioavailability of the drugs (Brannon-Peppas, 1995, S. A. Hagan et al., 1996; Budama-kilinc et al., 2018). Traditional methods for using PLGA involve manual or mechanical agitation. However, such stresses are conducive to controlled uniformity across the system (Shah et al., 2008). Controlling both the structure and function

of polymeric drug delivery has been optimised using microfluidic method, *via* the flow-directed shear processing in a two-phase microfluidic reactor (Bains et al., 2017). In general, such microfluid techniques have been accepted as applicate scale-up strategies, namely, Factory-on-Chip techniques which achieved high throughput synthesis of micro products for industrial scale production (Han et al., 2017). PLGA microparticles have now been effectively produced by combining modern technologies of artificial intelligence and microfluidics which improves the efficiency and performance of the production (Damiati et al., 2020).

1.3.2 How the project is going to expand other groups recommendations

In this project, we describe a microfluidic double emulsification method that encapsulates and retains the dipeptide carnosine and IONRs within the polymeric microbeads. The encapsulate is a spherical protective wall material (bead) consisting of empty chambers in a stable emulsion. These sequential emulsifications enable highly efficient encapsulation with precisely tuneable beads size (10 μm) with rigid shells. The mechanical trigger embeds the carnosine into the surface of the IONRs if they were in the same space and only a mild hyperthermia trigger (40 ˚C) is needed for the release (Habra et al., 2021). However, if the carnosine and IONRs were in different beads, the mechanically induced spinning of the IONRs releases the carnosine from the beads instead of attaching it. This methodology can be further extended to encapsulate multiple drugs and manipulate the release depending on the application requirement. The aim, therefore, is to use the paramagnetic magnetic nanoparticles IONRs as a controlled trigger for the release and medical imaging. The rotating movement of the IONRs damages the structure of the shells in the beads to allow part of the carnosine treatment to spread in the targeted area. Thereby avoiding the need to subject the patient to multiple therapeutic injections and enabling the physician to trigger the non-invasive delivery of carnosine at the optimised time and dose. This drug delivery methodology has the potential to be described as an on-demand wireless personalised smart drug delivery system, which can be conducted inside a conventional MRI scanner.

1.3.3 PLGA beads preparation

Empty beads of PLGA were prepared by using a Dolomite microfluidic flow focus system. Continuous microscopic monitoring was applied during the double emulsification to observe the mixing of the water and PLGA phases inside the micromixer chip. Microscopic images were taken for the PLGA beads on a glass slide directly after the double emulsification. The larger PLGA beads (> 100 μm) were observed to shrink after around 5 minutes in the air, drying to less than 100 μm, with complete solvent evaporation occurring after an additional 5 minutes achieving a final size of the PLGA around 10 μm, as seen in figure 61. The LC-MS detected the encapsulation efficiency (EE% > 99%), and the loading efficiency (LE% = 33.4%).

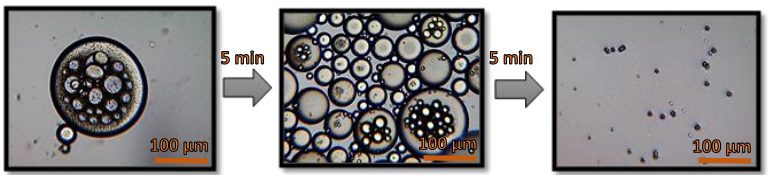

Figure 61. Microscopic images for PLGA beads after encapsulation and during evaporation.

1.3.4 PLGA beads characterisation and physio-chemical studies

FT-IR spectroscopy of the IONRs, L-carnosine, and PLGA empty beads (PLGA and PVA), resulted in characteristic IR vibrational peaks in the high-frequency region where the stretching vibration at 2162 cm^{-1} and 1643 cm^{-1} due to vibrational bending of carnosine imidazole (N–H),(Branham et al., 2011) stretching at 800 cm^{-1} from the IONR and the alkane (C-H) at 2200 cm^{-1},(Mohapatra et al., 2015) and a strong absorption peak at 1738 cm^{-1} from the carbonyl (C=O) group stretching for the loaded polymer beads (Schleich et al., 2013). These results provided evidence that the carnosine and IONRs were encapsulated with the PLGA, with the characteristic bands overlapped in the spectrum of the new drug delivery device (Figure 62).

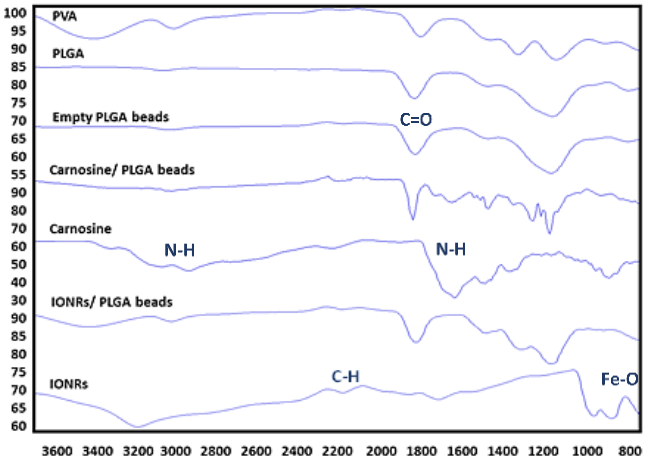

Figure 62. FT-IR spectra for PVA, PLGA, empty beads, L-carnosine (with/without PLGA), and IONRs (with/without PLGA).

Figure 61 shows the blank beads of 0.1% PLGA in organic phase with a sponge-like shape. Increasing the concentration of the PLGA to 1% in organic phase showed the morphology of tight PLGA beads with fewer holes on the walls. Rhodamine-B was used in 1% concentration to trace the aqueous phase which will facilitate later indication of carnosine during the carnosine encapsulation. A uniformity in water phase distribution was observed with the confocal images where the red small chambers like seeds with comparable size were evenly spread inside the PLGA beads. The microfluidic double emulsification using the microfluidic system was shown to be a highly reproducible method to synthesis uniform PLGA beads which ensures the uniformity of dosage form per sample (Damiati et al., 2020). Following the hydrothermal synthesis to produce IONRs of (86 ± 17 nm) length from chapter 2, (Habra

et al., 2021) the nanorods were encapsulated to obtain 0.1% PLGA microbeads. The mean final diameter of the dry IONR beads was (7.4 ± 2.3 µm) measured by SEM. The same method was applied to produce the carnosine beads. However, the LC-MS detection showed that carnosine leaked out of the beads instantly. Thus, the concentration of PLGA was changed to 1% with carnosine. The size of carnosine beads was (11.6 ± 7.0 µm). SEM/EDS for (carnosine & IONRs) loaded 1% PLGA beads proved the size shift of the beads to shells to be 10 times larger than the previous beads (~ 10 to 100 µm). All of them were open with fragile structures (Figure 63).

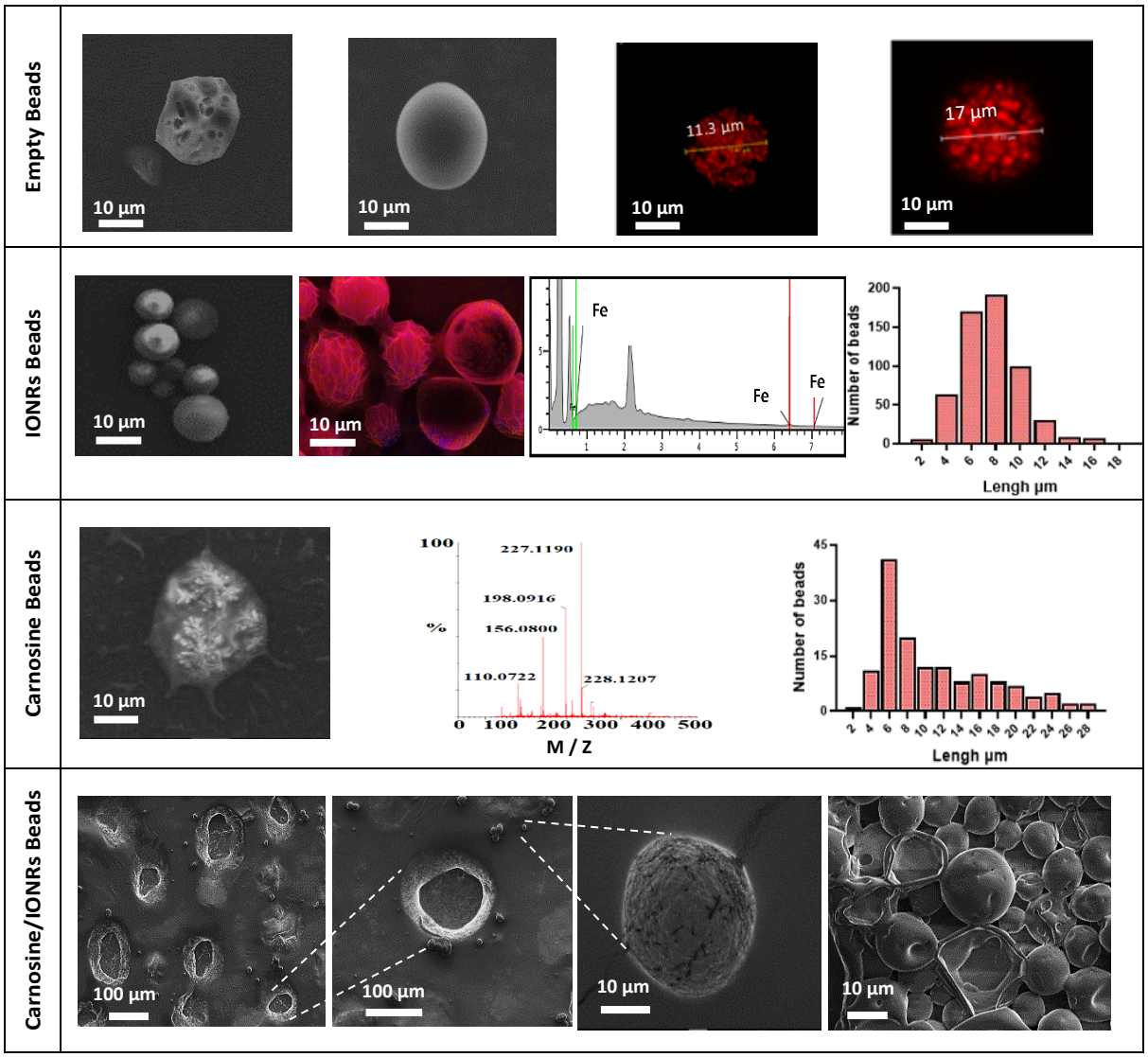

Figure 63. Empty Beads, SEM images compare the characterisation of empty (0.1%, 1% PLGA beads) and the uniform distribution of the water phase inside the beads. IONRs Beads, SEM images for IONRs loaded 0.1% PLGA beads, EDS mapping the blue colour of iron traces inside the red carbon colour of the PLGA, and the iron peaks confirm the images. The histogram refers to a mean diameter size of 7.4 ± 2.3 µm. Carnosine Beads, SEM images for carnosine loaded 1% PLGA beads showed the carnosine distribution and the MS spectrum identifies the peaks of carnosine pattern. The histogram refers to a mean diameter size of 11.6 ± 7.0 µm. Carnosine/IONRs Beads, SEM images for (carnosine & IONRs) loaded 1% PLGA beads. The size of the beads/shells shifts to 10 times larger than the previous beads.

It was evidenced that interstitial pressure, stiffness, and hyperproliferative pressure of fibrotic tumour enhance tumour growth development. Investing in new treatments or synergic adjuvants must be based on the inhibition of these tumorigenic mechanical (Broders-Bondon et al., 2018). Previously, 20 nm mitochondria-targeted zinc-doped iron oxide nano-cubes were designed as nano-spinners to exert mechanical forces under a rotating magnetic field to fight against cancer *via* targeting the mitochondria. The *in vitro* and *in vivo* applications showed damage to the cancer cells and reduced the brain tumour growth rate by the impact of the mechanical forces of the nano spinners on the cell adhesion, differentiation, migration, and death (Chen et al., 2019).

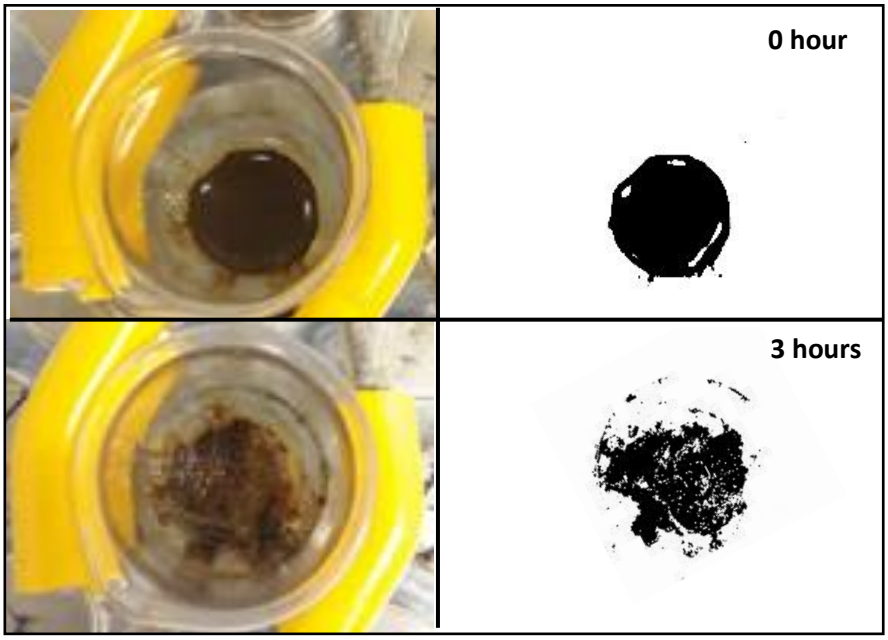

Figure 64. The effect of a rotating Halbach array on a suspension of nanorods embedded in agarose (2% w/v) over time. Masking the dark areas showed the difference before and after 3 hours of external magnetic rotation.

In this project, it was proven that IONRs with size of around 80 nm are not localised in the mitochondria which makes them safer as drug carriers. However, the same nanorods moved from the stiff tumour tissue to the soft healthy surrounding cells upon spinning them remotely by an external rotating magnetic field. A concentrated nano-rod suspension was placed in a premade hole inside a 2% agarose gel to mimic the movement of the nanorods over time as a result of an externally applied rotating magnetic field, applied in this case using a rotating Halbach array (NdFeB N45, Bunting, Berkhamsted UK). ImageJ was used to show only the dark areas representing the nanorods (Mohapatra et al., 2015). This showed a 2% increase, with an expansion of the perimeter of 25% after the application of the rotating magnetic field for 3 hours. Thus, the nanorods did not cluster or aggregate though they did cause disruption to the gel in which they were placed (Figure 64).

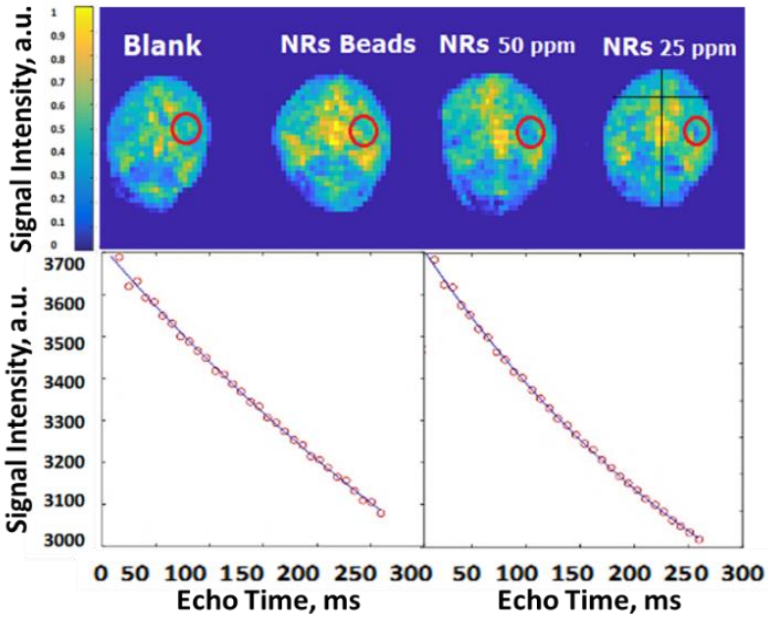

Figure 65. (A) *Ex vivo* MRI images of the mice brains injected with IONRs. The location of injected beads of IONRs or controls is shown by red circles. The colour codes the signal intensity which is proportional to the value of $T2^{eff}$ in ms. The signal is shown to decrease in intensity for the 50 ppm and 25 ppm areas confirming the presence of a negative contrast agent which is expected from the magnetic nanoparticles. (B) Comparative curves of the control (left) and IONRs beads (right) showed the drop in signal intensity as a function of echo time, with a steeper change in the case of free IONRs indicating a shorter $T2^{eff}$.

An *ex-vivo* study using 6 brains of sacrificed male mice showed that encapsulating the iron oxide nanorods inside PLGA microbeads ceased the spreading of the IONRs. After positioning the brain (2 mm lateral to the sagittal suture and 2 mm posterior to the coronal suture) 5 µL of IONRs suspensions (free/ encapsulated) were injected 3 mm deep using a neuro-syringe, then were compared with empty PLGA beads. The empty beads had no effect on the signal intensity of the MRI images, whilst the IONRs of 25 ppm and 50 ppm concentration showed a decrease in signal intensity. In comparison, the IONR beads of the same concentration showed less contrast. A further MRI analysis was undertaken simultaneously to evaluate this process by determining the effective spin lattice relaxation time constant ($T2^{eff}$) since the paramagnetic properties of the nanorods are known to shorten this value (Schleich et al., 2013). The coronal images were collected using the MRI system with multi echo imaging sequence. The echo time was 7.8 ms and 32 echo images were collected with a repetition time of 5000 ms. MATLAB (Mathworks, MA) was used to undertake pixelwise fitting of a monoexponentially function to the images to produce a $T2^{eff}$ map. The control empty beads $T2^{eff}$ (601 ms) was higher than the free IONRs $T2^{eff}$ (336 ms) (Figure 65). There is an observed decrease in the spin echo when the IONRs were inside the beads. However, the difference is not expected to be significant because the system is designed to enable free rotation of the IONR, resulting in both the shear and the contrast effects which will increase when they release from the beads.

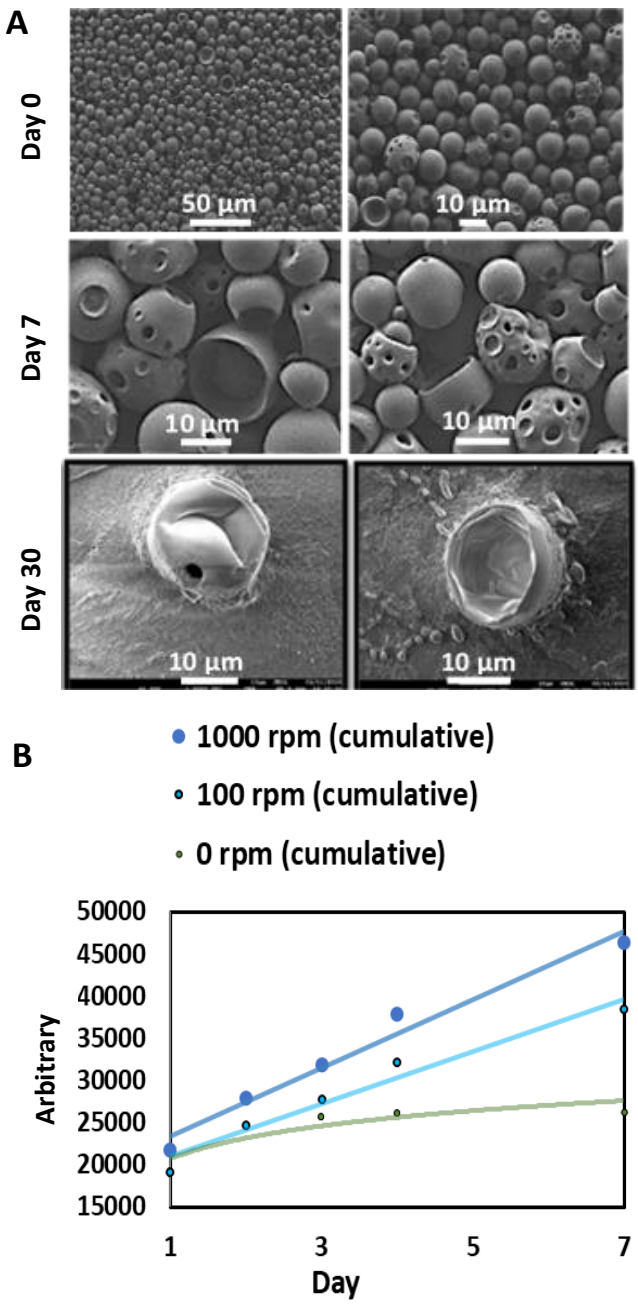

Figure 66. Membrane dialysis experiment. (A) SEM images show the PLGA beads in the beginning which had holes in the structure after a week and became completely empty after a month. (B) The LC-MS cumulative analysis for the released carnosine shows faster release from the beads which were exposed to the higher mechanical rotation.

For carnosine investigations, the sustained release simulation from PLGA beads was studied by performing a dialysis membrane experiment. The mechanical rotation was created by a magnetic stirrer bar rotating inside a semi-permeable membrane bag of (1–10 nm) pores contains the IONRs and carnosine loaded beads. With controlled speeds, the comparison was between 100 rpm which simulates human fluid dynamics and 1000 rpm which demonstrates the potential shear stress from the rotation of the IONRs (~ 80 nm) (Schneider, Rasband, and Eliceiri, 2012). The rotation of the IONRs (5 µg/mL)

produces both centrifugal and shear stress forces, much in the same way as the paddles of the described dissolution apparatus in the British Pharmacopoeia, dissolution testing monographs. Over a week of mechanical stirring, the SEM images showed the beads developing holes into the inner chambers which allowed the carnosine to release over time. The samples were retained for a month, then the beads were imaged 100% empty (Figure 66A). The IONRs were well tolerated by the U87 MG malignant and differentiated cells, and the tracking of the intracellular uptake showed their safety by using MTT assay and SEM imaging for track and trace them over time (Habra et al., 2021).

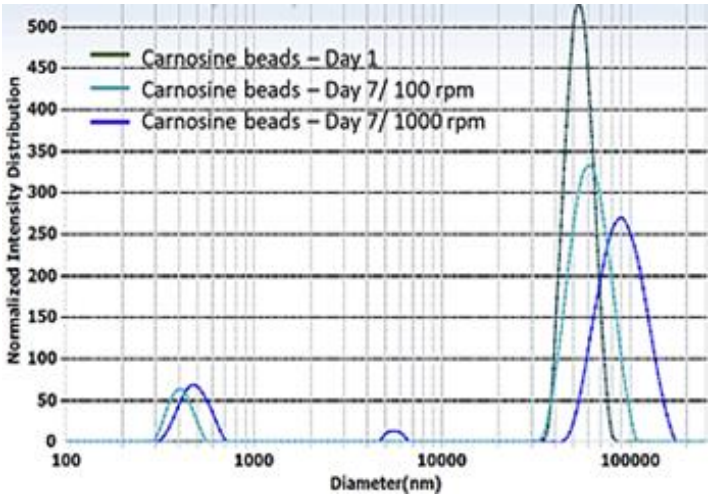

Figure 67. The DLS results of the normalised intensity distribution of the beads over a week with different stirring speeds.

The final component for the beads was either PLGA loaded with carnosine and the LC-MS was used for the assay, or PLGA loaded with iron oxide nanorods which were measured by the Inductively Coupled Plasma Mass Spectrometry (ICP-MS). The daily monitoring for the carnosine release by LC-MS showed that (50% w/w) of the total carnosine was released after 24 hours. Afterward, (10% w/w) of carnosine was released daily over a week (Figure 66B). The cumulative release of carnosine increased by (20% w/w) as a result of the mechanical forces applied by the rotating magnetic field. DLS measurements supported the change in the beads' diameters (Figure 67).

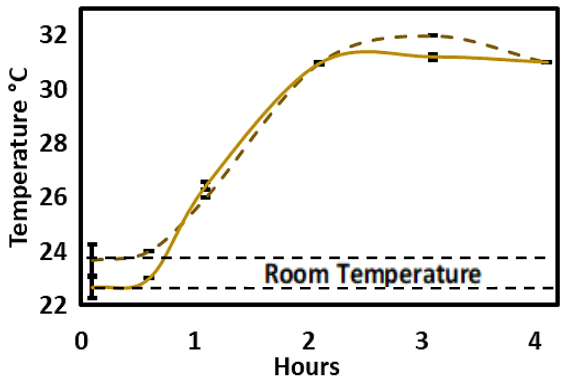

Figure 68. The temperature fluctuations for applying the rotating MF on __ water vs. _ _ PLGA beads.

Finally, to investigate the potential application of rotating magnetic fields for cancer treatment, we designed a combination formulation using carnosine loaded with IONRs to optimise a controlled delivery and targeted treatment. A schematic of the rotating magnetic system can be found in figure 69A supported the magneto-mechanical non-heating effect for a 1 Tesla rotating magnetic field during the first 30 minutes at 20 Hz (Cheng et al., 2016). To enhance the potential clinical uptake of this anti-cancer medical drug delivery device, PLGA-based carrier, and Fe_3O_4 SPIOs were targeted as a pre-approved FDA reagent for therapeutic applications. Micro-scale beads are predicted to circulate *in vivo* without aggregation while the submicron size of nanoparticles enables enhanced intracellular uptake (Verma et al., 2019). The carnosine was observed to instantly leach out of the beads due to its inherent smaller sizes and flexibility. A concentration of 1% PLGA was sufficient to retain the embedded carnosine and be released *via* the rotation of IONRs from the beads, while at 0.1% PLGA the dug was lost to the media without any stimuli. The preparation of the beads was reproducible by applying the same parameters of flow rate and pump pressure at room temperature.

Although the flow speed dominates directing the liquids towards creating a central stream for the inner phase, changing the hydrophobicity of the micromixer chip to match the outer phase of the emulsion was critical in each step (Figure 69B). The entrapped drug in a PLGA matrix releases at a sustained rate because of the degradation of the polymer which can be varied according to the block copolymer molecular weight and composition (Dinarvand et al., 2011). Each type of nano-shell (IONRs and carnosine) can be packaged in PLGA beads separately or as a mixture, before the second emulsification. Mixing the IONRs with the carnosine before the initial emulsion shows reduction in the detected carnosine over 3 hours (Figure 69B). The carnosine stays attached over time to the surface coating of the IONRs and retains until triggered by mild hyperthermia (40 ˚C) as the *in vitro* studies demonstrated (Habra et al., 2021). However, mixing the separate shells of carnosine and IONRs produces unstable beads, and both leak out during the evaporation step to get rid of the solvent after the synthesis of the beads. The drug release experiment using the 1 Tesla magnetic field as a trigger during 30 minutes at 20 Hz showed the trend of the release and monitoring the release by the IONRs by MR imaging could be the key for personalising the release according to the tumour response which has different reactions according to many variants such as the tumour location, size, and resistance.

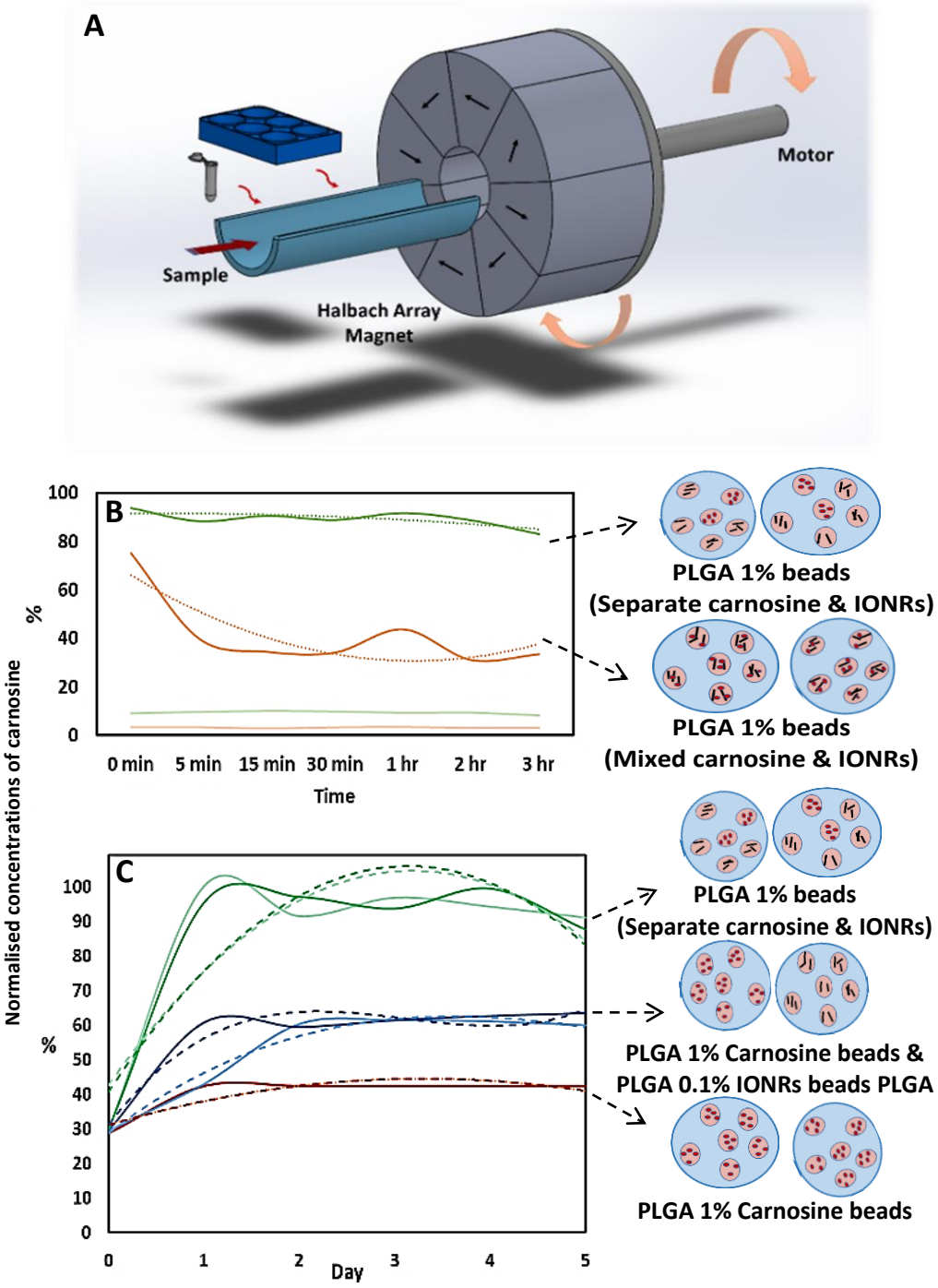

Figure 69. (A) Schematic illustration for the rotating magnet system designed for this application. The arrows indicate the direction of the magnetic field which produces an intense uniform magnetic field within their central air gap, and zero field outside. (B) LC-MS assay for the normalised concentrations of carnosine shows the advantage of using the hydrophobic chip (dark curves with high load of carnosine) and the hydrophilic chip (light curves with low load of carnosine) for the initial emulsification. (C) LC-MS assay for the normalised concentrations of carnosine shows the comparison between adding the encapsulated IONRs to the carnosine before or after the initial emulsification. Curves with light colours are for beads before the application of the magnetic field and the curves with dark colours are for after the application of the magnetic field. Red spheres are carnosine and black rods are IONRs. The dotted lines are trend lines fitted to the experimental data.

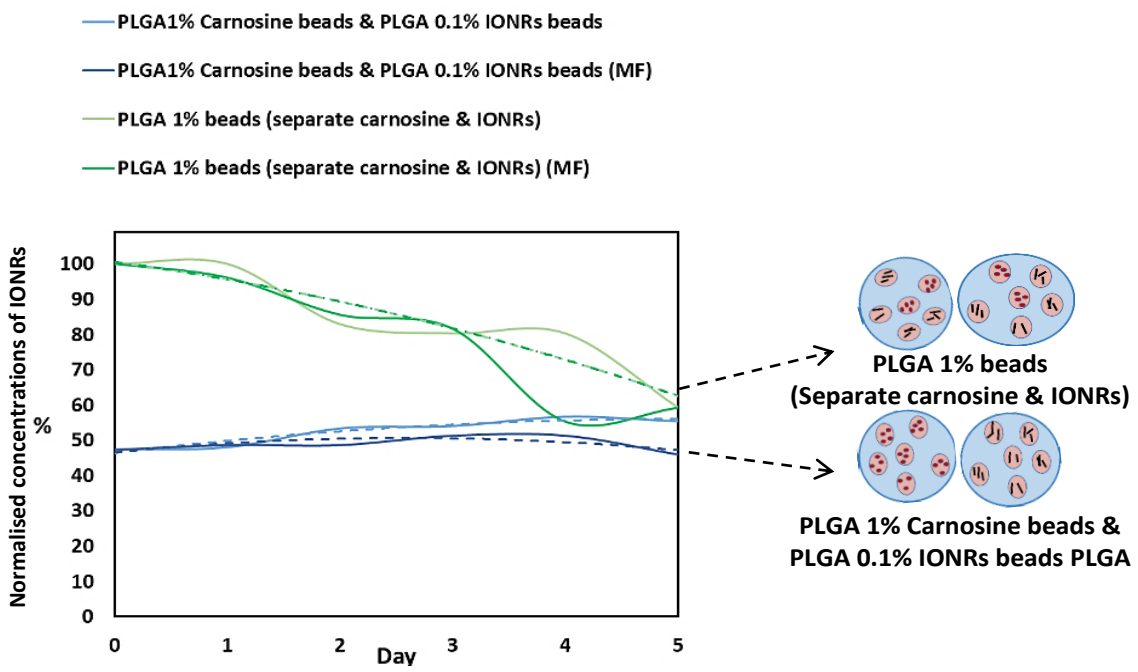

Figure 70. ICP assay for IONRs normalised concentrations shows the comparison between adding the encapsulated IONRs to the carnosine as seeds vs. beads. The decrease in the concentration is because of the attachment with the released carnosine over time. The dotted lines refer to the trend lines.

The ICP-MS assay supported the instantaneous release for the IONRs (Figure 70). The formulation of 1% PLGA carnosine beads and 0.1% PLGA IONRs beads found similar outcomes to the dialysis experiment by showing a surge in the total amount of carnosine when the IONRs were spun by the effect of 1 Tesla rotating magnetic field at 20 Hz for 30 minutes. Having the IONRs in the same vicinity with the carnosine attracted the carnosine out of the beads because of electric surface charge forces. However, applying the non-heating rotating magnetic field for 30 minutes increased the speed of carnosine release due to mechanical micro-deformation of the PLGA outer structure with the rotating nanoparticles. (Figure 69C). This degradation is an outside-in mechanical process, whereas *in vitro* inside-out degradation is thought to occur in PLGA microbeads as a result of the autocatalytic process (Zolnik and Burgess, 2008).

The comparison between the three previous formulations showed how changing any parameter may result in a critical change. However, these variables could always be utilised to produce several types of PLGA beads for controlled, delayed, or sustained release. Freeze drying the beads is crucial for long-term stability and storage conditions (4°C /ambient humidity) (Oster and Kissel, 2005; Astete and Sabliov, 2006; Andhariya et al., 2019). This keeps the product ready to be rehydrated with buffer or sterilised water at the time of use. However, zeta potential was measured before the sedimentation and showed that applying gentle vacuum drying induced the fragility of the beads which resulted in carnosine being released from the beads as waves over 15 days instead of the faster single initial burst because of the easy release of carnosine from the damaged structure of the beads (Figure 71).

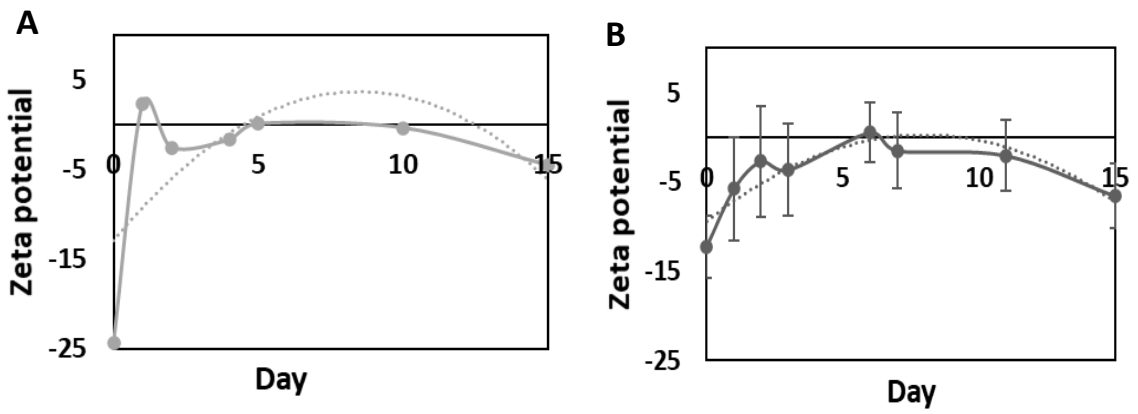

Figure 71. Zeta potential measurements for 15 days to compare the freeze frying effect on the stability profile. (A) Freeze drying the sample induced the initial release of carnosine, while (B) shows multiple waves for the released carnosine because of using vacuum oven. The dotted lines refer to the trend lines.

1.4 Conclusions

1.4.1 The potential use and limitations of liposome production by microfluidics

Carnosine exhibits anticancer activities through several mechanisms, but it is biodegraded by the carnosinase enzyme which hampered the *in vivo* efficacy. Microfluidic hydrodynamic flow focusing (MHFF) has been employed to encapsulate the carnosine and deliver it to the brain, but the reported system suffered from carnosine loading capacity less than the EC50 and the need for the mild hyperthermia (40 ˚C) as a trigger. Herein, we reported the development and optimisation of carnosine-loaded liposomal formulation using the MHFF technology. The loaded carnosine inside liposomes exhibited the robust formation of uniform dispersed liposomes with average diameter of (284.1 ± 91.1nm) with a low polydispersity index (<0.3) and excellent loading capacity of around 76.1 %. The liposomal suspension is a ready-to-use aqueous system stable when stored in fridge and safe to be applied intranasally when it is prepared in buffered solution. When co-administrated after the surgery or with chemo-drug, it has a potential of inhibiting the brain tumour growth non-invasively. The preliminary results suggest a significant potential of carnosine loaded liposomes for improving the nasal-to-brain therapy for hard-to-treat brain tumours. The micro-scale size of the liposomes and the mucoadhesive property will enhance the nasal bioavailability of carnosine for prolonged time. Also, due to the hydrophilic nature of the liposomes with phospholipid structure surrounding free carnosine, each released concentration will diffuse effectively through the olfactory route direct to the brain bypassing the BBB (Shah et al., 2021). The drug delivery system presented in this work is expected to offer the potential to be implanted into the post-surgical cavity and used as a complimentary treatment to improve the prognosis of this devastating disease. As such, future efforts should lead toward an *in vitro* animal model to demonstrate the potential clinical viability of this work and find the translation of this method to the industrial environment.

1.4.2 The controlled release of carnosine loaded PLGA beads

The product application is a non-invasive strategy of convection-enhanced delivery by direct injection and implementation inside the brain tumour tissues or after the surgery of tumour removal. The beads are not prepared for another route application such as intravenous. After applying the beads on U87MG cells, the beads showed attachment to the outer surface membrane of the monolayer cells due to the negative zeta potential. The cell membranes have an electrical potential across them, with the inside usually negative with respect to the outside. Thus, the beads stick to the outer surface, and it was not possible to remove them by washing with media or PBS after 24 hours. Bioerodible implants made up of polymeric materials have been discussed in the literature for over five decades. The ability to disperse drug molecules throughout thermally stable biodegradable polymers such as PLGA results in an active polymer matrix, which enabled a degree of control over this release profile while the polymers are metabolised by the body (Mundargi et al., 2008). However, clinical PLGA formulations are not yet widespread due to their low drug loading of hydrophilic small molecules, high initial burst release, and poor stability. Double-emulsion strategies, (Han et al., 2016) enable the synthesis of clinically viable *in-situ* swellable (carnosine or IONRs) loaded PLGA beads (~10 µm). The beads production is repeatedly and consistently performed using microfluidic hydrodynamic flow focusing systems enabling multiple emulsifications. The adoption of micromixer chips to such a device enabled the hydrophobic materials to be encapsulated inside shells of PLGA, then packaged by the second emulsification into PLGA microbeads.

Chapter 5: Experimental

All chemicals supplied by Sigma-Aldrich, analytical grade and used without further purification unless stated otherwise.

1.5 Synthesis of iron oxide nanorods

Aqueous branched polyethyleneimine BPEI (1 mL, 3000-6000 Mw, 50% aq) was dissolved in distilled water (80 mL) and transferred into a PTFE-lined 4748 Parr acid digestion vessel. Iron (II) sulphate heptahydrate (0.556 g, 2.0 mmol) and anhydrous iron (III) chloride (0.649 g, 4 mmol) were then added to the polymer solution and flowed by cyclohexane (16 mL). The reaction was gently stirred at room temperature until the iron salts were fully dissolved, with the cyclohexane layer helping to prevent unwanted oxidation. The stirring rate was then increased (900 rpm) and ethylene diamine (12 mL) was immediately added before sealing the reaction vessel. The reaction was then heated (120 ˚C) with stirring (900 rpm) for 20 hours. On cooling and pressure equalisations, the magnetite product was separated using a strong hand magnet and washed with dry dimethyl formamide (3 x 20 mL), before being stored as a suspension in dimethyl formamide.

1.6 Surface coating towards water dispersible colloid

The suspended iron oxide nanorods (120 mg / 10 mL) were transferred to a dry double-necked round bottom flask before the addition of branched polyethyleneimine (BPEI) (1.2 mL). The reaction mixture was stirred (1000 rpm) and heated (70 ˚C) overnight under a nitrogen atmosphere. The final product was separated strong magnet (0.5 Tesla) and washed with DMF (3 x 30 mL) thoroughly to remove the free PEI. The polymer coating was then protonated *via* the addition of HCl (6 M, 0.3 mL) resulting in an overall pH of 3. The coated nanorods were then separated *via* ultra-centrifugation (15 minutes, 15000 RPM) and stored under nitrogen as a dry powder. The synthesis yield is (84.4 ± 5.5) % with a coating ratio of (13.4 ± 2.3) % surrounding Iron Oxide Nano Rods (IONRs) of (85.9 ± 17.1) nm length.

1.7 Characterisation

1.7.1 General information

The morphology of PEI-coated Fe_3O_4 nanorods was characterised by scanning electron microscopy/ energy dispersive X-ray spectroscopy (SEM-EDS, Jeol JSM-7100f) integrated with Aztec software. Also, the dimensions were obtained by transmission electronic microscopy (TEM, JEM 2100, JEOL Ltd., Tokyo, Japan) at 200 kV followed by analysis using ImageJ software. The crystalline structure of the coated NRs was measured by powder X-ray diffraction (X'Pert PRO, PANalytical) generating Cu Kα radiation at a wavelength of 1.54 Å and analysed by high score software. Infra-red spectra were

recorded using the Infrared (FT-IR) spectrometer (PerkinElmer, UK). The thermogravimetric was carried out using a thermogravimetric analyser (TGA 4000, PerkinElmer, UK) in tandem with a GC-MS system (GC Clarus 580-MS Clarus SQ 8S, PerkinElmer, UK). To study the suspension stability profile, NanoPlus (Micromeritics, UK) was used to measure the dynamic light scattering (DLS) of the hydrodynamic diameter size and zeta potential for the surface charge.

1.7.2 SEM-EDS

EM-EDS were integrated to use electrons for imaging while the X-rays for characteristic chemical information of the iron oxide nanorods. SEM-EDS (Jeol JSM-7100f) device was used to identify the dried BPEI coated IONRs on a copper grid or the fixed cells on a plastic slip. Each sample was attached to a carbon tape on an aluminium stub (13 mm), then sputter coated with 5 nm conductive material (gold). EDS spectra were processed to localise the nanorods and analyse different elements like carbon, oxygen, and iron ions by Aztec software (Oxford Instruments).

1.7.3 TEM

TEM was used to determine the morphology and nanorods dimensions. One drop of the diluted BPEI coated IONRs colloid was placed on a formvar carbon-coated copper grid (300 mesh), then left to air dry and visualised using TEM (JEM 2100, JEOL Ltd., Tokyo, Japan) at 200 kV. The average dimensions with the standard deviation were determined by measuring the length, width, depth, and hypotenuse of rods from many images.

1.7.4 FT-IR

FT-IR spectra were acquired by spectrometer (PerkinElmer, UK) on the dry fine powder compounds or a drop of the suspensions after checking a blank background.

1.7.5 XRD

The crystalline structure of the iron oxide nanorods powder was analysed by high-score software after obtaining the diffractograms by the x-ray diffractometer (X'Pert PRO, PANalytical). The device is provided by a Cu Kα radiation source (λ=1.5406) and scans at 30 mA, 40 kV in slow mode over a range of (10 – 70, 2θ).

1.7.6 TGA-GC-MS

The thermogravimetric analyser (TGA 4000, PerkinElmer, UK) in tandem with a gas chromatography-mass spectroscopy GC-MS system (GC Clarus 580-MS Clarus SQ 8S, PerkinElmer, UK). The dry BPEI coated IONRs powder bare or coated with PEI was weighed in platin crucible after subtracting the crucible weigh. The gradual temperature was applied to start from 50 to 800 ˚C. The loss of weight

reflected the identification and quantification of the coating material. Carnosine alone or as the final surface coat was characterised using the same method.

1.7.7 DLS

DLS (Nanoplus, Particulate Systems) was used to measure the hydrodynamic diameter and zeta potential of the surface of the BPEI-coated IONRs. The suspension with final concertation of 100 µg/mL in distilled water was prepared in neutral distilled water and under acidic pH 3 conditions by adding a drop of HCl 1M. Each measurement consists of 60 accumulations repeated in triplicates and then averaged to minimise the error. For surface charge measurement, the zeta quartz cell was filled with the diluted suspension and after checking the optimum density for starting the test, the zeta potential was obtained in triplicate.

1.8 Inductively coupled plasma mass spectrometry (ICP-MS)

The levels of iron were determined by ICP-MS using a PerkinElmer NexION 1000 ICP-MS instrument (Waltham, MA, USA). Analysis was performed with standard calibration from Certipur® ICP (Merck, Watford, UK) Single-Element standards of iron. The sample was added to concentrated nitric acid and chloric acid and left overnight. The samples were filtered with a 0.2µm membrane syringe filter before being diluted with Deionized water ready for ICP-MS analysis. Standards were prepared in dilute ultrapure nitric acid (1%) ranging between 10, 20, 50, 100, 250, 500, 750 and 1000 ppb. Data were obtained as ppb.

1.9 Magnetic resonance imaging (MRI)

MRI measurements were performed at room temperature and used to measure T2 time. To investigate the correlation between relaxivity and sedimentation of the BPEI coated IONRs. Iron oxide nanorods of concentrations (50 µg/mL) were added to each solution in a 96-well plate. Samples were measured three times in triplicate and the results were averaged at the first hour and then after 48 hours. Images were processed using ImageJ software with a sedimentation plugin Installed. magnetic properties of the NRs were recorded by a 1.5 T whole-body MRI system (Avanti, Siemens, Germany) applied on a 2 mm thickness phantom.

1.10 Rotating magnet device

The rotating magnetic field station was built using a NdFeB Halbach Array magnet (Bunting Magnetics Europe Ltd., Hertfordshire, UK), which produces a uniform 1 Tesla magnetic field diametrically across the central air gap with a diameter of 3 cm. The magnet was mounted on a rotating motor to control its rotation to 200 RPM and the tested material was placed inside the central air gap inside the Eppendorf tube or x well slid-based tissue culture vessels by SARSTEDT AG & Co. KG. This rotating magnet

could be used for *in vitro* and *in vivo* experiments. Measurement of hyperthermia was conducted with FLIR C2 thermal camera. The experiments were performed with complete media (Opti-MEM+ FBS) with control to observe the changes during the duration of the experiment timeframe (30 minutes).

1.11 Preparation of poly lactic co glycolic acid (PLGA) microbeads

Using the microfluidic hydrodynamic flow focusing Dolomite system, direct powder encapsulation for the fine powder was applied. The powder was suspended uniformly through PLGA solution in acetone and the suspension was kept agitated throughout the encapsulation process. The powder could not pass through the filter placed on the tip of the tube of the Fluika pump. Thus, this method failed. In the case of carnosine or NRs, both are only solubilised in water. A multiple emulsion microfluidic method was required. The material was dissolved in 1% PVA solution and emulsified with PLGA dissolved in Dichloromethane (DCM.) Using a large droplet hydrophobic microfluidic chip (100 µm) seeds of approximately 2 µm diameter were created. This primary emulsion was then transferred to a second junction on the same chip, or to another larger hydrophilic chip (100 µm) where the second emulsification with 1% PVA solution was proceeded. PLGA beads were dried by gentle rotating for 2 hours. The PLGA beads were purified by applying three cycles of washing with sterilised water and centrifugation (10,000 rpm for 5 minutes), then lyophilised. The encapsulation yield resulting from this process typically did not exceed 5%. Trying the double emulsification using one droplet chip was like using two connected chips. Connecting micromixer chips (hydrophobic/ hydrophilic) or adding higher pressure using an advanced pump increased the speed but did not affect the yield significantly. During the primary step, the extra aqueous solution floated on the surface of the emulsion. Over 90% yield was obtained by recycling the floating layer during the first emulsification and using the bottom layer (seeds) for the second emulsification. That was done directly using a syringe with a cannulation needle, or by a separation funnel. The first emulsification was two times faster. In the future, trying to link the small droplet (hydrophobic) chip with the large droplet (hydrophilic) chip and using three advanced pumps may achieve the same yield according to Dolomite microfluidics company.

1.12 Dialysis membrane tubing

The sustained release simulation for carnosine was mimicked by applying the dialysis membrane experiment. Dialysis Visking tubing contains (1–10 nm) pores in diameter and is semi-permeable. A dialysis tubing was filled with different carnosine; free or loaded coated IONRs and suspended in a beaker of water under controlled conditions (0, 100, and 1000 RPM at 37 °C). Samples were collected each hour and the assay was performed using a SCIEX TripleTOF 5600^{+} system.

1.13 Liquid chromatography- mass spectrum (LC-MS)

Positive ion mass spectra were acquired with direct infusion for optimisation and a hyphenated LC system. For quantification, a standard curve of carnosine was prepared from concentrations (1.0, 2.0, 5.0, 10.0, 15.0 µM). The standards and samples mixed with water were introduced into the source at a flow rate of 5 µL min^{-1}. LC conditions were the following: The separation was performed on Eksigent ekspert nanoLC 425 system ACE AQ column (0.5 x 150 mm, 3 µm), ACE chromatography. The mobile phase is composed of MS-grade water with 0.1% formic acid (solvent A) and acetonitrile with 0.1% formic acid (solvent B), Merck, UK. The standardised gradient elution program in LC separation was: 0 min, 1% B; 1 min, 1% B; 3 min, 50% B; 6 min, 90% B; 9 min, 90% B; 10 min 1% B re-equilibrated for 3 minutes. To identify the transitions of carnosine, a full scan of MS/MS was performed by fragmenting the precursor ion (m/z 227.11) of carnosine at a fixed collision energy of 25 V, de-clustering potential 80. The transitions were acquired in the mass range of 100 to 300 m/z. The column temperature was controlled at 45 °C, and the sample chamber temperature was 8 °C. The injected volume was 2.0 µL. The ion spray voltage was fixed at 5.5 kV, Gas 1 12, Gas 2 0, using a Duo spray source and 50 µm electrode. Data were analysed using MultiQuant software 3.0.3 (SCIEX).

1.14 Quantitative estimation of carnosine by bicinchoninic acid (BCA)

Pierce™ BCA protein assay kit was used to perform carnosine assay within the range (10 to 100 mM). According to the company instructions, the working reagent WR was prepared to mix 50 parts of BCA Reagent A with 1 part of BCA Reagent B (50:1, Reagent A: B). 2.0 mL of the WR was pipetted to each tube. 0.1 mL of each standard and unknown sample was added to a test tube and mixed well, then cover and incubate in tubes at 37 °C for 30 minutes. Cool all tubes to room temperature. The spectrophotometer was set to a fixed wavelength of 562 nm. The UV-Vis instrument was zeroed by a cuvette filled only with water as a blank, then the absorbance of all the samples was measured within 10 minutes. The standard curve was plotted using the average blank corrected 562 nm measurement for each BSA standard, then the curve was used to determine the carnosine concentration of each unknown sample.

1.15 Cell studies

1.15.1 Cell culture

The human glioblastoma U87 MG-Red-FLuc (Bioware Brite, PerkinElmer, USA) was the authorised cell line in all bio experiments. These cells were incubated in Opti-MEM Reduced Serum Medium (Gibco™, Thermo Fisher Scientific, UK) culture medium, supplemented with fetal bovine serum up to 10%. The antibiotic puromycin (Gibco®, Thermo Fisher Scientific, UK) was added after the initial thaw at 2 µg/mL. The incubation was at 37 ˚C in a humidified atmosphere containing 5% CO_2.

1.15.2 Cell viability assay by tetrazolium dye (MTT)

The cell viabilities were assessed by the MTT test. U87 MG were seeded in 96-well plates with a seeding density of 4000 cells per well in 200 µL growth media. The cells were left for adherence (18 hours) before treatment. Media were then gently aspirated and replaced with different concentrations of carnosine dissolved in media. The BPEI-coated IONRs were sterilised by filtration through a 0.22 µM syringe filter, and concentrations of iron oxide (0, 1, 5, 10 µg/mL) were tested in three replicates using three passages. After treatment durations of 48 hours, 20 µL of MTT solution 3-(4,5-dimethylthiazol-2-yl)-2,5- diphenyltetrazolium bromide (0.5 mg/mL in Phosphate Buffer Solution (PBS) Sigma Aldrich) were added per well. Cells were incubated at 37 ˚C for 2 hours, then the media solution was gently aspirated and replaced with 100 mL dimethyl sulfoxide (DMSO). The plate was wrapped with tin foil and left on the shaker for 10 minutes. The plate reader (Clariostar, BMG LABTECH) was used to read the absorbance at 570 nm.

1.15.3 Cell cytotoxicity assay by lactate dehydrogenase (LDH)

Promega CytoTox 96® assay kit was used for the quantitative measures of lactate dehydrogenase. The cytosolic enzyme which was released upon cell lysis (necrosis) resulted in the amount of colour formed proportionally to the number of the lysed cells. 96-well assay plates were set up containing cells in the culture medium. Wells for the No-Cell/ Vehicle-Only Cells/ Maximum LDH Release controls were prepared. Test compounds and vehicle controls were added to appropriate wells, so the final volume is 100–150 µL in each well. The cells were incubated at 37 °C for the desired test exposure period. The positive control wells were set for 45 minutes before adding CytoTox 96® Reagent. 50 µL aliquots from all test and control wells were transferred to a fresh 96-well flat clear bottom plate. 50 µL of the CytoTox 96® reagent was added to each sample aliquot. The plate was covered with foil to be protected from light during the incubation for 30 minutes at room temperature. 50 µL of Stop Solution was added to each well of the 96-well plate. Any large bubbles were popped using a syringe needle and the absorbance at 490 nm was recorded within 1 hour after adding the Stop Solution.

1.15.4 Live cell imaging (Incucyte® system)

1.15.4.1 Proliferation and cytotoxicity

All studies were observed on U87 MG cells using the real-time live cell analysis after applying the treatment of different carnosine concentrations. For proliferation and cytotoxicity experiments, cells were seeded in a 96-well plate at a density of 4000 cells per well and left for 18 hours for adherence. Concentrations of carnosine (0, 10, 15, 25, 100 mM) were added in the presence of Incucyte® Cytotox red for counting dead cells (250 nM, Essen Bioscience). The cyanine nucleic acid dye permeated cells with compromised cell membranes. Using the Incucyte® live cell analysis system (Essen in each well, with ×10 objective lenses), images were snapped every three hours inside an incubator over 48 hours.

1.15.4.2 Migration and invasion

The ratio of proliferation phase, percentage of the red dye and cytotoxicity levels were calculated using the integrated Incucyte® standard software. For the migration and invasion tests, cells were seeded in a 96-well plate at a density of 10^4 cells per well and left for 18 hours for adherence. Treatment of carnosine (0, 50, 100, 150, 200 mM) was added following the optimised protocol from the Incucyte® scratch wound assay (Essen BioScience, Sartorius). The basement matrix of Matrigel for 3-Dimensional (3D) culture was prepared as reported in Corning Protocol guidelines. The migration test was repeated using mitomycin C (10 µg/mL, Sigma-Aldrich) added after cell seeding and settling, an hour before the final carnosine treatment. Cells viability by Trypan blue exclusion test and adherence by comparative counting experiments were conducted to assess the mitomycin C effect on interaction with carnosine before obtaining the proliferation Incucyte® phase images. The percentage of relative wound density and wound width were calculated using the integrated Incucyte® wound scratch software.

1.15.5 Uptake and localisation (SEM, TEM)

U87 MG cells were grown at a density of 4000 cells/well on coverslips using 6-well plates, then treated with BPEI coated IONRs 5 µm/mL or carnosine 25 µM and incubated for 24 hours at 37v ˚C and 5% CO_2. The media were aspirated, and the cell monolayer was washed with HEPES buffer followed by adding 4% paraformaldehyde for 10 minutes. Cells were then washed three times with HEPES and dehydrated in graded alcohol solutions of (50%, 60%, 70%, 80%, 90%, and 100% ethanol) for five minutes each. The slips were coated with gold (5 nm) using a sputter coater (Q150R ES, Quorum), then imaged by SEM (JEOL, JSM-7100f) with probe current (10 mA) and accelerating voltage (10 kV). By energy-dispersive X-ray spectroscopy (EDS), the spectrum was collected using Aztec software (Oxford Instruments).

For TEM imaging, cell fixation steps were applied. Double strength of fixative (6% glutaraldehyde in 0.2 M phosphate buffer pH 7.4 buffer) was added to complete growth media at a ratio of 1:1. The previously rinsed cells in a 96-well plate were subjected to a glutaraldehyde-media solution at normal growth conditions (37 ˚C, 5% CO_2). After 1 hour, the cells were gently washed with 1 mL of 0.2 M phosphate buffer pH 7.4 buffer three times. After 1 and 4 hours, the fixed cell monolayers were aspirated cautiously, then transferred to 5 mL centrifuge tubes and covered with an excess of phosphate buffer to be kept at 4 ˚C waiting overnight for sedimentation. The resin was prepared by mixing 25 mL Araldite CY212 resin, 15 mL Agar 100 resin, and 55 mL DDAS. Then 2 ml of Dibutyl phthalate and 1.5 mL of DMP 30 were blended with the resin mix. The intensive stirring continued until no striations were observed in the final combination. Finally, the cells were embedded with a mixture of resin: propylene oxide at 1:3 v/v ratio for 2 hours, followed by overnight 1:1 v/v ratio resin: propylene oxide. The next day, the resin was completely replaced with fresh resin utilising a new vial and left for 3 hours. Meanwhile, the cells were dehydrated by a series of ethanol (50%, 70%, 90%, and 100% ethanol) for

10 minutes. Osmium tetroxide has been added to produce excellent fixation of the cytoplasm, then 100% of propylene oxide was used twice for 10 minutes. Finally, the resin was added to the cell to polymerise by ex-posing to 60 ˚C for 3 days. Resin blocks were sectioned by the microtome with a diamond knife attached to a boat which was filled with DI water. The thickness of each slice was adjusted to 70 nm. Each section was mounted on a formvar film over copper TEM grid (200 mesh) and left for air drying. The images were obtained by TEM (JEM 2100, JEOL Ltd., Tokyo, Japan) with accelerating voltage (80 kV).

1.15.6 U87 MG cell differentiation

U87 MG cell line was differentiated by growing them in serum-free medium supplemented with dibutyryl cyclic adenosine monophosphate (dbcAMP; 0.3 mM) and B27 Supplement (1% v/v).

1.15.7 Flow cytometry analysis for cell life cycle by DNA staining (Hycult biotech)

Cell culture for three passages of U87 MG cell line were prepared to reach a density of (1 to 10) x 10^5. A confluent flask of cells was detached by trypsin and then 1 million cells were placed in a polystyrene flow cytometry tube, cells were washed with 2 mL of PBS by pipetting up and down to get a single cell suspension. The cells were spun at 100 g (5000 RPM) for 5 minutes and the supernatant was tipped off. Cells were re-suspended in 300 µL of PBS and fixed by placing the tube s on ice, then 700 µL of ice-cold 70% ethanol was added, and tubes were stored at -20 ˚C for 20 minutes. The ethanol was discarded, and the cells were washed twice with PBA (PBS/ BSA 0.1 % / Azide 0.05%) and spun down at 100 g (5000 RPM) for 5 minutes. The supernatant was poured, and the cells were resuspended in 1 ml PBA, then 10 µL of (10 mg/ mL) Rnase solution and 20 µL of (2.5 mg/ mL) propidium iodide solution were added and immediately incubated for 10 minutes at 37 ºC. The prepared mixture was analysed on a Gallios flow cytometer (Beckman Coulter, Indianapolis, USA) and data analysis was performed using Kaluza software (Beckman Coulter, Indianapolis, USA). The tubes were placed on ice and kept from light during the analysis. The fluorescence was detected in fl4 detectors because DNA fluorescence is emitted at 600 to 700 nm.

1.15.8 The controlled release of (NRs/carnosine) synergism (MTT)

MTT test was the index of cell viability. U87 MG were seeded and left to adhere for 18 hours as previous cell viability test. Media were then gently aspirated and replaced with carnosine (25 µM). The BPEI coated IONRs controls of (2.5, 5 µM) were prepared. Two sets of treatments were prepared by adding each of the BPEI coated IONRs for a row of (media/ carnosine) wells separately and repeated the same steps instantaneously on three plates. A plate was incubated for 3 hours at 40 ˚C and another plate for 5 hours at 40 ˚C, then each was moved to the normal growth conditions (37 ˚C, 5% CO_2) where the third plate was incubated. After an overall treatment duration of 48 hours, an MTT test was completed to obtain the absorbance. A similar test was applied on different plates after changing the order of

treatment addition in the final two mixtures by using vortixing them for 1 minute before adding the mixture to the media. Premixing allows the same concentration of carnosine to be embedded in the branches of two PEI concentrations as evidenced in the results of the experiment 1.3.3 in chapter 3.

1.16 Spheroid modelling

The human glioblastoma U87 MG-Red-FLuc (Bioware Brite, PerkinElmer, Waltham, Massachusetts, USA) was the used cell line in all experiments. These cells were incubated in Opti-MEM Reduced Serum Medium (Gibco™, Thermo Fisher Scientific, Waltham, Massachusetts, USA) culture medium, supplemented with fetal bovine serum up to 10%. The antibiotic puromycin (Gibco®, Thermo Fisher Scientific Waltham, Massachusetts, USA) was added after the initial thaw at 2 µg/mL. The incubation was at 37 ˚C in a humidified atmosphere containing 5% CO_2. Other cell lines were cultured in their specific media by following the same protocol outlines. The human Glioblastoma SEBTA-027 (Recurrent Glioblastoma multiforme (GBM) cell line derived from the right parieto-occipital region of a 59-year-old female) and SF188 (GBM cell line derived from an 8-year-old male) were cultured in Gibco™ Dulbecco Modified Eagle Medium (DMEM) high glucose, GlutaMAX™ Supplement, and 10% fetal calf serum (Gibco™, Thermo Fisher Scientific, Waltham, Massachusetts, USA). Both cell lines were a generous gift from the University of Portsmouth, neuro-oncology group. The human Prostate cancer DU145, HTB-81™ (American Type Culture Collection ATCC, Virginia, USA) were cultured in Eagle's minimum essential medium modified to contain Earle's Balanced Salt Solution, non-essential amino acids, 2 mM L-glutamine, 1 mM sodium pyruvate, and 10% fetal calf serum (BioWhittaker® Medium EMEM Cell Culture Media, Lonza, Maryland, USA), and the murine prostate cancer TRAMP-C1 (C57Bl/6 mice cells which are derived from prostate adenocarcinoma cells from TRAMP mice) were cultured in DMEM with 4.5 g/L Glucose with L-Glutamine with sodium pyruvate, and 10% fetal calf serum (DMEM 4.5 g/L glucose w/L-Gln w/ sodium pyruvate, Lonza, Maryland, USA). This cell line was provided by Matteo Bellone (University of Milan, Milan, Italy).

1.16.1 The protocol of spheroids generation

- A volume of 50 µL of anti-adherence rinsing solution (STEMCELL Technologies, Cambridge, UK) was added to each well of a 96-well round-bottom hydrophobic tissue culture plate with a growth surface for suspension (Green code: 83.3925.500, Sarstedt, Nümbrecht, Germany).
- After 15 minutes, the solution was discarded then each well was washed with 50 µl of serum-free media.
- The cells were grown as a monolayer and when the cells reached 70–80% confluence, they were sub-cultured using 0.05% Trypsin−0.53 mM EDTA (Sigma-Aldrich, St. Louis, Missouri, USA) for cell detachment.
- To generate a single-cell suspension, the cells were seeded (400 cells/ 100µl full media / well).

- Directly, the spheroid formation was initiated by centrifuging the plates with a benchtop centrifuge (Eppendorf 5810R Centrifuge, Hamburg, Germany) at 2454 rcf (3700 rpm) for 10 minutes.

The plates were incubated between (1 and 12 days) under standard cell culture conditions at 37 °C, and 5% CO_2 in humidified incubators. The full media had been replaced each other day and post-seeding cellular phenotype was checked by the microscopical observable physical properties of each spheroid including the appearance, development, and behaviour.

1.16.2 Localisation of cell death and proliferation within spheroids

The seeded cells were stained by IncuCyte® Cytotox red for counting dead cells (250 nM, Essen Bioscience) and the generated spheroids were transferred to the Incucyte® live cell analysis system (Essen Bioscience Inc., Ann Arbor, Michigan, USA). Live images were obtained with 4× objective lenses in each well every hour inside an incubator over 12 days. The culture medium was replaced every 2 days for maintaining the spheroid's survival. The localisation of the red dead cells within the spheroids was assessed by phase-contrast images using the red channel to evaluate the real-time cell membrane integrity and cell death. The total phase and the red fluorescent areas with mask were quantified for different days using IncuCyte® spheroid analysis software (Version. 2020B, Essen Bioscience Inc., Ann Arbor, Michigan, USA).

1.16.3 Imaging studies

The single spheroids were stained following the instructions of each kit. The dead cells were stained by IncuCyte® Cytotox red for counting dead cells (250 nM, Essen Bioscience) during the generation process. The cyanine nucleic acid dye permeated cells with compromised cell membranes. The green dye CFSE Cell Division Tracker Kit (BioLegend, San Diego, California, USA) and DAPI (Sigma-Aldrich, St. Louis, Missouri, USA) were used to stain the live cells and the nucleus before taking pictures. The morphology of the spheroids was assessed and recorded using the Incucyte® live cell analysis system and confocal laser scanning microscope (Leica, Wetzlar, Germany) by a ×5 objective using the following settings: sequential scanning, ex/em: Mitotracker: 543/599 nm, Hoechst: 405/461 nm. The size of the spheroids was analysed using Incucyte® spheroid analysis software (Version. 2020B, Essen Bioscience Inc., Ann Arbor, Michigan, USA), and ImageJ Software (Version. 1.44, National Institute of Mental Health, Bethesda, Maryland, USA).

1.16.4 Hematoxylin and eosin (H&E) stain of spheroid cross-sections

U87 MG spheroids were generated from 400 cells. Prior to staining, spheroids were cultivated individually after 1, 3, 5, 7, and 10 days washed once in phosphate-buffered saline (Corning®, Phosphate Buffer Solution (PBS), New York, USA) then fixed with 10% formalin (Merck, Darmstadt, Germany). The spheroids were washed in PBS and transferred to disposable biopsy embedding molds to

encapsulate them with Epredia™ HistoGel™ Specimen Processing Gel (Fisher-Scientific, UK). Each gel-coated spheroid was moved to a cassette and loaded inside a tissue processor (Excelsior AS, Thermo Scientific, Germany). The program was set to start with 6 times 70% ethanol, then 3 times xylene, and 3 times histology wax. Each cycle time was 10 minutes. Then the capsules were embedded in paraffin using (Histostar, Thermo Scientific, Germany) with a temperature range of -3 to -12 ˚C. Microtone (Leica, RM2235) sections of 5 µm were placed on Super Frost glass slides (Menzel-Glaser, Thermo Science, Germany) and allowed to dry for 2 hours at 37 °C. The sections were deparaffinised by 2 changes of xylene for 5 minutes, rehydrated by 2 changes of 100% ethanol, followed by washing in 70% ethanol for 1 minute. After a short single rinse in distilled water, the sections were stained for 20 minutes in Mayer's hematoxylin (Merck) and placed for 20 minutes under running tap water, then dipped in 1% Scott's Tap. The slides were observed under the microscope. Sections were counterstained with eosin (Merck) for 2 minutes, rinse quickly in tap water, dehydrated by a dip in 70% ethanol, followed by 2 changes in 100% ethanol for 2 minutes each, and 2 changes of xylene for 2 minutes. The slides were mounted in DPX (Sigma-Aldrich, Germany), and left to air dry for 2 hours. spheroid sections were assessed by bright field microscopy.

1.17 Carnosine effect on red blood cells

A haemolytic experiment was used to assess the effects of different concentrations of carnosine on the cell membrane. The whole sheep blood (Sheep Blood Defibrinated, TCS Biosciences, Buckingham, UK) was warmed and the erythrocytes were obtained by washing with saline buffer and centrifuging for 10 minutes at 2500 rpm several times until the supernatant was clear. Then, the saline buffer was added to obtain a 2% erythrocyte suspension. Sample tubes were prepared to contain 2 mL from carnosine concentrations (100, 200, and 400 mM). The prepared positive and negative control groups were 2 mL distilled water and saline buffer, respectively. Each tube was mixed with 2 mL of the 2% erythrocyte suspension, then all tubes were incubated for 1 hour at 37 °C and then centrifuged for 5 minutes at 2500 rpm. The absorbance of the supernatant was measured at 540 nm (HP 8453 UV-Visible Spectrophotometer G1103A, Agilent, California, USA). All experiments were conducted in triplicate. The haemolysis rate was calculated using the formula of haemolysis rate (%). When the concentration induces smaller haemolysis, the membrane damage is more significant. To reflect the haemolysis effect more intuitively, the ratio of more than 5% was regarded as haemolysis.

1.18 MAD Nasal™ device characterisation

The MAD Nasal™ Intranasal Mucosal Atomisation Device from Teleflex is a safe and painless way to deliver medications. It is approved for human use in a simple, non-sterile, reliable, and cost-effective delivery technique for rapid absorption across mucosal membranes into the bloodstream, avoiding first-pass metabolism. The device atomises the sprayed solution into a fine mist of particles 30-100 microns

in size. The tip of the device was modified to produce a spray that fits the diameter of the rodent nostril. The driving pressures of the device were tested before and after the modification. The pressure was measured using Honeywell MPRLS. The sensor was connected between the device and syringe using a coupling tee to measure the peak pressure required to drive solutions through the devices.

1.19 *Ex vivo* experiments

1.19.1 The BPEI-coated IONRs loaded PLGA microbeads as contract agents

The brains of naïve female mice aged approx. 18-19 weeks old and weighing 18-22 g were requested from the bioscience support facility in NTU. After sacrificing the mice for other experiments. Each brain was snap-frozen and stored in universal labelled tubes. To examine the NRs effect *in vivo*, the tested material was injected 2 mm lateral to the sagittal suture and 2 mm posterior to the coronal suture. After positioning the mouse brain, 5 µl were injected 3mm deep using a 100 µl Neuros Syringe (Model 1710 RN, 33-gauge, Point Style 3). MRI was applied to compare the injected control with BPEI-coated IONRs loaded in PLGA microbeads and free BPEI-coated IONRs with concentrations of 25 and 50 ppm.

1.19.2 Nasal cavity deposition

To test the nasal cavity deposition, Coomassie blue dye was traced after intranasal administration on the cadaver of mice. Each mouse received dye solution as a nasal instillation of 10 µl *via* a pipette into one nostril and modified MAD Nasal™ inside the other one, while in the supine position. Shortly after administration was complete (< 5 min), the skin was removed, and the tissues were examined for dye localisation. MRI was used to determine if the total desired volume was dispensed from the device to the olfactory area with each actuation. A study was performed on water and various concentrations of gadolinium sulphate $Gd_2(SO_4)_3$ range between (10– 2 and 10– 9 mol/ L). To trace the localisation of the sprayed formulations, rat heads were used as an ex vivo model. The heads were taped on a board and an MR image was taken as a background to exclude the specific shade of gadolinium liposomes. The heads were split into two groups and each group was treated using either a pipette or the modified MAD Nasal™.

1.20 *In vivo* suggested application

Atomised nasal medications are the optimal size to accelerate the absorption across mucosal membranes into the bloodstream and to avoid the first-pass metabolism. This application is non-invasive and needle-free. No risk of needle stick injury could be resulted from using this non-sterile technique.

1.20.1 Tumour implantation surgery

The procedure of the surgery lasts between 25 °C to 30 °C following the steps below:

1. Vapourised isoflurane (100% w/w) should be used for anaesthesia. The dose volume is calculated because it varies between animals depending on their tolerance.

2. The oxygen should be set to 2 litres per minute throughout and the isoflurane percentage should be changed to keep the animal at the required depth.

3. Once the mouse is knocked down it should be moved to a mask set at 2 % while placed into the ear bars on the surgery table.

4. After the mouse will be settled, the isoflurane should be turned down to an average of 1.5 % until the surgery is completed.

5. The rat should be positioned on the stereotactic frame and a burr hole will be drilled on the right side the mouse skull. The hole is centred 2 mm lateral to the sagittal suture and 2 mm posterior to the coronal suture.

6. The needle should be placed in the same stereotactic frame and injected in coordinates in relation to Bregma: M-L (-2), final height: (-3), the right side of the brain.

7. The needle should be inserted to a depth of 3.5 mm and left for 60 seconds, then it should be withdrawn to a depth of 3 mm before implanting the cells.

8. U87 MG cells in 3 x 10^5 density should be injected in a volume of 3 µL. A previous optimisation showed that with this dosage all mice were dead by 29 days (median survival was 26.5 days).

9. The cells should be injected at a rate of 1.5 µL per 60 seconds

10. After the implantation of the cells, there should be a waiting period of 60 seconds for the cells to diffuse. The needle should be removed at a rate of 0.1 mm every 2 seconds until clear of the brain.

11. Two pain reliefs (buprenorphine and carprofen) should be used subcutaneously at the base of the tail. Both are diluted with saline (1 part to 9 parts).

12. The dose of the pain reliefs is also based on bodyweight with round up/down to the nearest 10 µl.

13. The mice should be dosed pre-surgery with both pain reliefs and with buprenorphine 12 hours post-surgery. The two mornings following surgery they should be provided with carprofen.

14. Temperature should be kept stable at 36 °C all time until the mice recover and set back in the original cage.

1.20.2 Animal groups

After the surgery of the glioma cell implantation, mice should be divided randomly into 3 groups (n = 5 mice/ group), as follows:

- Untreated group as control receives buffer 6
- Treated group receives carnosine 0.5 M twice a day* for 20 days
- Treated group receives carnosine loaded liposomes 0.5 M twice a day* for 20 days

  *Twice a day: each mouse receives 30 µL per nostril at 9 am and 3 pm

1.20.3 Treatment application

Giving the mice pain relief on the day of surgery and the day after which will not impact the intranasal treatment from day 1 after surgery. The syringe should be warmed by the hand temperature before applying the treatment. The mice will receive the intranasal treatment administration from day 1 to day 22 and the inhibition of cancer and reoccurrence will be monitored.

1.20.4 Monitoring

The expressed firefly luciferase activity bioluminescence on the U87 MG cells will be imaged after intraperitoneal injection of D-luciferin (4.5 mg/animal in 150 µL of saline) twice a week post glioma cell implantation (day 4, 8, 12, 16, and 22).

1.20.5 Post treatment potential tests

- Flow cytometry will be used to check the intertumoral apoptosis.
- Histology H&E stain should be applied to investigate the effect of the carnosine biodistribution for different organs such as the brain, lung, liver, spleen, and kidney.
- *In vivo* animal images will be compared, and statistical analysis should be applied to decide the significance in the difference for the reported results.

1.21 Statistical Analysis

All data were presented as the mean ± standard error of the mean (SEM). For the statistical analyses, a student's t-test (unpaired samples) was applied to compare groups after applying different treatments. The one-way analysis of variance (ANOVA) was carried out for multiple comparisons between the control and each group by Dunnett's post-test. All graphs and analyses were demonstrated by GraphPad Prism software (Version. 8, La Jolla, CA, USA) or by Incucyte® software (Essen Bioscience Inc., Ann Arbor, Michigan, USA). The value 0.05 was selected as the statistical significance level and indicated with (*) for $p < 0.05$, (**) for $p < 0.01$, (***) for $p < 0.001$and (****) for $p < 0.0001$.

Chapter 6: Conclusions and Future work

Conclusions

All conclusions include the answers to the study questions from chapter 1. In addition, they summarise new validated methodologies and recommendations for the work of other researchers.

1.1 The functionalised superparamagnetic iron oxide nanorods as carriers for controlled drug delivery

This work has successfully demonstrated that carnosine inhibits the growth and mobility of U87 MG glioblastoma brain tumour cells. Loading the carnosine into a sponge-like dendritic polymer matrix in the form of branched polyethyleneimine significantly reduced the risk of the drug being metabolised. The polymer offered a stable environment where the drug could be released at the site of action and the carnosine was readily released from the polymer matrix upon mild hyperthymia (40 °C), without any degradation to the dipeptide or toxicity for healthy cells. Adding superparamagnetic iron oxide nanorods to the carrier enabled it to be traced *via* MRI. It could also be used to induce localised hyperthymia in the presence of an oscillating magnetic field. In conclusion, the project demonstrated a proof of concept that carnosine can be successfully loaded into a nanometre scale carrier that protects, localises and releases the active ingredient *via* a non-invasive external stimulus. Thereby, it provides a potential complementary theranostic concept, alongside traditional surgical techniques, to minimise the lethal dose (LD50) for the holistic treatment of glioblastoma brain tumours.

1.2 The potential of using carnosine-loaded liposomes for glioblastoma nasal sustained release therapy

The BBB has been shown to restrict access to any compounds arriving at the CNS. Recent direct nose-to-brain application routes have gained attention as a promising pathway to cross by the BBB to avoid the filtration system of the brain. Herein, this project collaborated the therapeutic effect of the carnosine with the biocompatible liposomal carriers to protect and deliver the carnosine to the brain tumour cells through the olfactory bulbs, the nerve and the epithelia in the nasal cavities. Spherical liposomes were prepared with a size < 300 nm and negative surface charge to make a stable suspension in InVivoPure pH 6 dilution buffer. The pH of the buffer matches the physiological liquids of the nose, and the negative charge -26 ± 1 prevents the liposomes from aggregating over time. Also, the surface charge is expected to attach the liposomes to the epithelium area that covers the large surface of nasal cavities. Thus, the preserved carnosine inside the stable liposomal formulation will probably defends mucociliary clearance and releases the undegraded carnosine sustainably. It was shown in the membrane dialysis

studies that the loading efficiency for carnosine was 75%, the primary pulse of carnosine was released after 30 minutes and 50% was released after 24 hours. Then, 5%–10% of the total carnosine concentration was released over a week at 37 ˚C. The assessment of the toxic effect showed that both buffered carnosine-loaded liposomes and free carnosine did not lysis the erythrocytes of the membrane cells in the nasal epithelium. The human-approved MAD Nasal™ device was modified to fit the narrow naris of the rodents in supine positioning to achieve successful deposition in the nasal cavity. Also, the direction of applying the treatment with 20 psi pressure was essential to fill the nasal turbinate instead of dragging the liposomes to the nasopharynx. The localisation of the liposomes close to the cribriform plate *ex vivo* in the head of the rat carcass, which should facilitate the brain uptake of carnosine-loaded liposomes, was demonstrated with MRI. This approach can be further optimised for preclinical applications to different brain diseases and diagnostic imaging.

1.3 The sustained release of carnosine treatments from PLGA beads by using the functionalised superparamagnetic iron oxide nanorods as triggers

Non-heating rotating magnetic field nanomechanical stimulation could trigger carnosine release from poly(lactic-co-glycolic acid) beads as a supplementary glioblastoma treatment. Nano-meter scale rods of superparamagnetic iron oxide have been encapsulated, along with the anti-cancer therapeutic carnosine, inside porous poly(lactic-co-glycolic acid) microbeads (~10 µm) with uniform morphology. The loading of carnosine inside the beads involves double emulsification using microfluidic arrays. The sustained and externally triggered controlled release from these micro vehicles was demonstrated using a rotating Halbach magnet array, then quantified *via* LC-MS and imaged *in situ* using magnetic resonance imaging. Without the external magnetic trigger, carnosine was released from the polymer in a linear profile. However, more than 50% of the drug could be released within 30 minutes of exposure to the rotating magnetic field. Additionally, the release of carnosine embedded on the surface of the nanorods was delayed if it was mixed with the iron oxide nanorods before the encapsulation because of the attraction to the positively charged branches of the coated surface. These new drug delivery vesicles have the potential to pave the way towards the safe and triggered release of onsite drug delivery as part of a theragnostic treatment for glioblastoma.

1.4 The validity of using a robust, cost-effective single spheroid model to bridge the gap between the *in vitro* and *in vivo* trials

Monolayer-cultured tumour cells exhibit less resistance to therapeutic interventions than *in vivo* cells. Developing a 3D model resembling solid tumours is essential, especially when bridging the gap between *in vitro* and *in vivo* tumour models. The use of 3D models is currently largely used, and significant updates follow the commonly used protocols. The protocol described in this thesis

demonstrated reproducible methodology in generating robust single spheroids using a simple, cost-effective step that other researchers and different laboratories can benefit from. Uniform single spheroids without any additives were consistently obtained. The spheroids exhibited a typical characteristic morphology consisting of a proliferating rim and a necrotic core. These spheroids can be used to assess drug EC50, as was demonstrated using carnosine treatment on U87 MG single spheroids. Preliminary optimisation for different cell lines of single spheroids was proposed to provide the research workers with an accessible and affordable method as compared to the ultra-low adherent plates for *in vitro* investigations. In the future, the reported data need further studies to find the validity of patient-derived tumour cells.

Future work

Following the reported results from the preliminary studies, further non-invasive carnosine applications are worth investigating. This project consisted of multidisciplinary research in chemistry (e.g., synthesis, analytical applications, characterisation, purification, stability, and release studies), physics (e.g., MRI and rotating Halbach magnet array applications), and biology (e.g., cell culturing and cancer treatment studies). Drug delivery targeting glioblastoma was the area of interest to investigate the theranostic potentials of using nano- or micro-scale therapies. Future inspections should involve refining the synthesis of nanomaterials and their encapsulation in novel drug delivery systems for *in vitro, in vivo,* and clinical applications. This thesis includes conclusions for developing novel sustained released formulations (liposomes and PLGA beads), including stability, cell delivery, viability, and safety studies, to represent promising drug-delivery approaches for curing aggressive brain tumours.

Furthermore, it is recommended to optimise biodegradable hydrogel encapsulation for carnosine with the use of a hydrodynamic flow focusing microfluidic system and to utilise the validated formulations to combine the carnosine effect with various chemotherapeutic drugs for local sustained release following resection. Also, *in vivo* trials are essential after the preliminary results for applying the non-invasive intranasal encapsulated supplementary treatment to rat animal models. The next step should be to design a fulfilling project that includes translating a developed drug-delivery system into clinical trials (phase l) to study the safety of carnosine treatment of GMB in humans.

1.1 The development of the nanobiotechnology-based delivery strategies in GBM targeted therapies

GBM therapeutics face the difficulty of BBB penetration. Chemo, antibodies, and immune therapy rely on supportive techniques or carriers to improve crossing the BBB. The focused ultrasound (FUS) has been the most applied technique (Etame et al., 2012). An enhancement in brain uptake without damaging the parenchyma was shown by the frequency of ultrasound waves disrupting the tight

junctions of the BBB. The cellular mechanisms of opening the cell membranes temporarily were studied, and MRI-guided focused ultrasonication was utilised *in vivo* to enable the opening of the BBB in the presence of gas microbubbles (Sheikov et al., 2004). For example, the recognised antigens of dopamine D4 receptor-targeting antibody in the murine brain proved the effectiveness of FUS in delivering therapeutic or diagnostic macromolecules non-invasively (Kinoshita et al., 2006). FUS induced localised delivery to animal models in various diseases, such as intravenous injections of Herceptin (trastuzumab) for breast cancer and liposomal Doxorubicin (DOX) for glioma treatment (Kinoshita et al., 2006; Treat et al., 2012). The positive side of FUS is the safety assessment after opening the BBB, which proves the reversed effect within the short term (24 hours) (Alonso et al., 2010; Baseri et al., 2010). The intravenous applications should either be positively charged to traverse the BBB by adsorption-mediated transcytosis or shuttle by receptor-mediated transcytosis (Razpotnik et al., 2017). Therefore, actively targeted functionalised liposomes with ligands are the most recent preclinical and clinical studies for the delivery of anticancer agents to GBM (Mojarad-Jabali et al., 2021). In addition, nanoparticles, such as iron, mediate the specified payload when incorporated with liposomes (Razpotnik et al., 2017). Other routes for applying glioma treatment became more attractive than the intravenous, including the personalised local implant or the direct nose-to-brain method (Mangraviti et al., 2016). The recommended state-of-the-art technologies for applying the optimised formulations are the following:

- Transplanted mini pumps for drug release applications on animal models of various sizes.
- The rotating magnetic field should be designed with safety assessment and validated for *in vivo* experiments.
- I*n vivo*-designed atomisers.

All previous devices are in the race to accomplish a non-invasive controlled therapeutic for GBM. Still, high costs are the main barrier for the researcher to design extended experiments. Instead of expensive devices, some research still uses one of the oldest tricks to increase BBB penetration, such as incorporating the mannitol into the formulation to shrink the endothelial cells by osmotic disruption. Unfortunately, the non-specificity in penetrating the BBB leads to an increase in the potential toxicity and fatal brain oedema (van Tellingen et al., 2015).

1.2 Combining the traditional therapies with immunotherapy

More research is still required to combine the therapeutic nano-vectors with traditional chemotherapy, surgical therapy, and radiotherapy. Also, incorporating immunotherapy by vaccines with standard therapies can be promising in GBM treatment (Platten, 2019). However, immunosuppressors, such as the common steroid anti-inflammatory (dexamethasone), are used. Dexamethasone inhibits the healthy CD8 and CD4 T cells. Thus, it should be ceased in patients receiving GBM vaccines (Giles et al., 2018). Replacing dexamethasone with the vascular endothelial growth factor antibody (bevacizumab) helps

reduce oedema without inhibiting the immune system (Ananthnarayan et al., 2008). The current gold standard therapy for GBM is the collaboration between temozolomide, which reduces the CD4 T-cell count and the immune response, and radiotherapy, which enhances the infiltration of the immune cells into the tumour cells (Grossman et al., 2011; Chow et al., 2015). Adding an anti-PD-1 immune checkpoint blockade to the previous combination avoids the regression of tumours at part of their eradication and prolongs survival (Chow et al., 2015; Ladomersky et al., 2018). Ultimately, it is expected that patients will require personalised combinations to develop resistance to some treatments.

1.3 Investigating the potential use of carnosine as a localised treatment for different tumours such as prostate cancer

Prostate cancer is the most common cancer occurring in men and the second leading cause of cancer death among them (Siegel, Miller, and Jemal, 2018). The five-year survival rate for patients with localised disease is almost 100% (McNeel et al., 2016). Treatment usually involves prostatectomy, radiation therapy, chemotherapy and hormone deprivation therapy. Many patients with intermediate to high-risk localised prostate cancer will be offered radical prostatectomy, brachytherapy or external beam radiotherapy depending on their age, prostate-specific antigen (PSA) level and digital rectal exam (DRE) (Yossepowitch et al., 2007). Radical prostatectomy (RP) has not been encouraged in the past for patients with locally advanced diseases. High-grade prostate cancer patients are not regarded as promising candidates for RP due to the high incidence of cancer-positive pelvic lymph nodes and poor long-term survival rates (Gerber et al., 1997; Khan et al., 2004). External beam radiotherapy uses high-energy beams, such as X-rays or protons, generated by a linear accelerator and directed towards the prostate gland to kill the cancer cells. At the same time, brachytherapy involves implanting small radioactive pellets into the prostate gland to deliver cancer-damaging radiation directly to the tumours. Chen et al. (2017) have compared these methods to treat localised prostate cancer. They showed that patients who chose RP had a decreased risk of overall and cancer-specific mortality and an improved 5- and 10-year overall remission and cause-specific survival. However, RP carries significant side effects, such as urinary incontinence and erectile dysfunction.

Additionally, many men with intermediate-risk localised prostate cancer refuse immediate radical prostatectomy or radiotherapy/brachytherapy. Radiation therapy and chemotherapy are also associated with adverse events due to their systemic toxicity, meaning that normal non-cancerous cells are also affected by therapy. Androgen deprivation therapy (ADT) with a gonadotropin-releasing hormone agonist is also used for treating prostate cancer. However, this treatment has been associated with obesity-related diseases, such as diabetes and cardiovascular disease (Alibhai et al., 2009). All men treated with ADT develop resistance to treatment and metastatic castration-resistant prostate cancer (mCRPC) (McNeel et al., 2016).

Overall, 10–20% of prostate cancer patients see their disease progress as castrate-resistant prostate cancer (CRPC) within five years following diagnosis. The treatments available for patients with CRPC are limited and not curative, with a median survival rate from diagnosis of 14 months. CRPC is linked to a mediocre quality of life for sufferers. Treatments include androgen signaling inhibitors (enzalutamide and abiraterone), chemotherapy (cabazitaxel), radiopharmaceutical agents (radium-223) and immunotherapy (sipuleucel-T) (Kirby, Hirst and Crawford, 2011). As highlighted by the considerable number of therapies currently under clinical trials, there is an urgent need for new effective therapeutic options to improve the prognosis of patients with CRPC. The side effects associated with standard therapy make them unattractive to patients. As a result, novel cancer-targeting therapeutics with little to no side effects need to be employed to prevent harmful side effects and prevent cessation of patient therapy.

Carnosine has demonstrated a protective role towards normal healthy cells, such as increasing the number of *in vitro* passages of primary human fibroblasts and rejuvenating already senescent cells. At the same time, it inhibits the proliferation of many cancer cells by interfering with the glycolysis pathway favoured by most cancer cells (Warburg effect). It affects cell supply in precursors for macromolecule biosynthesis, mitochondrial respiration or both, depending on the cell type investigated (Gaunitz and Hipkiss, 2012). In this project, the mechanisms of the carnosine effect were tested on PC346-Flu1 and TRAMP-C1 prostate cancer cells.

1.3.1 MTT assay (IC50/EC50)

Both prostate cancer cells were cultured in the absence or presence of varying carnosine concentrations (0–300 mM). Then, the cells were incubated under normal conditions for 48 hours at which point an MTT assay was used to measure cell viability indirectly. The resulting dose-response curve showed the EC50 to be ~100 mM for both cell lines (Figure 72).

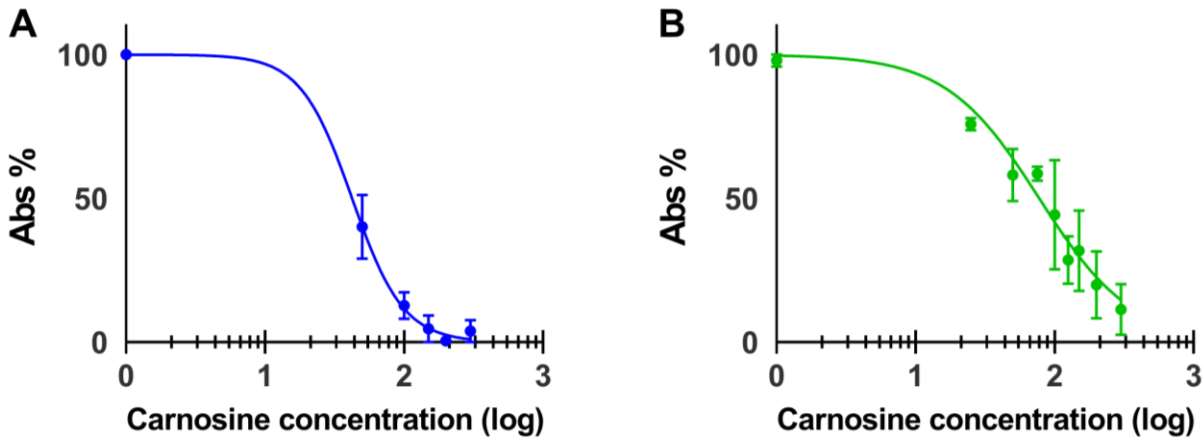

Figure 72. Carnosine affects mitochondrial functionality and slows down the proliferation of cells after 48 hours. (A) PC346Flu1 and (B) TRAMP-C1. MTT dose-response curve indicates that carnosine induces cell death and slows down proliferation dose-dependently with an EC50 of ~100 mM after 48 hours in both cell lines. (n=3)

1.3.2 Proliferation and cytotoxicity (IC50/EC50)

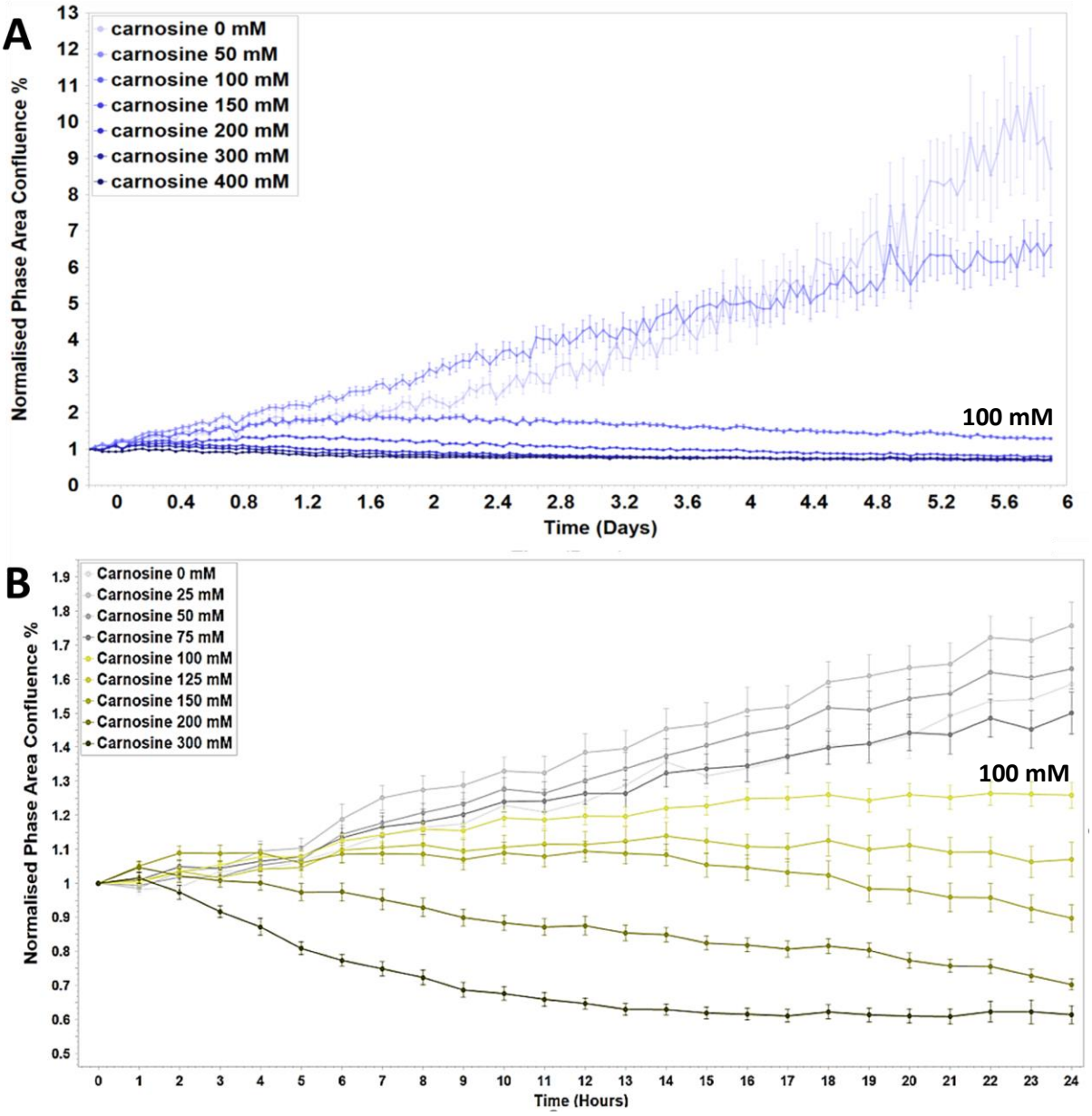

Figure 73. Incucyte® live cell system (×10), live cell image analysis shows that carnosine affects the mitochondrial functionality within hours for both PC346Flu1 cells (A) and TRAMP-C1 cells (B). Carnosine significantly inhibited the growth of each cell line in a dose and time dependent manner. The maximum effect on proliferation was shown at carnosine concentration 300 mM.The Incucyte® live cell imaging system was used to study the dose-dependent effect of carnosine on proliferation. PC346-Flu1 and TRAMP-C1 prostate cancer cells were cultured in the absence or presence of various carnosine concentrations using a density of 3×10^5 cells/well for PC346Flu1 and 10^3 cells/well for TRAMP-C1. Proliferation was observed on an hourly basis (Figure 73).

There was growth suppression in cells after nearly 3 hours. The cells were significantly affected after 24 hours when the carnosine applied was equal to or higher than 100 mM. Cells were first seeded, and their proliferation was monitored for 24 hours, before carnosine addition in order to confirm that this

was not due to cells being compromised in these wells. Moreover, the effect of carnosine was observed using phase-contrast images of the cells with and without carnosine. In contrast, Incucyte® Cytotox red reagent was used for real-time quantification of cell death (Figure 74).

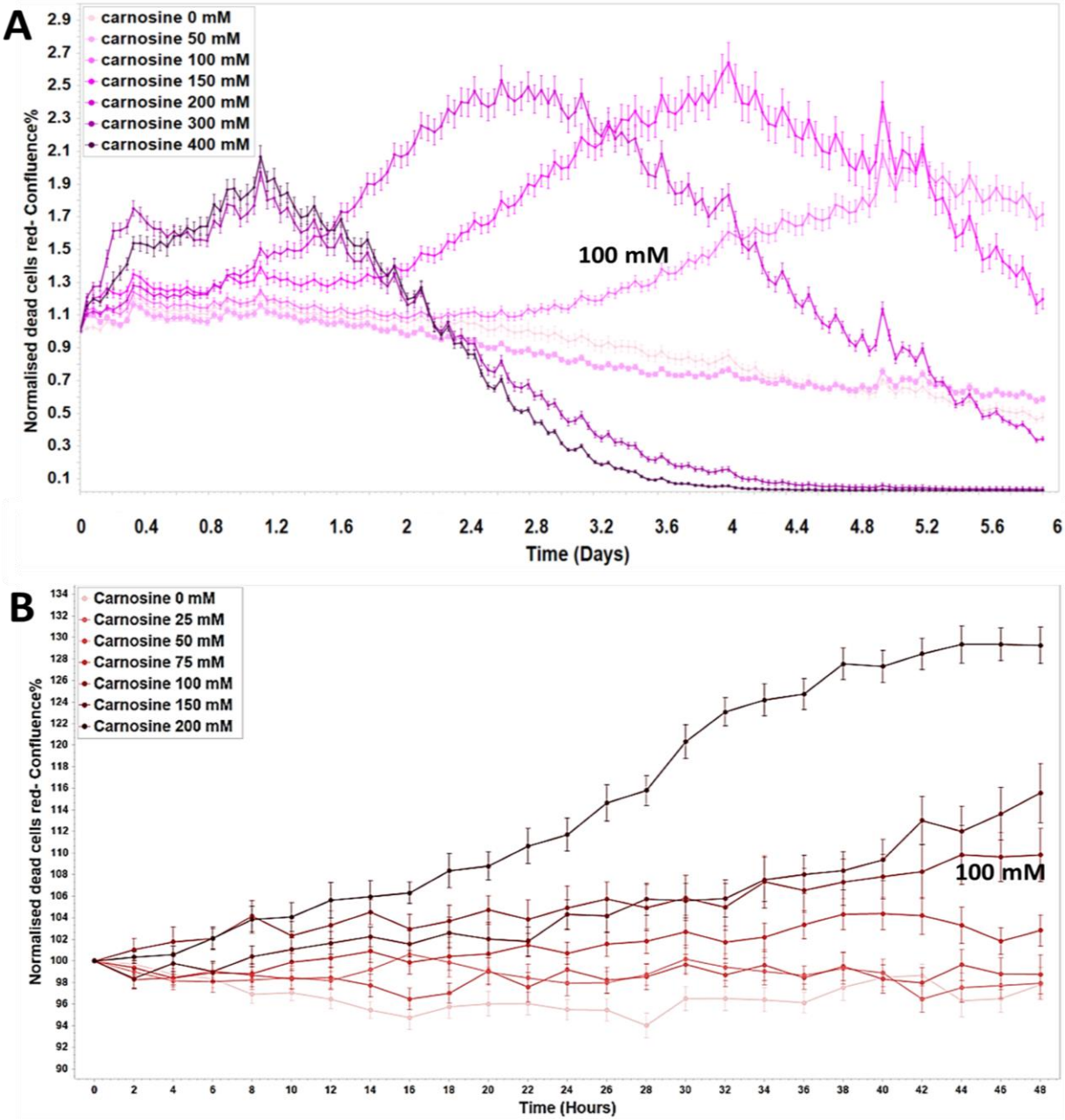

Figure 74. Incucyte® live cell system (×10), dead cell image analysis shows that carnosine increases death of A) PC346Flu1 cells, B) TRAMP-C1 cells. Carnosine significantly inhibited cell growth in a dose and time dependent manner due to the relatively different growth rates of the cells studied. The higher the dose of carnosine the shorter the time required for cell death over 6 days for the human cells and over 48 hours for the murine cells. The maximum effect was shown starting from carnosine concentration 300 mM for PC346Flu1 cells and 200 mM on TRAMP-C1.

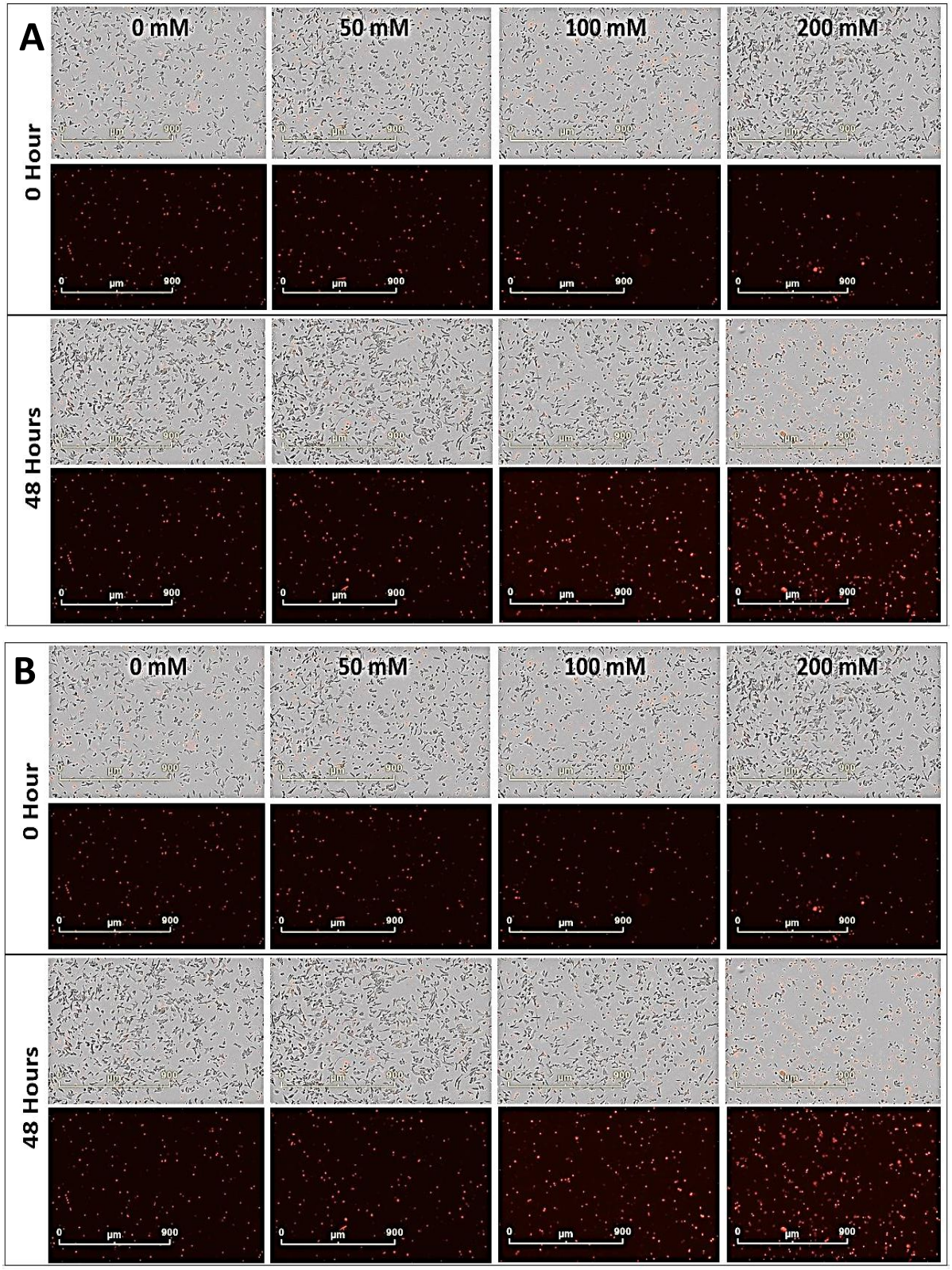

Figure 75. Incucyte® live cell system (×10) images show cytotoxicity upon carnosine exposure after 48 hours (A) PC346Flu1 cells. (B) TRAMP-C1 cells. Cells were treated with different carnosine concentrations in the presence of Cytotox Red dye (250 nM), which enters dead cells after membrane integrity is lost and binds to DNA to emit red fluorescence. Each photo was displayed as a phase and with a red mask for dead cells. Significant carnosine induced cell death was shown from a concentration of 100 mM upwards; Scale bars are 900 µm.

The number of live cells decreased, while the number of dying cells increased dose-dependently. The analysis of phase images and red channels enabled real-time evaluation of cell membrane integrity and cell death in response to carnosine exposure after 48 hours, (Figure 75).

The maximal effective concentration curve was defined (EC50 = 102 mM). Red fluorescent areas were masked and quantified for different carnosine treatments using Incucyte® standard analysis software. The curve was integrated with the previous proliferation test at IC50 (98 mM). Initially, there were no effects in the plots representing live and dead cells, followed by a cytostatic phase starting from around 100 mM of carnosine. However, the cell cytotoxicity could begin immediately after the integration point (Figure 76).

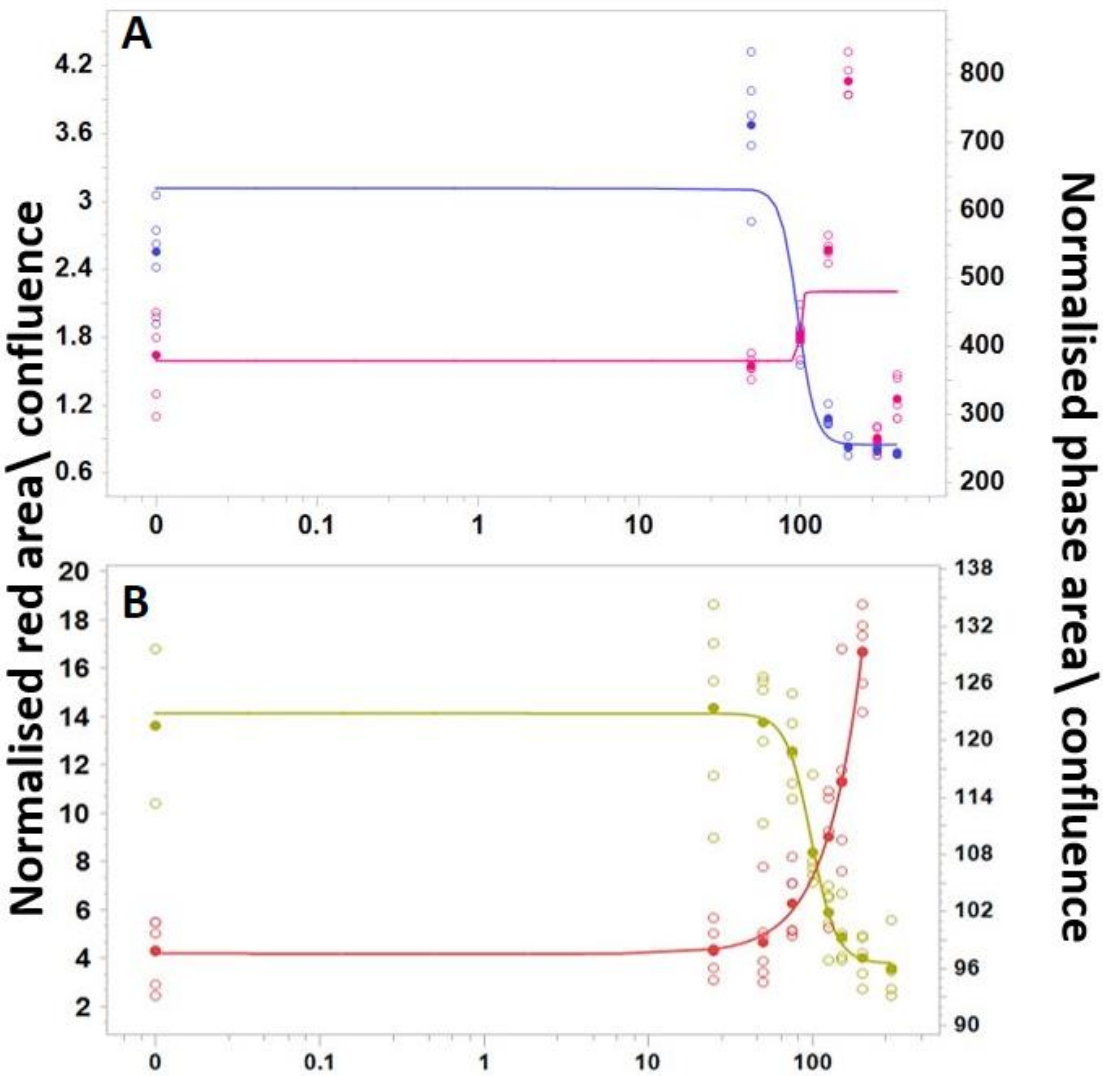

Figure 76. Incucyte® live cell system (×10), dead/live cell images analysis shows IC50/EC50 curves of the inhibition of cell proliferation and the efficiency of carnosine in killing the tumour cells. Upon carnosine exposure at different concentrations, ranging between 0 and 400 mM over 48 hours, the IC50 is indicated by the confluence phase ratio. At the same time, EC50 is the ratio of the Cytotox Red dye that enters dead cells. The carnosine effect has three phases: no effect, cytostatic, and cytotoxic.

1.3.3 Utilising carnosine within a sustained release designed experiment

When added in a sustained release manner, the long-term carnosine treatment reduced the growth of TRAMP-C1 and PC346Flu1 spheroids *in vitro* compared to the untreated spheroid. This experiment reflects the importance of the sustained release of carnosine for the treatment of hard-to-treat cancer cells. The change in the morphology of single spheroids was monitored using the Incucyte® spheroid software over five days. Single spheroids were grown initially for 24 hours, and then every 48 hours thereafter carnosine was added to the spheroids, (Figure 77) (Habra et al., 2022).

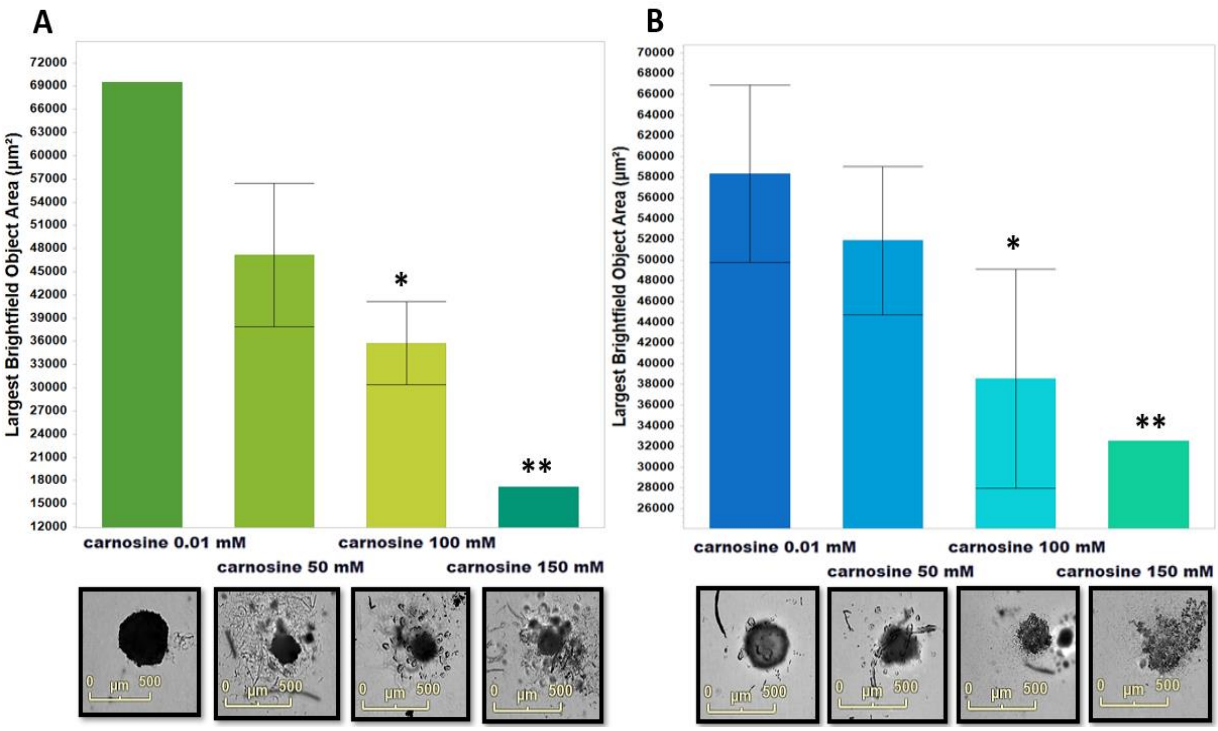

Figure 77. Carnosine Incucyte® images show the effect of sustained treatment using carnosine on single spheroids in (A) PC346Flu1 and (B) TRAMP-C1 cells. Carnosine was added every other day at different concentrations ranging from 0 to 150 mM. The images were collected after seven days. The spheroid tightness was affected by carnosine concentration > 100 mM and a significant difference was reported in the largest brightfield object area (µM2). The statistical significance level on day seven indicated with (*) for $p < 0.05$, (**) for $p < 0.01$. Scale bars 500 µM. (n=3)

1.3.4 Real-time ATP rate assay

The Agilent Seahorse XF Real-Time ATP Rate Assay is designed to measure total ATP production rates in living cells and to distinguish between the two main metabolic pathways responsible for ATP production in mammalian cells. Fractions of ATP were calculated as being generated by mitochondrial oxidative phosphorylation (OXPHOS) or glycolysis. OXPHOS is the rate of ATP production associated with oxidative phosphorylation in the mitochondria, and glycolysis is the rate of ATP production related to the conversion of glucose to lactate in the glycolytic pathway. Total ATP is the sum of both pathways.

The assay was applied to each cell line (PC346-Flu1 80K cells per well and TRAMP-C1 40K cells per well). It is shown in Figure 78 that carnosine treatment has an immediate effect on ATP production *via* the glycolysis pathway, as inhibition was observed within 20 minutes. Mitochondria still produced ATP, even with the highest concentration (150 mM). Still, a gradual reduction in ATP production was observed. Affecting the rate of mitochondrial OXPHOS took more prolonged exposure than the timeframe of this test in both cell lines.

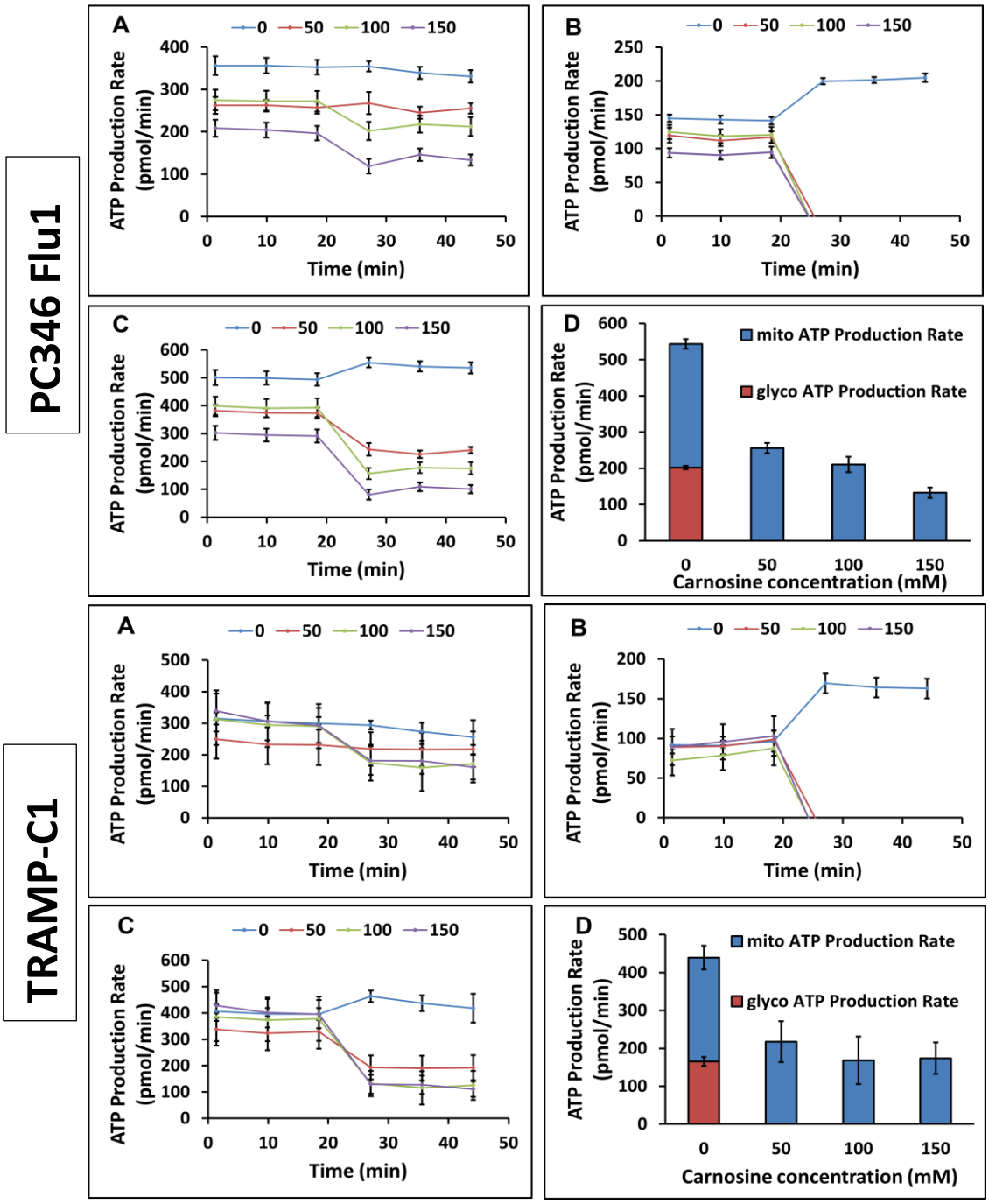

Figure 78. Seahorse flux analysis of cells treated with carnosine. (A) mitochondrial ATP production rate data (basal and induced rates), (B) glycolysis ATP production rate data (basal and induced rates), (C) total ATP production rate data (basal and induced rates), (D) induced rates average of ATP production.

This study aimed to investigate the potential anti-cancer properties of carnosine for the first time on TRAMPC1 cells and PC346Flu1, a primary androgen-resistant prostate cancer cell line. It was shown in the MTT assay and proliferation results that carnosine affects mitochondrial function in these cells from 3 to 48 hours in maximal effective concentration dosage EC50 (Figure 72). The effect of carnosine on both cell lines was observed using phase contrast images of the cells with and without carnosine, using the Incucyte® Cytotox red reagent for real-time quantification of cell death. The number of live cells decreased, while dying cells increased in a dose-dependent manner (Figure 73). The red fluorescent areas were quantified for different carnosine treatments using Incucyte® standard analysis software (Figure 74). This was integrated with the proliferation phase areas. The plots representing live and dead cells initially showed no effect and were followed by a cytostatic phase starting from 100 mM carnosine (Figure 75). The significant cell death could be seen to begin immediately after the integration point. Mechanistically, carnosine has been shown to affect mitochondria functions as evidenced by the reduced ATP production and decreased reactive species formation seen in carnosine treated cells (Cerrato and Caruso, 2022).

This is the first time that the effect of carnosine has been investigated on prostate cancer cells. However, the first potential antineoplastic effect of carnosine was proposed nearly four decades ago (Hipkiss, Brownson and Carrier, 2001). Sarcoma tumour cells were implanted subcutaneously *in vivo*, and carnosine was administered near the implantation site every other day. As a result, both tumour growth and mortality were reduced (Nagai and Suda, 1986). Since then, other publications have supported the selective effect of carnosine in suppressing transformed and neoplastic cells (Holliday and McFarland, 1996; Renner et al., 2008; Renner et al., 2010). Daily application of *in vivo* intraperitoneal treatment with 1 M carnosine resulted in a delay in aggressive tumour growth, albeit there was an incomplete reverse in tumour formation (Renner et al., 2010). Moreover, a significant advantage of carnosine administration is its contradictory effect on healthy cells, which have been reported to increase their viability (Gaunitz and Hipkiss, 2012).

Healthy cells utilise oxidative phosphorylation to produce energy in non-monic conditions. However, this results in lactate generation during mitosis due to the Warburg effect (Oppermann et al., 2016). It was shown in the data obtained herein that the primary action mechanism of carnosine in prostate cancer cells is to inhibit glycolysis (Renner et al., 2013). A mechanism whereby the activity of the glycolytic enzyme, glyoxalase, regulating protein glycation, cell apoptosis, gene expression, redox biology, and metastasis were modulated by carnosine was reported in a previous review (Hipkiss and Gaunitz, 2014). Primarily, the cellular real-time ATP rate assay was a highly informative method to examine cellular metabolism due to ATP being the dominant energy currency for cells. Cellular metabolic regulation allows adjustments, according to ATP demand, with subsequent changes in cell conditions to maintain total intracellular ATP levels. Oligomycin and a mix of rotenone and antimycin A are used in the Seahorse XFe24 Real-Time ATP Rate Assay to calculate the mitochondrial and glycolytic ATP production rates in real-time with a quantitative phenotype of cellular energy poise (Figure 78). Most

cellular ATP in mammalian cells is provided by the OXPHOS and glycolysis pathways. Both contribute to the acidification of the assay medium. However, OXPHOS consumes O_2 driving the oxygen consumption rate (OCR), while conversion of glucose to lactate through glycolysis is accompanied by extrusion of one H^+ per lactate. The sum of these reactions is the extracellular acidification rate (ECAR). The flux of H^+ production (ECAR) and O_2 consumption (OCR) are measured in real-time by the Seahorse test after the serial addition of carnosine, oligomycin and rotenone/antimycin A. The series of calculations used to transform the OCR and ECAR data into ATP production rates were performed post-data acquisition. Then, the simultaneous effect of adding carnosine to the live cells was shown.

In conclusion, anti-cancer effects on the PC346Flu1 cell line are exerted by carnosine by altering the metabolic profile of these cells. As a result, it is of great interest to further study the use of carnosine and its analogues in prostate (and other) cancer settings.

1.4 Summary

Throughout the optimisation for preclinical evaluations, multi-disciplinary research and development is the key to the future design, characterisation, and testing of drug delivery depots for anti-tumour therapeutics. Future work should focus on the design of carnosine-loaded beads and liposomes predominantly and explore the potential to control the kinetics of therapeutic release and the degradation of the vehicles by tuning the chemistry of the building block and properties of the functionalisation. Collaborating closely with industrial and clinical partners is vital to testing the optimised formulations for therapeutic activity and early safety inspections. Through such collaboration, it will be possible to contribute to developing innovative anti-tumour products and make their translations to help the growth of commercial activities. Clinic trial (phase I) studies for the safe application of localised or supplementary carnosine treatment after surgery are recommended as the aim of the following project.

References

General guidelines Incucyte ® Scratch Wound Assay. (2018).

Patent. US3887699A, Biodegradable polymeric article for dispensing drugs. (1970).

Protocol 2. Embedded MDCK 3D culture. (2017).

LMA MAD Nasal ™. https://www.youtube.com [Accessed 08/08/2022]. (2014).

WHA58.22 Cancer prevention and control. https://apps.who.int/iris/bitstream/handle/10665/20372/WHA58_22-en.pdf?sequence=1&isAllowed=y [Accessed 20/08/2022]. (2005)

WHO Action Plan for the Global Strategy for the Prevention and Control of Noncommunicable Diseases. (2008-2013).

WHO Cancer overview. Available from: https://www.who.int/health-topics/cancer#tab=tab_1 [Accessed 11/07/21c]. (2021)

WHO Follow up the political declarationof the high-level meeting of the general assembly on the prevention and controlof non-communicable diseases. https://apps.who.int/iris/handle/10665/150161 [Accessed 20/10/2022]. (2013)

A

AFSHORDEL, S. et al. (2015) Lovastatin and perillyl alcohol inhibit glioma cell invasion, migration, and proliferation - Impact of Ras-/Rho-prenylation. *Pharmacological Research*, 91, pp. 69–77.

AFTAB, A. et al. (2020) Microfluidic platform for encapsulation of plant extract in chitosan microcarriers embedding silver nanoparticles for breast cancer cells. *Applied Nanoscience*, 10(7), pp. 2281–2293.

AIME, S. and CARAVAN, P. (2009) Biodistribution of gadolinium-based contrast agents, including gadolinium deposition. *Journal of Magnetic Resonance Imaging*, pp. 1259–1267.

AKBARZADEH, A. et al. (2013) Liposome: Classification, preparation, and applications. *Nanoscale Research Letters*, 8(1), pp. 1–9.

ALAM, S. et al. (2012) Development and evaluation of thymoquinone-encapsulated chitosan nanoparticles for nose-to-brain targeting: a pharmacoscintigraphic study. *International Journal of Nanomedicine*, 7, p. 5705.

ALIBHAI, S.M.H. et al. (2009) Impact of Androgen Deprivation Therapy on Cardiovascular Disease and Diabetes. *Journal of clinical oncology*, 27(21), p. 3452.

ALLEN, M. et al. (2016) Origin of the U87MG glioma cell line: good news and bad news. Science Translational Medicine, 8(354), p. 354.

ALLEN, T.M. and CULLIS, P.R. (2013) Liposomal drug delivery systems: From concept to clinical applications. *Advanced Drug Delivery Reviews*, 65(1), pp. 36–48.

ALMEIDA, T.P. et al. (2010) Hydrothermal growth mechanism of α-Fe_2O_3 nanorods derived by near in situ analysis. *Nanoscale*, 2(11), pp. 2390–2399.

ALONSO, A. et al. (2010) Reorganization of gap junctions after focused ultrasound blood-brain barrier opening in the rat brain. *Journal of Cerebral Blood Flow and Metabolism*, 30(7), pp. 1394–1402.

ALY, A.E.E. and WASZCZAK, B.L. (2015) Intranasal gene delivery for treating Parkinson's disease: overcoming the blood–brain barrier. *Expert Opinion on Drug Delivery*, 12(12), pp. 1923–1941.

AMIDI, M. et al. (2010) Chitosan-based delivery systems for protein therapeutics and antigens. *Advanced Drug Delivery Reviews*, 62(1), pp. 59–82.

AMMAR, S. and FIÉVET, F. (2020) Polyol Synthesis: A Versatile Wet-Chemistry Route for the Design and Production of Functional Inorganic Nanoparticles. *Nanomaterials*, 10(6), p. 1217.

ANANTHNARAYAN, S. et al. (2008) Time course of imaging changes of GBM during extended bevacizumab treatment. *Journal of Neuro-Oncology*, 88(3), pp. 339–347.

ANDHARIYA, J. V. et al. (2019) Effect of minor manufacturing changes on stability of compositionally equivalent PLGA microspheres. *International Journal of Pharmaceutics*, 566, pp. 532–540.

ANTONARAKIS, E.S. and DRAKE, C.G. (2012) Combining immunological and androgen-directed approaches: an emerging concept in prostate cancer immunotherapy. *Current opinion in oncology*, 24(3), p. 258.

APOSTOLATOS, A. et al. (2012) Insulin Promotes Neuronal Survival via the Alternatively Spliced Protein Kinase Cell Isoform. *Journal of Biological Chemistry*, 287(12), pp. 9299–9310.

APPU, A.P. et al. (2016) Rapid intranasal delivery of chloramphenicol acetyltransferase in the active form to different brain regions as a model for enzyme therapy in the CNS. *Journal of Neuroscience Methods*, 259, pp. 129–134.

ARACHCHIGE, M.P. et al. (2017) Functionalized nanoparticles enable tracking the rapid entry and release of doxorubicin in human pancreatic cancer cells. *Micron*, 92, pp. 25–31.

ARMENIA, I. et al. (2019) Enzyme activation by alternating magnetic field: Importance of the bioconjugation methodology. *Journal of Colloid and Interface Science*, 537, pp. 615–628.

ARTEAGA-CARDONA, F. et al. (2016) Improving the magnetic heating by disaggregating nanoparticles. *Journal of Alloys and Compounds*, 663, pp. 636–644.

ARTIOLI, G.G., SALE, C. and JONES, R.L. (2018) Carnosine in health and disease. *European Journal of Sport Science*, 19(1), pp. 30–39.

ASTETE, C.E. and SABLIOV, C.M. (2006) Synthesis and characterization of PLGA nanoparticles. *Journal of Biomaterials Science*, 17(3), pp. 247–289.

AU, C. et al. (2007) Effects of nanoparticles on the adhesion and cell viability on astrocytes. *Biological Trace Element Research*, 120(1–3), pp. 248–256.

AVOLIO, M. et al. (2019) Elongated magnetic nanoparticles with high-aspect ratio: a nuclear relaxation and specific absorption rate investigation. *Physical Chemistry Chemical Physics*, 21(34), pp. 18741–18752.

B

BAE, D.S. et al. (1998) Synthesis of ultrafine Fe_3O_4 powder by glycothermal process. *Materials Letters*, 37(4–5), pp. 255–258.

BAINS, A. et al. (2017) Controlling Structure and Function of Polymeric Drug Delivery Nanoparticles Using Microfluidics. *Molecular Pharmaceutics*, 14(8), pp. 2595–2606.

BALOG, S. et al. (2015) Characterizing nanoparticles in complex biological media and physiological fluids with depolarized dynamic light scattering. *Nanoscale*, 7(14), pp. 5991–5997.

BAMRUNGSAP, S. et al. (2012) Nanotechnology in therapeutics: A focus on nanoparticles as a drug delivery system. *Nanomedicine*, 7(8), pp. 1253–1271.

BASERI, B. et al. (2010) Multi-Modality Safety Assessment of Blood-Brain Barrier Opening Using Focused Ultrasound and Definity Microbubbles: A Short-Term Study. *Ultrasound in Medicine & Biology*, 36(9), pp. 1445–1459.

BÉDUNEAU, A., SAULNIER, P. and BENOIT, J.P. (2007) Active targeting of brain tumours using nanocarriers. *Biomaterials*, 28(33), pp. 4947–4967.

BELAADI, N., AUREILLE, J. and GUILLUY, C. (2016) Under Pressure: Mechanical Stress Management in the Nucleus. *Cells*, 5(2), p. 27.

BHATTACHARJEE, S. (2016) DLS and zeta potential – What they are and what they are not? *Journal of Controlled Release*, 235, pp. 337–351.

BINNS, C. et al. (2002) Magnetic behaviour of nanostructured films assembled from preformed Fe clusters embedded in Ag. *Physical Review B*, 66(18), p. 184413.

BLAKELEY, J.O. et al. (2008) Effect of blood brain barrier permeability in recurrent high-grade gliomas on the intratumoral pharmacokinetics of methotrexate: a micro dialysis study. *Journal of Neuro-Oncology*, 91(1), pp. 51–58.

BLEEKER, F.E., MOLENAAR, R.J. and LEENSTRA, S. (2012) Recent advances in the molecular understanding of glioblastoma. *Journal of Neuro-Oncology*, 108(1), pp. 11–27.

BOLDYREV, A.A. (2012) Carnosine: New Concept for the Function of an Old Molecule. *Biochemistry (Moscow)*, 77(4), pp. 313–326.

BOLDYREV, A.A., ALDINI, G. and DERAVE, W. (2013) Physiology and pathophysiology of carnosine. *Physiological reviews*, 93(4), pp. 1803–1845.

BOLHASSANI, A., SAFAIYAN, S. and RAFATI, S. (2011) Improvement of different vaccine delivery systems for cancer therapy. *Molecular cancer*, 10(1), pp. 1-20.

BORN, J. et al. (2002) Sniffing neuropeptides: a transnasal approach to the human brain. *Nature Neuroscience*, 5(6), pp. 514–516.

BOYLES, D.A. et al. (2021) Development of Rift valley fever encephalitis in rats is mediated by early infection of olfactory epithelium and neuroinvasion across the cribriform plate. *The Journal of General Virology*, 102(2), p. 1522.

BOZZUTO, G. and MOLINARI, A. (2015) Liposomes as nanomedical devices. *International Journal of Nanomedicine*, 10, p. 975.

BRANHAM, M.L. et al. (2011) Preparation, Spectrochemical, and Computational Analysis of L-Carnosine (2-[(3-Aminopropanoyl)amino]-3-(1H-imidazol-5-yl)propanoic Acid) and Its Ruthenium (II) Coordination Complexes in Aqueous Solution. *Molecules*, 16(12), pp. 10269–10291.

BRANNON-PEPPAS, L. (1995) Recent advances on the use of biodegradable microparticles and nanoparticles in controlled drug delivery. *International Journal of Pharmaceutics*, 116(1), pp. 1–9.

BREDLAU, A.L. et al. (2016) Thermal Therapy Approaches for Treatment of Brain Tumours in Animals and Humans. *Critical Reviews & trade; in Biomedical Engineering*, 44(6), pp. 443–457.

BREKHMAN, V. and NEUFELD, G. (2009) A novel asymmetric 3D in-vitro assay for the study of tumour cell invasion. *BMC Cancer*, 9(1), pp. 1–12.

BRIGGER, I., DUBERNET, C. and COUVREUR, P. (2012) Nanoparticles in cancer therapy and diagnosis. *Advanced Drug Delivery Reviews*, 64, pp. 24–36.

BRIGNOLE, C. et al. (2010) Therapeutic Targeting of TLR9 Inhibits Cell Growth and Induces Apoptosis in Neuroblastoma. *Cancer Research*, 70(23), pp. 9816–9826.

BRODERS-BONDON, F. et al. (2018) Mechanotransduction in tumour progression: The dark side of the force. *Journal of Cell Biology*, 217(5), pp. 1571–1587.

BROERS, J.L. V. et al. (1987) Immunocytochemical Detection of Human Lung Cancer Heterogeneity Using Antibodies to Epithelial, Neuronal, and Neuroendocrine Antigens. *Cancer Research*, 47(12).

BRONSTEIN, L.M. et al. (2007) Influence of iron oleate complex structure on iron oxide nanoparticle formation. *Chemistry of Materials*, 19(15), pp. 3624–3632.

BUDAMA-KILINC, Y., CAKIR-KOC, R. and KECEL-GUNDUZ, S. (2018) Novel NAC-loaded poly (lactide-co- glycolide acid) nanoparticles for cataract treatment: preparation, characterization, evaluation of structure, cytotoxicity, and molecular docking studies. *PeerJ*, 6, e4270.

BULL, J.A. et al. (2020) Mathematical modelling reveals cellular dynamics within tumour spheroids. *PLOS Computational Biology*, 16(8), p. e1007961.

BURROWS, F. et al. (2010) Energy losses in interacting fine-particle magnetic composites. *Journal of Physics D: Applied Physics*, 43(47), p. 474010.

BUTKUS, M.A. and GRASSO, D. (1998) Impact of aqueous electrolytes on interfacial energy. *Journal of Colloid and Interface Science*, 200(1), pp. 172–181.

C

CABRERA, D. et al. (2018) Dynamical Magnetic Response of Iron Oxide Nanoparticles Inside Live Cells. *ACS Nano*, 12(3), pp. 2741–2752.

CAI, H. et al. (2013) Facile hydrothermal synthesis and surface functionalization of polyethyleneimine-coated iron oxide nanoparticles for biomedical applications. *ACS Applied Materials and Interfaces*, 5(5), pp. 1722–1731.

CAI, S. et al. (2007) Micelles of different morphologies - Advantages of worm-like filomicelles of PEO-PCL in paclitaxel delivery. *Pharmaceutical Research*, 24(11), pp. 2099–2109.

CAIRNCROSS, G. et al. (2006) Phase III Trial of Chemotherapy Plus Radiotherapy Compared with Radiotherapy Alone for Pure and Mixed Anaplastic Oligodendroglioma: Intergroup Radiation Therapy Oncology Group Trial 9402. *Journal of Clinical Oncology*, 24, pp. 2707–2714.

CAIZER, C. (2020) Optimization Study on Specific Loss Power in Superparamagnetic Hyperthermia with Magnetite Nanoparticles for High Efficiency in Alternative Cancer Therapy. *Nanomaterials*, 11(1), pp. 1–22.

CAMPBELL, L.L. and POLYAK, K. (2007) Breast Tumour Heterogeneity: Cancer Stem Cells or Clonal Evolution? *Cell cycle*, 6(19), pp. 2332–2338.

CAO, D. et al. (2019) Liposomal doxorubicin loaded PLGA-PEG-PLGA based thermogel for sustained local drug delivery for the treatment of breast cancer. *Artificial cells*, 47(1), pp. 181–191.

CAPRETTO, L. et al. (2013) Microfluidic and lab-on-a-chip preparation routes for organic nanoparticles and vesicular systems for nanomedicine applications. *Advanced Drug Delivery Reviews*, 65(11–12), pp. 1496–1532.

CARLO, E. DI et al. (2009) The Lack of Epithelial Interleukin-7 and BAFF/BLyS Gene Expression in Prostate Cancer as a Possible Mechanism of Tumour Escape from Immunosurveillance. *Clinical Cancer Research*, 15(9), pp. 2979–2987.

CARLSSON, J. et al. (1983) Formation and growth of multicellular spheroids of human origin. *International Journal of Cancer*, 31(5), pp. 523–533.

CARLSSON, J. and YUHAS, J.M. (1984) Liquid-Overlay Culture of Cellular Spheroids. Recent results in cancer research. *Fortschritte der Krebsforschung. Progrès dans les recherches sur le cancer*, 95, pp. 1–23.

CARUGO, D. et al. (2016) Liposome production by microfluidics: Potential and limiting factors. *Scientific Reports*, 6(1), pp.1-15.

CERRATO, P. and CARUSO, G. (2022) Unveiling the Hidden Therapeutic Potential of Carnosine, a Molecule with a Multimodal Mechanism of Action: A Position Paper. *Molecules*, 27(10), p. 3303.

CHAMP, C.E. et al. (2014) Targeting metabolism with a ketogenic diet during the treatment of glioblastoma multiforme. *Journal of Neuro-Oncology*, 117(1), pp. 125–131.

CHAMPION, J.A. and MITRAGOTRI, S. (2006) Role of target geometry in phagocytosis. *Proceedings of the National Academy of Sciences*, 103(13), pp. 4930–4934.

CHAMPION, J.A. and MITRAGOTRI, S. (2009) Shape induced inhibition of phagocytosis of polymer particles. *Pharmaceutical Research*, 26(1), pp. 244–249.

CHANG, H.I. and YEH, M.K. (2012) Clinical development of liposome-based drugs: formulation, characterization, and therapeutic efficacy. *International Journal of Nanomedicine*, 7, p. 49.

CHAPMAN, S. et al. (2013) Nanoparticles for cancer imaging: The good, the bad, and the promise. *Nano Today*, 8(5), pp. 454-460

CHEMMARAPPALLY, J.M. et al. (2020) A co-culture nanofibre scaffold model of neural cell degeneration in relevance to Parkinson's disease. *Scientific Reports*, 10(1), pp. 1–14.

CHEN, L. et al. (2017) Comparison on efficacy of radical prostatectomy versus external beam radiotherapy for the treatment of localized prostate cancer. *Oncotarget*, 8(45), p. 79854.

CHEN, L.F. et al. (2016) Operative Management of Intraventricular Central Neurocytomas: An Analysis of a Surgical Experience with 32 Cases. *Turkish Neurosurgery*, 26(1), pp. 21–28.

CHEN, M. et al. (2020) Remote Control of Mechanical Forces via Mitochondrial-Targeted Magnetic Nanospinners for Efficient Cancer Treatment. *Small*, 16(3), p. 1905424.

CHEN, M.Y. et al. (1999) Variables affecting convection-enhanced delivery to the striatum: a systematic examination of rate of infusion, cannula size, infusate concentration, and tissue-cannula sealing time. *Journal of Neurosurgery*, 90(2), pp. 315–320.

CHENG, Y. et al. (2016) Rotating magnetic field induced oscillation of magnetic particles for in vivo mechanical destruction of malignant glioma. *Journal of Controlled Release*, 223, pp. 75–84.

CHOW, K.K.H. et al. (2015) Combining immunotherapy with radiation for the treatment of glioblastoma. *Journal of Neuro-Oncology*, 123(3), pp. 459–464.

CHRISTIAN, D.A. et al. (2009) Flexible filaments for in vivo imaging and delivery: Persistent circulation of filomicelles opens the dosage window for sustained tumour shrinkage. *Molecular Pharmaceutics*, 6(5), pp. 1343–1352.

CHU, L.-Y. et al. (2007) Controllable Monodisperse Multiple Emulsions. *Angewandte Chemie*, 119(47), pp. 9128–9132.

COHEN, M.H. et al. (2009) FDA Drug Approval Summary: Bevacizumab (Avastin)as Treatment of Recurrent Glioblastoma Multiforme. *The oncologist*, 14(11), pp. 1131-1138.

CONTE, V. et al. (2010) Analysis of propofol/remifentanil infusion protocol for tumour surgery with intraoperative brain mapping. *Journal of Neurosurgical Anesthesiology*, 22(2), pp. 119–127.

CONTE, V. et al. (2013) Bispectral index during asleep-awake craniotomies. *Journal of Neurosurgical Anesthesiology*, 25(3), pp. 279–284.

CORRIGAN, M., WILSON, S.S. and HAMPTON, J. (2015) Safety and efficacy of intranasally administered medications in the emergency department and prehospital settings. *American Journal of Health-System Pharmacy*, 72(18), pp. 1544–1554.

CUNNINGHAM, J. et al. (2008) Biodistribution of Adeno-associated Virus Type-2 in Nonhuman Primates after Convection-enhanced Delivery to Brain. *Molecular Therapy*, 16(7), pp. 1267–1275.

CURTIS, C. et al. (2012) The genomic and transcriptomic architecture of 2,000 breast tumours reveals novel subgroups. *Nature*, 486(7403), pp. 346–352.

CUZZUBBO, S. et al. (2021) Cancer Vaccines: Adjuvant Potency, Importance of Age, Lifestyle, and Treatments. *Frontiers in Immunology*, 11, p. 3850.

D

DAHIYA, R. et al. (1997) High frequency of genetic instability of microsatellites in human prostatic adenocarcinoma. *Journal of Cancer*, 72, pp. 762–767.

DAMIATI, S.A. et al. (2020) Artificial intelligence application for rapid fabrication of size tunable PLGA microparticles in microfluidics. *Scientific Reports*, 10(1), pp. 1–11.

DANHIER, F. et al. (2012) PLGA-based nanoparticles: An overview of biomedical applications. *Journal of Controlled Release*, 161(2), pp. 505–522.

DAS, R. et al. (2016) Tunable High Aspect Ratio Iron Oxide Nanorods for Enhanced Hyperthermia. *Journal of Physical Chemistry C*, 120(18), pp. 10086–10093.

DAUNYS, S. et al. (2021) 3D Tumour Spheroid Models for In Vitro Therapeutic Screening of Nanoparticles. *Advances in Experimental Medicine and Biology*, 1295, pp. 243–270.

DEATSCH, A.E. and EVANS, B.A. (2014) Heating efficiency in magnetic nanoparticle hyperthermia. *Journal of Magnetism and Magnetic Materials*, 354, pp. 163–172.

DEB, P. and BASUMALLICK, A. (2001) Characteristics of α-Fe2O3 nanoparticles prepared by thermolysis of a nonaqueous precursor. *Applied Surface Science*, 182(3–4), pp. 398–402.

DECUZZI, P. et al. (2009) Intravascular delivery of particulate systems: Does geometry really matter? Pharmaceutical Research, 26(1), pp. 235–243.

DERAVE, W. et al. (2010) Muscle carnosine metabolism and beta-alanine supplementation in relation to exercise and training. *Sports medicine*, 40(3), pp. 247–263.

DESHPANDE, K., MUKASYAN, A. and VARMA, A. (2004) Direct Synthesis of Iron Oxide Nanopowders by the Combustion Approach: Reaction Mechanism and Properties. *Chemistry of Materials*, 16(24), pp. 4896–4904.

DESHPANDE, S. et al. (2016) Octanol-assisted liposome assembly on chip. *Nature Communication*, 7(1), pp. 1–9.

DIAB, D.E.H. et al. (2018) Combined Treatments of Magnetic Intra-Lysosomal Hyperthermia with Doxorubicin Promotes Synergistic Anti-Tumoral Activity. *Nanomaterials*, 8(7), p. 468.

DILNAWAZ, F. et al. (2012) The transport of non-surfactant-based paclitaxel loaded magnetic nanoparticles across the blood brain barrier in a rat model. Biomaterials, 33(10), pp. 2936–2951.

DIMARAS, H. and CORSON, T.W. (2019) Retinoblastoma, the visible CNS tumour: A review. *Journal of Neuroscience Research*, 97(1), pp. 29–44.

DINARVAND, R. et al. (2011) Polylactide-co-glycolide nanoparticles for controlled delivery of anticancer agents. *International journal of nanomedicine*, 6, pp. 877–95.

DING, Y., LIU, F. and JIANG, Q. (2013) 12-Hydrothermal Synthesis and Characterization of Fe_3O_4. *Nanorods*. pp. 379–384.

DITTE, Z. et al. (2014) Carnosine inhibits carbonic anhydrase IX-mediated extracellular acidosis and suppresses growth of HeLa tumour xenografts. *BMC Cancer*, 14(1), pp. 1–13.

DJUPESLAND, P.G. (2013) Nasal drug delivery devices: Characteristics and performance in a clinical perspective-a review. *Drug Delivery and Translational Research*, 3(1), pp. 42–62.

DONG, W. and ZHU, C. (2002) Use of ethylene oxide in the sol–gel synthesis of α-Fe_2O_3 nanoparticles from Fe (iii) salts. *Journal of Materials Chemistry*, 12(6), pp. 1676–1683.

DUNCAN, R. and GASPAR, R. (2011) Nanomedicine (s) under the microscope. *Molecular pharmaceutics*, 8(6), pp. 2101-2141.

E

EBRAHIMINEZHAD, A. et al. (2012) Impact of Amino-Acid Coating on the Synthesis and Characteristics of Iron-Oxide Nanoparticles (IONs). *Bulletin of the Korean Chemical Society*, 33(12), pp. 3957–3962.

EDWARDS, S.A. and WILLIAMS, D.R.M. (2004) Double layers and interparticle forces in colloid science and biology: Analytic results for the effect of ionic dispersion forces. *Physical Review Letters*, 92(24), p. 248303.

EL-HAMMADI, M.M. and ARIAS, J.L. (2019) An update on liposomes in drug delivery: a patent review (2014-2018). *Expert Opinion on Therapeutic Patents*, 29(11), pp. 891–907.

ENGELMANN, U.M. et al. (2018) Magnetic relaxation of agglomerated and immobilized iron oxide nanoparticles for hyperthermia and imaging applications. *IEEE Magnetics Letters*, 9, pp. 1-5.

ETAME, A.B. et al. (2012) Focused ultrasound disruption of the blood-brain barrier: a new frontier for therapeutic delivery in molecular neuro-oncology. *Neurosurgical Focus*, 32(1), p. E3.

F

FAN, X. et al. (2013) Magnetic Fe3O4-graphene composites as targeted drug nanocarriers for pH-activated release. *Nanoscale*, 5(3), pp. 1143–1152.

FANG, Y. JIA et al. (2020) Carnosine suppresses human glioma cells under normoxic and hypoxic conditions partly *via* inhibiting glutamine metabolism. *Acta Pharmacologica Sinica*, 42(5), pp. 767–779.

FAZIL, M. et al. (2012) Development and evaluation of rivastigmine loaded chitosan nanoparticles for brain targeting. *European Journal of Pharmaceutical Sciences*, 47(1), pp. 6–15.

FINE, H.A. (2014) Bevacizumab in Glioblastoma– Still Much to Learn. *New England Journal of Medicine*, 370(8), pp. 764–765.

FOGED, C. et al. (2005) Particle size and surface charge affect particle uptake by human dendritic cells in an *in vitro* model. *International journal of pharmaceutics*, 298(2), pp. 315-322.

FOX, C.B. et al. (2014) A nanoliposome delivery system to synergistically trigger TLR4 AND TLR7. *Journal of Nanobiotechnology*, 12(1), pp. 1-9.

FREY, W.H. (2013) Intranasal insulin to treat and protect against posttraumatic stress disorder. *Journal of Nervous and Mental Disease*, 201(7), pp. 638–639.

FULOP, T. et al. (2018) Complement activation in vitro and reactogenicity of low-molecular weight dextran-coated SPIONs in the pig CARPA model: Correlation with physicochemical features and clinical information. *Journal of Controlled Release*, 270, pp. 268–274.

G

GABRILOVICH, D.I. (2017) Myeloid-Derived Suppressor Cells. *Cancer Immunology Research*, 5(1), pp. 3–8.

GALE, E.M. and CARAVAN, P. (2018) Gadolinium-Free Contrast Agents for Magnetic Resonance Imaging of the Central Nervous System. *ACS Chemical Neuroscience*, 9(3), pp. 395–397.

GAUNITZ, F. and HIPKISS, A.R. (2012) Carnosine and cancer: a perspective. *Amino Acids*, 43(1), pp. 135–142.

GAUTAM, P. et al. (2012) Proteins with Altered Levels in Plasma from Glioblastoma Patients as Revealed by iTRAQ-Based Quantitative Proteomic Analysis. *PLOS ONE*, 7(9), p. e46153.

GAVILAN, H., SANCHEZ, E.H., et al. (2017) Formation Mechanism of Maghemite Nanoflowers Synthesized by a Polyol-Mediated Process. *ACS Omega*, 2(10), pp. 7172–7184.

GAVILAN, H., POSTH, O., et al. (2017) How shape and internal structure affect the magnetic properties of anisometric magnetite nanoparticles. *Acta Materialia*, 125, pp. 416–424.

GENG, Y. et al. (2007) Shape effects of filaments versus spherical particles in flow and drug delivery. *Nature Nanotechnology*, 2(4), pp. 249–255.

GERBER, G.S. et al. (1997) Results of Radical Prostatectomy in Men with Locally Advanced Prostate Cancer: Multi-Institutional Pooled Analysis. *European Urology*, 32(4), pp. 385–390.

GHAGHANDA, K.B. et al. (2009) New Dual Mode Gadolinium Nanoparticle Contrast Agent for Magnetic Resonance Imaging. *PLOS ONE*, 4(10), p. e7628.

GILES, A.J. et al. (2018) Dexamethasone-induced immunosuppression: Mechanisms and implications for immunotherapy. *Journal for ImmunoTherapy of Cancer*, 6(1), pp. 1–13.

DI GIOIA, S. and CONESE, M. (2008) Polyethylenimine-mediated gene delivery to the lung and therapeutic applications. *Drug design, development, and therapy*, 2(2), p. 163.

GOLOVIN, Y.I. et al. (2021) Non-Heating Alternating Magnetic Field Nanomechanical Stimulation of Biomolecule Structures *via* Magnetic Nanoparticles as the Basis for Future Low-Toxic Biomedical. *Nanomaterials*, 11(9), p. 2255.

GOLOVIN, Y.I. et al. (2015) Towards nanomedicines of the future: Remote magneto-mechanical actuation of nanomedicines by alternating magnetic fields. *Journal of Controlled Release*, 219, pp. 43–60.

GOMES, F.C.A., PAULIN, D. and MOURA NETO, V. (1999) Glial fibrillary acidic protein (GFAP): modulation by growth factors and its implication in astrocyte differentiation. *Brazilian journal of medical and biological research*, 32, pp. 619-631.

GOMEZ, D. et al. (2012) Intranasal treatment of neurodegenerative diseases and stroke. *Frontiers in Bioscience-Scholar*, 4(1), pp. 74–89.

GREF, R. et al. (1994) Biodegradable Long-Circulating Polymeric Nanospheres. *Science*, 263(5153), pp. 1600–1603.

GREGORIADIS, G. Liposome Technology Third Edition Volume I Liposome Preparation and Related Techniques. (Vol. 3). CRC press.

GREGORIADIS, G. (2016) Liposomes in Drug Delivery: How It All Happened. *Pharmaceutics*, 8(2), p. 19.

GROSSMAN, S.A. et al. (2011) Immunosuppression in patients with high-grade gliomas treated with radiation and temozolomide. *Clinical Cancer Research*, 17(16), pp. 5473–5480.

GUARDIA, P. et al. (2012) Water-soluble iron oxide nanocubes with high values of specific absorption rate for cancer cell hyperthermia treatment. *ACS Nano*, 6(4), pp. 3080–3091.

GUASTELLA, A.J. et al. (2013) Recommendations for the standardisation of oxytocin nasal administration and guidelines for its reporting in human research. *Psychoneuroendocrinology*, 38(5), pp. 612–625.

GUEVARA, M.L. et al. (2019) Codelivery of mRNA with α-galactosylceramide using a new lipopolyplex formulation induces a strong antitumor response upon intravenous administration. *ACS Omega*, 4(8), pp. 13015–13026.

GUO, T. et al. (2015) A comprehensive review on synthesis methods for transition-metal oxide nanostructures. *CrystEngComm*, 17(19), pp. 3551–3585.

GUPTA, A.K. et al. (2007) Recent advances on surface engineering of magnetic iron oxide nanoparticles and their biomedical applications. *Nanomedicine*, 2(1), pp. 32–39.

GUPTA, A.K. and GUPTA, M. (2005) Synthesis and surface engineering of iron oxide nanoparticles for biomedical applications. *Biomaterials*, 26(18), pp. 3995–4021.

H

HABRA, K. et al. (2022) Controlled release of carnosine from poly(lactic- co -glycolic acid) beads using nanomechanical magnetic trigger towards the treatment of glioblastoma. *Nanoscale Advances*, 4(10), pp. 2242-2249.

HABRA, K. et al. (2021) Synthesis and Functionalisation of Superparamagnetic Nano-Rods towards the Treatment of Glioblastoma Brain Tumours. *Nanomaterials*, 11(9), p. 2157.

HAISLER, W.L. et al. (2013) Three-dimensional cell culturing by magnetic levitation. *Nature Protocols*, 8(10), pp. 1940–1949.

HAMANO, N. et al. (2019) Robust microfluidic technology and new lipid composition for fabrication of curcumin-loaded liposomes: effect on the anticancer activity and safety of cisplatin. *Molecular Pharmaceutics*, 16(9), pp. 3957–3967.

HAMMOND, T.G. and HAMMOND, J.M. (2001) Optimized suspension culture: The rotating-wall vessel. *American Journal of Physiology - Renal Physiology*, 281(1), pp. 12-25.

HAN, F.Y. et al. (2016) Bioerodible PLGA-Based Microparticles for Producing Sustained-Release Drug Formulations and Strategies for Improving Drug Loading. *Frontiers in Pharmacology*, 6, p. 185.

HAN, T. et al. (2017) Factory-on-chip: Modularised microfluidic reactors for continuous mass production of functional materials. *Chemical Engineering Journal*, 326, pp. 765–773.

HANAHAN, D. and WEINBERG, R.A. (2011) Hallmarks of Cancer: The Next Generation. *Cell*, 144(5), pp. 646–674.

HANAHAN, D. and WEINBERG, R.A. (2000) The Hallmarks of Cancer. *Cell*, 100(1), pp. 57–70.

HARBAUGH, R.E., SAUNDERS, R.L. and REEDER, R.F. (1988) Use of Implantable Pumps for Central Nervous System Drug Infusions to Treat Neurological Disease. *Neurosurgery*, 23(6), pp. 693–698.

HASANI-SADRABADI, M.M. et al. (2016) Microfluidic Manipulation of Core/Shell Nanoparticles for Oral Delivery of Chemotherapeutics: A New Treatment Approach for Colorectal Cancer. *Advanced Materials*, 28(21), pp. 4134–4141.

HASHIZUME, R. et al. (2008) New therapeutic approach for brain tumours: Intranasal delivery of telomerase inhibitor GRN163. *Neuro-Oncology*, 10(2), pp. 112–120.

HASS, D.T. and BARNSTABLE, C.J. (2016) Uncoupling protein 2 in the glial response to stress: implications for neuroprotection. *Neural Regeneration Research*, 11(8), p. 1197.

HASSEL, J.C. et al. (2017) Combined immune checkpoint blockade (anti-PD-1/anti-CTLA-4): Evaluation and management of adverse drug reactions. *Cancer Treatment Reviews*, 57, pp. 36–49.

HAYASHI, K. et al. (2014) Magnetically Responsive Smart Nanoparticles for Cancer Treatment with a Combination of Magnetic Hyperthermia and Remote-Control Drug Release. *Theranostics*, 4(8), pp. 834–844.

HE, Y. et al. (2020) Fabrication of micro-cages and caged tumour spheroids for microfluidic chip-based assays. *Microelectronic Engineering*, 225, p. 111256.

HEDLEY, D., OGILVIE, L. and SPRINGER, C. (2007) Carboxypeptidase G2-based gene-directed enzyme–prodrug therapy: a new weapon in the GDEPT armoury. *Nature Reviews Cancer*, 7(11), pp. 870–879.

HERVAULT, A. and THANH, N.T.K. (2014) Magnetic nanoparticle-based therapeutic agents for thermo-chemotherapy treatment of cancer. *Nanoscale*, 6(20), pp. 11553–11573.

HEBELMANN, V. et al. (2017) Accuracy of High-Field Intraoperative MRI in the Detectability of Residual Tumour in Glioma Grade IV Resections. *RoFo Fortschritte auf dem Gebiet der Rontgenstrahlen und der Bildgebenden Verfahren*, 189(6), pp. 519–526.

HIPKISS, A.R. et al. (1998) Pluripotent protective effects of carnosine, a naturally occurring dipeptide. *Annals of the New York Academy of Sciences*, 854, pp. 37–53.

HIPKISS, A.R., BROWNSON, C. and CARRIER, M.J. (2001) Carnosine, the anti-ageing, antioxidant dipeptide, may react with protein carbonyl groups. *Mechanisms of Ageing and Development*, 122(13), pp. 1431–1445.

HIPKISS, A.R. and GAUNITZ, F. (2014) Inhibition of tumour cell growth by carnosine: Some possible mechanisms. *Amino Acids*, pp. 327–337.

HJELSTUEN, M.H. et al. (2009) Penetration and Binding of Monoclonal Antibody in Human Osteosarcoma Multicell Spheroids: Comparison of confocal laser scanning microscopy and autoradiography. *Acta Oncologica*, 35(3), pp. 273–279.

HOEKMAN, J.D. and HO, R.J.Y. (2011) Effects of Localized Hydrophilic Mannitol and Hydrophobic Nelfinavir Administration Targeted to Olfactory Epithelium on Brain Distribution. *AAPS PharmSciTech*, 12(2), pp. 534–543.

HOLA, K. et al. (2015) Tailored functionalization of iron oxide nanoparticles for MRI, drug delivery, magnetic separation and immobilization of bio substances. *Biotechnology Advances*, 33(6), pp. 1162–1176.

HOLLAND, E.C. (2000) Glioblastoma multiforme: The terminator. *Proceedings of the National Academy of Sciences*, 97(12), pp. 6242–6244.

HOLLIDAY, R. and MCFARLAND, G.A. (1996) Inhibition of the growth of transformed and neoplastic cells by the dipeptide carnosine. *British Journal of Cancer*, 73(8), pp. 966–971.

HONG, S.S. et al. (2019) Liposomal Formulations for Nose-to-Brain Delivery: Recent Advances and Future Perspectives. *Pharmaceutics*, 11(10), p. 540.

HOOD, RENEE R et al. (2015) High-Throughput Continuous Flow Production of Nanoscale Liposomes by Microfluidic Vertical Flow Focusing. *Small*, 11(43), pp. 5790–5799.

HOOD, R.R. et al. (2014) A facile route to the synthesis of monodisperse nanoscale liposomes using 3D microfluidic hydrodynamic focusing on a concentric capillary array. *Lab on a Chip*, 14(14), pp. 2403–2409.

HOOD, R.R. et al. (2013) Microfluidic Synthesis of PEG- and Folate-Conjugated Liposomes for One-Step Formation of Targeted Stealth Nanocarriers. *Pharmaceutical Research*, 30(6), pp. 1597–1607.

HOTTINGER, A.F., PACHECO, P. and STUPP, R. (2016) Tumour treating fields: a novel treatment modality and its use in brain tumours. *Neuro-Oncology*, 18(10), pp. 1338–1349.

HOUJEGHANI, S. et al. (2018) l-Carnosine supplementation attenuated fasting glucose, triglycerides, advanced glycation end products, and tumour necrosis factor-α levels in patients with type 2 diabetes: a double-blind placebo-controlled randomized clinical trial. *Nutrition research*, 49, pp. 96–106.

HSIEH, M.H. and NGUYEN, H.T. (2005) Molecular mechanism of apoptosis induced by mechanical forces. *International review of cytology*, 245, pp. 45–90.

HU, M. et al. (2012) Hierarchical magnetic iron (III) oxides prepared by solid-state thermal decomposition of coordination polymers. *RSC Advances*, 2(11), pp. 4782–4786.

I

ILLUM, L. et al. (2002) Intranasal Delivery of Morphine. Journal of Pharmacology and Experimental *Therapeutics*, 301(1), pp. 391–400.

ILLUM, L. (2000) Transport of drugs from the nasal cavity to the central nervous system. European *Journal of Pharmaceutical Sciences*, 11(1), pp. 1–18.

IOVINE, B. et al. (2016) l-carnosine dipeptide overcomes acquired resistance to 5-fluorouracil in HT29 human colon cancer cells via downregulation of HIF1-alpha and induction of apoptosis. *Biochimie*, 127, pp. 196–204.

IVASCU, A. and KUBBIES, M. (2006) Rapid Generation of Single-Tumour Spheroids for High-Throughput Cell Function and Toxicity Analysis. *SLAS Discovery*, 11(8), pp. 922-932

J

JAHN, A. et al. (2007) Microfluidic Directed Formation of Liposomes of Controlled Size. *Langmuir*, 23(11), pp. 6289–6293.

JAHN, A. et al. (2010) Microfluidic mixing and the formation of nanoscale lipid vesicles. *ACS Nano*, 4(4), pp. 2077–2087.

JAIN, K.K. (2018) A critical overview of targeted therapies for glioblastoma. *Frontiers in oncology*, 8, p. 419.

JAIN, R. et al. (2010) Micellar nanocarriers: Potential nose-to-brain delivery of zolmitriptan as novel migraine therapy. *Pharmaceutical Research*, 27(4), pp. 655–664.

JAIN, RAKESH K., MARTIN, J.D. and STYLIANOPOULOS, T. (2014) The role of mechanical forces in tumour growth and therapy. *Annual Review of Biomedical Engineering*, 16, pp. 321–346.

VAN DER JEUGHT, K. et al. (2018) Dendritic Cell Targeting mRNA Lipopolyplexes Combine Strong Antitumor T-Cell Immunity with Improved Inflammatory Safety. *ACS Nano*, 12(10), pp. 9815-9829.

JIANG, Y., LI, Y. and LIU, X. (2015) Intranasal delivery: circumventing the iron curtain to treat neurological disorders. *Expert opinion on drug delivery*, 12(11), pp. 1717–1725.

K

KALVIAINEN, R. (2015) Intranasal therapies for acute seizures. *Epilepsy & Behaviour*, 49, pp. 303–306.

KANDASAMY, G. and MAITY, D. (2015) Recent advances in superparamagnetic iron oxide nanoparticles (SPIONs) for *in vitro* and in vivo cancer nano theranostics. *International Journal of Pharmaceutics*, 496(2), pp. 191–218.

KANG, M.L., CHO, C.S. and YOO, H.S. (2009) Application of chitosan microspheres for nasal delivery of vaccines. *Biotechnology Advances*, 27(6), pp. 857–865.

KANTOFF, P.W. et al. (2010) Sipuleucel-T Immunotherapy for Castration-Resistant Prostate Cancer. *New England Journal of Medicine*, 363(5), pp. 411–422.

KASTNER, E. et al. (2014) High-throughput manufacturing of size-tuned liposomes by a new microfluidics method using enhanced statistical tools for characterization. *International Journal of Pharmaceutics*, 477(1–2), pp. 361–368.

KASTNER, E. et al. (2015) Microfluidic-controlled manufacture of liposomes for the solubilisation of a poorly water-soluble drug. *International Journal of Pharmaceutics*, 485(1–2), pp. 122–130.

KHAN, A.R. et al. (2017) Progress in brain targeting drug delivery system by nasal route. *Journal of controlled release*, 268, pp. 364–389.

KHAN, A.R. et al. (2018) Recent progress of drug nano formulations targeting to brain. *Journal of Controlled Release*, 291, pp. 37–64.

KHAN, M.A. et al. (2004) Impact of surgical delay on long-term cancer control for clinical localized prostate cancer. *The Journal of Urology*, 172(5), pp. 1835–1839.

KHOLLAM, Y.B. et al. (2002) Microwave hydrothermal preparation of submicron-sized spherical magnetite (Fe_3O_4) powders. *Materials Letters*, 56(4), pp. 571–577.

KIM, I.D. et al. (2012) Intranasal Delivery of HMGB1 siRNA Confers Target Gene Knockdown and Robust Neuroprotection in the Postischemic Brain. *Molecular Therapy*, 20(4), pp. 829–839.

KIM, Y.S. et al. (2018) PLGA nanoparticles with multiple modes are a biologically safe nanocarrier for mammalian development and their offspring. *Biomaterials*, 183, pp. 43–53.

KINOSHITA, M. et al. (2006) Non-invasive localized delivery of Herceptin to the mouse brain by MRI-guided focused ultrasound-induced blood-brain barrier disruption. *Proceedings of the National Academy of Sciences of the United States of America*, 103(31), pp. 11719–11723.

KINOSHITA, M. et al. (2006) Targeted delivery of antibodies through the blood–brain barrier by MRI-guided focused ultrasound. *Biochemical and Biophysical Research Communications*, 340(4), pp. 1085–1090.

KIRBY, M., HIRST, C. and CRAWFORD, E.D. (2011) Characterising the castration-resistant prostate cancer population: a systematic review. *International Journal of Clinical Practice*, 65(11), pp. 1180–1192.

KLIBANOV, A.L. et al. (1990) Amphipathic polyethylene glycols effectively prolong the circulation time of liposomes. *FEBS Letters*, 268(1), pp. 235–237.

KOLENDA, J. et al. (2011) Effects of hypoxia on expression of a panel of stem cell and chemoresistance markers in glioblastoma-derived spheroids. *Journal of Neuro-Oncology*, 103(1), pp. 43–58.

KOLEN'KO, Y. V. et al. (2014) Large-scale synthesis of colloidal Fe3O4 nanoparticles exhibiting high heating efficiency in magnetic hyperthermia. *Journal of Physical Chemistry C*, 118(16), pp. 8691–8701.

KRISHNAN, J.K.S. et al. (2017) Effect of administration method, animal weight and age on the intranasal delivery of drugs to the brain. *Journal of Neuroscience Methods*, 286, pp. 16–21.

KRISHNAN, J.K.S. et al. (2016) Intranasal delivery of obidoxime to the brain prevents mortality and CNS damage from organophosphate poisoning. *NeuroToxicology*, 53, pp. 64–73.

KROMER, C. et al. (2017) Estimating the annual frequency of synchronous brain metastasis in the United States 2010–2013: a population-based study. *Journal of Neuro-Oncology*, 134(1), pp. 55–64.

KUNG, C. TE et al. (2020) Microfluidic synthesis control technology and its application in drug delivery, bioimaging, biosensing, environmental analysis and cell analysis. *Chemical Engineering Journal*, 399, p. 125748.

KUNZ-SCHUGHART, L.A. (1999) Multicellular tumour spheroids: intermediates between monolayer culture and *in vivo* tumour. *Cell Biology International*, 23(3), pp. 157–161.

KYRIAZIS, M. (2010) Aging. *Drug Discovery Today: Therapeutic Strategies*, 3–4(7), pp. 45–49.

L

DE LA PRESA, P. et al. (2015) Particle interactions in liquid magnetic colloids by zero field cooled measurements: Effects on heating efficiency. *Journal of Physical Chemistry C*, 119(20), pp. 11022–11030.

LABARBERA, D. V., REID, B.G. and YOO, B.H. (2012) The multicellular tumour spheroid model for high-throughput cancer drug discovery. *Expert opinion on drug discovery*, 7(9), pp. 819–830.

LADOMERSKY, E. et al. (2018) IDO1 inhibition synergizes with radiation and PD-1 blockade to durably increase survival against advanced glioblastoma. *Clinical Cancer Research*, 24(11), pp. 2559–2573.

LAI, C. et al. (2018) The enhanced antitumor-specific immune response with mannose- and CpG-ODN-coated liposomes delivering TRP2 peptide. *Theranostics*, 8(6), pp. 1723–1739.

LANDIS, M.S., BOYDEN, T. and PEGG, S. (2012) Nasal-to-CNS drug delivery: where are we now and where are we heading? An industrial perspective. *Therapeutic delivery*, 3(2), pp. 195–208.

LEARY, E. et al. (2018) Quantitative Live-Cell Confocal Imaging of 3D Spheroids in a High-Throughput Format. *SLAS Technology*, 23(3), pp. 231–242.

LENZI, P. et al. (2016) The autophagy oproteasome a novel cell clearing organelle in baseline and stimulated conditions. *Frontiers in Neuroanatomy*, 10(7), p. 78.

LESHUK, T., KRISHNAKUMAR, H. and GU, F. (2015) Size-tunable Fe3O4 spherical nanoclusters through a one-pot hydrothermal synthesis. *Journal of Nanoscience and Nanotechnology*, 15(7), pp. 5378–5383.

LEU, M.P. et al. (2020) Easy mass production of homogenous and uniform 3D spheroids for high-throughput screening applications. chayon.co.kr, https://www.chayon.co.kr/wp-content/uploads/2021/02/MPLeu-et-al-V17-20200703.pdf [Accessed 11/05/2022].

LI, H. and ZHU, Y.J. (2020) Liquid-Phase Synthesis of Iron Oxide Nanostructured Materials and Their Applications. *Chemistry – A European Journal*, 26(42), pp. 9180–9205.

LI, Y. HUA et al. (2015) Intranasal delivery of stem cells as therapy for central nervous system disease. *Experimental and Molecular Pathology*, 98(2), pp. 145–151.

LI, Z. et al. (2008) Direct Coprecipitation Route to Monodisperse Dual-Functionalized Magnetic Iron Oxide Nanocrystals Without Size Selection. *Small*, 4(2), pp. 231–239.

LIAN, Z. et al. (2020) Microfluidic formation of highly monodispersed multiple cored droplets using needle-based system in parallel mode. *Electrophoresis*, 41(10–11), pp. 891–901.

LIANG, C.-C., PARK, A.Y. and GUAN, J.-L. (2007) In vitro scratch assay: a convenient and inexpensive method for analysis of cell migration *in vitro*. *Nature Protocols*, 2(2), pp. 329–333.

LIANG, X. et al. (2006) Synthesis of Nearly Monodisperse Iron Oxide and Oxyhydroxide Nanocrystals. *Advanced Functional Materials*, 16(14), pp. 1805–1813.

LIM, J.H. et al. (2009) Protective effect of bromocriptine against BH4-induced Cath.a cell death involving up-regulation of antioxidant enzymes. *Neuroscience Letters*, 451(3), pp. 185–189.

LINZ, N. et al. (2016) Wavelength dependence of femtosecond laser-induced breakdown in water and implications for laser surgery. *Physical Review B*, 94(2), pp. 024113.

LIPPENS, R.J.J. (1999) Liposomal daunorubicin (Daunoxome) in children with recurrent or progressive brain tumours. *Pediatric Hematology and Oncology*, 16(2), pp. 131–139.

LIU, H. et al. (2019) Differentiation of human glioblastoma U87 cells into cholinergic neuron. *Neuroscience Letters*, 704, pp. 1–7.

LIU, P. et al. (2012) Cytotoxic effect of disulfiram/copper on human glioblastoma cell lines and ALDH-positive cancer-stem-like cells. *British Journal of Cancer*, 107(9), pp. 1488–1497.

LIU, Q. et al. (2015) PH-Responsive poly(D,L-lactic-co-glycolic acid) nanoparticles with rapid antigen release behaviour promote immune response. *ACS Nano*, 9(5), pp. 4925–4938.

LIU, X. et al. (2020) Comprehensive understanding of magnetic hyperthermia for improving antitumor therapeutic efficacy. *Theranostics*, 10(8), pp. 3793–3815.

LIU, Y. et al. (2011) Studies of Fe_3O_4-chitosan nanoparticles prepared by co-precipitation under the magnetic field for lipase immobilization. *Catalysis Communications*, 12(8), pp. 717–720.

LOCHHEAD, J.J. and THORNE, R.G. (2012) Intranasal delivery of biologics to the central nervous system. *Advanced Drug Delivery Reviews*, 64(7), pp. 614–628.

LU, C.T. et al. (2014) Current approaches to enhance CNS delivery of drugs across the brain barriers. *International Journal of Nanomedicine*, 9(1), p. 2241.

LUNDQVIST, M. et al. (2008) Nanoparticle size and surface properties determine the protein corona with possible implications for biological impacts. *Proceedings of the National Academy of Sciences*, 105(38), pp. 14265–14270.

LV, Y. et al. (2009) Synthesis, characterization, and growing mechanism of monodisperse Fe_3O_4 microspheres. *Journal of Crystal Growth*, 311(13), pp. 3445–3450.

M

MACDONALD, N. et al. (2020) Global vaccine action plan lessons learned I: Recommendations for the next decade. *Vaccine*, 38(33), pp. 5364–5371.

MAHMOUDI, M. et al. (2009) Cell toxicity of superparamagnetic iron oxide nanoparticles. *Journal of Colloid and Interface Science*, 336(2), pp. 510–518.

MAHMOUDI, M., SIMCHI, A. and IMANI, M. (2010) Recent advances in surface engineering of superparamagnetic iron oxide nanoparticles for biomedical applications. *Journal of the Iranian Chemical Society*, 7(S2), pp. S1–S27.

MAHMUD, A. et al. (2017) Spray stability of self-assembled filaments for delivery. *Journal of Controlled Release*, 263, pp. 162–171.

MAI, Y. et al. (2020) Intranasal delivery of cationic liposome-protamine complex mRNA vaccine elicits effective anti-tumour immunity. *Cellular Immunology*, 354, p. 104143.

MAJEWSKI, P. and THIERRY, B. (2008) Functionalized Magnetite Nanoparticles—Synthesis, Properties, and Bio applications. *Particulate Systems in Nano- and Biotechnologies*, pp. 331–352.

MAKADIA, H.K. and SIEGEL, S.J. (2011) Poly Lactic-co-Glycolic Acid (PLGA) as Biodegradable Controlled Drug Delivery Carrier. *Polymers*, 3(3), pp. 1377–1397.

MANGRAVITI, A. et al. (2016) Nanobiotechnology-based delivery strategies: new frontiers in brain tumour targeted therapies. *Journal of Controlled Release*, 240, pp. 443–453.

MARTINEZ-BOUBETA, C. et al. (2013) Learning from Nature to Improve the Heat Generation of Iron-Oxide Nanoparticles for Magnetic Hyperthermia Applications. *Scientific Reports*, 3(1), pp. 1–8.

MASON, M. (2009) Management of prostate cancer: future treatment approaches. *Future Prescriber*, 10(3), pp. 9–12.

MASTER, A.M. et al. (2016) Remote Actuation of Magnetic Nanoparticles for Cancer Cell Selective Treatment Through Cytoskeletal Disruption. *Scientific Reports*, 6(1), pp. 1–13.

MAZZITELLI, S. et al. (2013) Preparation of cell-encapsulation devices in confined microenvironment. *Advanced Drug Delivery Reviews*, 65(11–12), pp. 1533–1555.

MCCARROLL, J.A. et al. (2004) Pancreatic stellate cell migration: Role of the phosphatidylinositol 3-kinase (PI3-kinase) pathway. *Biochemical Pharmacology*, 67(6), pp. 1215–1225.

MCCARTNEY, L.N. and LEVINE, S. (1969) An improvement on Derjaguin's expression at small potentials for the double layer interaction energy of two spherical colloidal particles. *Journal of Colloid and Interface Science*, 30(3), pp. 345–354.

MCGUIRE, S. (2016) World Cancer Report 2014. Geneva, Switzerland: World Health Organization, International Agency for Research on Cancer, WHO Press, 2015. *Advances in Nutrition*, 7(2), pp. 418–419.

MCNEEL, D.G. et al. (2016) The Society for Immunotherapy of Cancer consensus statement on immunotherapy for the treatment of prostate carcinoma. *Journal for Immunotherapy of Cancer*, 4(1), pp. 1–12.

MD, S. et al. (2014) Drug Development and Industrial Pharmacy Preparation, characterization, in vivo biodistribution and pharmacokinetic studies of donepezil-loaded PLGA nanoparticles for brain targeting Preparation, characterization, in vivo biodistribution and pharmacoki-netic studies of donepezil-loaded PLGA nanoparticles for brain targeting. *Drug Dev Ind Pharm*, 40(2), pp. 278–287.

MEDEIROS, S.F. et al. (2015) Synthesis and characterization of stable aqueous dispersion of functionalized double-coated iron oxide nanoparticles. *Materials Letters*, 160, pp. 522–525.

MEHDAOUI, B. et al. (2013) Increase of magnetic hyperthermia efficiency due to dipolar interactions in low-anisotropy magnetic nanoparticles: Theoretical and experimental results. *Physical Review B - Condensed Matter and Materials Physics*, 87(17), p. 174419.

MIJAJLOVIC, M. et al. (2013) Microfluidic hydrodynamic focusing based synthesis of POPC liposomes for model biological systems. *Colloids and Surfaces B: Biointerfaces*, 104, pp. 276–281.

MILLER, J.L. et al. (2008) Comparison of Intranasal Administration of Haloperidol with Intravenous and Intramuscular Administration: A Pilot Pharmacokinetic Study. *Pharmacotherapy*, 28(7), pp. 875–882.

MIRVAKILI, S.M. and LANGER, R. (2021) Wireless on-demand drug delivery. *Nature Electronics*, 4(7), pp. 464–477.

MISTRY, A., STOLNIK, S. and ILLUM, L. (2009) Nanoparticles for direct nose-to-brain delivery of drugs. *International Journal of Pharmaceutics*, 379(1), pp. 146–157.

MITSIADES, N. et al. (2012) Distinct Patterns of Dysregulated Expression of Enzymes Involved in Androgen Synthesis and Metabolism in Metastatic Prostate Cancer Tumours. *Cancer Research*, 72(23), pp. 6142–6152.

MITTAL, S. et al. (2017) Alternating electric tumour treating fields for treatment of glioblastoma: rationale, preclinical, and clinical studies. *Journal of Neurosurgery*, 128(2), pp. 414–421.

MOHAPATRA, J. et al. (2015) Iron oxide nanorods as high-performance magnetic resonance imaging contrast agents. 7(20),

MOJARAD-JABALI, S. et al. (2021) An update on actively targeted liposomes in advanced drug delivery to glioma. *International Journal of Pharmaceutics*, 602, p. 120645.

MOORE, B.A. and BARNETT, J.E. (2015) Oxford Handbook of Oncology. Case Studies in Clinical Psychological Science: Bridging the Gap from Science to Practice, pp. 1–7.

MOSELLA, M. et al. (2017) Gene-52. Epigenomic Glioma Subtype Evaluation Across 31 Tumour Type. *Neuro-Oncology*, 19(6), pp. 103–104.

MOUGIN, J., BOURGAUX, C. and COUVREUR, P. (2021) Elongated self-assembled nanocarriers: From molecular organization to therapeutic applications. *Advanced Drug Delivery Reviews*, 172, pp. 127–147.

MUNDARGI, R.C. et al. (2008) Nano/micro technologies for delivering macromolecular therapeutics using poly (D, L-lactide-co-glycolide) and its derivatives. *Journal of Controlled Release*, 125(3), pp. 193-209.

N

NAGAI, K. and SUDA, T. (1986) Antineoplastic effects of carnosine and beta-alanine--physiological considerations of its antineoplastic effects. *Journal of the Physiological Society of Japan*, 48(11), pp. 741–747.

NAKAMURA, T. et al. (2017) Modifying Cationic Liposomes with Cholesteryl-PEG Prevents Their Aggregation in Human Urine and Enhances Cellular Uptake by Bladder Cancer Cells. *Biological and Pharmaceutical Bulletin*, 40(2), pp. 234–237.

NANCE, E. et al. (2021) Drug delivery to the central nervous system. *Nature Reviews Materials*, 7(4), pp. 314–331.

NAUD, C. et al. (2020) Cancer treatment by magneto-mechanical effect of particles, a review. *Nanoscale Advances*, 2(9), pp. 3632–3655.

NEE KOO, K. et al. (2019) Preparation and characterization of superparamagnetic magnetite (Fe_3O_4) nanoparticles: A short review. *Malaysian Journal of Fundamental and Applied Sciences*, 15(1), pp. 23–31.

NEELAPU, S.S. et al. (2004) Human Autologous Tumour-Specific T-Cell Responses Induced by Liposomal Delivery of a Lymphoma Antigen. *Clinical Cancer Research*, 10(24), pp. 8309-8317

NEMATI, Z. et al. (2018) Improving the Heating Efficiency of Iron Oxide Nanoparticles by Tuning Their Shape and Size. *Journal of Physical Chemistry C*, 122(4), pp. 2367–2381.

NI, S. et al. (2009) Hydrothermal synthesis of Fe_3O_4 nanoparticles and its application in lithium-ion battery. *Materials Letters*, 63(30), pp. 2701–2703.

NIE, S. (2010) Editorial: Understanding and overcoming major barriers in cancer nanomedicine. *Nanomedicine*, 5(4), pp. 523–528.

O

OCANA, M., MORALES, M.P. and SERNA, C.J. (1995) The Growth Mechanism of α-Fe_2O_3 Ellipsoidal Particles in Solution. *Journal of Colloid and Interface Science*, 171(1), pp. 85–91.

OGURA, I. et al. (1996) Characterization of Low-Molecular-Weight Using GC/CI-MS and GC Polyethyleneimines. *Nanomaterials*, 11(9), p. 2157

OLOV HEDLUND, P. et al. (2008) Parenteral estrogen versus combined androgen deprivation in the treatment of metastatic prostatic cancer: part 2. Final evaluation of the Scandinavian Prostatic. *Taylor & Francis*,42 (5), pp. 220–229.

OPPERMANN, H., ALVANOS, A., et al. (2019) Carnosine influences transcription via epigenetic regulation as demonstrated by enhanced histone acetylation of the pyruvate dehydrogenase kinase 4 promoter in glioblastoma cells. *Amino Acids*, 51(1), pp. 61–71.

OPPERMANN, H. et al. (2018) Carnosine selectively inhibits migration of IDH-wildtype glioblastoma cells in a co-culture model with fibroblasts. *Cancer Cell International*, 18(1), pp. 1–10.

OPPERMANN, H., PURCZ, K., et al. (2019) Carnosine's inhibitory effect on glioblastoma cell growth is independent of its cleavage. *Amino Acids*, 51(5), pp. 761–772.

OPPERMANN, H. et al. (2016) Pyruvate attenuates the anti-neoplastic effect of carnosine independently from oxidative phosphorylation. *Oncotarget*, 7(52), p. 85848.

OPPERMANN, H., HEINRICH, M., et al. (2019) The proton-coupled oligopeptide transporters PEPT2, PHT1 and PHT2 mediate the uptake of carnosine in glioblastoma cells. *Amino Acids*, 51(7), pp. 999–1008.

OSTER, C.G. and KISSEL, T. (2005) Comparative study of DNA encapsulation into PLGA microparticles using modified double emulsion methods and spray drying techniques. *Journal of Microencapsulation*, 22(3), pp. 235–244.

OTA, S., YOSHIZAWA, S. and TAKEUCHI, S. (2009) Microfluidic Formation of Monodisperse, Cell-Sized, and Unilamellar Vesicles. *Angewandte Chemie International Edition*, 48(35), pp. 6533–6537.

OVEJERO, J.G. et al. (2016) Effects of inter- and intra-aggregate magnetic dipolar interactions on the magnetic heating efficiency of iron oxide nanoparticles. *Physical Chemistry Chemical Physics*, 18(16), pp. 10954–10963.

P

P. SHAH, P. et al. (2012) Enhanced skin permeation using polyarginine modified nanostructured lipid carriers. *Journal of Controlled Release*, 161(3), pp. 735–745.

PAN, Z. and DING, J. (2012) Poly(lactide-co-glycolide) porous scaffolds for tissue engineering and regenerative medicine. *Interface Focus*, 2(3), pp. 366–377.

PANDURANGAN, M. et al. (2016) Efficacy of carnosine on activation of caspase 3 and human renal carcinoma cell inhibition. *International Journal of Biological Macromolecules*, 92, pp. 377–382.

PANYAM, J. and LABHASETWAR, V. (2003) Biodegradable nanoparticles for drug and gene delivery to cells and tissue. *Advanced Drug Delivery Reviews*, 55(3), pp. 329–347.

PARDRIDGE, W.M. (2007) Blood brain barrier delivery. *Drug Discovery Today*, 12(1–2), pp. 54–61.

PARDRIDGE, W.M. (2005) The Blood Brain Barrier: Bottleneck in Brain Drug Development. *NeuroRX*, 2(1), pp. 3–14.

PARK, J.S. et al. (2017) Construction of PLGA nanoparticles coated with polycistronic SOX5, SOX6, and SOX9 genes for chondrogenesis of human mesenchymal stem cells. *ACS Applied Materials and Interfaces*, 9(2), pp. 1361–1372.

PATIL, R.M. et al. (2018) Comprehensive cytotoxicity studies of superparamagnetic iron oxide nanoparticles. *Biochemistry and biophysics reports*, 13, pp. 63-72.

PAUTOT, S., FRISKEN, B.J. and WEITZ, D.A. (2003) Engineering asymmetric vesicles. *Proceedings of the National Academy of Sciences*, 100(19), pp. 10718–10721.

PEARSON, J.R.D. et al. (2019) Abstract B122: Development of a new immunotherapy treatment for glioblastoma multiforme. *Cancer Immunology Research*, 7(2), p. 122.

PEREIRA, C. et al. (2012) Superparamagnetic MFe_2O_4 (M = Fe, Co, Mn) nanoparticles: Tuning the particle size and magnetic properties through a novel one-step coprecipitation route. *Chemistry of Materials*, 24(8), pp. 1496–1504.

PERRIE, Y. et al. (2016) Designing liposomal adjuvants for the next generation of vaccines. *Advanced Drug Delivery Reviews*, 99, pp. 85–96.

PETERSON, A. et al. (2014) A systematic review of inhaled intranasal therapy for central nervous system neoplasms: an emerging therapeutic option. *Journal of Neuro-Oncology*, 116(3), pp. 437–446.

PILLAI, J.D. et al. (2011) Novel platforms for vascular carriers with controlled geometry. *IUBMB Life*, 63(8), pp. 596–606.

PLA, A., PASCUAL, M. and GUERRI, C. (2016) Autophagy Constitutes a Protective Mechanism against Ethanol Toxicity in Mouse Astrocytes and Neurons. *PLOS ONE*, 11(4), p. e0153097.

PLATTEN, M. (2019) How to integrate immunotherapy into standard of care in glioblastoma. *Neuro-Oncology*, 21(6), pp. 699–700.

PONTEN, J. and MACINTYRE, E.H. (1968) LONG TERM CULTURE OF NORMAL AND NEOPLASTIC HUMAN GLIA. *Acta Pathologica Microbiologica Scandinavica*, 74(4), pp. 465–486.

POPAT JADHAV, S. et al. (2020) Review on novel approaches for targeting drugs to the brain. *World Journal of Pharmaceutical Research*, 9.

POZAROWSKI, P. and DARZYNKIEWICZ, Z. (2004) Analysis of Cell Cycle by Flow Cytometry. *Methods in molecular biology*, 281, pp. 301–311.

Q

QIANG, L. et al. (2009) Isolation and characterization of cancer stem like cells in human glioblastoma cell lines. *Cancer Letters*, 279(1), pp. 13–21.

QIU, M. et al. (2018) Small-Sized and Robust Chimaeric Lipopepsomes: A Simple and Functional Platform with High Protein Loading for Targeted Intracellular Delivery of Protein Toxin in Vivo. *Chemistry of Materials*, 30(19), pp. 6831–6838.

QUARTA, A. et al. (2019) Nanoheterostructures (NHS) and their applications in nanomedicine: focusing on *in vivo* studies. *Materials*, 12(1), p. 139.

R

RACCA, L. and CAUDA, V. (2021) Remotely Activated Nanoparticles for Anticancer Therapy. *Nano-Micro Letters*, 13(1).

RACHAKATLA, R.S. et al. (2010) Attenuation of Mouse Melanoma by A/C magnetic field after delivery of Bi-magnetic nanoparticles by neural progenitor cells. *ACS Nano*, 4(12), pp. 7093–7104.

RAJAGOPALAN, S. et al. (2017) Airway management for caesarean delivery performed under general anaesthesia. *International Journal of Obstetric Anaesthesia*, 29, pp. 64–69.

RAMVIKAS, M. et al. (2017) Nasal Vaccine Delivery. In: Micro- and Nanotechnology in Vaccine Development. *Elsevier Inc.*, pp. 279–301.

RAN, R. et al. (2019) A Microfluidic Tumour-on-a-Chip for Assessing Multifunctional Liposomes' Tumour Targeting and Anticancer Efficacy. *Advanced Healthcare Materials*, 8(8), p. 1900015.

RAO, L. et al. (2017) Microfluidic Electroporation-Facilitated Synthesis of Erythrocyte Membrane-Coated Magnetic Nanoparticles for Enhanced Imaging-Guided Cancer Therapy. *ACS Nano*, 11, p. 0.

RAVI, M. et al. (2015) 3D Cell Culture Systems: Advantages and Applications. *Journal of Cellular Physiology*, 230(1), pp. 16–26.

RAZAZAN, A. et al. (2017) Conjugated nanoliposome with the HER2/ neu-derived peptide GP2 as an effective vaccine against breast cancer in mice xenograft model. *PloS one*, 12(10), e0185099.

RAZPOTNIK, R. et al. (2017) Targeting malignant brain tumours with antibodies. *Frontiers in Immunology*, 8(9), p. 1181.

REES, J.A. et al. (2018) Evaluating the potential of chelation therapy to prevent and treat gadolinium deposition from MRI contrast agents. *Scientific Reports*, 8(1), pp. 1–9.

RENNER, C. et al. (2013) Carnosine inhibits ATP production in cells from malignant glioma. *Neurological research*, 32(1), pp. 101–105.

RENNER, C. et al. (2008) Carnosine inhibits growth of cells isolated from human glioblastoma multiforme. *International Journal of Peptide Research and Therapeutics*, 14(2), pp. 127–135.

RENNER, C. et al. (2010) Carnosine retards tumour growth in vivo in an NIH3T3-HER2/neu mouse model. *Molecular Cancer*, 9(1), pp. 1–7.

RIGNEAU, P. et al. (1999) Microwave flash-synthesis of iron oxides nanoparticles. *The European Physical Journal - Applied Physics*, 7(1), pp. 41–43.

RIVERA GIL, P. et al. (2010) Nanopharmacy: Inorganic nanoscale devices as vectors and active compounds. *Pharmacological Research*, 62(2), pp. 115–125.

ROCA, A.G. et al. (2009) Progress in the preparation of magnetic nanoparticles for applications in biomedicine. *Journal of Physics D: Applied Physics*, 42(22), p. 224002.

S

S. A. HAGAN et al. (1996) Polylactide−Poly(ethylene glycol) Copolymers as Drug Delivery Systems. 1. Characterization of Water Dispersible Micelle-Forming Systems. *Langmuir*, 12(9), pp. 2153–2161.

SADER, J.E., CARNIE, S.L. and CHAN, D.Y.C. (1995) Accurate Analytic Formulas for the Double-Layer Interaction between Spheres. *Journal of Colloid and Interface Science*, 171(1), pp. 46–54.

SAINI, S. et al. (1987) Ferrite particles: A superparamagnetic MR contrast agent for enhanced detection of liver carcinoma. *Radiology*, 162(1), pp. 217–222.

SAKANE, T. et al. (2009) Transnasal Delivery of 5-Fluorouracil to the Brain in the Rat. *Journal of drug targeting*, 7(3), pp. 233–240.

SALAMEH, T.S. et al. (2015) Central Nervous System Delivery of Intranasal Insulin: Mechanisms of Uptake and Effects on Cognition. *Journal of Alzheimer's Disease*, 47(3), pp. 715–728.

SALAVATI-NIASARI, M., MAHMOUDI, T. and AMIRI, O. (2012) Easy Synthesis of Magnetite Nanocrystals *via* Coprecipitation Method. *Journal of Cluster Science*, 23(2), pp. 597–602.

SALONI, B. et al. (2021) Strategic Drug Delivery Targeted to the Brain: A Review. *Pharmaceutical Resonance*, 3(2).

SAWYERS, C. (2004) Targeted cancer therapy. *Nature*, 432(7015), pp. 294–297.

SCHLEICH, N. et al. (2013) Dual anticancer drug/superparamagnetic iron oxide-loaded PLGA-based nanoparticles for cancer therapy and magnetic resonance imaging. *International Journal of Pharmaceutics*, 447(1–2), pp. 94–101.

SCHLENOFF, J.B. (2014) Zwitteration: Coating surfaces with zwitterionic functionality to reduce nonspecific adsorption. *Langmuir*, 30(32), pp. 9625–9636.

SCHNEIDER, C.A., RASBAND, W.S. and ELICEIRI, K.W. (2012) NIH Image to ImageJ: 25 years of image analysis. *Nature methods*, 9(7), pp. 671–675.

SCHULZ, A.K. et al. (2021) Suction feeding by elephants. *Journal of the Royal Society Interface*, 18(179), p. 20210215.

SCHWENDENER, R.A. (2014) Liposomes as vaccine delivery systems: a review of the recent advances. *Therapeutic advances in vaccines*, 2(6), pp. 159–82.

SEJU, U., KUMAR, A. and SAWANT, K.K. (2011) Development and evaluation of olanzapine-loaded PLGA nanoparticles for nose-to-brain delivery: In vitro and in vivo studies. *Acta Biomaterialia*, 7(12), pp. 4169–4176.

SEMETE, B. et al. (2010) In vivo evaluation of the biodistribution and safety of PLGA nanoparticles as drug delivery systems. Nanomedicine: Nanotechnology, *Biology and Medicine*, 6(5), pp. 662–671.

SERRES, S. et al. (2012) Molecular MRI enables early and sensitive detection of brain metastases. *Proceedings of the National Academy of Sciences of the United States of America*, 109(17), pp. 6674–6679.

SERWER, L.P. and JAMES, C.D. (2012) Challenges in drug delivery to tumours of the central nervous system: An overview of pharmacological and surgical considerations. *Advanced Drug Delivery Reviews*, 64(7), pp. 590–597.

SFANOS, K.S. and MARZO, A.M. DE (2012) Prostate cancer and inflammation: the evidence. *Histopathology*, 60(1), pp. 199–215.

SHADAB, M.D. et al. (2013) Bromocriptine loaded chitosan nanoparticles intended for direct nose to brain delivery: Pharmacodynamic, Pharmacokinetic and Scintigraphy study in mice model. European *Journal of Pharmaceutical Sciences*, 48(3), pp. 393–405.

SHAH, B., KHUNT, D. and MISRA, M. (2021) Comparative evaluation of intranasally delivered quetiapine loaded mucoadhesive microemulsion and polymeric nanoparticles for brain targeting: pharmacokinetic and gamma scintigraphy studies. *Future Journal of Pharmaceutical Sciences*, 7(1), p. 1-12.

SHAH, R. et al. (2008) Designer emulsions using microfluidics. *Elsevier*, *Materials Today*, 11(4), 18-27.

SHARMA, G. et al. (2010) Polymer particle shape independently influences binding and internalization by macrophages. *Journal of Controlled Release*, 147(3), pp. 408–412.

SHARMA, V.K. and AGRAWAL, M.K. (2021) A historical perspective of liposomes-a bio nanomaterial. *Materials Today: Proceedings*, 45, pp. 2963–2966.

SHEIKOV, N. et al. (2004) Cellular mechanisms of the blood-brain barrier opening induced by ultrasound in presence of microbubbles. *Ultrasound in Medicine & Biology*, 30(7), pp. 979–989.

SHEN, Y. et al. (2014) Carnosine Inhibits the Proliferation of Human Gastric Cancer SGC-7901 Cells through Both of the Mitochondrial Respiration and Glycolysis Pathways. *PLOS ONE*, 9(8), p. e104632.

SHI, W. et al. (2018) Facile Tumour Spheroids Formation in Large Quantity with Controllable Size and High Uniformity. *Scientific Reports* 2018 8:1, 8(1), pp. 1–9.

SHINGAKI, T. et al. (2009) The transnasal delivery of 5-fluorouracil to the rat brain is enhanced by acetazolamide (the inhibitor of the secretion of cerebrospinal fluid). *International Journal of Pharmaceutics*, 377(1–2), pp. 85–91.

SHINGAKI, T. et al. (2010) Transnasal delivery of methotrexate to brain tumours in rats: A new strategy for brain tumour chemotherapy. *Molecular Pharmaceutics*, 7(5), pp. 1561–1568.

SIEGEL, R.L., MILLER, K.D. and JEMAL, A. (2018) Cancer statistics, *2018. CA: A Cancer Journal for Clinicians*, 68(1), pp. 7–30.

SIMEONIDIS, K. et al. (2016) In-situ particles reorientation during magnetic hyperthermia application: Shape matters twice. *Scientific Reports*, 6(1), pp. 1–11.

SIMONE, E.A., DZIUBLA, T.D. and MUZYKANTOV, V.R. (2008) Polymeric carriers: role of geometry in drug delivery. *Expert opinion on drug delivery*, 5(12), pp. 1283–1300.

SIRENKO, O. et al. (2016) Phenotypic characterization of toxic compound effects on liver spheroids derived from ipsc using confocal imaging and three-dimensional image analysis. *Assay and Drug Development Technologies*, 14(7), pp. 381–394.

SOANE, R.J. et al. (2001) Clearance characteristics of chitosan-based formulations in the sheep nasal cavity. *International Journal of Pharmaceutics*, 217(1–2), pp. 183–191.

STACHOWIAK, J.C. et al. (2008) Unilamellar vesicle formation and encapsulation by microfluidic jetting. *Proceedings of the National Academy of Sciences of the United States of America*, 105(12), pp. 4697–4702.

STADLER, M. et al. (2018) Exclusion from spheroid formation identifies loss of essential cell-cell adhesion molecules in colon cancer cells. *Scientific Report*, 8(1), pp. 1–16.

STOCKE, N.A. et al. (2017) Toxicity evaluation of magnetic hyperthermia induced by remote actuation of magnetic nanoparticles in 3D micrometastasic tumor tissue analogs for triple negative breast cancer. *Biomaterials*, 120, pp. 115–125.

STOLK, D.A. et al. (2020) Lipo-Based Vaccines as an Approach to Target Dendritic Cells for Induction of T- and iNKT Cell Responses. *Frontiers in Immunology*, 11, p. 990.

STUPP, R. et al. (2005) Radiotherapy plus Concomitant and Adjuvant Temozolomide for Glioblastoma. *New England Journal of Medicine*, 352(10), pp. 987–996.

SUH, S.K. et al. (2012) Synthesis of nonspherical superparamagnetic particles: In situ coprecipitation of magnetic nanoparticles in microgels prepared by stop-flow lithography. *Journal of the American Chemical Society*, 134(17), pp. 7337–7343.

SUMA, D. and DENG, D. (2015) Facile synthesis of Fe_3O_4g-C nanorods for reversible adsorption of molecules and absorption of ions. *ACS Sustainable Chemistry and Engineering*, 3(1), pp. 133–139.

SUN, H. et al. (2012) Solvothermal Synthesis of Tunable Electroactive Magnetite Nanorods by Controlling the Side Reaction. *The Journal of Physical Chemistry C*, 116(9), pp. 5476–5481.

SURESH, S. (2007) Biomechanics and biophysics of cancer cells. *Acta Materialia*, 55(12), pp. 3989–4014.

SVENSKAYA, Y. et al. (2013a) Anticancer drug delivery system based on calcium carbonate particles loaded with a photosensitizer. *Biophysical Chemistry*, 182, pp. 11–15.

T

TAFAGHODI, M. et al. (2004) Evaluation of the clearance characteristics of various microspheres in the human nose by gamma-scintigraphy. *International Journal of Pharmaceutics*, 280(1–2), pp. 125–135.

TAGHAVI, S. et al. (2017) Chitosan-modified PLGA nanoparticles tagged with 5TR1 aptamer for in vivo tumour-targeted drug delivery. *Cancer Letters*, 400, pp. 1–8.

TAHARA, K. et al. (2013). Quantum dot-loaded liposomes to evaluate the behavior of drug carriers after oral administration. *Journal of pharmaceutics*, 2013, pp. 6.

TAKI, H. et al. (2012) Intranasal Delivery of Camptothecin-Loaded Tat-Modified Nanomicells for Treatment of Intracranial Brain Tumours. *Pharmaceuticals*, 5(10), pp. 1092–1102.

TAY, S.K. (2012) Cervical cancer in the human papillomavirus vaccination era. *Current Opinion in Obstetrics and Gynaecology*, 24(1), pp. 3–7.

VAN TELLINGEN, O. et al. (2015) Overcoming the blood–brain tumour barrier for effective glioblastoma treatment. *Drug Resistance Updates*, 19, pp. 1–12.

TEMIZOZ, B., KURODA, E. and ISHII, K.J. (2016) Vaccine adjuvants as potential cancer immunotherapeutic. *International Immunology*, 28(7), pp. 329–338.

VON TEMPELHOFF, W., ULRICH, F. and SCHWARZMAIER, H.J. (2014) Interstitial laser irradiation of cerebral gliomas - Neurobiological background, technique and typical results. *Photonics and Lasers in Medicine*, 3(2), pp. 129–141.

THOMAS, S. et al. (2010) Studies on adsorption of carnosine on silver nanoparticles by SERS. *Chemical Physics Letters*, 491(1–3), pp. 59–64.

THORNE, R.G. et al. (2004) Delivery of insulin-like growth factor-I to the rat brain and spinal cord along olfactory and trigeminal pathways following intranasal administration. *Neuroscience*, 127(2), pp. 481–496.

TIMMINS, N., DIETMAIR, S. and NIELSEN, L. (2004) Hanging-drop multicellular spheroids as a model of tumour angiogenesis. *Angiogenesis*, 7(2), pp. 97–103.

TOMASZ, M. (1995) Mitomycin C: small, fast, and deadly (but very selective). *Chemistry & Biology*, 2(9), pp. 575–579.

TREAT, L.H. et al. (2012) Improved Anti-Tumour Effect of Liposomal Doxorubicin After Targeted Blood-Brain Barrier Disruption by MRI-Guided Focused Ultrasound in Rat Glioma. *Ultrasound in Medicine & Biology*, 38(10), pp. 1716–1725.

TREDAN, O. et al. (2007) Drug Resistance and the Solid Tumour Microenvironment. *JNCI: Journal of the National Cancer Institute*, 99(19), pp. 1441–1454.

TRPKOV, D. et al. (2018) Hydrothermal synthesis, morphology, magnetic properties and self-assembly of hierarchical α-Fe_2O_3 (hematite) mushroom-, cube- and sphere-like superstructures. *Applied Surface Science*, 457, pp. 427–438.

TRUONG, N.P. et al. (2014) The importance of nanoparticle shape in cancer drug delivery. *Expert opinion on drug delivery*, 12(1), pp. 129–142.

U

UEDA, K. and KOMANO, T. (1984) Sequence-specific DNA damage induced by reduced mitomycin C and 7-N-(p -hydroxyphenyl)mitomycin C. *Nucleic Acids Research*, 12(17), pp. 6673–6683.

UJIFUKU, K. et al. (2010) miR-195, miR-455-3p and miR-10a∗ are implicated in acquired temozolomide resistance in glioblastoma multiforme cells. *Cancer Letters*, 296(2), pp. 241–248.

UNTERWEGER, H. et al. (2018) Dextran-coated superparamagnetic iron oxide nanoparticles for magnetic resonance imaging: Evaluation of size-dependent imaging properties, storage stability and safety. *International Journal of Nanomedicine*, 13, pp. 1899–1915.

V

VALDIGLESIAS, V. et al. (2016) Are iron oxide nanoparticles safe? Current knowledge and future perspectives. *Journal of Trace Elements in Medicine and Biology*, 38, pp. 53–63.

VARYPATAKI, E.M. et al. (2016) Synthetic long peptide-based vaccine formulations for induction of cell mediated immunity: A comparative study of cationic liposomes and PLGA nanoparticles. *Journal of Controlled Release*, 226, pp. 98–106.

VASIR, J.K. and LABHASETWAR, V. (2008) Quantification of the force of nanoparticle-cell membrane interactions and its influence on intracellular trafficking of nanoparticles. *Biomaterials*, 29(31), pp. 4244–4252.

VEISEH, O. et al. (2010) Chlorotoxin bound magnetic nanovector tailored for cancer cell targeting, imaging, and siRNA delivery. *Biomaterials*, 31(31), pp. 8032–8042.

VENKATARAMAN, S. et al. (2011) The effects of polymeric nanostructure shape on drug delivery. *Advanced Drug Delivery Reviews*, 63(14–15), pp. 1228–1246.

VERHAAK, R.G.W. et al. (2010) Integrated Genomic Analysis Identifies Clinically Relevant Subtypes of Glioblastoma Characterized by Abnormalities in PDGFRA, IDH1, EGFR, and NF1. *Cancer Cell*, 17(1), pp. 98–110.

VERMA, R. et al. (2019) Computational fluid dynamic analysis of hydrodynamic shear stress generated by different impeller combinations in stirred bioreactor. *Biochemical Engineering Journal*, 151, p. 107312.

W

WACH, J. et al. (2019) Dual-Use Intraoperative MRI in Glioblastoma Surgery: Results of Resection, Histopathologic Assessment, and Surgical Site Infections. *Journal of Neurological Surgery, Part A: Central European Neurosurgery*, 80(6), pp. 413–422.

WALTER, A. et al. (2014) Mastering the shape and composition of dendronized iron oxide nanoparticles to tailor magnetic resonance imaging and hyperthermia. *Chemistry of Materials*, 26(18), pp. 5252–5264.

WALTER, J. et al. (2015) New possibilities of accurate particle characterisation by applying direct boundary models to analytical centrifugation. *Nanoscale*, 7(15), pp. 6574–6587.

WAN, J. et al. (2005) A soft-template-assisted hydrothermal approach to single-crystal Fe_3O_4 nanorods. *Journal of Crystal Growth*, 276, pp. 571–576.

WANG, D., GAO, Y. and YUN, L. (2005) Study on brain targeting of raltitrexed following intranasal administration in rats. *Cancer Chemotherapy and Pharmacology*, 57(1), pp. 97–104.

WANG, R. et al. (2018) PEI-Coated Fe_3O_4 Nanoparticles Enable Efficient Delivery of Therapeutic siRNA Targeting REST into Glioblastoma Cells. *International Journal of Molecular Sciences*, 19(8), p. 2230.

WANG, X. et al. (2009) Control of aggregate size of polyethyleneimine-coated magnetic nanoparticles for magnetofection. *Nano Research*, 2(5), pp. 365–372.

WANG, Y. et al. (2012) One-pot reaction to synthesize superparamagnetic iron oxide nanoparticles by adding phenol as reducing agent and stabilizer. *Journal of Nanoparticle Research*, 14(4), pp. 1–7.

WANG, Y. and KOHANE, D.S. (2017) External triggering and triggered targeting strategies for drug delivery. *Nature Reviews Materials*, 2(6), pp. 1–14.

WANG, Y.-Y. et al. (2008) Addressing the PEG Mucoadhesivity Paradox to Engineer Nanoparticles that "Slip" through the Human Mucus Barrier. *Angewandte Chemie*, 120(50), pp. 9872–9875.

WANI, I.A. (2017) Recent advances in synthesis and biomedical applications of magnetic nanoparticles: Magnetic nanoparticles for biomedical applications. *Integrating Biologically Inspired Nanotechnology into Medical Practice*, pp. 74-101

WEBB, C. et al. (2020) Using microfluidics for scalable manufacturing of nanomedicines from bench to GMP: A case study using protein-loaded liposomes. *International Journal of Pharmaceutics*, 582, p. 119266.

WEN, P.Y. and JUNCK, L. (2014) Bevacizumab for glioblastoma. *Neurology*, 82(19), pp. 1670–1671.

WHITTAKER, M.R. and DAVIS, T.P. (2009) The design and utility of polymer-stabilized iron-oxide nanoparticles for nanomedicine applications. Molecular Systems Biology, *NPG Asia Materials*, 2(1), pp. 23-30.

WINTER, G. et al. (2003) Making Antibodies by Phage Display Technology. *Annual review of immunology*, 12, pp. 433–455.

VAN WOENSEL, M. et al. (2013) Formulations for Intranasal Delivery of Pharmacological Agents to Combat Brain Disease: A New Opportunity to Tackle GBM? *Cancers*, 5(3), pp. 1020–1048.

WONG-MOLINA, A. et al. (2008) Development of Receptor Targeted Magnetic Iron Oxide Nanoparticles for Efficient Drug Delivery and Tumour Imaging. *Journal of Biomedical Nanotechnology*, 4(1), pp. 52–61.

WOO, K. et al. (2004) Easy synthesis and magnetic properties of iron oxide nanoparticles. *Chemistry of Materials*, 16(14), pp. 2814–2818.

WU, S. et al. (2011) Fe3O4 magnetic nanoparticles synthesis from tailings by ultrasonic chemical co-precipitation. *Materials Letters*, 65(12), pp. 1882–1884.

WU, W. et al. (2015) Recent progress on magnetic iron oxide nanoparticles: synthesis, surface functional strategies and biomedical applications. *Science and Technology of Advanced Materials*, 16(2), p. 023501.

X

XIAO, C. et al. (2013) Brain Transit and Ameliorative Effects of Intranasally Delivered Anti-Amyloid-β Oligomer Antibody in 5XFAD Mice. *Journal of Alzheimer's Disease*, 35(4), pp. 777–788.

XIE, W. et al. (2018) Review Shape-, size-and structure-controlled synthesis and biocompatibility of iron oxide nanoparticles for magnetic theranostics. *Theranostics*, 8(12), pp. 3284–3307.

XIN, Y. et al. (2017) PLGA nanoparticles introduction into mitoxantrone-loaded ultrasound-responsive liposomes: In vitro and in vivo investigations. *International Journal of Pharmaceutics*, 528(1–2), pp. 47–54.

XING, L. et al. (2019) Carnosine a natural bioactive dipeptide: bio accessibility, bioavailability, and health benefits. *Journal of Food Bioactives*, 5, pp. 8–17.

XU, F. et al. (2012) Release of magnetic nanoparticles from cell-encapsulating biodegradable nano biomaterials. *ACS Nano*, 6(8), pp. 6640–6649.

Y

YANG, Z.Z. et al. (2013) Enhanced brain distribution and pharmacodynamics of rivastigmine by liposomes following intranasal administration. *International Journal of Pharmaceutics*, 452(1–2), pp. 344–354.

YOON, H.Y. et al. (2014) Glycol chitosan nanoparticles as specialized cancer therapeutic vehicles: Sequential delivery of doxorubicin and Bcl-2 siRNA. *Scientific Reports*, 4(1), pp. 1-12.

YOSSEPOWITCH, O. et al. (2007) Radical Prostatectomy for Clinically Localized, High Risk Prostate Cancer: Critical Analysis of Risk Assessment Methods. *The Journal of Urology*, 178(2), pp. 493–499.

YOUNG, R.M. et al. (2015) Current trends in the surgical management and treatment of adult glioblastoma. *Annals of Translational Medicine*, 3(9), doi.org/10.3978/J.ISSN.2305-5839.2015.05.10 [Accessed 02/11/2021].

YU, L. et al. (2019) Microfluidic formation of core-shell alginate microparticles for protein encapsulation and controlled release. *Journal of Colloid and Interface Science*, 539, pp. 497–503.

ZANGANEH, S. et al. (2016) Iron oxide nanoparticles inhibit tumour growth by inducing pro-inflammatory macrophage polarization in tumour tissues. *Nature Nanotechnology*, 11(11), pp. 986–994.

Z

ZHANG, D.E. et al. (2008) Fabrication and characterization of hollow Fe_3O_4 nanospheres in a microemulsion. *Materials Letters*, 62(24), pp. 4053–4055.

ZHANG, F. et al. (2009) Controlled synthesis and gas-sensing properties of hollow sea urchin-like α-Fe_2O_3 nanostructures and α-Fe_2O_3 nano cubes. *Sensors and Actuators B: Chemical*, 141(2), pp. 381–389.

ZHANG, J., STEVENS, M.F.G. and BRADSHAW, T.D. (2012) Temozolomide: Mechanisms of Action, Repair and Resistance. *Current Molecular Pharmacology*, 5, pp. 102–114.

ZHANG, P. et al. (2017) One-step synthesis of flowerlike C/Fe_2O_3 nanosheet assembly with superior adsorption capacity and visible light photocatalytic performance for dye removal. *Carbon*, 116, pp. 59–67.

ZHANG, Q.Z. et al. (2006) The brain targeting efficiency following nasally applied MPEG-PLA nanoparticles in rats. *Journal of Drug Targeting*, 14(5), pp. 281–290.

ZHANG, X.P. et al. (2018) Astragalus Saponins and Liposome Constitute an Efficacious Adjuvant Formulation for Cancer Vaccines. *Cancer Biotherapy and Radiopharmaceuticals*, 33(1), pp. 25–31.

ZHANG, X.Q. et al. (2012) Interactions of nanomaterials and biological systems: Implications to personalized nanomedicine. *Advanced drug delivery reviews*, 64(13), pp. 1363–1384.

ZHANG, Z. et al. (2012) Activation of the AXL kinase causes resistance to EGFR-targeted therapy in lung cancer. *Nature Genetics*, 44(8), pp. 852–860.

ZHANG, Z. et al. (2018) Development of a novel morphological paclitaxel loaded PLGA microspheres for effective cancer therapy: In vitro and in vivo evaluations. *Drug Delivery*, 25(1), pp. 166–177.

ZHANG, Z. et al. (2016) Ultrasmall Fe2O3 Nanoparticles Anchored on Three-Dimensional Hierarchical Porous Graphene-like Networks for High-Rate Capability Supercapacitors. *ChemElectroChem*, 3(11), pp. 1820–1826.

ZHAO, J. et al. (2017) Fabrication of pH responsive PLGA(UCNPs/DOX) nano capsules with up conversion luminescence for drug delivery. *Scientific Reports*, 7(1), pp. 1–11.

ZHAO, Q. et al. (2012) Magnetic Nanoparticle-Based Hyperthermia for Head & Neck Cancer in Mouse Models. *Theranostics*, 2(1), p. 113.

ZHAO, Z. et al. (2019) Effect of physicochemical and surface properties on in vivo fate of drug nanocarriers. *Advanced Drug Delivery Reviews*, 143, pp. 3–21.

ZHONG, Z. et al. (2010) A novel liposomal vaccine improves humoral immunity and prevents tumour pulmonary metastasis in mice. *International Journal of Pharmaceutics*, 399(1–2), pp. 156–162.

ZHOU, G. and LEVITSKY, H. (2012) Towards curative cancer immunotherapy: Overcoming posttherapy tumour escape. *Clinical and Developmental Immunology*, doi.org/10.1155/2012/124187 [Accessed 28/11/2021].

ZOLNIK, B.S. and BURGESS, D.J. (2008) Evaluation of *in vivo–in vitro* release of dexamethasone from PLGA microspheres. *Journal of Controlled Release*, 127(2), pp. 137–145.

ZOU, G. et al. (2005) Fe_3O_4 Nanocrystals with Novel Fractal. *Journal of Physical Chemistry B*, 109(39), pp. 18356–18360.

ZRAIKAT, M. and ALSHELLEH, T. (2020) Comparison Between Different 3D Spheroid Tumour Invasion Models. *Assay and Drug Development Technologies*, 18(5), pp. 239–242.

ZRINYI, M., BARSI, L. and BUKI, A. (1997) Ferrogel: a new magneto-controlled elastic medium. *Polymer Gels and Networks*, 5(5), pp. 415–427.

ZUCCOLI, G. et al. (2010) Metabolic management of glioblastoma multiforme using standard therapy together with a restricted ketogenic diet: Case Report. *Nutrition and Metabolism*, 7(1), pp. 1–7.

Appendices

1.1 Appendix A: Published papers

- **K. Habra**, J.R.D. Pearson, P. Le Vu, M.J. Cripps, M.A. Khan, M.D. Turner, C. Sale, and S. E. B. McArdle, Investigating the Potential Use of Carnosine as a First Side-Effect-Free Treatment of Localized Prostate Cancer (under review)
- **K. Habra**, J.R.D. Pearson, and S. E. B. McArdle, Robust Formation of Optimal Single Spheroids towards Cost-Effective *In-Vitro* 3-Dimensional Tumor Models, FEBS Open Bio, 2023, DOI:10.1002/2211-5463.13614
- **K. Habra**, S. E. B. McArdle, R. H. Morris, G. W. V. Cave, Controlled release of carnosine from poly(lactic-co-glycolic acid) beads using nanomechanical magnetic trigger towards the treatment of Glioblastoma, Nanoscale Advanced, 2022, DOI: 10.1039/d2na00032f
- **K. Habra**, S. E. B. McArdle, R. H. Morris, G. W. V. Cave, Synthesis and Functionalisation of Superparamagnetic Nano-Rods Towards the Treatment of Glioblastoma Brain Tumours, Nanomaterials, 2021, DOI: 10.3390/nano11092157
- S. Cuzzubbo, S. Mangsbo, D. Nagarajan, **K. Habra**, A. G. Pockley and S. E. B. McArdle, Cancer Vaccines: Adjuvant Potency, Importance of Age, Lifestyle, and Treatments, Frontiers, 2021, 11, DOI: 10.3389/fimmu.2020.615240

1.2 Appendix B: Copy of ethics approval

The pre-clinical studies for evaluation of cancer therapies in orthotopic cancer models were approved by the UK Home Office under the Animals (Scientific Procedures) Act 1986 (PPL number: PP8369045, granted: 08 Oct 21, Expires: 08 Oct 26). All animals will be housed and handled in accordance with the UK Home Office Codes of Practice for the Housing and Care of Animals. The final animal study protocols will be approved by the Institutional Review Board (Animal Welfare Ethical Review Board, AWERB) at Nottingham Trent University.